UniMe
1548

UNIVERSITY OF MESSINA

DEPARTMENT OF ENGINEERING

Doctoral Program in
Engineering and Chemistry of Materials and Constructions

CYCLE XXXVII

COORDINATOR Prof. Proverbio Edoardo

A Thermochemical Strategy for Enhanced Low-Temperature Building Comfort: From Novel Salt Hydrate to Thermally Active Mortars

Disciplinary Scientific Sector S.S.D. IMAT-01/A

Candidate
Dott. Previti Emanuele

Supervisor
Prof. Calabrese Luigi

Anni 2023/2024

UNIONE EUROPEA
Fondo Sociale Europeo

Ministero dell'Università e della Ricerca

PON RICERCA E INNOVAZIONE 2014 - 2020

REACT EU

Index

ABSTRACT i

NOMENCLATURE iii

LIST OF FIGURES v

LIST OF TABLES ix

SCOPE OF THE THESIS xi

Chapter 1 Introduction 1

1.1. Energy demand in buildings: background and effective solutions to restrain it 1

1.2. Thermal energy storage (TES) technologies 10

1.2.1. Sensible heat storage (SHS) 14

1.2.2. SHS solutions for buildings 16

1.3. Latent heat storage (LHS) 21

1.3.1. Classifications of Phase Change Materials (PCMs) 24

1.3.2. PCM composites 29

1.3.3. PCMs in building applications 33

1.4. Thermochemical energy storage (TCES) 38

1.4.1. Classifications of thermochemical materials (TCMs) 41

1.4.2. Salt hydrates for low-temperatures applications 47

1.4.3. Deliquescence phenomenon in traditional inorganic salt hydrates 50

1.4.4. TCM composites for low-temperatures applications 53

1.4.5. Novel organic salt hydrates 56

1.4.6. TCMs in building applications 58

Chapter 2 Calcium L-lactate pentahydrate (CL) 62

2.1. CL: from pharmaceutical excipient to promising TCM 62

2.2. Dehydration and hydration kinetics models for CL 64

2.3. Materials and methods 65

2.3.1. Physical, structural, chemical, and morphological characterizations 65

2.3.2. Thermal stability 67

2.3.3. Thermochemical characterization under isothermal conditions 67

2.3.4. Evaluation of the heat storage capacity 67

2.3.5. Thermogravimetric dynamic vapor sorption analyses 68

2.4. Results and discussion 68
2.4.1. Thermochemical and structural stability 68
2.4.2. Dehydration/Hydration cyclic reversibility 72
2.4.3. Heat storage capacity 81
2.5. General remarks and future outlooks 83
Chapter 3 Deposition of CL on sepiolite matrix 85
3.1. Influence of porous matrices in enhancing TES properties 85
3.2. Sepiolite: an abundant and low-cost mineral matrix 86
3.3. Materials and methods 91
3.3.1. Reagents and preparation method 91
3.3.2. Structural, chemical and physical characterization analyses 93
3.3.3. Thermogravimetric characterization 94
3.3.4. Thermogravimetric dynamic vapor sorption analyses 94
3.3.5. Thermochemical characterization under saturated vapor conditions 95
3.3.6. Morphological characterization 95
3.4. Results and discussion 95
3.4.1. Structural and chemical characterizations 95
3.4.2. Physical characterization 100
3.4.3. Thermal stability 102
3.4.4. Thermogravimetric dynamic vapor sorption characterization 109
3.4.5. Evaluation of materials heat release capacities 113
3.4.6. Morphological observations on sepiolite-based composite materials 117
3.5. General remarks and future outlooks 119
Chapter 4 Composite plaster mortars with CL 121
4.1. Composite mortars integrated with PCMs and TCMs 121
4.2. Mortars with CL for self-healing 123
4.3. Plaster mortars with CL 125
4.4. Materials and methods 127
4.4.1. Plaster mortar preparation 127
4.4.2. Characterization of fresh plaster mortars 131
4.4.3. Mechanical characterization 132

4.4.4. Physical, structural and morphological characterizations 133
4.4.5. Isotherms of water vapor sorption/desorption 134
4.4.6. Thermo-physical characterization under controlled boundary conditions 134
4.5. Results and discussion 136
4.5.1. Characterization of fresh plaster mortar 136
4.5.2. Mechanical characterization of plaster mortars 137
4.5.3. Physical, structural and morphological characterizations of plaster mortars 139
4.5.4. Thermogravimetric dynamic vapor sorption (DVS) analysis 144
4.5.5. Thermal monitoring analysis 145
4.6. General remarks and future outlooks 149
Chapter 5 Composite plaster mortars with CL reinforced with basalt fibers 151
5.1. Basalt fibers for reinforcing mortar composites 151
5.2. Materials and methods 155
5.2.1. Preparation of composite plaster mortars with basalt fibers 155
5.2.2. Characterization of fresh plaster mortar reinforced with basalt fibers 156
5.2.3. Mechanical characterizations 156
5.3. Results and discussion 157
5.3.1. Characterization of fresh plaster mortar reinforced with basalt fibers 157
5.3.2. Flexural behavior 157
5.4. General remarks and future outlooks 163
CONCLUSIONS 165
DISSEMINATION 171
REFRENCES 174

ABSTRACT

The building sector is a major consumer of energy, accounting for a significant portion of global energy consumption and CO_2 emissions. To mitigate the environmental impact of this sector and improve energy efficiency, this research explores the application of an organic salt hydrate as thermochemical materials (TCMs) for low-temperatures thermal energy storage (TES) in buildings. The study focuses on calcium L-Lactate pentahydrate (CL) as a novel TCM and investigates its properties, enhancement through composite materials, and integration into building systems. This thesis work is divided into five chapters, each addressing different aspects of the research.

Chapter 1 provides an overview of the energy demand in the building sector and the importance of developing sustainable solutions to reduce energy consumption. It discusses the various factors influencing energy usage in residential and commercial buildings, highlighting the need for improved energy efficiency and the adoption of renewable energy sources. The chapter also reviews different TES technologies, including sensible heat storage (SHS), latent heat storage (LHS), and thermochemical energy storage (TCES). It introduces the concept of TCMs and their potential for low-temperatures applications in buildings, with a particular focus on organic salt hydrates.

Chapter 2 delves into the characterization of calcium L-Lactate pentahydrate (CL) as a promising TCM. The research explores its thermal and structural stability, as well as its dehydration/hydration cyclic reversibility. Various techniques, including X-ray diffraction (XRD), thermogravimetric-differential scanning calorimetric (TG-DSC), scanning electron microscopy (SEM), Fourier-transform infrared spectroscopy (FTIR), and thermogravimetric dynamic vapor sorption (DVS) were employed. The results demonstrate that CL offers several advantages over traditional inorganic salt hydrates, such as the absence of deliquescence at high relative humidity levels, because of its low water solubility, no risks of generating harmful by-products, robust performance under a wide range of operating conditions, and no decomposition below 200 °C. Its heat storage capacity (471 kWh m^{-3}) and operational characteristics make it a compelling alternative for low-temperatures TES applications.

Chapter 3 focuses on enhancing the thermochemical properties of CL by depositing it onto a sepiolite porous matrix. Sepiolite, a low-cost and abundant

mineral, was shown to be an effective support material for CL dispersion. Composites with varying CL content were realized, and characterization revealed an optimal composition for promoting salt dispersion and vapor exchange. The materials were found to be thermally stable for low-temperatures thermochemical heat storage, with sepiolite playing a crucial role in improving the hydration kinetics of CL. The resulting composite materials exhibited improved thermal stability and a good balance between sorption capacity and material density. These findings demonstrate the potential of sepiolite-based composites for TCES, with the possibility of integration into the building sector where sepiolite already has various applications.

Chapter 4 and **Chapter 5** detail the development and characterization of composite plaster mortars incorporating CL. The addition of CL to the mortars improved heat absorption and delayed the time required for specimens to reach equilibrium temperature, demonstrating the potential for energy savings and enhanced thermal comfort in buildings. The use of natural hydraulic lime (NHL) as an environmentally safe mortar binder contributed to the system's high breathability and crystalline lattice structure. **Chapter 5** further explores the reinforcement of these mortars with rock fibers. Particularly, the inclusion of basalt fibers enhanced the mechanical performance of the composite mortars, significantly improving their toughness. This aspect also addresses the possibility of storing energy, considering not only TCES solutions, but also the energy absorption through residual post-crack resistance processes. The enhanced mechanical performance, coupled with the improved thermal characteristics, indicates that CL-modified fiber reinforced mortars can provide a balance between thermal and structural properties. This balance is vital for their effective implementation in building systems, where materials must satisfy both thermal performance and structural integrity requirements.

In conclusion, this thesis demonstrates the potential of CL as a viable TCM for low-temperatures building applications. The innovative use of CL, both in its pristine form and when integrated with sepiolite and mortar, offers a range of possibilities for enhancing the energy efficiency and thermal comfort of buildings. The findings contribute to the development of more sustainable building materials and provide a foundation for future research and development in this field.

NOMENCLATURE

Abbreviations

APS	Announced Pledges Scenario
BET	Brunauer–Emmett–Teller
BJH	Barrett–Joyner–Halenda
CHPs	Chemical heat pumps
CL	Calcium L-lactate pentahydrate
CL DEH	Dehydrated calcium L-lactate
CL/H*n*h	Calcium L-lactate rehydrated for *n* hours
CSP	Concentrated solar power
DHW	Domestic hot water
DMF	*N,N*-dimethylformamide
DRH	Deliquescence relative humidity
DSC	Differential scanning calorimetry
DTG	Differential thermogravimetric
DVS	Dynamic vapor sorption
ESEM	Environmental scanning electron microscopy
FRMs	Fiber reinforced mortars
FTIR	Fourier-transform infrared spectroscopy
HTF	Heat transfer fluid
HVAC	Heating ventilation air conditioning
ICP-OES	Inductively coupled plasma optical emission spectroscopy
IEA	International Energy Agency
LHS	Latent heat storage
MOFs	Metal organic frameworks
MS	Mass spectrometer
NHL	Natural hydraulic lime
NZE	Net Zero Emission
OECD	Organisation for Economic Co-operation and Development
PCMs	Phase change materials
PEG	Polyethylene glycol
PV	Photovoltaic
RH	Relative humidity
SEM	Scanning electron microscopy
SHS	Sensible heat storage
STA	Simultaneous thermal analyzer
TCES	Thermochemical energy storage
TCMs	Thermochemical materials
TES	Thermal energy storage
TG	Thermogravimetric
TG-DSC	Thermogravimetric-differential scanning calorimetric
TG-DTA	Thermogravimetric-differential thermal analysis
TRL	Technology readiness level
VAV	Variable air volume
XRD	X-ray diffraction

Symbols

%void	Void percentage
A_{CL}	Area of hysteresis for calcium L-lactate
$A_{composite}$	Area of hysteresis for generic composite
b	Width of beam in three-point bending test
Cp	Specific heat
Cp_L	Average specific heat of the liquid phase
Cp_S	Average specific heat of the solid phase
ΔA	Ratio of hysteresis area
ΔH	Enthalpy of reaction
Δm_{th}^{D}	Theoretical mass change linked to dehydration process
Δm_{th}^{H}	Theoretical mass change linked to hydration process
ΔV	Volume change
F	Bending force
h	Height in three-point bending test
hf	Heat flow
L	Span length in three-point bending test
λ	Latent heat of the phase change process
m	Mass of heat storage medium
M_{CL}	Molecular weight of calcium L-lactate pentahydrate
$M_{CL\ DEH}$	Molecular weight of anhydrous calcium L-lactate
n_{CL}	Number of moles of calcium L-lactate
n_{H2O}	Number of moles of water
n_{mol}	Number of moles
Q_{bind}	Binding Heat
Q_{charg}	Heat for charging sorption systems
Q_{cond}	Condensation heat
Q_{des}	Heat for desorbing sorption systems
Q_S	Quantity of heat stored
Q_S^m	Heat storage capacity per mass unit
Q_S^v	Heat storage capacity per volume unit
Q_{sens}	Sensible heat in sorption systems
ρ_A	Density of anhydrous calcium L-lactate
ρ_P	Density of pentahydrate calcium L-lactate
S_{BET}	Specific surface area
σ_{cs}	Compressive strength
σ_{fs}	Flexural strength
T_f	Final temperature
t_f	Final time
T_i	Initial temperature
t_i	Initial time
T_m	Melting temperature
V_g	Geometric volume
V_p	Pycnometric volume
w/c ratio	Water to cement ratio
w/l ratio	Water to lime ratio

LIST OF FIGURES

Figure 1.1 CO_2 emissions by end-use in the buildings sector in the Announced Pledges (APS) and Net Zero Emissions (NZE) by 2030 scenarios. Other includes emissions from desalination, lighting and fossil fuel-powered appliances [3]. 1
Figure 1.2 Residential building primary energy end uses [12]. 3
Figure 1.3 Commercial building primary energy end uses [12]. 4
Figure 1.4 Energy density values and comparison of the required storage volumes of various TES materials including SHS materials, PCMs, and TCMs [52]. 12
Figure 1.5 Stored heat at different temperatures in a SHS material. 15
Figure 1.6 Thermal energy storage (TES) integration in buildings [78]. 17
Figure 1.7 Solar heated water tank integrated in the living area of an apartment [78]. 18
Figure 1.8 Operating scheme of a packed pebble bed storage unity [81]. 20
Figure 1.9 Stored heat at different temperatures in a LHS material. 22
Figure 1.10 Classification of phase change materials (PCMs). 25
Figure 1.11 Spherical microcapsule of PCM [102]. 31
Figure 1.12 Micronal® PCM-integrated gypsum wallboard [119]. 35
Figure 1.13 Operating scheme of a thermochemical material (TCM). 39
Figure 1.14 Thermochemical storage systems studied for medium and high temperatures [147]. 42
Figure 1.15 Open (left) and closed (right) systems for TCES [61]. 44
Figure 1.16 Schematic representation of a) deliquescence phenomenon during hydration of inorganic salt hydrate; b) formation of a wetting layer during hydration of organic salt hydrate, which prevents deliquescence. 52
Figure 2.1 Calcium L-lactate Pentahydrate (CL) unit formula structure. The constituent elements are: Carbon (grey), Oxygen (red), Hydrogen (white) and Calcium (yellow). 62
Figure 2.2 Schematic representation of environmental scanning electron microscopy (ESEM) conditions. 67
Figure 2.3 TG profile of CL as purchased heating up the sample from r.T. up to 900 °C by 10 °C min^{-1} under an inert atmosphere (Ar 120 mL min^{-1}). Detected gaseous evolved species by MS: ionic masses (m x^{z+}) 44 (CO_2) and 18 (H_2O). 69
Figure 2.4 Isothermal TG analyses in the temperature range 40-80 °C. 71
Figure 2.5 XRD analysis on ex situ thermally treated CL at varying temperature (from r.T to 80 °C). 72
Figure 2.6 Three dehydration/hydration isothermal cycles at 30 °C. 73
Figure 2.7 DVS analysis of CL DEH under isobaric conditions. 75
Figure 2.8 FTIR spectra of fresh CL, after dehydration at 80 °C for 2h (CL DEH), hydrated for 2h (CL/H2h) and 6h (CL/H6h) at 30 °C under a p/p_0 of 80%. 76
Figure 2.9 SEM micrographs of (a) low and (b) high magnification of fresh CL, (c) CL DEH, (d) CL/H2h and (e) CL/H6h. 77

Figure 2.10 XRD patterns comparison of fresh CL, after dehydration at 80 °C for 2h (CL DEH), hydrated for 2h (CL/H2h) and 6h (CL/H6h) at 30 °C under a p/p_0 of 80%. 78
Figure 2.11 Selected ESEM micrographs of CL DEH under varying temperature and water vapor pressure in the ranges of 5-60 °C and 10-810 Pa, respectively. The selected conditions mimic a hydration/dehydration cycle. Micrograph (a) is taken at the beginning of in situ analysis on ex situ dehydrated sample. Micrograph (b) is taken at increasing p/p_0. Micrographs (c), (d), (e) are taken at the highest p/p_0 at different holding times of 30, 60 and 120 minutes, respectively. Micrograph (f) is taken after holding the sample at 60 °C for 12h under 0% p/p_0. 80
Figure 2.12 Dehydration TG-DSC profiles for the evaluation of the heat storage capacity of CL. 81
Figure 3.1 a) Unit cell of sepiolite projected on the ab plane. The c-axis points towards the reader. b) Three-dimensional representation of sepiolite structure showing open channels and internal cavities (tunnels). c) Representation of a single sepiolite fiber showing structural intracrystalline microporosity. d) Schematic representation of sepiolite fibers reunited in a bundle highlighting the textural porosity. 89
Figure 3.2 Synthetic procedure for preparing sepiolite and CL based composite materials, using DMF as dispersing medium. 92
Figure 3.3 Description of the system used for hydrating sample. 93
Figure 3.4 XRD patterns of sepiolite and dehydrated composite materials. It is furnished a comparison among pristine sepiolite and the reference PDF. 96
Figure 3.5 XRD patterns of hydrated composite materials. Phase identification of calcium L-lactate pentahydrate is provided according to the referred phase (PDF 00-070-1076). Diffractogram of sepiolite is reported for comparison. 97
Figure 3.6 FTIR spectra of CL DEH, sepiolite DEH and composite materials. 98
Figure 3.7 FTIR spectra of CL, sepiolite and hydrated composite materials. 100
Figure 3.8 Nitrogen adsorption/desorption isotherms at -196 °C of sepiolite and S-CL30. 101
Figure 3.9 a) TG and DTG profiles of pristine sepiolite from 30 to 600 °C in air atmosphere. The three dehydration steps are marked. b) FTIR spectra of exhausted gases developed during the TGA of pristine sepiolite collected at different temperatures. 103
Figure 3.10 a) TG and DTG profiles of pristine calcium L-lactate pentahydrate (CL) from 30 to 600 °C in air atmosphere. The three thermal events are marked. b) FTIR spectra of exhausted gases developed during the TGA of pristine CL collected at different temperatures. 105
Figure 3.11 TG and DTG profiles of prepared composite materials from 30 to 600 °C in air atmosphere. Like the case of CL, three main thermal events were detected. 106
Figure 3.12 a) FTIR spectra of exhausted gases developed during the TGA of S-CL30 collected at different temperatures. b) FTIR spectra of exhausted gases developed during the TGA of S-CL65 collected at different temperatures. 108
Figure 3.13 Water vapour sorption/desorption isotherms at 30 °C of pristine and synthesized materials. The isotherms of composites were normalized with respect to the CL content in each material. 110
Figure 3.14 Hysteresis reduction efficiency of investigated materials. 112

Figure 3.15 TG profiles of investigated materials recorded during the temperature decrease from 80 °C to 28 °C under a water vapor pressure of 3150 Pa. 113
Figure 3.16 SEM micrographs of pristine sepiolite at different magnifications. 117
Figure 3.17 SEM micrographs of: a-b) S-CL30 before and after hydration treatment, respectively; c-d) S-CL50 before and after hydration treatment, respectively; e-f) S-CL65 before and after hydration treatment, respectively. Red circles indicate the presence of CL particle. Yellow circles indicate the presence of pores. 118
Figure 4.1 Description of dehydration and hydration processes undergone by the salt hydrate respectively during the day and the night. IN and OUT indicate the indoor and external temperatures, respectively. The light blue arrow (RH) exemplifies the relative humidity variation during the day and the night..... 127
Figure 4.2 Schematic procedure for preparing fresh plaster mortars with CL. 130
Figure 4.3 100×100×20 mm^3 square base block specimens after 28 days of aging. 131
Figure 4.4 Spread of a fresh plaster mortar after 15 jolts of flow table. 131
Figure 4.5 Schematic procedure for preparing 160x40x40 mm^3 prism mortars destined to mechanical characterization. 132
Figure 4.6 a) Picture of the system used for thermal monitoring of the prepared mortar samples; b) 24 h cycle in which the controlled boundary conditions are varied. 135
Figure 4.7 Values of flexural (a) and compressive (b) strength after 14 and 28 days of aging, at varying salt content in the mixture. 138
Figure 4.8 Diffractograms of calcium L-lactate pentahydrate (CL) and grinded plaster mortars..... 141
Figure 4.9 a) Formation of superficial efflorescence over an exceed mortar at 5%wt. after 2 days of curing. b) Diffractograms of efflorescence crystals and identified PDF..... 142
Figure 4.10 SEM micrographs of mortars with (A1, A3 and A5) and without CL (A0). a-b) A0 mortar; c-d) A1 mortar; e-f) A3 mortar; g-h) A5 mortar. Red circles indicate the presence of CL phase. Yellow and light blue arrow indicate the presence of calcite (CC) and aluminum silicate (AS) phases, respectively..... 143
Figure 4.11 Water vapour sorption/desorption isotherms at 30 °C of prepared composite materials. 145
Figure 4.12 Monitoring of specimen mass during a diurnal hydration/dehydration cycle under controlled boundary conditions. 145
Figure 4.13 Monitoring internal surface temperatures of mortar composites during controlled hydration/dehydration conditions. 147
Figure 4.14 a) Enlargement of temperature transitions observed during the heating phase. b) Enlargement of temperature transitions observed during the heating phase. 148
Figure 5.1 a) Effect of bending force on micro cracks present in a mortar. The applied force provokes specimen failure. b) Effect of bending force on micro cracks present in a fiber hooked-end reinforced mortar (FRM). The fibers contain the crack propagation, under the action of the applied force. 152
Figure 5.2 a) Commercial straight basalt fibers (13 mm length) used for preparation of reinforced plaster mortars. b) Magnification of broken piece of reinforced mortars at highest basalt fibers content (0.2%wt.)..... 155

Figure 5.3 Load vs displacement curves for (a) mortars without CL and (b) mortars with 3%wt. of CL, under three-point flexural test. 158
Figure 5.4 Flexural performance parameters on the three-point flexural curve. 160
Figure 5.5 Relationship between basalt fiber content and the toughness of mortar composites at specified L/50 and L/25 deflections. 162

LIST OF TABLES

Table 1.1 Key differences between active and passive systems. 5
Table 1.2 Characteristic of the different TES technologies. In "Maturity of technology" section is reported the technology readiness level (TRL) for each TES system. 14
Table 1.3 Physical properties of most investigated liquid SHS storage mediums at 20-25 °C [45]. ... 19
Table 1.4 Physical properties of most investigated solid SHS storage mediums at 20-25 °C. 20
Table 1.5 Thermophysical properties of organic PCMs for building applications. 36
Table 1.6 Thermophysical properties of inorganic PCMs for building applications. 37
Table 1.7 Theoretical (Th.) and experimental (Ex.) energy density and reaction temperature conditions of promising material couples for chemical heat storage in residential applications. 59
Table 2.1 Density values of calcium L-lactate pentahydrate and calcium L-lactate anhydrous expressed in kg m^{-3} and measured through an He pycnometer at 20 °C. 82
Table 2.2 Comparison of the thermophysical characteristics (molecules of H_2O involved in the dehydration process (n_{mol}); heat storage capacity per mass (Q^m) and volume (Q^v) of material and working conditions (dehydration (T_{deh}) and hydration (T_{hyd}) temperatures)) of CL and other selected common inorganic salt hydrates. 83
Table 3.1 Chemical composition of Pangel S9 (sepiolite 85%) detected by ICP-OES. 91
Table 3.2 Code of realized composite materials with the corresponding nominal weight fraction of constituents. 93
Table 3.3 BET surface area and total pore volume of host matrix and composite materials. 101
Table 3.4 Percentage variations of investigated materials DVS hysteresis, calculated as the ratios of the areas between the desorption and sorption curves, according to Equation (3.1). 111
Table 3.5 List of calculated hydration enthalpies, measured real densities and estimated volumetric release capacities (QRv) of investigated materials. 114
Table 3.6 List of most investigated PCMs/TCMs combined with sepiolite to prepare composite materials for TES applications. For each material, the corresponding class (PCMs or TCMs) and its nominal weight fraction in the composite are reported. Additionally, for PCMs, the enthalpy associated with the melting process and the corresponding temperature are specified. For TCMs, the gravimetric energy storage/release capacities, the temperature range for the dehydration reaction, and the investigated temperature of hydration are included. 115
Table 4.1 Constituents of plaster mortar divided by type. Furthermore, the weight percentages (%wt.) of the various constituents are indicated. 128
Table 4.2 Codes of all prepared plaster mortar specimens. For each formulation is reported CL and water contents. 130
Table 4.3 Measured spread for investigated fresh plaster mortars. It has been reported also the corresponding water content used for preparing mortar and the theoretical w/l ratio. 136
Table 4.4 Percentage increase in flexural ($\Delta\sigma_{fs}$) and compressive ($\Delta\sigma_{cs}$) strengths of the CL specimens at 14 and 28 days of hardening, calculated with respect to the corresponding values for A0 samples. 138

Table 4.5 Bulk and real densities of investigate plaster mortars. The percentage of voids (%void) calculated according to Equation (4.1) is also reported. 139
Table 5.1 Codes of all prepared plaster mortar specimens. For each formulation is reported CL, basalt fibers and water contents. 156
Table 5.2 Measured spread for investigated fresh plaster mortars reinforced with basalt fibers. It has been reported also the corresponding water content used for preparing mortar. 157
Table 5.3 Flexural loads, deflections and toughness for all investigated composite mortars. 162

SCOPE OF THE THESIS

This thesis aims to develop innovative composite mortars that integrate passive thermal insulation strategies for enhanced energy efficiency in buildings. In response to the increasing global energy demand and the significant contribution of the building sector to energy consumption and CO_2 emissions, this research seeks to address the need for sustainable and energy-efficient building materials.

To this end, scientific research has focused on identifying innovative materials that can effectively harness solar energy by capturing heat that would otherwise be lost. The selection of these materials has focused on thermal energy storage (TES) materials, particularly thermochemical materials (TCMs). Compared to other TES systems, TCMs offer greater energy storage capacity per unit volume and minimal energy losses during charging and discharging phases. In the typical temperature and pressure conditions found in buildings, inorganic hydrated salts are commonly employed. Although these salts exhibit high energy density, they are susceptible to the phenomenon of deliquescence, which poses challenges from an application standpoint. Furthermore, limited research exists on the direct integration of TCMs into building systems. To overcome these limitations, this thesis discusses the use of a promising organic hydrated salt. This recent class of hydrated salts exhibits low or negligible water solubility, providing greater resistance to deliquescence issues. Specifically, the selected salt, calcium L-lactate pentahydrate (CL), was chosen for its interesting properties, including wide availability, chemical and thermal stability, and non-toxicity. This salt also presents a high energy storage capacity due to the dehydration of its five coordinated water molecules. Evaluating this material as a low-temperatures thermochemical energy storage medium was the first objective of this thesis. This assessment was carried out using various characterization techniques to determine the storage capacity and verify the reversibility of the hydration and dehydration processes.

The second objective focused on enhancing the thermochemical properties of CL by depositing it onto a porous sepiolite matrix. The aim was to improve the distribution of salt particles onto the sepiolite surface, in order to facilitate the vapor exchange with the environment and enhance the mass transfer efficiency. This strategy involved the synthesis of composite materials with varying matrix content, and the subsequent

characterization of their physical, structural, morphological, and thermochemical properties.

The third objective explored the ability of CL to influence indoor climate. To this end, the integration of the salt into plaster mortar materials was investigated. Using a binder that ensures high breathability of the mortar matrix, the prepared materials demonstrated interesting capacities, under the investigated conditions, in enhancing thermal comfort inside buildings. Specifically, the composite mortars were designed to capture solar heat during the day, by shielding the indoor environment, and release the stored heat during the night, thereby increasing indoor temperature. Lastly, with the aim of reinforcing the investigated mortars, basalt fibers of appropriate dimensions were added to the mixture. The fibers ensured improved mechanical features, particularly affecting the toughness of the mortars and adding a supplementary form of energy storage related to the residual post-crack resistance processes.

In addition, the development of plaster mortars with CL represents an advancement in the technology readiness level (TRL). In fact, the TRL 1 (basic principle observed) was achieved during the early-stage investigations of CL and its potential as a TCM. The observation of its thermal properties, stability, and hydration/dehydration behavior falls under this level. TRL 2 (technology concept formulated) involves the exploration of possible applications of CL for TES. The concept of utilizing CL's properties for building applications and enhancing its performance through composite materials is developed at this stage. TRL 3 (experimental proof of concept at laboratory scale) was instead achieved when experimental validation of the technology concept is performed. This stage involves the development and characterization of CL-based composite materials, particularly the sepiolite composites and the plaster mortars. The experimental results from these studies provide proof that the CL-based TCM concept can be realized.

The presented objectives are discussed in depth throughout this thesis work. The division into chapters allows for more efficient identification of the topics addressed and the strategies implemented to achieve the corresponding objectives. Finally, the findings obtained contribute to the development of more sustainable building materials and provide a foundation for future research and advancement in this field.

Chapter 1 Introduction

1.1. Energy demand in buildings: background and effective solutions to restrain it

Recent reports from the International Energy Agency (IEA) show that energy use in the building sector accounts for nearly a third of global energy consumption [1–3]. In 2023, total final energy consumption for buildings was estimated at around 125 EJ (exajoules), within a slight 0.7% decrease from 2022. This drop was primarily due to a warmer winter, which reduced demand for space heating. A closer examination of the types of energy consumed reveals that the use of fossil fuels has decreased significantly, in part due to the rising prices resulting from recent geopolitical events. Conversely, electricity consumption in buildings has continued to rise over the past decade, reaching 37% of total worldwide electricity usage in 2023. As a result, in 2023, direct CO_2 emissions from buildings were estimated at 3 Gt (gigatons), or 15% of end-use sector emissions. This percentage increases to nearly 30% when including indirect CO_2 emissions derived from the electricity and heat used in buildings [3]. **Figure 1.1** presents prospects for reductions in direct CO_2 emissions, the primary anthropogenic greenhouse gas, under two potential scenarios.

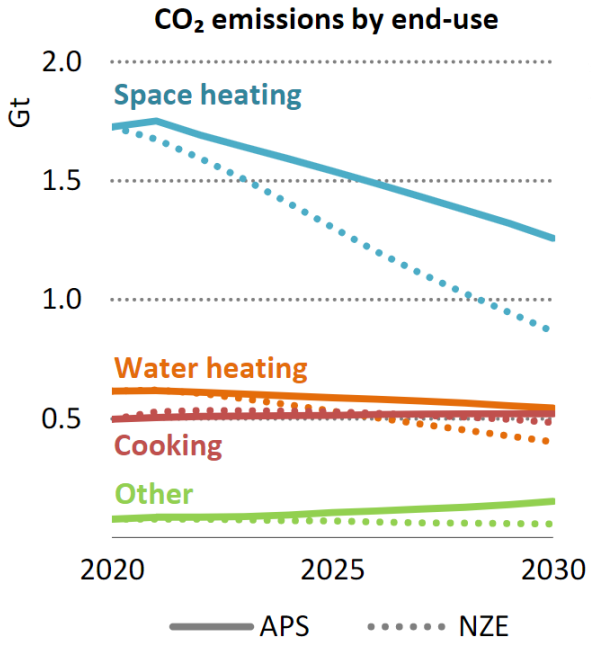

Figure 1.1 CO_2 emissions by end-use in the buildings sector in the Announced Pledges (APS) and Net Zero Emissions (NZE) by 2030 scenarios. Other includes emissions from desalination, lighting and fossil fuel-powered appliances [3].

These scenarios depict different pathways the energy sector could follow. The Announced Pledges Scenario (APS) examines the outcome if all national energy and climate targets, including net-zero goals, are fully and timely achieved. The Net Zero Emissions (NZE) by 2050 scenario outlines an increasingly constrained path to reach net-zero emissions by mid-century and limit global warming to 1.5 °C. According to trends up to 2030 in these two pathways, most emissions derive from space heating, which also includes cooling buildings. Many systems like air conditioning, refrigerators, and heat pumps consume substantial electricity and emit large quantities of greenhouse gases. The buildings sector energy consumption balance will shift significantly from space heating towards space cooling in the coming decades [1]. In the APS, demand falls by 13 EJ due to new initiatives such as the European Union's Energy Performance of Buildings Directive [4], the 6th Strategic Energy Plan in Japan [5], and the Zero Emissions Building Standard in the United States [6]. However, in emerging and developing economies, space heating demand remains heavily concentrated in a few large markets, notably China and Russia.

The demand for space cooling in emerging markets and developing economies is, on the other hand, projected to grow significantly, with the APS scenario indicating a tripling from 2.6 EJ to 7.7 EJ by 2050. This mounting energy demand for cooling is the primary driver of increasing peak electricity consumption from buildings in these regions. Among countries that have set net-zero emissions targets, the focus of pledges to reduce cooling-related emissions by 2030 has so far been on improving the efficiency of cooling appliances [1].

Energy usage across all consumption sectors is rising, but the building sector exhibits the fastest growth rate [7]. This growing trend, coupled with unprecedented shifts in living standards and economic circumstances, underscores the importance of the building sector developments in shaping future global energy landscapes. Within the building sector, two distinct end-use domains can be identified: residential and commercial [8].

The residential sector encompasses the energy used in homes and other living spaces for powering appliances and equipment for heating, cooling, lighting, water heating, and other domestic needs (**Figure 1.2**). Energy consumption, household income, and energy prices all influence residential energy usage patterns. However, residential energy use is also shaped by various other factors, such as building location,

building characteristics, weather conditions, appliance type and efficiency, access to energy sources, and energy policies [9,10]. Consequently, household energy consumption can vary significantly within the same geographic area and across regions and countries [11]. Generally, the average household in Organisation for Economic Co-operation and Development (OECD) nations consumes more energy compared to non-OECD households, primarily due to higher income levels enabling OECD households to occupy larger homes and acquire more energy-intensive appliances. For instance, total residential energy demand in Europe is projected to rise from 12.7 EJ in 2010 to 14.8 EJ by 2040, corresponding to an average annual increase of 0.6% [7].

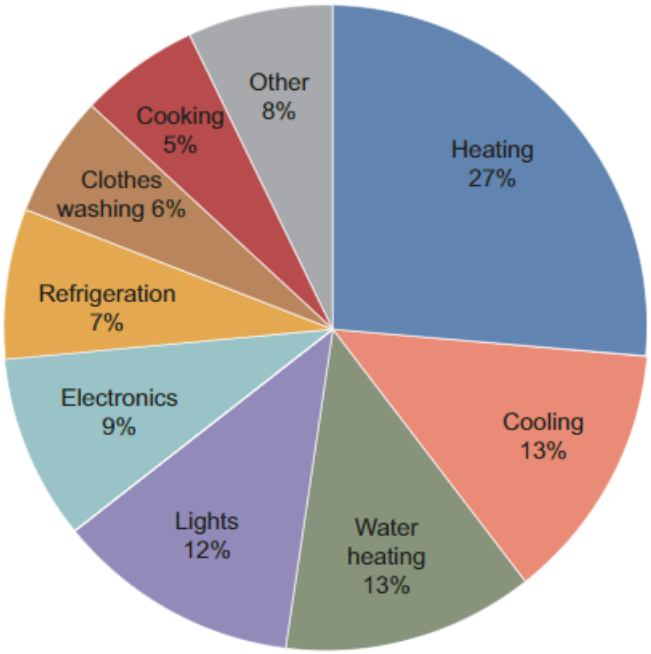

Figure 1.2 Residential building primary energy end uses [12].

While the commercial sector includes the energy consumed in office buildings, retail establishments, schools, hospitals, and other non-residential structures. The commercial sector energy usage also encompasses heating, cooling, lighting, water heating, and other equipment (**Figure 1.3**) [13]. This energy consumption is influenced by factors such as occupancy levels, productivity, climate, resource availability, and energy efficiency. The energy efficiency of commercial buildings is largely determined by management choices during the construction phase, which may be driven by national energy policies and regulations [14]. Many European nations have implemented comprehensive plans to enhance energy efficiency in the commercial

building sector. Projections indicate that total energy consumption in Europe will rise from 6.9 EJ in 2010 to 9.5 EJ by 2040, with an average annual increase of 1.1% [7].

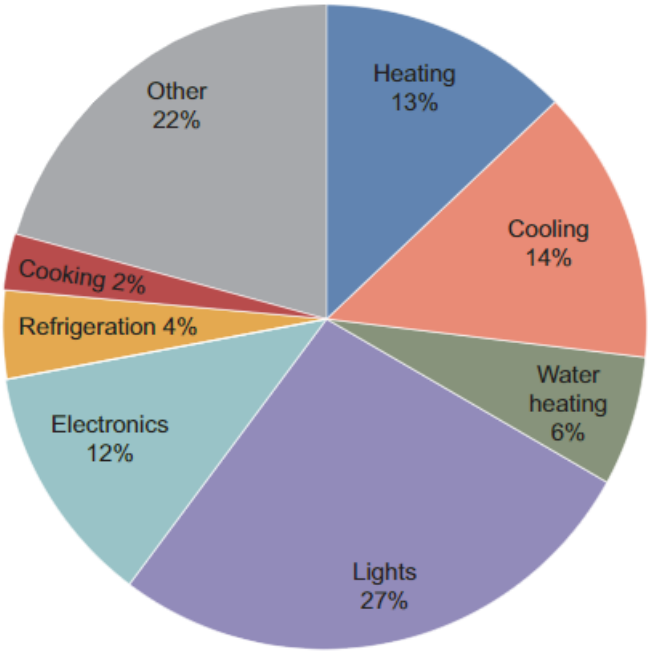

Figure 1.3 Commercial building primary energy end uses [12].

Significant efforts have been made to improve energy efficiency in buildings, but substantial work remains. For instance, the widespread adoption of energy-efficient light-emitting diode lighting in buildings offers substantial gains in efficiency and convenience compared to other lighting options, suggesting a need for a comprehensive shift towards this technology [15]. Additionally, to achieve the ambitious goal of net-zero emissions, the average energy efficiency of global appliances must double by 2050 [16,17]. Further improvements are also necessary in the areas of cooking, where developing countries still heavily rely on fossil fuels like liquefied petroleum gas and natural gas, as well as space heating, which accounts for 60% of the building sector global CO_2 emissions [3]. Particularly in emerging markets and developing economies, rapid urbanization and development necessitate substantial investments to ensure that new buildings are designed and constructed with zero-carbon emissions in mind [7].

In the European context, or generally in most industrialized nations, the building sector represents a distinct scenario. Buildings are the single largest energy consumer in Europe, making this sector crucial for achieving the continent's energy and climate objectives. Estimates indicate that 85% of European buildings were constructed before

2000, and among these, 75% exhibit poor energy performance, with around 80% of residential energy use devoted to heating, cooling, and hot water. Consequently, improving the energy efficiency of buildings is a key strategy for reducing energy consumption, lowering costs for citizens and small enterprises, and attaining a 60% decrease in greenhouse gas emissions by 2030, as well as a zero-emission and fully decarbonized building stock by 2050 [4].

Overall, the building sector presents immense opportunities for advancing energy efficiency and decarbonization efforts globally. The building sector is a critical focus area for driving progress towards sustainable energy and climate goals worldwide. Significant gains can be achieved by improving the energy performance of buildings, shifting to renewable energy sources, and implementing innovative design and technology solutions. Concerted efforts in the building sector have the potential to yield substantial reductions in greenhouse gas emissions and energy consumption, while also benefiting citizens, businesses, and the environment. In conclusion, addressing the challenges and unlocking the potential of the building sector is crucial for a sustainable, low-carbon future.

To further reduce energy use and emissions in the building sector, several strategies can be implemented [12]. However, all these strategies can be broadly categorized into two distinct approaches: active and passive systems [18,19]. Active systems require an external energy source to function. They actively modify the indoor environment to achieve desired conditions, such as heating or cooling. Passive systems, on the other hand, rely on natural processes and design strategies to regulate indoor conditions without consuming external energy. They leverage natural elements like sunlight, wind, and thermal mass to achieve comfort. The main differences of the two strategies are summarized in **Table 1.1**.

Table 1.1 Key differences between active and passive systems.

Feature	Active systems	Passive systems
Energy source	External energy required	No external energy required
Mechanism	Active modification of environment	Leverage natural processes

The need for active systems arises from several factors. Firstly, fluctuating external temperatures and weather conditions often exceed the buffering capacity of passive measures. In many climates and building types, active systems are indispensable for

maintaining desired indoor temperatures and humidity levels. Secondly, modern buildings, particularly those with large glazing areas or high internal heat loads, can experience significant thermal imbalances. Thirdly, stringent comfort requirements for specific building types, such as hospitals or laboratories, necessitate precise environmental control. Finally, urban environments with limited natural ventilation and high levels of pollution often necessitate mechanical ventilation and air filtration [20,21].

Active systems, while energy-intensive, offer the advantage of precise control and responsiveness. They enable buildings to adapt to changing conditions and maintain consistent comfort levels throughout the year. However, their reliance on energy consumption raises concerns about environmental impact and operational costs. Therefore, the selection and design of active systems should prioritize energy efficiency, integration with passive strategies, and the use of renewable energy sources.

In the pursuit of energy-efficient building climate control, heat pumps have emerged as a pivotal technology. They offer a versatile solution for both heating and cooling, presenting a significant advancement over traditional heating and air conditioning systems. Heat pumps operate by transferring heat rather than generating it. They use a refrigeration cycle, similar to air conditioners, but with the ability to reverse the refrigerant flow [22]. In heating mode, the heat pump extracts heat from the outside air, ground, or water source, and transfers it indoors. In cooling mode, it reverses the process, removing heat from the indoor air and expelling it outdoors. This reversible cycle makes heat pumps efficient, as they can provide both heating and cooling with a single unit [23]. There are two main heat pumps types: compression heat pumps and absorption heat pumps. The latter are distinct from compression heat pumps, which are driven by mechanical energy. Absorption heat pumps can be powered by various thermal sources, including natural gas, steam, solar-heated water, or geothermal-heated water. While more complex and requiring larger units compared to compressor-based systems, the primary advantage of absorption heat pumps is their reduced electricity demand, which is limited to liquid circulation [18].

Another example of forced-air active system are variable air volume (VAV) systems. VAV is the most popular form of heating, ventilation, and air conditioning (HVAC) system used in large commercial buildings, where it provides energy efficiency and individualized zone climate control [24,25]. This technology, indeed,

regulates the airflow to specific zones based on their thermal demands. A central air handling unit conditions the air and then supplies it through ductwork to VAV boxes located in each zone. Each VAV box contains a damper that adjusts the airflow based on the zone's thermostat. When a zone requires more cooling or heating, the damper opens, increasing the airflow. When the zone reaches the desired temperature, the damper closes, reducing the airflow. The air handling unit also modulates the supply air temperature and volume to meet the overall building demand. This system design necessitates sophisticated control systems, proper airflow balancing, and may generate noise concerns [26].

Radiant walls are, instead, technologies that use water as heat transfer medium. These systems circulate heated or cooled water through pipes embedded in walls, directly interacting with the building's thermal mass to regulate temperature. They can operate both in heating and cooling mode [27,28]. In heating mode, boiler heats water, which is then circulated through pipes embedded in floors, walls, or ceilings. The heated surfaces radiate heat into the room, providing a comfortable and even warmth. In cooling mode, chilled water is circulated through the pipes, absorbing heat from the room and providing radiant cooling. Radiant walls are adequate for a wide range of buildings, offering efficient heating and cooling with reduced air movement and dust circulation. On the other hand, they require careful design and installation, slower response time compared to forced-air systems, and potential for condensation in cooling mode [29].

Although active systems are very efficient and tuneable, they are extremely energy intensive. For instance, HVAC accounts for 38% of buildings consumption, equivalent to 12% of global final energy use [30]. Due to the large active systems energy consumption, many authors in the literature advocate for a combination of active and passive technologies to enhance the energy efficiency of buildings [31–33]. Passive technologies offer lower energy consumption but are dependent on the ambient environment. Incorporating both active and passive approaches can leverage the advantages of each, optimizing building energy performance while maintaining comfortable indoor conditions [19].

Passive building design strategies aim to minimize the need for mechanical heating and cooling by leveraging natural environmental factors. The core principle of passive design is to work in harmony with the local climate. This involves careful

consideration of the building orientation, form, and materials, as well as the surrounding landscape. Passive strategies are most effective when integrated into the early stages of the design process [34].

In fact, by strategically positioning the building it is possible to maximize solar heat gain in winter or minimize it in summer [35]. In colder climates, south-facing windows allow sunlight to penetrate deep into the building, providing passive solar heating. In hotter climates, shading devices, such as overhangs and external blinds, block direct sunlight, preventing overheating [18]. Shading elements such as awnings, louvers, and exterior vegetation can effectively block direct sunlight during hot periods [34]. Deciduous trees, for instance, offer a dual benefit: shading in summer while allowing sunlight to penetrate in winter. Furthermore, optimizing window size, placement, and glazing type can manage solar heat gain. High-performance glazing may also minimize heat transfer while allowing daylight [36]. In environments where reduced solar exposure is desirable, reflective surfaces play a crucial role. Light-coloured roofs and walls can reflect sunlight, thereby reducing heat absorption. Cool roofs are specifically designed for this purpose [37].

Building orientation also influences wind exposure, which can be harnessed for natural ventilation. Particularly, natural ventilation helps circulate fresh air through a building. The strategic placement of windows and vents creates airflow patterns that remove heat and improve indoor air quality. Techniques such as cross-ventilation and stack ventilation could enhance airflow [18]. Specifically, cross-ventilation system consists in properly placed windows and vents which create air currents, drawing cooler outside air in and pushing warmer inside air out [38]. Windcatchers and other architectural features can enhance this effect. In addition, stack ventilation is based on warm air rises, creating a natural upward flow. Designing spaces with high ceilings and vents at different heights allows warm air to escape, drawing cooler air in at lower levels [18].

Passive systems, on the other hand, can provide a more sustainable and cost-effective solution by taking advantage of the building envelope materials. Particularly, it is possible to operate by insulation or directly inside building structure. Insulation is a key component of passive design. Materials like polyurethane, mineral wool, and polystyrene reduce heat transfer through walls, roofs, and floors, keeping indoor

temperatures stable [19]. Proper insulation and air sealing are essential to maximizing efficiency.

In the case of materials embedded inside building structure, it is important that the strategy is integrated into the early stages of the design process [34]. Although solutions can also be found during the renovation phase of the building envelope. An effective method to mitigate cooling load peaks and indoor temperature fluctuations is to store excess heat within the structural materials of the building, a concept referred to as thermal mass [34]. Specifically, thermal mass describes materials that have the ability to slowly absorb, store, and release heat. Thick walls constructed from concrete, brick, or rammed earth, for instance, can absorb heat during the day and gradually release it at night, moderating temperature variations [19]. This effect is particularly advantageous in climates characterized by significant diurnal temperature swings. The high thermal mass of a building allows it to store more heat and provide enhanced thermal inertia to its components. Thermal mass thereby promotes thermal stability and smoothens the thermal fluctuations between indoor and outdoor conditions. The efficacy of thermal mass is influenced by numerous parameters, such as climatic conditions, construction techniques, material properties, and building orientation [39,40].

This approach allows for greater energy efficiency by leveraging waste heat in buildings through the use of natural processes like solar energy. The temperature difference between day and night is exploited using thermal energy storage (TES) systems. TES is a technology that stores thermal energy by heating or cooling a storage medium, enabling the stored energy to be utilized later for heating, cooling, and energy production applications. TES systems are particularly employed in buildings and industrial processes and have been extensively studied in the literature [41–45].

By strategically combining these passive techniques, building designers can create comfortable indoor environments while significantly reducing or eliminating the need for energy-intensive heating and cooling systems [31]. Implementing energy-efficient technologies is crucial for reducing energy consumption in the construction sector. Energy efficiency is a fundamental step towards sustainable, green buildings. Renovation and new construction should focus on thermal modernization to significantly reduce energy demand and improve indoor climate. Measures such as optimizing the building envelope, minimizing heat losses, and integrating automation

and control systems can achieve this. In fact, highly energy-efficient buildings have an adequate envelope, excellent thermal properties, and autonomous heating and electrical systems with high efficiency and heat recovery. Incorporating renewable energy sources adds complexity to the design and construction process but reduces fossil fuel use and environmental pollution. Ultimately, encouraging individuals to adopt daily practices that safeguard the environment, conserve natural resources, and reduce energy waste is crucial to ensuring a sustainable future for all of humanity.

For what has been said, building sector is a field with enormous opportunities and of great scientific research interest. The strategies to make buildings sustainable from an energy perspective are numerous and well-known. Many of these systems are the subject of ongoing studies by the international scientific community, with continuous implementations. This paragraph has presented only a portion of these technologies, as a comprehensive and detailed description of the active and passive systems for building energy efficiency would exceed the main scope of this thesis work. The focus will now shift to the description of TES systems, concentrating on the different classes of materials used and their application for passive building efficiency. The materials for TES are diverse, with a wide range of characteristics, enabling their use in various fields. Investigating new materials for the storage and release of waste heat presents an intriguing engineering challenge and a broader scientific research opportunity, which could pave the way for improved global energy efficiency.

1.2. Thermal energy storage (TES) technologies

Thermal energy storage (TES) technologies involve the storage of thermal energy through the heating and cooling of a storage medium [46]. The stored energy can subsequently be utilized for various applications, such as heating, cooling, or power generation. TES systems play a crucial role in bridging the gap between energy supply and demand, particularly in applications involving renewable energy sources and building climate control [47]. By storing thermal energy during periods of excess supply and releasing it when needed, TES systems enhance energy efficiency, reduce peak demand, and improve the reliability of thermal systems [48]. In fact, the "peak shift" phenomenon, where electricity demand surges during specific high-usage times, can be mitigated through the use of TES systems. These periods of heightened demand often occur during hot summer afternoons when air conditioning usage spikes, or

during cold winter evenings when heating loads increase. This concentrated demand places a strain on the electrical grid, leading to issues like higher infrastructure costs, grid instability, elevated electricity prices, and environmental impacts. For example, TES systems have been shown to reduce CO_2 emissions in the United Kingdom by 14-46% by shifting electric load to off-peak periods [49,50]. TES systems offer a valuable solution by decoupling energy supply from demand. They can store thermal energy during off-peak hours when electricity is cheaper and demand is lower, and then release it during peak hours to reduce the burden on the electrical grid [51]. Additionally, TES technologies can increase overall efficiency from around 50% to almost 100%, leading to better economics, reduced investment, and lower operating costs [52]. Thermal storage systems can be employed for short-term (hours or days), medium-term, and long-term (several months) storage applications, allowing for the use of the stored energy when needed [46]. These systems are widely utilized in buildings [41,42] and industrial processes [53], enhancing the overall energy efficiency and reducing the environmental impact by storing waste heat that would otherwise be dissipated into the environment, contributing to global warming.

TES technologies can be categorized into three fundamental principles differing in the way they store thermal energy (heat):

- Sensible heat storage (SHS): this is the most common TES technology, based on raising and lowering the temperature of a liquid or solid medium to store and release thermal energy for low to medium temperature applications [54,55].

- Latent heat storage (LHS): this technology relies on the absorption or release of energy at a constant temperature during the phase change of a material. The most common phase change used is the solid-liquid transition, but solid-solid phase changes are also utilized. Owing to their physical state transformations, LHS materials are also known as phase change materials (PCMs) [56–58].

- Thermochemical energy storage (TCES): this technology operates through two mechanisms: chemical reactions and sorption processes. The first stores energy as reaction heat of reversible chemical reactions, while the second stores energy through adsorption or absorption processes. Materials employed for TCES purposes are designated as thermochemical materials (TCMs) [59–61].

Figure 1.4 reports the energy storage densities of various TES materials as a function of temperature. Volumetric energy storage density represents the amount of energy that can be stored per unit volume. It is commonly expressed either in units of MJ m^{-3} or in kWh m^{-3}. It appears clear that TCMs through chemical reactions present the highest energy density, although heat storage in the form of sensible and latent heat are the most studied technologies, and they are at an advanced state of development [62].

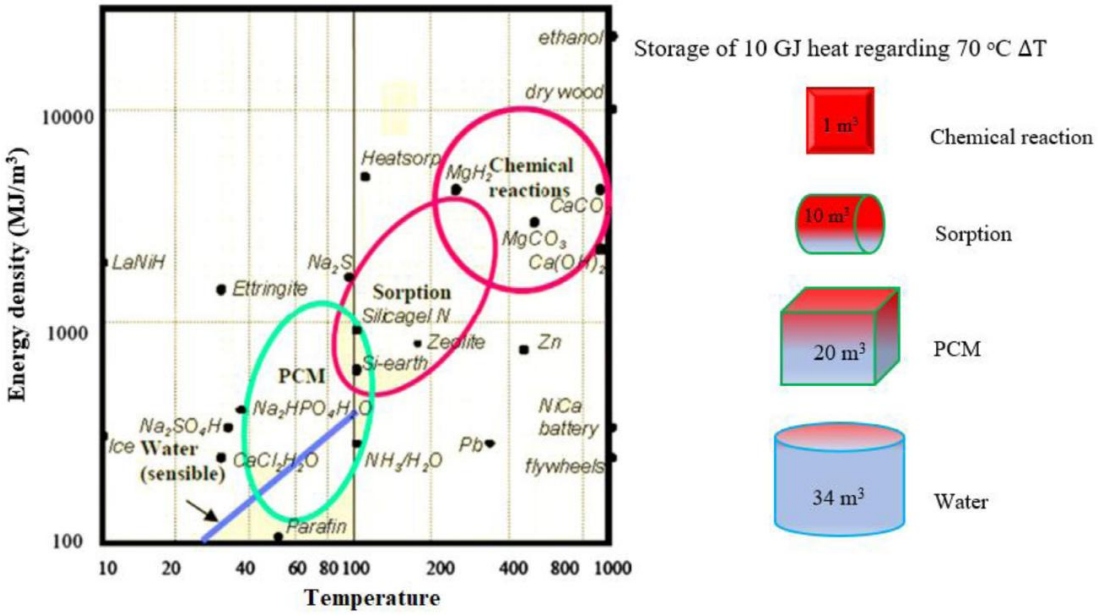

Figure 1.4 Energy density values and comparison of the required storage volumes of various TES materials including SHS materials, PCMs, and TCMs [52].

Based on the operating temperature conditions in which TES materials should store heat, TES systems can operate across a wide range of temperature intervals. These temperature ranges vary significantly depending on the specific application and the storage medium used (i.e. TES materials) [56,63]. Typical low-temperatures applications range from 0 °C to around 100 °C, encompassing space heating and cooling in buildings, domestic hot water (DHW) storage, and agricultural applications like greenhouse heating. For these types of technologies, the most commonly employed storage media are water and PCMs with low melting points [64]. Mid-temperatures applications involve processes in the 100-400 °C range, such as the recovery of industrial waste heat and solar thermal power generation. The storage materials investigated for these applications are molten salts and certain synthetic oils [65]. Lastly, high-temperatures TES (above 400 °C) applications include concentrated

solar power (CSP) with power towers, high-temperature industrial processes like cement, steel, and glass production, as well as advanced nuclear reactors. In these cases, the storage mediums involved are specific molten salts, ceramic materials, and liquid metals [66]. Importantly, the three classes of TES materials are generally capable of operating across different temperature ranges, depending on the specific properties and thermal resistance of the materials used.

The different TES systems can be compared on the basis of various characteristics [46,67]:

- Capacity: defines the energy stored in the system and depends on the storage process, the medium and the size of the system.
- Power: defines how fast the energy stored in the system can be discharged and charged.
- Efficiency: is the ratio of the energy provided to the user to the energy needed to charge the storage system. It accounts for the energy loss during the storage period and the charging/discharging cycle.
- Storage period: defines how long the energy is stored and lasts hours to months (i.e. hours, days, weeks and months for seasonal storage).
- Cost: refers to either capacity (€/kWh) or power (€/kW) of the storage system and depends on the capital and operation costs of the storage equipment and its lifetime (i.e. the number of cycles).

All these features, and others, are summarized for the three main classes of TES materials in **Table 1.2**. In the following paragraphs, each materials class will be discussed in detail, focusing on their characteristics and applications in the building sector.

Table 1.2 Characteristic of the different TES technologies. In "Maturity of technology" section is reported the technology readiness level (TRL) for each TES system.

Characteristics	TES systems			Ref.
	SHS	LHS	TCES	
Heat storage process	Increase of temperature	Heat of fusion	Enthalpy of reaction	[52]
Energy storage density (kWh m^{-3})	50 (small)	100 (moderate)	~500 (high)	[52]
Storage capacity (kWh t^{-1})	10-50	50-150	120-250	[46,67]
Power (MW)	0.001-10	0.001-1	0.01-1	[46,67]
Efficiency (%)	50-90	75-90	75-100	[46,67]
Storage period (h-d-m)	d/m	h/m	h/m	[46,52]
Energy cost (€ kWh^{-1})	0.1-10 (low)	10-50 (moderate)	8-100 (high)	[46,52]
Heat loss during storage	High	High	Minor	[52]
System complexity	Low	Low	High	[52]
Maturity of technology	Commercialized (TRL = 8-9)	Pilot-scale (TRL = 5-7)	Lab-scale (TRL = 4)	[52,68]

1.2.1. Sensible heat storage (SHS)

Sensible heat storage (SHS) is the most established and simplest TES technology. It stores thermal energy by utilizing the temperature difference in a liquid or solid medium (**Figure 1.5**). The SHS system accumulates heat as the temperature increases and releases energy as the temperature decreases [67,68]. A typical SHS system comprises a storage medium, a container, and input/output devices. The containers must retain the storage material and prevent thermal energy loss [69,70]. Due to the high thermal conductivity of SHS materials, they tend to rapidly release the stored energy after the charging phase [54]. As a result, thermal insulation strategies are desirable for SHS systems to enhance their performance [55,71]. The main benefits of SHS are its low cost, being the least expensive TES technology, and the absence of risks associated with toxic materials [46]. The primary drawbacks are the low energy density (the lowest among all TES systems) and the variable discharge temperature [52].

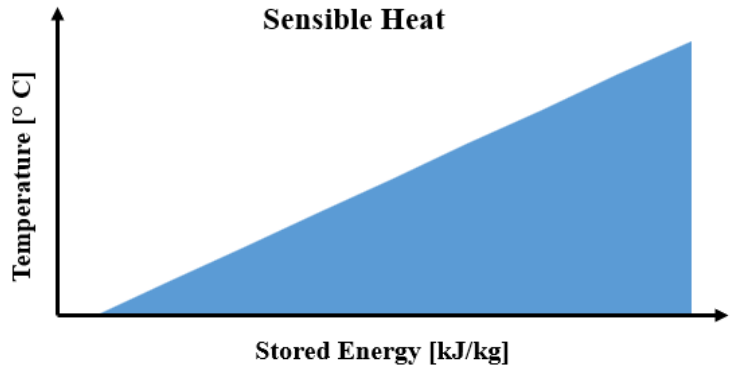

Figure 1.5 Stored heat at different temperatures in a SHS material.

The amount of thermal energy stored in SHS systems is determined by the quantity of storage material, the specific heat capacity of the medium, and the change in temperature, as expressed by the following equation [72]:

$$Q_S = \int_{T_i}^{T_f} m\ Cp\ dT = m\ Cp\ (T_f - T_i) \qquad (1.1)$$

Where Q_S is the amount of heat stored, m is the mass of storage medium, Cp is the material specific heat, T_i is the initial temperature and T_f the final temperature.

To maximize the efficiency of the sensible heat storage process and minimize the size and cost of the storage tank, the materials used should have a high specific heat capacity [69,70]. The most common SHS materials include water, molten salts, nanofluids, sand, rock, brick, gravel, and concrete [54,55]. Water is the most economical option and has numerous industrial and residential applications. Due to the potential for water evaporation at temperatures above 100 °C, oils, molten salts, and liquid metals are used instead [55]. The listed SHS materials present working temperatures from around 0 °C to 1200 °C, enabling the use of this technology from low to high temperatures [54]. Rock bed-type storage materials are used for air heating applications [73]. Other typical applications of SHS technology include underground storage in both liquid and solid media [47], as well as the molten salts-based SHS systems installed in all commercial CSP plants with TES systems.

These plants use mirrors to concentrate sunlight and generate heat, which is then used to produce electricity. TES systems allow CSP plants to store this heat and generate electricity even when the sun is not shining, enabling them to provide dispatchable power [74]. Molten salts are heated by concentrated sunlight and stored in tanks. Because of their low cost, high heat capacity, and wide temperature range (up

to 600 °C), they are suitable materials for TES [75,76]. When electricity is needed, the molten salts are used to generate steam, which drives a turbine. This is a typical example of how TES systems can capture and store waste heat from various renewable energy processes, improving overall energy efficiency. Renewable energy sources such as solar and wind power are dependent on weather conditions (are inherently intermittent), which can lead to fluctuations in energy production. The variability of renewable energy sources can create challenges for grid stability. TES systems, as shown, can store excess energy generated during periods of high production and release it during periods of low production, ensuring a more consistent and reliable energy supply [48]. Furthermore, TES technologies can help to smooth out the intermittent grid fluctuations, maintaining a stable balance between energy supply and demand [46]. Simply by providing a means of storing excess renewable energy, TES systems can increase the overall penetration of renewable energy sources into the energy grid. All discussed aspects acquire importance by considering clean energy sources will become the largest source of energy in the mid-2030s, led by surging solar photovoltaic (PV) and wind power [2]. It is expected that this will happen, in particular way, in the European Union, which continues to be a clean energy leader, with energy-related CO_2 emissions in 2023 declining more steeply than in 2022, driven by increased electricity production from renewables, a recovery in hydro and nuclear power, reduced emissions in industry, plus a mild winter. Clean energy transitions provide an opportunity for European member states to reduce their average electricity system costs. Continuing the shift from coal and gas-fired power plants to low-emissions electricity sources could reduce total European electricity system costs by around 12% by 2035 [1].

1.2.2. SHS solutions for buildings

Integrating TES systems into active systems like renewable energy facilities or energy-efficient HVAC systems necessitates a holistic design approach. Numerous studies have focused on enhancing building energy efficiency by incorporating TES systems that require additional storage volume [77]. **Figure 1.6** presents various methods to integrate active TES systems, such as positioning them within the building core (ceiling, floor, walls), in external solar facades, as a suspended ceiling, in the ventilation system, or for thermal management of building-integrated PV systems.

Figure 1.6 also considers the integration of heat storage water tanks and ground-based or seasonal storage systems. However, some of these systems may introduce additional challenges to the building physics, such as thermal bridges, air tightness, or humidity issues. Therefore, architects and engineers must pay careful attention to the integration of these systems to maximize their efficiency [78].

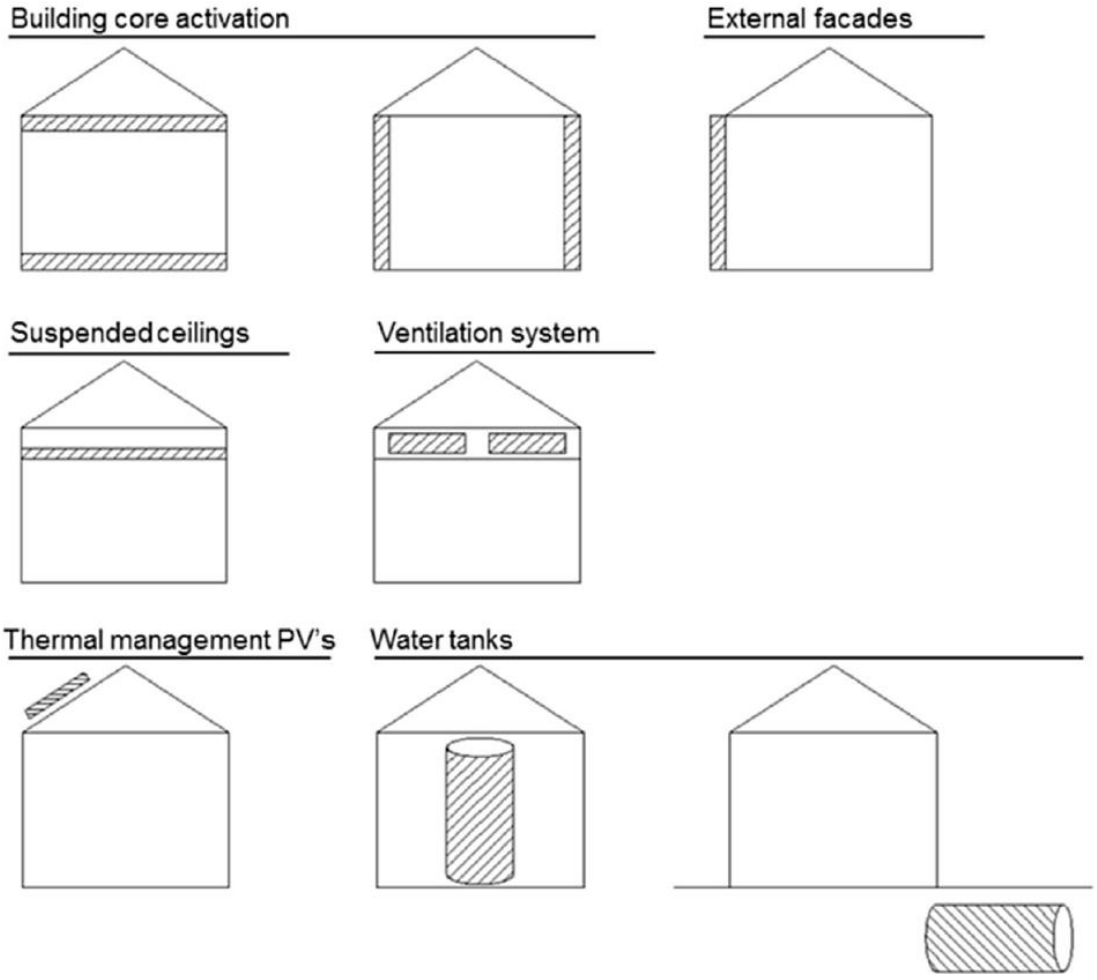

Figure 1.6 Thermal energy storage (TES) integration in buildings [78].

Water is the most commonly used storage medium for SHS solutions in buildings [45]. It is typically utilized as a storage medium for brief durations, typically ranging from one to two days. Employing water as a heat storage medium negates the necessity for a heat exchanger, as the transport fluid and storage medium are effectively the same. This approach offers several advantages: water is abundant, non-toxic, non-combustible, and possesses both a high specific heat and density (**Table 1.3**). Particularly, water high specific heat capacity makes it an excellent medium for storing thermal energy. However, there are notable disadvantages, including a high vapor

pressure that necessitates the use of costly pressure vessels for temperatures exceeding its normal boiling point, susceptibility to leaks, corrosive properties, the potential for freezing and subsequent destructive expansion, and challenges associated with stratification [45].

In DHW systems, water is heated by a heat source (e.g., solar thermal collectors, heat pumps, or electric heaters) and stored in an insulated tank. Proper tank insulation is crucial to minimize heat losses [71]. Additionally, the tank size must match the hot water demand. Temperature stratification within the tank can improve the system efficiency [79]. Despite, stratified tanks may experience a tendency to de-stratify over time due to diffusion and wall conduction [45]. When hot water is needed, it is drawn from the tank, and cold water replaces it, which is then heated. This technology provides a readily available supply of hot water for bathing, washing, and other domestic uses, ensuring thermal comfort [80]. Solar thermal DHW systems, in particular, can significantly reduce reliance on fossil fuels, contributing to sustainable building practices. Water reservoirs for DHW systems is a technology already broadly commercialized and used in different projects (*Das Sonnenhaus*); it has been reported here just an example (**Figure 1.7**) of water tank heated by solar systems which has been architecturally integrated in the living area of an apartment, demonstrating the feasible application of this technology [78].

Figure 1.7 Solar heated water tank integrated in the living area of an apartment [78].

Alternative liquids, in place of water, can be utilized for thermal storage at temperatures exceeding 100 °C without the need for a pressurized container. These liquids are typically organic compounds that possess low density and specific heat

capacities, along with a high degree of flammability. However, due to their elevated boiling points, they enable the storage of significant quantities of energy per unit volume [45]. **Table 1.3** lists physical properties of the most investigated organic liquid SHS storage mediums, comparing them to water.

Table 1.3 Physical properties of most investigated liquid SHS storage mediums at 20-25 °C [45].

Material	Specific heat (kJ kg^{-1} K^{-1})	Density (kg m^{-3})	Boiling point (°C)
Water	4.2	1000	100
Ethanol	2.4	790	78
Propanol	2.5	800	97
Butanol	2.4	809	118
Isobutanol	3.0	808	100
Isopentanol	2.2	831	148
Octane	2.4	704	126

Rock is another viable SHS material due to its cost-effectiveness, although its thermal storage capacity is approximately half that of water. For instance, the rock storage bin utilized in residential air-heating systems represents a practical solution [73]. The primary advantage of rock over water is its ability to be employed for SHS applications exceeding 100 °C [55]. Particularly, rocks, or generally, solid materials are advantageous in SHS in high-temperatures applications. For example, a solar heating system can store heat in a bed of pebbles or rock pile for later building heating. The storage beds, formed from uniform solid particles, act as both storage medium and heat exchanger. Air is commonly circulated through the bed to add or remove heat [45]. Airflow and ventilation with fans are important for distributing stored heat [56]. In fact, optimal storage requires minimal temperature gradient and pressure drop. Thermal stratification occurs due to bed voids and poor pebble contact. Pebbles on average occupy 50-60% of the storage volume, resulting in high air-solid heat transfer. As the bed charges, the hot air entering the storage bed loses its energy rapidly, with the exit air temperature remaining similar to the initial bed temperature. As time progresses, the temperature then gradually rises along the length of the bed. When the storage bed is fully charged, the air flow is reversed to begin discharging the stored heat at a relatively constant temperature. The exit air temperature will gradually decrease as the stored thermal energy is depleted until the bed is completely discharged [45]. **Figure 1.8** reports a schematization of a packed pebble bed storage unity operating in charging and discharging phases.

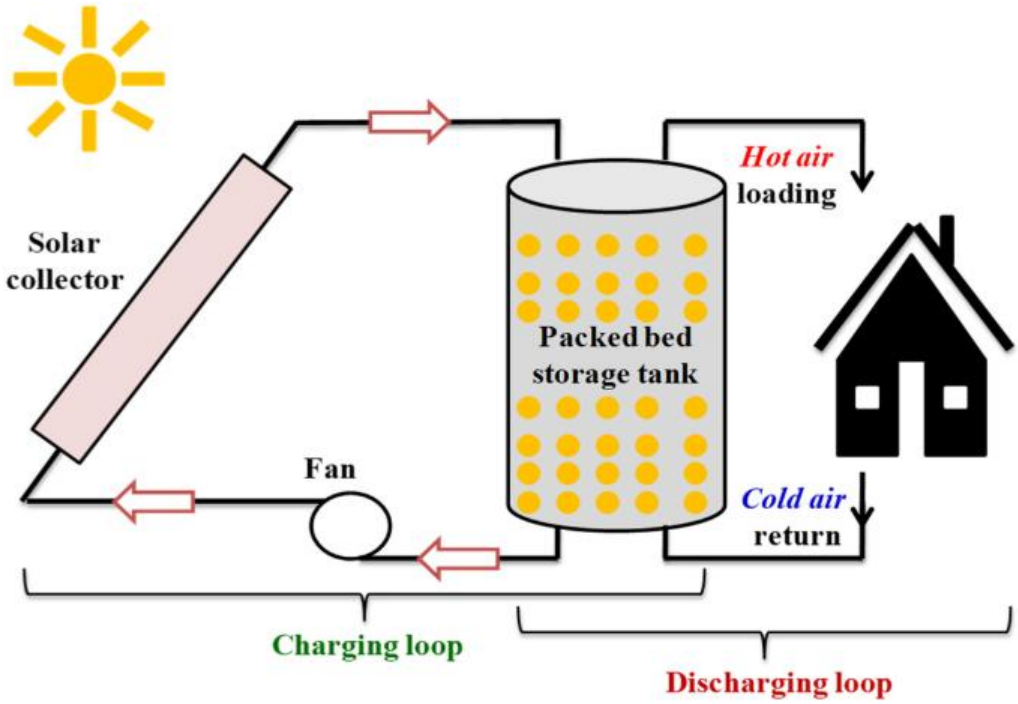

Figure 1.8 Operating scheme of a packed pebble bed storage unity [81].

During the projection phase, it is crucial to select suitable materials and ensure proper insulation to minimize heat losses. Material density and thermal conductivity significantly impact heat storage and release rates [82]. For this application, naturally available earth materials like rocks, sands, and gravel are commonly used. These materials are inexpensive, readily available, non-toxic, non-flammable, and serve as both heat transfer surfaces and storage mediums. Regarding rock-type materials (granite, marble and basalt), they exhibit similar thermophysical characteristics and are suitable for operating temperatures up to 350 °C [56]. **Table 1.4** summarizes the physical parameters of some of the most investigated solid SHS materials.

Table 1.4 Physical properties of most investigated solid SHS storage mediums at 20-25 °C.

Material	Specific heat ($kJ\ kg^{-1}\ K^{-1}$)	Density ($kg\ m^{-3}$)	Thermal conductivity ($W\ m^{-1}\ K^{-1}$)	Ref.
Granite	0.6-1.2	2530-2620	2.8	[56]
Marble	0.7-1	2510-2860	7.7	[56]
Basalt	1.47	2610-2670	3.2	[56]
Concrete	~0.7	2350	~0.5	[56]
Brick	0.84	1698	0.6-0.7	[45]
Aluminium	0.88	2700	204-206	[45]

Other commonly employed solid SHS materials include concrete and bricks, which can be integrated into passive solar design strategies, such as thermal mass walls and

floors [45,56]. Notably, concrete is a cost-effective material that offers good mechanical properties, eliminating the need for a separate container and further reducing overall costs [56].

In conclusion, SHS technologies, utilizing materials like water and rocks, are pivotal for enhancing building energy efficiency and thermal comfort. Water, with its high specific heat, excels in DHW applications, despite challenges like pressure requirements and corrosion. Rock-based SHS, conversely, offers cost-effective solutions for high-temperatures applications, particularly in air-heating systems, proving robust and versatile. The choice between water and rock depends heavily on application specifics, including temperature demands and cost considerations. Both systems emphasize the importance of proper insulation and material selection to minimize heat losses and maximize efficiency. The integration of these SHS systems, especially with renewable energy sources like solar thermal, is crucial for sustainable building practices. Ultimately, the successful deployment of SHS technologies contributes significantly to reducing reliance on fossil fuels and ensuring consistent thermal comfort in buildings.

1.3. Latent heat storage (LHS)

Latent heat storage (LHS) systems enable the storage of significant quantities of heat at a constant temperature, specifically at the phase change temperature [47]. The materials utilized in these systems are referred to as phase change materials (PCMs), as they can either release or absorb energy during a transition in their physical state [67,68]. A PCM subjected to a temperature gradient, including its phase transition temperature, can absorb heat through two distinct processes. It can store energy by simply increasing the temperature, as usual to conventional SHS materials; additionally, it can store energy at a constant temperature during the phase transition (**Figure 1.9**). In this way, PCMs can store significantly higher amounts of heat compared to SHS materials [46,52].

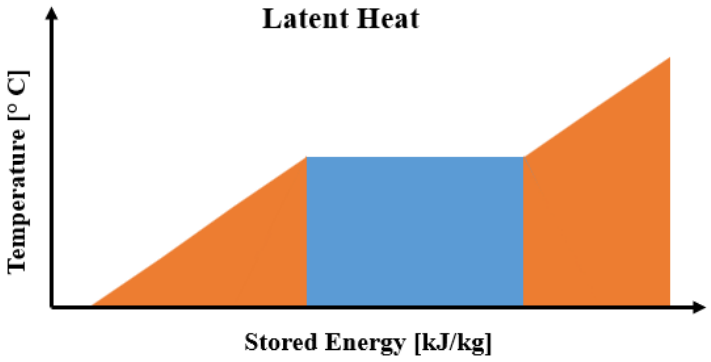

Figure 1.9 Stored heat at different temperatures in a LHS material.

As mentioned, the storage capacity of a PCM can be expressed through the following equations [54,72]:

$$Q_S = \int_{T_i}^{T_m} m\ Cp\ dT + m\ \lambda + \int_{T_m}^{T_f} m\ Cp\ dT \quad (1.2)$$

$$Q_S = m[Cp_S(T_m - T_i) + \lambda + Cp_L(T_f - T_m)] \quad (1.3)$$

Where T_m is the melting temperature, m is the mass of PCM, Cp_S is the average specific heat of the solid phase between T_i and T_m, Cp_L is the average specific heat of the liquid phase between T_m and T_f and λ is the latent heat of the phase change process. The equations presented previously focus on the case of fusion, as solid-liquid phase transition processes are among the most extensively studied and employed, particularly for TES applications at low-temperatures [77]. However, the considerations discussed are also applicable to all other phase change processes, including transitions between the same physical states (e.g. solid-solid).

Compared to SHS systems, LHS systems exhibit higher energy storage densities and occupy less volume, thus resulting in a more compact TES system [77]. This aspect is particularly advantageous in building applications, where the space saving can be exploited to store a greater quantity of storage medium, leading to a greater system efficiency due to the enhanced accumulation capacity of PCMs (latent heat is 50-100 times larger than sensible heat) [56]. Furthermore, PCMs can be used for both short-term (daily) and long-term (seasonal) energy storage, using a variety of techniques and materials [46]. Due to described properties, PCMs offer a compelling solution for TES and management across a wide range of applications. Like SHS materials, PCMs can operate in different temperature ranges according to their physicochemical properties and transition temperature.

PCMs find applications in low-temperatures settings (from below 0 °C), such as refrigerated transport, cold storage, and food packaging, where they help maintain consistent temperatures, reducing spoilage and energy consumption [83]. Additionally, in vaccine transportation, PCMs ensure critical temperature stability, preserving vaccine efficacy and demonstrating the technology applicability in the logistics and cold chain of pharmaceuticals and sensitive equipment [84]. The cooling effect of PCMs is crucial for dissipating heat generated by electronic devices, preventing overheating and enhancing reliability. They find applications in heat sinks, thermal interface materials, and electronic packaging, as well as in the automotive sector for thermal management of batteries [85]. PCMs are also used in textiles to regulate body temperature, providing comfort in clothing, footwear, and protective gear like vests and blankets, which can enhance comfort in extreme environments [86,87]. Additionally, they enhance the insulation and thermal stability of building materials when integrated, reducing energy consumption for heating and cooling [57,88,89]. PCMs, as well as enhance the efficiency and reliability of solar water heating systems by storing solar thermal energy and providing hot water even during periods of low solar radiation [90]. The usage of PCMs for the building sector will be discussed in more detail in § **1.3.3** section.

Mid- and high-temperatures applications of PCMs share similarities but differ in the involved temperatures and materials employed. For mid-temperatures applications, PCMs can capture and store waste heat from industrial processes, power plants, and engines, enabling its reuse. This improves energy efficiency and reduces greenhouse gas emissions [91]. Additionally, PCMs can be integrated into TES systems within CSP plants, providing dispatchable power [92].

High-temperature PCMs store thermal energy for extended periods, enabling continuous power generation from CSP plants. This enhances the dispatchability and reliability of solar power [92]. PCMs are also employed in high-temperature industrial processes (e.g., metallurgy, ceramics) to store and release heat, improving energy efficiency and process control [93]. Additionally, advanced PCM applications are being explored for use in next-generation energy storage systems, including high-temperature nuclear applications [94].

Lastly, PCMs offer a suitable alternative to SHS materials, enhancing energy storage density and efficiency. Furthermore, they maintain a relatively constant

temperature during phase change, providing stable thermal environments. In this way, PCMs regulate temperatures, improving comfort in buildings and personal applications. However, LHS systems present some disadvantages that can limit their performance, especially after several cycles. These aspects will be discussed in the following paragraphs.

1.3.1. Classifications of Phase Change Materials (PCMs)

A first classification of PCMs is based on the temperature ranges involved in the TES process and the characteristic phase transition observed. The phase changes generally occur in the following increasing order of temperatures: solid-solid < solid-liquid < liquid-gas. Solid-solid PCMs typically exhibit the lowest specific latent heat, while liquid-gas PCMs have the highest, but the latter's substantial volume change during the phase transition is a significant drawback for commercial applications. Despite their relatively low latent heat, solid-solid PCMs offer the notable advantage of avoiding the leakage issues associated with materials that undergo liquid or gaseous phase changes [56].

In addition, LHS systems, similar to SHS systems, can be distinguished as either direct or indirect systems. Direct systems achieve heat transfer through the immediate contact of the heat transfer fluid (HTF) with the LHS materials. On the other hand, indirect systems utilize a solid heat transfer medium to separate the HTF from the storage material, which allows for the transfer of heat to a container filled with PCM [95].

Nevertheless, PCMs can be divided into two primary classes based on their chemical composition: organic and inorganic materials. Organic PCMs are well-suited for low-temperatures applications, but their cost and flammability are significant drawbacks. In contrast, inorganic PCMs exhibit higher latent heat and are commonly employed for high-temperatures applications [52]. Additionally, PCMs can be formulated as eutectic mixtures, which are combinations of organic and/or inorganic materials with similar melting and freezing points. However, these eutectic mixtures could present relatively low latent and specific heat capacities, dependent to the composition [58]. **Figure 1.10** provides a schematic representation of the different classes of PCMs.

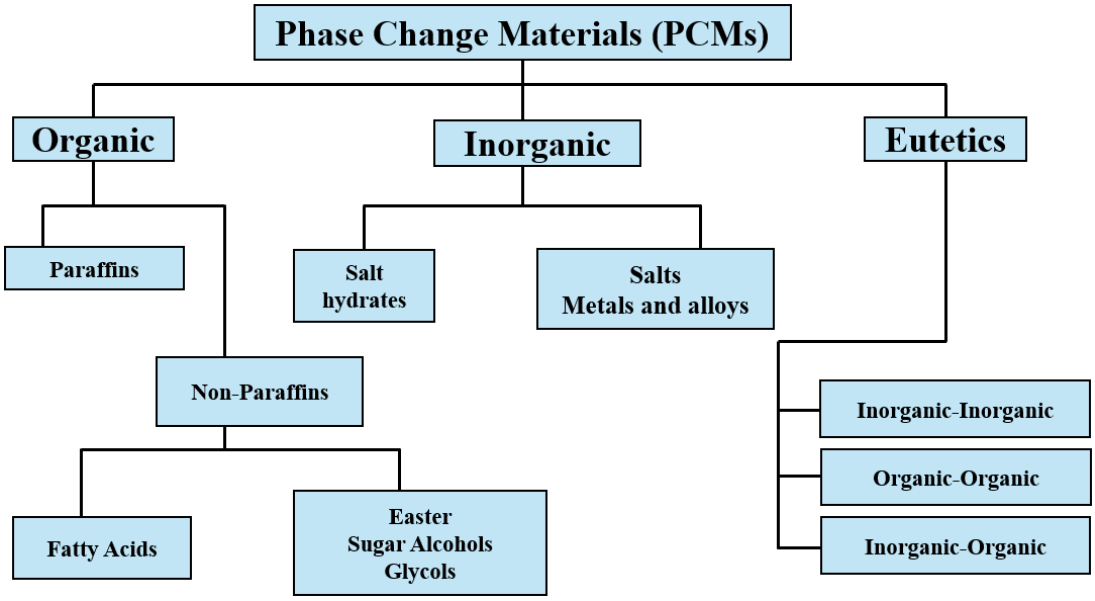

Figure 1.10 Classification of phase change materials (PCMs).

Many organic materials possess the unique quality of having their solid-liquid phase change temperature within or close to the human thermal comfort range, typically between 18 °C and 30 °C. Additionally, organic materials are chemically stable, non-toxic, non-corrosive, and readily available in nature. Therefore, organic materials are the most commonly used TES materials for providing thermal comfort in buildings, textiles, and other applications. However, they tend to decompose at higher temperatures and have relatively poor thermal conductivity [56]. The various classes of organic PCMs are presented as shown in **Figure 1.10**.

Paraffins are the most commonly used organic TES materials in commercial applications, also because of their very high thermal cycle life (between 3000 and 10000 cycles) [77]. These saturated n-alkane aliphatic hydrocarbons are represented by a general formula CH_3-$(CH_2)_{(n-2)}$-CH_3, where n denotes the number of carbon atoms. The melting point of paraffins increases with the length of the carbon backbone chain [58]. For TES applications, the range of n is typically 15 to 30, with n = 18 (*n*-octadecane) being the most widely used paraffin (its melting point at 28 °C is the most comfortable temperature for humans) [56]. Due to the difficulty and expense of obtaining pure paraffin compounds, a mixture of various paraffins is commonly used to form a paraffin wax. These waxes melt over a range of temperatures rather than at a single specific temperature [56,58].

Fatty acids offer a more cost-effective alternative to pure paraffin. These materials possess a carboxylic functional group (-COOH) on the aliphatic chain, resulting in sharp melting points that increase with the number of carbon atoms in the backbone [58]. Saturated fatty acids containing 8 to 18 carbon atoms have suitable phase change temperatures (16-69 °C) within the low-temperatures thermal application range [96]. While unsaturated fatty acids typically exhibit lower phase change temperatures, some, like oleic acid, have appropriate phase change points around 14 °C [56]. Furthermore, the range of phase change temperatures can be expanded through the use of fatty acid eutectics [56].

Another approach to lower the melting temperature of fatty acids is through esterification reactions [56]. This process allows the synthesis of compounds with two different aliphatic groups, following the general formula R-COO-R^1. However, since esterification is a controlled catalytic process to ensure the desired products, this can result in higher costs for fatty acid materials [56].

Among organic PCMs, sugar alcohols exhibit the highest melting points and the greatest latent heat. Their phase change temperatures make them suitable heat storage media for mid-temperatures (90-250 °C) applications such as solar heaters or waste heat recovery [97]. Additionally, sugar alcohols are non-toxic and cost-effective PCMs. These materials also display polymorphism, and the different polymorphic forms can exhibit significant variations in their physicochemical properties, contributing to their specific latent heat.

Among glycols, polyethylene glycol (PEG) has potential for TES. PEG is a linear polymer with a generic formula H-(O-CH_2-CH_2)$_n$-H, available in a wide range of molecular weights. Interestingly, the phase change temperature of PEG tends to be close to room temperature and increases with the polymer molecular weight [56].

Although organic PCMs are chemically stable, non-corrosive, and have fusion temperatures that nearly coincide with solidification, they face some operational limitations that hinder their full utilization [77]. They exhibit drawbacks such as odor, flammability, low density, and low thermal conductivity, which can impact on heat exchange, as well as large volume changes (~10 %) during phase transitions. In contrast, inorganic PCMs overcome these features, as they are thermally stable and possess higher specific latent heats. However, inorganic compounds present two

common disadvantages associated with PCMs: phase segregation and the supercooling effect.

The segregation phenomenon primarily concerns salt hydrate materials and is related to incongruent melting [56]. During thermal charging, salt hydrates absorb heat and undergo complete or partial dehydration as here reported:

- full dehydration:

$$\text{Anhydrous salt}\cdot n\text{H}_2\text{O} \rightarrow \text{Anhydrous salt} + n\text{H}_2\text{O}$$

- partial dehydration:

$$\text{Anhydrous salt}\cdot n\text{H}_2\text{O} \rightarrow \text{Anhydrous salt}\cdot(n\text{-}m)\text{H}_2\text{O} + m\text{H}_2\text{O}$$

After full dehydration, if the anhydrous salt is completely soluble in the water of crystallization, it results in congruent melting [56,77]. Conversely, if the anhydrous salt is only partially soluble in the water of crystallization, it leads to incongruent melting [56,57]. Congruent melting is desirable, as the difference in density between the water and salt components of the salt hydrate can result in segregation, causing the salt hydrate PCM to gradually decrease its latent heat with increasing thermal cycles [56]. Consequently, the thermal properties and performance of PCMs decline [57]. This issue can be mitigated by adding additive materials, such as polymers, in a process known as gelling [71]. In this way, salt hydrate particles are held together in a three-dimensional network. Another solution is thickening, which involves incorporating additional materials to increase viscosity and maintain the salt hydrate cohesion [57,77].

Meanwhile, the supercooling effect corresponds to a physical phenomenon that delays the solidification process [57]. Solidification begins with a nucleation effect, requiring the formation and propagation of initial crystals (the nucleus). For some PCMs (particularly salt hydrates), the energy released during solidification does not compensate for the energy used to create the solid-liquid interface, causing the solidification process to start at a lower temperature than the fusion temperature [77]. Possible strategies to address the issue include the usage of nucleators or the employment of an immiscible HTF in direct contact with the salt hydrate solution [57].

Despite these drawbacks, salt hydrates represent the most commonly utilized inorganic TES materials in commercial settings, and they are the sole inorganic PCMs that function effectively in low-temperatures applications related to human thermal comfort [56,58]. The major advantages of salt hydrates are their large latent heat per

unit volume, the relatively high thermal conductivity (almost double with respect to paraffins) and the small volume changes during melting process [58]. The most used salt hydrate in practical use is calcium chloride hexahydrate ($CaCl_2 \cdot 6H_2O$). It has a melting point (28-30 °C) suitable for low-temperatures applications and presents a large specific latent heat of 190 kJ kg^{-1} [56].

Inorganic PCMs are thermally stable and some of them can be used for mid or high-temperatures applications. Among these, salts can be classified into several types, including nitrates, hydroxides, chlorides, carbonates, sulfates, and fluorides. Nitrates present the lowest melting temperatures and are the most widely used salts and salt eutectics in CSP plants. Hydroxides have a melting point that falls within the medium range of 250 °C to 600 °C. Conversely, chlorides, carbonates, sulfates, and fluorides are characterized by high melting points that surpass 600 °C. Selecting a suitable salt that possesses a melting point within the operational temperature range of TES application is pivotal and can significantly improve the volumetric energy storage capacity [56]. When the fusion temperature aligns with the operating temperature range, the storage capacity is notably enhanced due to the effects of latent heat accumulation in addition to sensible heat (Equations (1.2) and (1.3)). Nevertheless, it is important to note that inorganic salts typically exhibit low thermal conductivity, generally ranging from 0.5 to 1 W m^{-1} K^{-1} [56].

Considering this perspective, metals and alloys exhibit superior thermal conductivity. Furthermore, these materials demonstrate the highest volumetric energy storage capacity among all TES systems, attributable to their enormous density [58]. While metals and alloys exhibit significant promise as high-temperatures PCMs, several challenges must be addressed. Repeated thermal cycling can lead to alterations in their microstructure due to phenomena such as precipitation, oxidation, and segregation. These changes can subsequently affect their properties, including phase change temperatures and specific latent heat. To mitigate oxidation, an inert atmosphere is necessary; however, the inert gases may be absorbed by the metals during the melting and solidification processes, potentially influencing the thermophysical properties of the metals and alloys [56].

Finally, eutectic mixtures represent valid candidates as PCMs due to their sharp and well-defined melting and freezing points, which are tunable based on their composition [56]. A eutectic mixture is a specific combination of two or more

substances that results in a melting temperature lower than that of any individual component. This unique property arises from the specific ratio of the components, allowing them to solidify simultaneously into a crystalline structure [58]. These mixtures can be formed using only inorganic materials, only organic materials, or a combination of the two. Additionally, eutectic mixtures are able to store and release significant amounts of latent heat during their phase transition, according to their physicochemical properties, making them efficient TES materials. Raud *et al.* reviewed theoretical equations and geometric techniques to predict the properties of eutectic mixtures of salt species, such as eutectic composition, melting point, latent heat, density, and thermal conductivity of molten eutectic salts [98]. However, the chemical nature of the components can present corresponding limitations. For instance, inorganic eutectics can encounter phase segregation, corrosion, or supercooling, while organic eutectics may face excessive volume changes that can lead to leakages.

In summary, PCMs offer diverse advantages for TES, with applications spanning low to high-temperatures. Organic PCMs, particularly paraffins and fatty acids, excel in providing thermal comfort due to their melting points aligning with human comfort ranges, despite challenges like flammability and low thermal conductivity. Inorganic PCMs, especially salt hydrates, boast high latent heat and thermal conductivity, making them suitable for commercial use, though they face with phase segregation and supercooling issues. Metals and alloys, while promising for high-temperatures applications due to their superior thermal conductivity, face challenges related to microstructure changes and oxidation. Finally, eutectic mixtures, with their tunable melting points and high latent heat, present a versatile option, though their performance is contingent on the physicochemical properties of their components. Each class of PCM presents unique strengths and limitations, necessitating careful selection based on specific application requirements.

1.3.2. PCM composites

The use of pure compounds as PCMs is often accompanied by various drawbacks, including leakages, corrosiveness, flammability, incongruent melting and crystallization, phase separation, and supercooling. These limitations constrain the heat storage capacity and reliability of pure PCMs during repeated heating and cooling

cycles. An effective approach to mitigating these drawbacks is the development of composite materials [99]. A PCM composite consist of a PCM combined with at least one additional material. The inclusion of the secondary material serves to enhance at least one of the PCM properties, commonly its handling characteristics. Furthermore, the secondary component can also improve the cycling stability of the composite by introducing microscopic structures that reduce phase separation, or by improving heat transfer through the addition of highly conductive materials [57].

The most investigated strategy to prevent leakages in PCMs is encapsulation. This technology could be essential for the technical use of PCMs, as the liquid phase could otherwise flow away from the application site [89]. There are two main encapsulation methods: microencapsulation and macro encapsulation. Microencapsulation involves small, spherical or rod-shaped PCM particles coated in a thin, high molecular weight polymer film, which can then be incorporated into a compatible matrix. Macro encapsulation refers to the inclusion of PCMs in containers like tubes, pouches, or panels, which can serve as heat exchangers or be integrated into building products. Macro encapsulation is the more common approach, as it helps retain the liquid PCM, improves material compatibility, and reduces external volume changes. Microencapsulation, although less prevalent, can improve heat transfer and cycling stability by restricting phase separation to a microscopic scale [57]. The possibility of integrating microencapsulated PCMs in surface layers of building structures represents an interesting and potential technology for construction sector. In this way is possible to reduce PCMs reactivity towards environment and to improve thermal properties by increasing the heat transfer area [100]. When PCMs are encapsulated with a hard and more elastic shell could be directly mixed with building materials (e.g. concrete or gypsum plaster). The microcapsules, as shown in **Figure 1.11**, have usually a spherical shape with vary small diameters (1-5 μm) [101]. The fabrication processes are usually classified into two groups: physical and chemical. Physical procedures comprise spray drying or centrifugal and fluidized bed processes. While, chemical methods mainly include interfacial polymerization, *in situ* polymerization, coacervation and sol-gel methods [102].

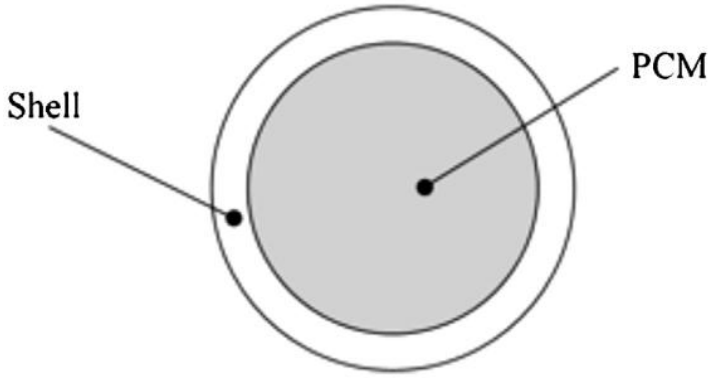

Figure 1.11 Spherical microcapsule of PCM [102].

The main disadvantages of this technique are related to the low thermal conductivity of most materials used for realizing microcapsules and to the small mass-fraction of PCM that can be used, strongly limiting the heat storage capacity of the whole system [102].

The low thermal conductivity in LHS materials represents a primary challenge. In fact, it limits the heat transfer rate and affects the efficiency of the energy storage system. To address this issue, researchers have explored a variety of heat transfer enhancement techniques, including the use of fins, modifying the geometry of the heat exchanger and using cascaded PCM systems [57]. Choure *et al.* highlighted also the importance of high thermal conductivity materials in enhancing heat transfer in PCM-based systems [103]. Actually, different PCM composites were studied for integrating the active phase with high thermal conductivity materials, such as carbon-based and metal-based materials. Carbon-based materials like graphene [104], carbon nanotubes [105], and expanded graphite [106], as well as metal-based materials like metal foams [107], and nanoparticles [108] can significantly improve the thermal conductivity of PCM, thereby enhancing the overall heat transfer rate. In addition, studies have shown that using fins, adding nanomaterials, and employing high heat conductive materials can help reduce supercooling effect and improve PCM performance [109]. In summary, by employing these techniques, it is possible to overcome the challenge of low thermal conductivity in PCM and pave the way for more efficient and effective energy storage solutions [103].

Another significant limitation, particularly affecting organic PCMs, is flammability. Given the primary applications of this PCMs class, it is necessary to address this issue. Presently, stringent safety codes and flammability requirements have been

implemented for building materials to mitigate fire hazards. The most common approach, in this context, is to combine flame retardant compounds with PCMs [57,77]. Different types of fire retardants such as magnesium hydroxide, aluminium hydroxide, expanded graphite, ammonium polyphosphate and treated montmorillonite have been suggested for increasing thermal stability of composite materials without changing the PCM thermophysical properties [110].

One of the newest approaches, for enhancing the reliability of TES systems consists in realizing composite materials involving a porous matrix and the active heat storage compound. Porous silica materials are attractive matrices for PCMs and TCMs due to their high porosity, adsorption capacity, chemical and thermal resistance, and customizable properties. In this sense, research in this area has accelerated since 2010 [99]. The possibility of encapsulating into porous silica prevents leakage of molten PCMs, and reduces corrosiveness, as the PCM surface area exposed to the exterior is diminished. In fact, incorporating PCMs into high-porosity silica matrices results in shape-stabilized PCMs that maintain their solid state even when the PCM melts, due to capillary forces. Concurrently, matrices with smaller pore sizes and greater pore volumes can accommodate a higher quantity of PCM, thereby enhancing TES capacity. Furthermore, silica is non-toxic, non-flammable, and non-explosive. However, the high specific surface area of the silica matrix may promote undesired chemical reactions, so the long-term stability of any new shape-stabilized PCM should be investigated [111].

The two common approaches used for realizing porous silica-phase change composites are: direct synthesis and impregnation. Direct synthesis involves a one-pot sol-gel process that encapsulates the PCM within the silica framework, although this permits less control over the pore structure [112]. On the contrary, the main advantage of the impregnation approach is the ability to tailor the porous matrix properties before adding the heat storage material. This is crucial for organic PCMs with long alkyl chains, which are hydrophobic, while the silica framework is hydrophilic, leading to poor compatibility. Hydrophobic functionalization of the silica surface can improve this. The impregnation method can be further classified according to the PCM physical state: using solid solutions, molten PCMs, or even gaseous PCMs. The impregnation can also be carried out under different atmospheres, such as ambient, inert gas, or directly under vacuum [113].

The present work discusses just a few examples of shape stabilized PCMs composites of scientific research interest towards low-temperatures applications in building sector.

Liu *et al.* designed two types of meso-silica/*n*-eicosane phase-change nanocomposites in the forms of uniform nanospheres and core-shell nanocapsules through self-templating. These nanocomposites exhibited enhanced thermal performance, including good thermal storage, stability, and phase change reliability. The hierarchical nanostructures significantly improved thermal conductivity and reduced supercooling, too. In fact, the matrices have pore diameters of 7.9 and 3.3 nm and have been used to achieve good latent heat values of 122 and 113 J g^{-1}, respectively for nanospheres and nanocapsules. The thermal conductivity increased from 0.15 for the pure paraffin to 1.17 W m^{-1} K^{-1} for the nanocapsules. The nanocapsules also demonstrated exceptional thermal stability after 1000 cycles, indicating that the solid silica shell can provide an extra protection for the encapsulated *n*-eicosane [114].

As mentioned, the tunable properties of nanomaterials offer great potential for developing increasingly efficient and suitable composites for TES systems. From this perspective, Li *et al.* fabricated nanocomposites using commercial silica nanoparticles and $CaCl_2 \cdot 6H_2O$ as PCM. They demonstrated that smaller pore dimensions in the matrix allow for higher loadings of PCM. Specifically, an optimal balance was found by incorporating the salt hydrate (75% w.t.), using the melting adsorption method, into 15 nm pore size silica. The resulting composite exhibits a latent heat capacity of 148.2 kJ kg^{-1} and a phase change temperature of 25.1 °C. Moreover, the system displays high stability and reliability, with only a slight decrease in energy storage capacity (~10 kJ kg^{-1}) after 500 thermal cycles [115].

1.3.3. PCMs in building applications

The use of PCMs for thermal storage in buildings was one of the earliest applications studied [71]. In fact, the first applications of PCMs described in the literature were their use for heating and cooling in buildings, as pioneered by Telkes in 1975 [116], and Lane in 1986 [117]. PCMs offer significant advantages in building heating and cooling applications by leveraging their ability to store and release latent heat. They enhance indoor thermal comfort, energy efficiency, and thermal inertia [118].

Over the past several decades, a variety of bulk-encapsulated PCM products have been commercialized for both active and passive solar applications. Nevertheless, the surface area of most commercially available encapsulated PCMs was insufficient to effectively transfer the stored heat to the building interior after the PCM had been melted by direct solar irradiation [89]. Conversely, the walls and ceilings of a building provide extensive surface areas that can facilitate passive heat transfer across the various zones of the structure. For improving the heat transfer efficiency, PCMs have been directly integrated in building envelopes, including roofs, ceilings, wallboards, and floors. PCMs help increase the thermal mass of these key building envelope components, leading to a reduction in heat transfer between the outdoor environment and the building, especially during peak periods. This contributes to decreasing the peak heating or cooling load of the building. Furthermore, PCMs mitigate the impact of fluctuations in ambient temperature on these key building envelope components, resulting in smaller variations in indoor room temperature. Thus, it is an efficient method for maintaining the room temperature within the occupants' thermal comfort range [90].

As concerns the impregnation of PCMs in wallboards, it is a promising technology, particularly for gypsum wallboards. These materials serve as an ideal supporting medium for PCMs due to their high void volume (~40%) [89]. The most common method of incorporating PCMs in wallboards is direct immersion, which involves immersing the wallboard in a bath of molten PCM or a PCM solution. Another route involves the mixture of PCM additive directly in the wet wallboard mixture. In this way the wallboards gain major energy efficiency. **Figure 1.12** shows panels realized by direct mixing with gypsum of Micronal® (BASF, Germany), used as PCM [119]. For instance, Karaipekli and Sari have shown the positive effect of organic PCMs mixtures integrated into gypsum wallboards in reducing indoor air fluctuations and improving thermal comfort [120]. While, Feldman *et al.* demonstrated the reliability of a laboratory scale TES system, realized through the incorporation of butyl stearate, at mixing stage, into gypsum wallboards. The inclusion of butyl stearate was considerably aided by the use of various dispersing agents. The physical and mechanical characteristics of the produced wallboard are quite similar to those of standard gypsum board. The energy storage capability of wallboard has a tenfold increase in capacity for storing and releasing heat compared to regular gypsum

wallboard [121]. Again, Kissock *et al.* conducted an experimental investigation into the thermal performance of wallboards imbibed with 30% wt. of a commercial paraffinic PCM (K18). Through their simulations, the researchers continuously monitored solar radiation, ambient temperature, and interior temperatures in the test cells for a period of 14 days. The findings revealed that the peak temperature in the PCM enhanced test cell was up to 10 °C lower than in the control test cell during sunny days [122].

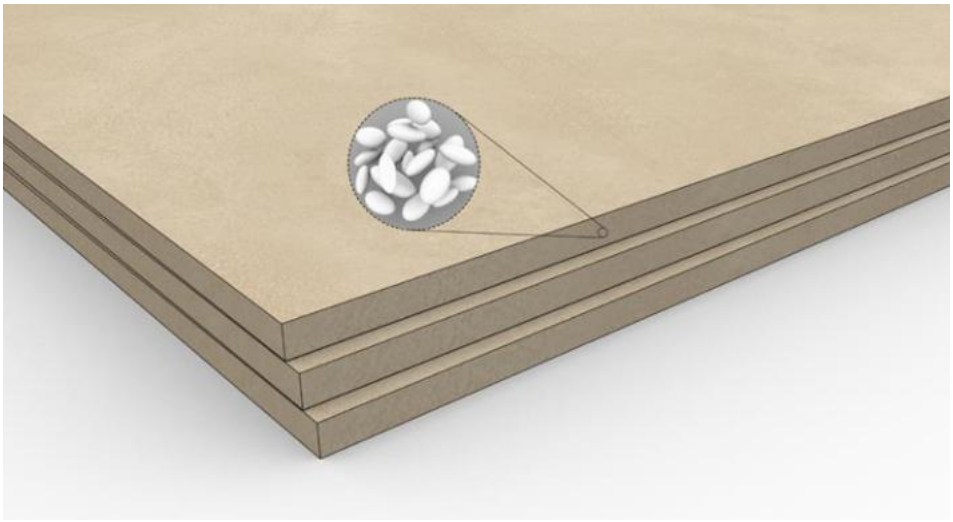

Figure 1.12 Micronal® PCM-integrated gypsum wallboard [119].

Other than gypsum wallboards, PCMs could be integrated in concrete with promising results [123], although often the mortar formulation needs to be adjusted [124]. For instance, Hadjieva *et al.* demonstrated the impregnation of sodium thiosulfate pentahydrate ($Na_2S_2O_3 \cdot 5H_2O$) into a porous concrete matrix, filling up to 60% of the concrete pore and capillary spaces. They found that the large absorption area of the porous concrete provided a suitable supporting matrix for the PCM incongruent melting, improving its structural stability during thermal cycling [125]. This microencapsulation technique may prove efficient in containing the PCM in an inexpensive way and could help address issues associated with the use of hydrated salts, such as supercooling and phase segregation [89]. In parallel, Mohseni *et al.* explored the macro encapsulation of organic, commercial grade PCMs for use in lightweight structural cementitious composites. They developed an effective system that can enhance indoor thermal efficiency while also being suitable for structural applications. The resulting composite material demonstrated impressive thermal

stability, withstanding up to 500 thermal cycles without any PCM leakage [126]. Particularly, lightweight building materials represent a great area of interest for TES technology. In fact, these materials tend to have high temperature fluctuations, because of their low thermal mass, which result in a high heating and cooling demand [71].

Floors are another promising area for optimizing building energy performance. PCMs can significantly enhance the efficiency of active underfloor heating systems (radiant walls) during winter [90]. Some studies have reported impressive reductions in heating loads (~40%) through the use of PCM floors [127]. In this context, the work of Farid and Chen is noteworthy. They developed a computer model to simulate underfloor heating with and without a PCM layer. The simulation results showed that incorporating a PCM layer led to more stable and consistent surface temperatures, as well as improved heat retention capabilities, compared to a standard concrete floor. This PCM-enhanced system demonstrated superior thermal performance and energy efficiency over a conventional concrete floor design [128].

This thesis has provided examples of LHS systems used to enhance the energy efficiency of buildings. The materials most commonly employed in this sector include paraffins, fatty acids, esters, and salt hydrates. **Table 1.5** and **Table 1.6** list some of the most widely used PCMs in the building sector, categorized by their chemical nature.

Table 1.5 Thermophysical properties of organic PCMs for building applications.

Material	**Melting temperature (°C)**	**Heat of fusion (kJ kg^{-1})**	**Thermal conductivity (W m^{-1} K^{-1})**	**Ref.**
Oleic acid	14	81	0.17	[57]
Caprylic acid	16	148	0.15	[52]
Butyl stearate	17	140	0.15	[52]
n-Heptadecane	19	240	0.21	[57]
Paraffin C_{16}–C_{18}	20-22	152	-	[57]
Polyglycol E600	22	127	0.19	[57]
Paraffin C_{13}–C_{24}	22-24	189	0.21	[57]
n-Octadecane	28	244	0.28	[52]
Vinyl stearate	29	122	0.25	[52]
Methyl stearate	29	169	-	[57]
Capric acid	32	152	0.15	[52]
Paraffin C_{16}–C_{28}	42-44	189	0.21	[57]
Paraffin C_{20}–C_{33}	48-50	189	0.21	[57]
Palmitic acid	57.8	185	0.22	[52]
Stearic acid	69.4	199	-	[58]

Table 1.6 Thermophysical properties of inorganic PCMs for building applications.

Material	Melting temperature (°C)	Heat of fusion (kJ kg^{-1})	Thermal conductivity (W m^{-1} K^{-1})	Ref.
$FeBr_3 \cdot 6H_2O$	21	105	-	[57]
$CaCl_2 \cdot 6H_2O$	29	190	0.54	[57]
$LiNO_3 \cdot 2H_2O$	30	296	-	[57]
$Na_2SO_4 \cdot 10H_2O$	32	251	0.50	[52]
$CaBr_2 \cdot 6H_2O$	34	115.5	-	[57]
$Na_2CO_3 \cdot 10H_2O$	36	247	0.45	[52]
$Na_2HPO_4 \cdot 12H_2O$	36	280	0.47	[52]
$K_2HPO_4 \cdot 3H_2O$	48	99	-	[57]
$Na_2S_2O_3 \cdot 5H_2O$	48	200	0.50	[52]
$MgSO_4 \cdot 7H_2O$	48.5	202	-	[57]

The effective functionality of PCMs can evoke several enhancements in thermal performance metrics. They can significantly decrease maximum temperature fluctuations and improve overall thermal comfort. Several studies have shown that the implementation of PCMs can lead to significant reductions in energy usage, with energy savings reaching up to 50% for cooling and 45% for heating applications, depending on the type and thickness of PCM used [129]. Furthermore, the ability of these systems to function over the years has been demonstrated even up to a decade [130].

Despite the potential benefits of using PCMs in building materials to improve passive heating or cooling, there are several critical issues and limitations that could hinder their widespread adoption:

- Limited thermal properties: PCMs have capacity, cost, and construction feasibility limitations, requiring careful encapsulation to optimize performance and stability.
- Miscibility and workability: compatibility of PCMs with the concrete, mortar, or wallboard matrix is crucial to ensure structural stability and uniform material distribution. High PCM amounts can compromise uniformity and stability, requiring careful evaluation.
- Economics: the use of PCMs in building materials can significantly increase initial costs, necessitating the development of tools to evaluate and forecast life cycle costs.

- Environmental impact: the environmental impact of PCM production, use, and disposal must be thoroughly evaluated to ensure sustainability.

In conclusion, the advantages of PCMs in building heating and cooling applications are multifaceted, including enhanced energy efficiency, improved thermal comfort, and the potential to contribute to sustainable building practices. The array of available materials, coupled with their desirable characteristics, positions PCMs as a critical component in contemporary architectural and energy strategies. However, challenges still remain in a universal implementation of PCMs in building envelops that require precise evaluations.

1.4. Thermochemical energy storage (TCES)

Thermochemical energy storage (TCES) is the less developed TES technology despite presenting the highest energy storage density (up to 500 kWh m^{-3}) [131,132]. TCES has emerged as a promising alternative, offering distinct advantages over traditional sensible and latent heat storage systems. TCES systems can store heat through sorption processes and chemical reactions. Both methods can store substantial amounts of heat [133]. These technologies leverage a three stages reversible process for charging and discharging heat.

In the case of the sorption processes the sorbent material absorbs (absorption) or adsorbs (adsorption) the sorbate, during the charging phase. In fact, the process requires an energy input, usually in the form of heat [134]. Once the sorbate is captured by the sorbent, the energy is stored in the form of potential energy. The key advantage of sorption TES is that if the sorbent and sorbate are kept separate, there are minimal energy losses during storage [135]. This allows for long-term or seasonal storage of thermal energy [136]. Finally, to release the stored energy in discharging phase, the sorbent and sorbate are brought back into contact under different conditions (e.g., lower pressure or higher temperature) [135]. The released heat can then be used for various applications, such as heating buildings or industrial processes. According to the physical state of sorbent, sorption TES systems can be classified into two categories [137]:

- Absorption: involves a liquid sorbent absorbing a sorbate.
- Adsorption: involves a solid sorbent attracting a sorbate to its surface.

In the case of chemical reactions, the mechanisms involved are akin to the previous case. Heat is stored and released through endothermic and exothermic chemical reactions, respectively. Employing chemical reactions, the compounds involved in the processes are referred to as thermochemical materials (TCMs). **Figure 1.13** illustrates the typical operation of a TCM, which occurs through a reversible chemical process. Similarly to sorption TES, the overall process comprises three stages: charging, storing, and discharging of the waste heat.

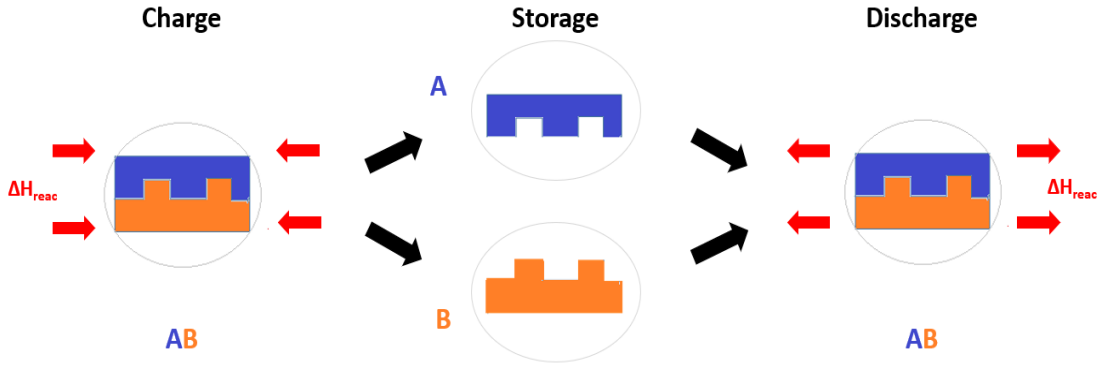

Figure 1.13 Operating scheme of a thermochemical material (TCM).

During the charging step, the thermal energy drives the endothermic reaction, where the compound "AB" is converted into the reaction products (“A” and “B”). The process utilizes the waste heat to provide the energy (enthalpy of reaction, ΔH) required for breaking the chemical bonds and separating the components "A" and "B". These separated components can then be stored individually, maintaining the stored energy for extended periods and theoretically without heat loss. The exothermic reverse reaction, corresponding to the discharge step, is achieved by the recombination of the reaction products (“A” and “B”), releasing the previously stored heat of reaction. Compared to previously discussed TES systems, the potentialities of TCMs are significantly greater, as the energy is used for breaking and reforming chemical bonds, allowing for the storage and release of larger amounts of heat [60,138].

The general process taking place in a TCES system can also be written in the form of a chemical reaction [139]:

$$AB + \Delta H \leftrightarrows A + B$$

The energy stored for the described reaction can be calculated using the following equation [59]:

$$Q_S = n_{mol} \Delta H \quad (1.4)$$

Where the amount of heat stored (Q_S) is proportional to the reaction enthalpy (ΔH), with a factor depending on the number of moles of the limiting reactant (n_{mol}). When determining the energy stored in a TCES system, it must be considered that the reaction may not occur completely, as it could be limited by the presence of a limiting agent or by conditions (temperature or pressure) that do not allow the reaction to reach completion.

The use of a reversible sorption or chemical process guarantees that TCES systems are extremely efficient. Furthermore, the proper conservation of materials during the storage stage allows energy to be stored for long periods with minimal heat losses [140]. Other key advantages of TCES systems include their high energy densities, leading to compact storage systems. Compared to other TES solutions, TCES energy storage density can be up to fifteen times greater than the SHS energy density and six times greater than the LHS one [59]. Additionally, this technology offers high operational flexibility, being suitable for a wide range of applications due to the large number of available reversible reactions at different temperatures [141]. However, some limitations hinder the widespread adoption of TCES technology [56]. These limitations are related to the moderate or high cost of TCMs and the challenge of realizing efficient systems over multiple thermal cycles, as TCES is the most complex technology among TES options.

From this perspective, the choice of suitable materials is critical. When selecting material candidates for TCES, the most important requirements are [59,142]:

- Complete reaction reversibility.
- Suitable reaction temperature.
- High storage density.
- High reaction enthalpy.
- Non-toxicity.
- Good thermal stability during cycling within the operation temperature range.
- Low-cost.

The selection of TCMs should aim to satisfy as many of these requirements as possible.

Given the interesting properties of TCES systems, they have a wide range of applications due to their high energy density and ability for long-term storage [143]. Key areas include:

- Concentrated Solar Power (CSP): TCES can provide a reliable and dispatchable energy source for CSP plants, enabling continuous electricity generation even when solar radiation is unavailable. This is crucial for grid stability and maximizing solar energy utilization [144,145].
- Industrial process heat: TCES can efficiently store and deliver the high temperatures required for many industrial processes like drying, calcination, steam generation, and heat treatments in industries such as cement, glass, and metal production [146,147].
- Building heating and cooling: TCES can be used for space heating and cooling, improving energy efficiency and reducing fossil fuel dependence. This includes seasonal TES and enhancing heat pumps or air conditioning systems [148,149].
- District heating: TCES can be integrated into district heating networks to store and distribute heat efficiently, reducing energy losses and improving overall system performance [143,150].
- Long-duration energy storage: TCES's potential for long-term storage makes it valuable for balancing supply and demand in renewable energy systems [151,152].

In conclusion, TCES is being developed to bridge the gap between energy supply and demand, particularly in applications involving renewable energy and industrial heat requirements.

1.4.1. Classifications of thermochemical materials (TCMs)

Since thermochemical energy storage (TCES) is the most complex and least developed technology within TES systems, further investigations are required. This section addresses the classification of different reactions and highlights the most promising materials.

Energy storage through thermochemical reversible reactions can be categorized into five types according to the states of the materials [61,153]: gas-gas, liquid-gas, liquid-liquid, solid-gas, and solid-solid reactions. Notably, solid-gas reactions have received

considerable interest because they offer a wide range of operational temperatures and facilitate the separation of the reactants [61,154].

TCMs can be classified not only by their physical state, but also according to the operating temperature range, based on classical low-, mid- and high-temperatures applications. For low-temperatures, sorption systems and salt hydrates are commonly employed. These classes of materials are able to store and release energy through dehydration and hydration reactions, respectively. Materials for higher temperatures leverage additional types of reactions. Pardo *et al.* schematized these other systems in a diagram here reported (**Figure 1.14**) [147].

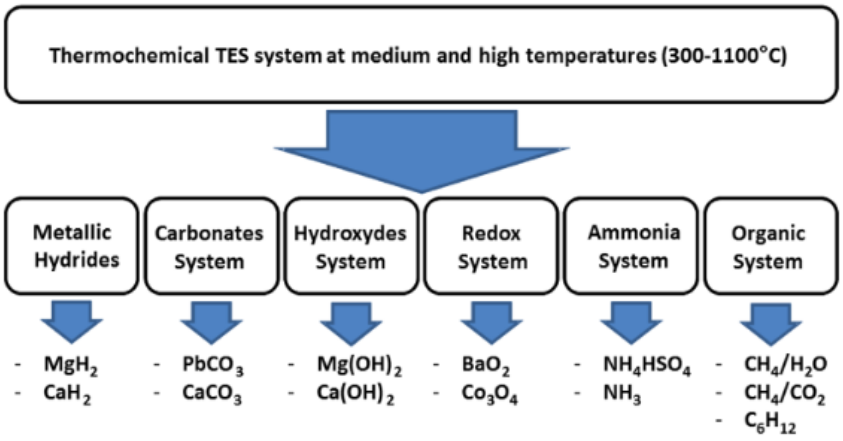

Figure 1.14 Thermochemical storage systems studied for medium and high temperatures [147].

Certain TCES materials are not viable due to harmful properties or technical difficulties. For example, lead-based compounds like $PbCO_3$ pose human health risks, while sulfate-based systems can produce corrosive gas products [155]. Or even, ammonia systems also face challenges such as high-pressure needs and slow reaction kinetics. These limitations complicate the development of effective TCES technologies [156]. This section discusses the primary solid-gas reactions and sorption processes that have been investigated for TCES.

Regarding sorption systems, the technology involves a sorption process followed by a desorption process. These systems can utilize either liquid or solid materials, as discussed in the previous section. The energy stored in sorption storage systems can be represented as sum of different contributions. In this way, the amount of heat stored (Q_{charg}) within charging process is expressed by following equations [59,157]:

$$Q_{charg} = Q_{sens} + Q_{cond} + Q_{bind} \quad (1.5)$$

$$Q_{des} = Q_{cond} + Q_{bind} \quad (1.6)$$

Where, Q_{sens} represents the sensible heat needed to raise the reactor temperature to the desired desorption temperature. The heat of condensation (Q_{cond}) refers to the energy associated with the phase transition from liquid to gas at a specific temperature (normally condensation temperature at the condenser), which is assumed constant. The binding heat (Q_{bind}) represents the sorption forces between the sorbent and the sorbate [157]. From Equation (1.6), it results clear that for desorbing any system, it is necessary to furnish an amount of energy (Q_{des}), sufficient to break the sorption bonds between sorbent and sorbate, and, additionally, to vaporize the liquid. This thermodynamic requirement explains why open adsorption cycles are generally considered more efficient when adsorption occurs at lower temperatures, as the energy input for vaporization is minimized [134]. Open sorption systems, as the name indicates, are designed to interact with the surrounding environment. The working fluid is typically water vapor. During the discharging process, the sorption reaction occurs by directly utilizing the moisture present in the ambient air, as illustrated in **Figure 1.15** (left), or in some cases from an external moisture source such as a humidifier. This design feature renders open sorption systems dependent on weather conditions. On the other hand, a closed system has no mass exchange with the environment and requires an evaporator/condenser for the evaporation of water when needed as a reactant and for its condensation during storage, as shown in **Figure 1.15** (right) [67]. A comparison between open and closed systems has been published by Michel *et al.* They conclude that for the closed system, heat transfer is the main limitation, and a small increase in thermal conductivity significantly improves the reaction rate. For the open system, mass transfer is the primary limitation, and the hydration rate can be enhanced by optimizing the bed permeability [158]. In addition, closed systems have been extensively researched for use in refrigeration, heat pumps, and energy storage. These systems are particularly well-suited for small-scale applications that require compact and highly efficient devices [159]. In contrast, open systems have lower investment costs, and, additionally, maintenance costs or failures of auxiliary elements (evaporator/condenser) are avoided [160]. As a result, practical projects for TCES often utilize open systems [161].

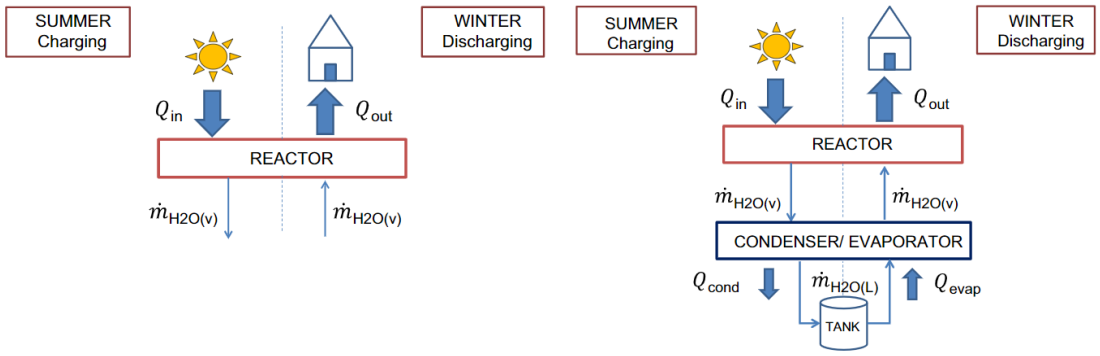

Figure 1.15 Open (left) and closed (right) systems for TCES [61].

Regarding materials for sorption systems, adsorption processes often involve activated carbon/methanol, silica gel/H_2O, zeolites/H_2O, and other sorbent-sorbate pairs. Absorption-based systems, on the other hand, utilize materials like NaOH/H_2O, LiCl/H_2O, $CaCl_2$/H_2O, LiBr/H_2O, and so on [67]. The latter materials class are generally classified as salt hydrates and their usage as TCMs for low-temperatures applications will be delved into the next section. Finally, the selection of appropriate materials is critical for optimizing the performance and efficiency of both adsorption and absorption based TES systems [162].

Like most common adsorption materials, metal oxides can undergo hydration and dehydration reactions, at near atmospheric pressures, to store thermal energy at mid- and high-temperatures. The temperature range depends on the specific metal oxide utilized. The following reactions describe their operation [163]:

Exothermic reaction: $MO_{(s)} + H_2O_{(g)} \rightarrow M(OH)_{2(s)} + \Delta H$

Endothermic reaction: $M(OH)_{2(s)} + \Delta H \rightarrow MO_{(s)} + H_2O_{(g)}$

Where $MO_{(s)}$ and $M(OH)_{2(s)}$ represent the metal oxide and metal hydroxide, respectively. The H_2O partial pressure and the temperature drive the hydration/dehydration reactions [60,147]. Typical hydroxides, such as calcium hydroxide and magnesium hydroxide, are cheap, abundant, and non-toxic. These materials have been extensively studied for high-temperatures TCES applications in chemical heat pumps (CHPs), due to their high volumetric energy density [164,165]. Typical metal oxides with the potential to be reaction candidates for TES at less than 200 °C are nickel oxide (NiO) and cobalt oxide (CoO). While suitable candidates for the storage at over 700 °C are strontium oxide (SrO) and barium oxide (BaO) [60]. The common issues with TCMs for hydration reactions include deterioration during

cycling, inadequacy for the application temperature range, side chemical reactions, corrosion, pulverization, and deliquescence [166]. Commonly metal oxides reach a stable active state after multiple hydration-dehydration cycles. However, macro-crystals may crack during these cycles, necessitating the use of additional stabilizing materials [59].

Focusing on other TCMs, carbonation and redox processes play an important role, especially in mid- and high-temperatures technologies. These reactions offer high energy storage densities and the potential for long-term storage with minimal energy loss [59].

Alkaline-earth metal carbonates are ideal candidates for thermochemical applications owing to their elevated decomposition temperatures, substantial energy density, and cost-effectiveness [153]. Initially, these materials were utilized for capturing CO_2. The resulting process of calcination/carbonation chemical looping operates in cycles and can effectively achieve the necessary storage temperature (above 800 °C), along with desired energy density and discharge rates [167]. The calcination/carbonation reactions can be described as [168]:

$$MCO_{3(s)} + \Delta H \leftrightarrows MO_{(s)} + CO_{2(g)}$$

Carbonates undergo decomposition via an endothermic calcination process, typically involving an alkaline-earth metal denoted as M. This reaction occurs in a solid-gas reactor maintained at near-ambient pressure. The reaction temperature is influenced by the equilibrium partial pressure of CO_2. Upon completion of calcination, CO_2 and the resulting metal oxide are stored separately, with CO_2 sometimes being compressed into a liquid form to minimize storage volume [168]. When energy recovery is required, both the metal oxide and CO_2 are directed to a solid-gas reactor for carbonation, which releases the energy that was previously stored. A significant challenge associated with carbonates is sintering that occurs after numerous calcination and carbonation cycles at elevated temperatures [169]. To address this issue, several techniques are employed to enhance the active surface area and maintain the stability of the pore structure, including the use of rigid porous materials as support, the incorporation of additives to boost thermal stability, reducing particle size, and synthesizing materials with a microporous structure [167].

Among the carbonation reactions, the most well-established process is based on calcium carbonate ($CaCO_3/CaO$) [170]. However, there are alternative systems that utilize barium carbonate ($BaCO_3/BaO$) [167], strontium carbonate ($SrCO_3/SrO$) [171], or magnesium carbonate ($MgCO_3/MgO$) [172].

Typical operational issues associated with TCES processes are not involved in metal oxide redox systems. These systems guarantee high reaction temperature, non-corrosive products and no need for gas storage. The redox reactions involved in this process can be described as [173]:

Reduction: $M_xO_y \rightarrow M_xO_{y-1} + ½\ O_2$ $\Delta H > 0$

Oxidation: $M_xO_{y-1} + ½\ O_2 \rightarrow M_xO_y$ $\Delta H < 0$

Initially, metal oxides (M_xO_y) undergo reduction through an endothermic reaction at elevated temperatures, which allows them to store heat. Subsequently, these reduced metal oxides (M_xO_{y-1}) are re-oxidized to their original state via an exothermic reaction, releasing the energy that was previously stored. The oxidation process requires a source of oxygen. When the oxygen source is water or CO_2, the reaction produces hydrogen (H_2) or carbon monoxide (CO), respectively [174]. Air is the most frequently utilized oxygen source. During the charging phase, the reduction can occur either through solar irradiation of the metal oxide or by heating the HTF. When air serves as oxygen source, it coincides with the HTF. This technology offers several advantages. In fact, the involved reactions are generally simple and do not require catalysts. Furthermore, most of redox pairs present relatively small environmental impact and involved metal oxides present medium or high energy storage densities (230-850 kJ kg^{-1}) [59].

Redox systems can be categorized into two groups based on the number of metal oxides involved: pure and mixed metal oxide redox systems. In the pure oxide system, only a single metal element is present in the oxides. Some of the most promising pure oxide materials include BaO_2/BaO, CuO/Cu_2O, Fe_2O_3/Fe_3O_4, Mn_2O_3/Mn_3O_4, and Co_3O_4/CoO. Typically, the synthesis of pure redox systems is more straightforward, but mixed metal oxide systems offer advantages such as improved reversibility and lower costs [155]. Mixed metal oxide redox systems, on the other hand, contain more than one metallic element in the oxide. Recently, perovskite oxides have gained significant interest as mixed oxide thermochemical materials due to their intriguing

characteristics. The general formula for perovskite oxides is ABO_3, where A is typically a rare earth or alkaline earth cation, while B is generally a transition metal cation. Their structure is ideally cubic, with A cations surrounded by 12 coordinated O anions and B cations occupying the octahedral holes created by the oxygen lattice. Perovskites undergo reversible non-stoichiometric reduction at specific temperatures and oxygen partial pressures. The oxygen release/uptake phenomena in these materials induce significant heat effects, with reduction being highly endothermic and oxidation highly exothermic, making perovskites attractive for TES applications [60]. Typical perovskite oxides used as TCMs include $CaMnO_3$, $SrCoO_3$, $SrFeO_3$, and $BaCoO_3$ [175]. However, doping the perovskite oxide structure with expensive and atomically heavy rare earth and/or metal cations can increase their thermochemical properties, but also increase costs and decrease the mass-specific energy storage densities [176,177].

In conclusion, while TCES presents the most complex challenges within TES systems, the diverse range of reversible reactions, particularly solid-gas interactions and sorption processes, offers significant potential. Ongoing research into promising materials like salt hydrates, metal carbonates, and metal oxides (including perovskites) is crucial for overcoming current limitations such as material stability, reaction kinetics, and environmental concerns. Further investigation and development in these areas will pave the way for the realization of efficient and effective TCES technologies for various temperature applications.

1.4.2. Salt hydrates for low-temperatures applications

Salt hydrates demonstrate advantageous properties for TES in low-temperatures applications. These advantages include high volumetric energy storage capacity, the ability to tune the operating temperature, self-separation of the reacting components, and the utilization of water vapor as a safe and inexpensive gaseous reactant [61,178]. Storage and release of low temperature heat by using salt hydrates comprise dehydration and hydration processes and can be described by the following reversible reaction [60]:

$$Salt{\cdot}mH_2O_{(s)} + \Delta H \leftrightarrows Salt{\cdot}(m\text{-}n)H_2O_{(s)} + nH_2O_{(g)} \qquad (m \geq n)$$

Where, $Salt{\cdot}mH_2O_{(s)}$ represents salt hydrate and $Salt{\cdot}(m\text{-}n)H_2O_{(s)}$ is the salt partially or completely dehydrated. In fact, the dehydration (as well as hydration) reaction can occur in different steps at different desorption (sorption) temperatures and intermediate

hydrates phases can appear in the system. During the charging phase, these materials absorb heat and undergo an endothermic dehydration reaction. In this way the energy is stored by breaking chemical bonds of water with salt. Once energy is needed, the reverse exothermic hydration reaction is triggered, leading to the release of the accumulated thermal energy. The cyclic functionality of TCMs allows for the effective storage and release of greater thermal energy quantities per unit mass compared to SHS and LHS systems, resulting in a favorable high energy density. When selecting a suitable material for a TCES system with salt hydrates as TCMs, several key factors must be considered to ensure system reliability. Given that the primary applications for such systems are building cooling and heating, the choice of material must meet specific requirements [61,67]:

- High energy density: to store larger energy in the minimum possible volume.
- Reaction temperature reachable by a solar collector: the salt dehydration process should take place at temperature below 150 °C (known as the maximum reachable temperature by a solar collector).
- Non-toxicity and non-flammability: essential for implementation in buildings, ensuring compliance with health and safety standards.
- Non-corrosiveness: particularly concerning the materials in contact with the reactor.
- Stability after multiple dehydration/hydration cycles: to guarantee the system's long-term effectiveness.
- Cost-effectiveness: to maintain competitiveness in the market.

The current research into novel salt hydrates exhibiting specific properties relevant to specific applications, is quite dynamic [41,142,179–181]. A theoretical framework was suggested by Donkers *et al.* [41] and Deutsch *et al.* [180], whereas N'Tsoukpoe *et al.* [142] presented a combination of theoretical and experimental approaches. For instance, Donkers *et al.* conducted a comprehensive study to evaluate the theoretical potential and limitations of salt hydrates as TCMs for seasonal TES in the building environment. They compiled and analysed thermodynamic data for a large number of salt hydrate reactions, filtering the data to identify a shortlist of 25 TCM hydrate reactions that met specific criteria, including a hydration reaction capacity higher than

1.3 GJ m^{-3}, a hydration temperature of 50 °C or higher, and a dehydration temperature below 120 °C. The shortlisted reactions were then further analysed considering factors such as price, chemical stability, reaction kinetics, and safety for domestic environments. At the conclusion of this evaluation process, K_2CO_3 was identified as the most promising candidate for open or closed TCES systems, although it exhibited a relatively low energy density [41]. On an experimental point of view, N'Tsoukpoe *et al.* conducted a comprehensive assessment of 125 salt hydrates for their suitability as TCES materials, targeting an application that would meet both heating and domestic hot water demands with a minimum discharge temperature of 60 °C. Their evaluation process involved a three-step approach. Initially, they performed a preliminary selection, considering factors such as toxicity and explosion risk. In the subsequent steps, the authors implemented a combined methodology, integrating theoretical calculations and experimental measurements using thermogravimetric analysis. The net energy storage density and thermal efficiency of the materials were then used to evaluate the potential of 45 pre-selected salt hydrates for low-temperatures TCES applications. According to the authors, $SrBr_2 \cdot 6H_2O$ and $LaCl_3 \cdot 7H_2O$ were identified as the most promising salt hydrates from a thermodynamic perspective, but their evaluation did not consider economic factors [142]. The authors also concluded that the thermal efficiency of classical TCES processes remains low. To address this, they agreed on the need to adopt strategies to modify the properties of salts, such as adding a supplementary salt [41,142].

Trausel *et al.* identified $MgCl_2 \cdot 6H_2O$, $Na_2S \cdot 9H_2O$, $CaCl_2 \cdot 6H_2O$, and $MgSO_4 \cdot 7H_2O$ as the most promising candidates for TCES based on theoretical energy density, price, and workability. While the theoretical energy density ranged from 1.85 to 3.17 GJ m^{-3}, with Na_2S having the highest value, the actual energy density under operating conditions was lower for most salts. However, Na_2S still achieved the highest practical value [182]. The main drawbacks of these salts include the formation of toxic and corrosive gases, such as H_2S and HCl. Other challenging drawbacks, for discussed salts, include deliquescence and/or low melting points below the hydration temperature, leading to low material stability [183]. To improve the stability of salt hydrates, the primary strategies adopted are encapsulation of the active phase and impregnation in porous inactive materials to create composite materials [60]. The limitations to the ready implementation of salt hydrates TCMs in operating systems,

as well as possible solutions to mitigate them, will be discussed in § **1.4.4** section. While § **1.4.6** section present a list of most employed salt hydrates, together with their thermochemical parameters, used as TCMs in building sector.

In conclusion, salt hydrates present a compelling option for low-temperatures TES due to their high energy density and tuneable operating temperatures. However, salt hydrates present some drawbacks which hinder their practical implementation such as toxicity, corrosiveness, deliquescence, low melting points, and the need for enhanced thermal efficiency and stability over multiple cycles. Research is addressed to explore new reaction systems, as well as, to develop composite materials for overcoming described issues.

1.4.3. Deliquescence phenomenon in traditional inorganic salt hydrates

One of the most intriguing limitations to the ready implementation of salt hydrates in operating systems is the issue of deliquescence during repeated dehydration/hydration cycles. In theory, the rehydration process should be fully reversible when the salt regains the same number of crystal water molecules. However, in certain instances, a saturated salt solution is formed instead of a salt hydrate during the hydration reaction. This phenomenon, known as deliquescence, occurs when a solid substance absorbs moisture from the atmosphere to such an extent that it dissolves in the absorbed water, forming a liquid solution. This happens when the vapor pressure of the saturated solution of the salt hydrate is lower than the partial pressure of water vapor in the surrounding air. Here is presented a step-by-step breakdown of how deliquescence occurs in salt hydrates [184,185]:

1) Hygroscopic nature: salt hydrates are inherently hygroscopic, meaning they have an affinity for water molecules in the air. This is due to the presence of water molecules within their crystal lattice and the ionic nature of the salt, which attracts polar water molecules.
2) Water vapor absorption: when a salt hydrate is exposed to air with a sufficiently high partial pressure of water vapor, water molecules from the atmosphere begin to condense and adsorb onto the surface of the solid crystal.
3) Formation of a saturated solution: as more water molecules are absorbed, a thin layer of aqueous solution forms on the surface of the salt hydrate. The

concentration of the dissolved salt in this layer increases until it reaches saturation.

4) Vapor pressure difference: the crucial factor driving deliquescence is the difference in vapor pressure. The saturated solution of the salt hydrate has a specific vapor pressure of water above it, which is lower than that of pure water at the same temperature due to the presence of the dissolved salt. If the partial pressure of water vapor in the air is higher than the vapor pressure of the saturated salt hydrate solution, there is a thermodynamic driving force for more water vapor to condense onto the surface.
5) Continuous dissolution: because the atmospheric water vapor pressure is higher than that of the saturated solution, the absorbed water does not readily evaporate. Instead, it continues to dissolve more of the solid salt hydrate. This process continues as long as the atmospheric humidity remains above the deliquescence relative humidity (DRH) of the salt hydrate.
6) Formation of a pool of solution: over time, the accumulated absorbed water becomes sufficient to form a visible pool of concentrated salt solution. The solid crystal may fully dissolve in this process.

Different factors influence the deliquescence phenomenon in salt hydrate [186–188]. Are now listed the principal ones:

- Relative humidity (RH): deliquescence occurs when the ambient RH exceeds the DRH of the salt hydrate. Each deliquescent substance has a characteristic DRH at a given temperature.
- Temperature: temperature can influence the DRH and the rate of water absorption. Generally, the DRH of salts with a positive heat of dissolution decreases as temperature increases.
- Solubility of the salt hydrate: highly soluble salt hydrates tend to have lower DRH values and are more prone to deliquescence.
- Presence of impurities: impurities can sometimes lower the DRH of a salt mixture, causing it to deliquesce at lower humidity levels than the pure salt.

The deliquescence phenomenon mainly affects inorganic salt hydrates due to their high hygroscopic nature, which drives the absorption of water vapor to form a

saturated solution in which the solid starts to dissolve. This is attributed to the high solubility of inorganic salts in water. Recently, innovative organic salt hydrates have been proposed as TCMs to overcome the deliquescence issue [189,190]. These promising materials have the interesting property of being much less soluble in water, with their water solubility at least an order of magnitude lower than that of common inorganic salt hydrates at the same temperature. This aspect excludes the deliquescence phenomenon by stabilizing the formation of a wetting layer during water absorption and preventing the establishment of a saturated solution, because salt can not dissolve in it. **Figure 1.16** provides a schematic representation for illustrating the deliquescence in common inorganic salt hydrates (**Figure 1.16a**) and how it is excluded with organic salt hydrates (**Figure 1.16b**).

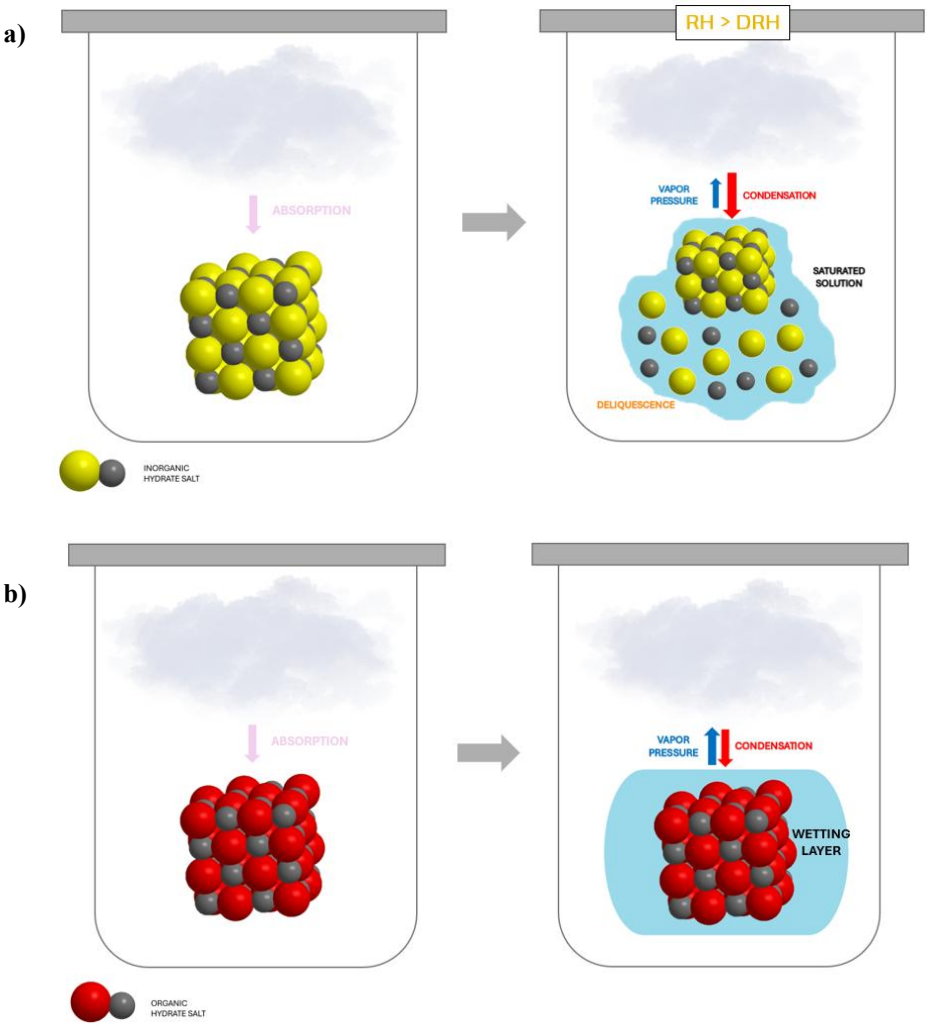

Figure 1.16 Schematic representation of a) deliquescence phenomenon during hydration of inorganic salt hydrate; b) formation of a wetting layer during hydration of organic salt hydrate, which prevents deliquescence.

1.4.4. TCM composites for low-temperatures applications

As seen previously, pure salt hydrates can present several issues that necessitate finding smart solutions to address them. In addition to the deliquescence phenomenon discussed in § **1.4.3** section, which leads to the formation of a liquid phase that can impede the reaction and cause salt leakage and corrosion, other common problems include low thermal conductivity that hinders efficient heat transfer during charging and discharging processes. Furthermore, salt hydrates often suffer from poor cycling stability during repeated dehydration and hydration reactions. The causes of this problem can be attributed to deliquescence and salt volume changes. Specifically, salt hydrates typically expand (swelling) in volume during the hydration reaction due to water uptake, while they reduce (shrinking) in volume when water is released during dehydration. These phenomena primarily cause cracking within the material and subsequently lead to mechanical stress on the system. Additionally, salt hydrate particles tend to agglomerate, reducing the surface area available for reaction and resulting in performance degradation over successive cycles [191–193].

At this purpose, composite materials are increasingly deployed to improve the properties of hydrated salts due to their multifunctional advantages in thermochemical applications. The integration of composites enhances, for instance, thermal conductivity and mechanical stability while reducing issues such as deliquescence and related leakage, all critical aspects for effective implementation [194].

One significant benefit of composite materials is their ability to enhance thermal conductivity. Embedding salt hydrates within a suitable matrix can significantly improve the overall thermal conductivity of the material, resulting in faster charging and discharging rates and enhanced heat transfer within the storage system. The most commonly used conductive fillers are carbon materials, although metallic nanoparticles are also employed. Examples of carbonaceous matrix include exfoliated graphite [165] and carbon nanotubes [164] and activated carbon. In addition, the use of described fillers guarantees an improved reaction kinetics, good durability and structural support (e.g., by increasing ease of materials pelletization).

The TCM stabilization into a well-designed matrix prevents salt leakage, especially in cases of deliquescence. This also helps to mitigate corrosion issues with the surrounding components. For instance, $LiCl{\cdot}H_2O$ exhibits a high-energy density, suitable for low-temperature heat storage applications. However, the hygroscopic

nature of lithium chloride leads to deliquescence resulting in various operational difficulties. For this reason, usually LiCl is combined with adsorbent porous matrices. In fact, materials like silica gel, zeolites, alumina, vermiculite, clay and metal organic frameworks (MOFs) provide a porous structure to disperse the salt hydrate, improve vapor transport, and limit agglomeration. Their high thermal stability represents also an interesting advantage [157,195,196].

Taking into account the case of LiCl, Calabrese *et al.* proposed a composite material made from silicone vapor-permeable foam filled with the salt (40%wt.). The foam can provide excellent thermal conductivity and structural support. In addition, this system confines LiCl within a flexible matrix, allowing the salt to undergo volume changes during dehydration and hydration cycles without compromising the foam structure [197]. *In situ* X-ray diffraction (XRD) and environmental scanning electron microscopy (ESEM) were used to investigate the material's structural and morphological changes during these cycles. The results show the salt is effectively embedded, minimizing salt solution release upon overhydration. The energy density of the stabilized foam, estimated at 1854 kJ kg^{-1}, indicates it is a competitive option among other LiCl salt hydrate composites [198]. In two distinct studies, Calabrese and coworkers explored an innovative $MgSO_4 \cdot 7H_2O$-filled silicone composite foam for sorption TES applications [199,200]. The composite foams exhibited a mixed structure of open and closed cells, with the morphology influenced by the salt hydrate filler content. Foams with lower salt concentrations (40-50%wt.) had more open cell structures, while those with higher concentrations (60-70%wt.) had more limited cell interconnections, partially hindering the vapor exchange. The composite foams demonstrated a significant capacity for hydration and dehydration compared to pure salt, and the foaming process did not interfere with the reaction between water and salt [200]. Further studies evaluated the progressive loss of salt during cycling, finding a 13% decrease after 50 cycles, but showing that this loss did not substantially impact the sorption storage efficiency of the silicone foams [199]. Overall, the research confirmed that composite systems with salt hydrates and foams are a viable strategy to overcome the limitations of using pure hydrated salts.

As previously said, an efficient alternative to foam composites is represented by salt dispersion into porous matrix. These composite materials utilize salt hydrates that are embedded within a porous structure. This approach helps to resolve many of the

difficulties associated with pure salt, as the porous matrix not only supports and disperses the salt but also enhances heat and mass transfer properties while reducing the potential for agglomeration and swelling. For instance, Hongois *et al.* reported that the combination of 15%wt. of $MgSO_4$ with zeolite 13X resulted in an energy storage capacity of 166 kWh m^{-3}, which corresponds to 45% of the expected theoretical value. Notably, this energy density is 23% greater than that of pure zeolite 13X's theoretical energy density [201]. Instead with silica gel matrix, Courbon *et al.* reported a $CaCl_2 \cdot 6H_2O$ (43%wt.) composite that shows an energy storage density of 211 kWh m^{-3}, which is greater than the energy density of $CaCl_2$ with aluminosilicate (180 kWh m^{-3}) and significantly higher than that of $MgSO_4$ with zeolite 13X (166 kWh/m^3) [202]. Permyakova *et al.*, instead, evaluated $CaCl_2$ impregnated with six different water-stable MOFs, and they obtained composites which had varying properties due to variation of pore properties of the host matrix. Increasing the desorption temperature from 80 to 100 °C improves the cyclic loading lift, consequently enhancing the energy storage capacity [203].

Other than poor thermal conductivity, salt hydrates can present slow reaction kinetics, which limit the power output and efficiency of TCM-based systems. In some cases, the porous structure of the matrix can facilitate improved mass transport of water vapor to the salt hydrate, enhancing the hydration and dehydration kinetics. In this perspective, the development of thin, porous coatings that enable efficient vapor exchange with the environment is highly recommended. For the preparation of such coatings, the TCM is typically blended with a polymeric matrix. Polymers can serve as binders or encapsulating materials, improving the mechanical stability and preventing salt leakage. Additionally, polymeric coatings can offer high water vapor permeability and reversible deformability, minimizing resistance to water transport and accommodating the volumetric changes of the TCM during repetitive dehydration and hydration processes [204]. In brief, the application of coatings aids in controlling the reaction rate. For instance, a coating can reduce moisture access to the salt, promoting a more gradual and stable hydration. Moreover, coatings can also improve the thermal stability of hydrated salts. This is particularly important to ensure that the salts can reliably store and release heat without undergoing structural changes that would compromise their efficiency. Some coatings can also influence the solubility of

salts, improving heat storage capacity and reducing energy loss due to too rapid or inefficient dissolution and crystallization reactions [205].

In conclusion, composite materials offer a versatile approach to thermal energy storage by enabling the combination of materials with tailored thermal, mechanical, and chemical properties for specific applications [206]. By improving overall performance and stability, composites can lead to more compact and efficient thermal energy storage systems with higher energy storage density at the system level. However, the cost of materials and manufacturing, along with the complexity of composite preparation methods, remains a barrier to commercialization. Future research should focus on optimizing the composition, microstructure, and preparation methods of these composites, while using low-cost matrices, to achieve high-performance and cost-effective materials for widespread energy storage applications [207].

1.4.5. Novel organic salt hydrates

The deliquescence phenomenon and its negative impact on inorganic salt hydrates have been described in § **1.4.3** section. One possible solution to this issue is the use of TCMs with low water solubility. Particularly, it has been found that organic salt hydrates possess this characteristic and have been proposed as novel materials for TCES in low-temperatures applications [189,190].

The use of organic hydrated salts as TCMs is already known in literature and one of the first to be used was calcium oxalate monohydrate ($CaC_2O_4 \cdot H_2O$). Knoll *et al.* examined the dehydration and hydration behavior as well as the cyclic stability of this material [208]. Its selection was determined through the application of an algorithm capable of systematically evaluating a database of potentially suitable reversible reactions [180]. Authors have determined that the dehydration and hydration reactions of calcium oxalate monohydrate are completely reversible, in contrast to other salt hydrates. Furthermore, they discovered that the rehydration temperature is highly dependent on the water vapor concentration. Complete reversibility can be achieved not only at room temperature, but also at up to 200 °C, depending on the water vapor concentration. This enables isothermal switching of the material between charging and discharging by altering the partial pressure of H_2O. Additionally, the material exhibits rapid reaction kinetics and complete reversibility over 100 cycles, without any

observed aging effects [208]. The researchers have further investigated these promising characteristics by developing and evaluating a pilot-scale thermochemical heating system directly integrated within a real building environment. They have successfully demonstrated the technological feasibility of all the process steps and the system's ability to provide heat supply at the required operating conditions for practical applications. This research represents a significant advancement in the TRL of TCES, validating its performance in a relevant environment [209]. Based on the promising results of the calcium oxalate systems, the researchers investigated other calcium dicarboxylate salt hydrates as potential heat storage materials. These materials were synthesized by neutralizing corresponding acidic precursors with a calcium base, followed by crystallization. Different characterization techniques demonstrated that all candidates were suitable for low-grade storage and thermally stable up to 220 °C. Among these, calcium malonate dihydrate (637 kJ kg^{-1}), calcium terephthalate trihydrate (695 kJ kg^{-1}), and tetrafluoro calcium terephthalate tetrahydrate (657 kJ kg^{-1}) exhibited higher enthalpies of dehydration than calcium oxalate monohydrate. Furthermore, *in situ* powder X-ray diffraction (XRD) studies were conducted to examine the dehydration and rehydration reactions of the most promising candidates, revealing the structural changes between the hydrate and anhydrate states [210].

The studies highlighted in current section pave the way for the use of organic hydrated salts as innovative TCMs. Having an organic component in the molecule allows for modulation of the physicochemical and thermochemical properties of the salt by varying the molecular structure. From this perspective, organic chemistry reactions enable tailoring the structure to meet specific objectives, unlike inorganic synthetic procedures. However, it is important to note that increased structural complexity often leads to higher costs for the final product.

The first attempt to promote organic salt hydrates as a solution for overcoming deliquescence was proposed by Mastronardo *et al.* in 2022 [190]. In their study, the authors explored new strategies to develop suitable materials based on low-soluble or insoluble organic hydrated salts. The goal was to reduce or avoid deliquescence phenomena under operating conditions, ensure the ability to coordinate a high number of water molecules, and maintain stability [211]. The researchers selected calcium ceftriaxone, which can combine up to seven water molecules, as the target salt. This compound was synthesized through an ion exchange reaction starting from a

pharmaceutical precursor (disodium ceftriaxone hemiheptahydrate). In fact, the precursor was not an ideal candidate for TCES applications due to its low water content (i.e., 3.5 water molecules per unit formula) and high water solubility. The synthesized material was found to be capable of operating in the temperature range of 30-150°C and did not exhibit deliquescence phenomena when exposed to relative humidity between 10 and 100%. The observed heat storage capacity of 595.2 kJ kg^{-1}, along with the demonstrated thermal stability and good reversibility after dehydration/hydration cycles, highlight the potential of this class of materials. These findings have opened new research paths for the development and investigation of innovative organic salt hydrates as TCES materials [190].

Pushed by these interesting results and considering that the exploration and assessment of new TCMs, especially of organic nature is certainly interesting, a new work has been recently published on the thermochemical assessment of calcium L-lactate pentahydrate (CL) [189]. The investigated material represents the main objective of this thesis work. CL presents a low solubility in water, and it is competitive with other inorganic salt hydrates in term of heat storage capacity. Furthermore, CL is inexpensive, non-toxic, non-corrosive, environmentally safe and during dehydration/hydration reactions does not generate toxic or corrosive gases, like HCl or H_2S. Its thermochemical properties will be discussed in detail in § **Chapter 2**.

1.4.6. TCMs in building applications

Salt hydrates are promising TCMs for TES in buildings due to their high energy density and potential for long-term, near-lossless storage. Integrating them directly into building materials like concrete or mortars (i.e., in building envelops) or in auxiliary reactors/tanks offers a unique approach to create multifunctional systems capable of storing and releasing thermal energy on demand [212].

In buildings, TCM storage is assessed to have many advantages over other types of TES, but it is still in the experimental stage [63]. The analysis of the literature, indeed, showed that there are still very few studies that carried out environmental or economic assessments of this kind of system, indicating that this technology has not yet reached maturity [213].

The introduction of TCMs in the building sector is usually studied for their implementation in reactors, such as solar DHW applications. When designing the

system and selecting the TCM, key considerations should include the operating conditions (vacuum vs. atmospheric) and their impact on reaction temperatures and the system configuration (open vs. closed). Energy density is also influenced by factors like sample scale, reactor geometry, characterization methods, and operating temperatures. However, there is currently no standard procedure to determine the thermophysical properties of these materials [61]. In addition, most of the systems have only been studied at the material scale (TRL = 1-2), with only a few reaching the reactor scale (TRL = 4) in advanced project [133].

Therefore, material selection remains a controversial research field due to the limitations discussed in § **1.4.4** section. A list of the most promising pure inorganic salt systems used for TCES applications in buildings is provided in **Table 1.7**, including their theoretical and experimental energy densities, as well as their reaction temperature conditions for charging and discharging.

Table 1.7 Theoretical (Th.) and experimental (Ex.) energy density and reaction temperature conditions of promising material couples for chemical heat storage in residential applications.

Reaction (TCM)	Th. energy density (GJ m^{-3})	Ex. energy density (GJ m^{-3})	Reaction temperature (°C) (charging/discharging)	Ref.
$MgCl_2 \cdot 6H_2O \leftrightarrow MgCl_2 \cdot H_2O + 5H_2O$	2.5	0.71	150/30-50	[61]
$MgCl_2 \cdot 6H_2O \leftrightarrow MgCl_2 \cdot 2H_2O + 4H_2O$	2.2	-	115-130/35	[133]
$MgSO_4 \cdot 7H_2O \leftrightarrow MgSO_4 + 7H_2O$	1.5	-	122-150/35	[61,133]
$MgSO_4 \cdot 6H_2O \leftrightarrow MgSO_4 \cdot H_2O + 5H_2O$	2.37	1.83	72/-	[61]
$CaCl_2 \cdot 2H_2O \leftrightarrow CaCl_2 \cdot H_2O + H_2O$	0.7	-	95/35	[61,133]
$SrBr_2 \cdot 6H_2O \leftrightarrow SrBr_2 \cdot H_2O + 5H_2O$	2.3	2.08	70-80/23.5	[61,133]
$LiCl \cdot H_2O \leftrightarrow LiCl + H_2O$	2.08	-	72/66	[52]
$LiBr \cdot H_2O \leftrightarrow LiBr + H_2O$	2.01	-	110/103	[52]
$K_2CO_3 \cdot 1.5H_2O \leftrightarrow K_2CO_3 + 1.5H_2O$	1.3	-	65/59	[52]
$Al_2(SO_4)_3 \cdot 6H_2O \leftrightarrow Al_2(SO_4)_3 + 6H_2O$	1.9	-	150/-	[61]
$CaSO_4 \cdot 2H_2O \leftrightarrow CaSO_4 + 2H_2O$	1.4	-	-/89	[61]
$CuSO_4 \cdot 5H_2O \leftrightarrow CuSO_4 \cdot H_2O + 4H_2O$	2.07	1.85	92/-	[61]
$Na_2S \cdot 5H_2O \leftrightarrow Na_2S \cdot 0.5H_2O + 4.5H_2O$	2.7	-	80-83/65-35	[61,133]

Considering, instead, the direct integration of TCMs in building materials, such as mortar or concrete matrix, shows promising potential as well as challenges to be faced. First of all, embedding TCMs within the mortar matrix distributes the energy storage capacity throughout the building envelope (walls, floors), potentially leading to more uniform temperature regulation and reduced reliance on energy supply for heating and cooling. In this context, the incorporation of salt hydrates can increase the overall thermal mass of the building element, further contributing to temperature stabilization [214]. The integration of salt hydrates into mortars allows for passive TES, where the hydration and dehydration reactions can absorb or release heat in response to changes in humidity and temperature. Furthermore, directly incorporating the TCMs into the building eliminates the need for separate storage tanks or units, saving valuable indoor space.

However, integrating salt hydrates into mortars for TES requires careful consideration. The main issues involve compatibility between the salt hydrate and the mortar matrix. Ensuring chemical compatibility is crucial, as the salt hydrate may negatively impact on the mortar's mechanical strength, setting time, or long-term durability. Conversely, the mortar matrix must protect the salt hydrate from degradation and performance loss over repeated hydration/dehydration cycles, by ensuring controlled processes and preventing deliquescence [215]. The confined pore structure of the mortar could hinder the hydration and dehydration of the salt hydrate, impacting the power output and charging/discharging times of the TES system. Thus, optimizing the pore structure and water vapor transport within the mortar is essential. Additionally, salt hydrates undergo volume changes during hydration and dehydration, and the mortar matrix must be able to accommodate these changes without cracking or losing its structural integrity. Encapsulation or the use of flexible additives could be a suitable solution for mitigating salt leakage and potentially accommodating volume changes. It is important that the shell of microcapsules is permeable to water vapor [19,31,216].

Examples of composite mortars with directly integrated TCMs will be investigated in § **4.1** section.

In conclusion, integrating salt hydrates directly into mortars for TCES in buildings presents an innovative and potentially space-saving approach to enhance energy efficiency and thermal comfort. However, significant research and development are

needed to overcome the challenges related to material compatibility, durability, hygrothermal stability, thermal conductivity, reaction kinetics, and volume changes. By employing appropriate composite strategies and optimizing the integration process, it may be possible to create multifunctional building materials that contribute to more sustainable and energy-efficient buildings. Further research focusing on material characterization, long-term performance evaluation, and cost-effective implementation methods is crucial for the successful adoption of this technology.

Chapter 2 Calcium L-lactate pentahydrate (CL)

2.1. CL: from pharmaceutical excipient to promising TCM

Calcium L-lactate pentahydrate (CL) is an organic salt hydrate with important economic interest due to its broad spectrum of applications, mainly in the food and pharmaceutical industries [217,218]. In the food industry, CL usage was explored as food additive, stabilizer and thickener, nutritional supplement, leavening and firming agent, flavor enhancer and pH stabilizer [219,220]. While salt employment in pharmaceutical field includes the treatment of calcium deficiency and the use as an excipient for tablet formulations considering its high flowability and compressibility [221,222]. As described, CL holds promise as an excipient in pharmaceutical formulations, and for this reason the physicochemical properties of the molecule have been deeply investigated over the last 20 years [218,222,223]. The synthesis of CL typically involves the neutralization of L-lactic acid with a calcium base [224], such as calcium hydroxide or calcium carbonate [225], followed by crystallization under controlled conditions to obtain the pentahydrate form [219,226]. Despite being a small organic molecule, CL molecular structure is complex, involving coordinated interactions between calcium cations, L-lactate anions, and water molecules [225]. This intricate network contributes to its unique physicochemical properties and has been characterized by X-ray diffraction (XRD) analyses [227]. In **Figure 2.1** is shown the CL unit formula structure.

Figure 2.1 Calcium L-lactate Pentahydrate (CL) unit formula structure. The constituent elements are: Carbon (grey), Oxygen (red), Hydrogen (white) and Calcium (yellow).

As discussed in the previous chapter, the deliquescence resistance of CL is contingent upon its crystalline structure and the interactions between its constituent ions and water molecules. The choice to use calcium-based hydrated salt is strategic, as calcium is a relatively abundant and inexpensive element, contributing to the

potential cost-effectiveness of related materials. Besides, calcium ions (Ca^{2+}) possess relatively high positive charge density, allowing them to strongly attract and coordinate polar water molecules. The size of the calcium ion is also suitable for coordinating a relatively large number of water molecules in its hydration sphere [210]. In fact, Apelblat *et al.* established that in the range of temperatures suitable for low-temperatures applications, calcium L-lactate is the only metal L-lactate compound able to coordinate five water molecules per unit formula. In contrast, other divalent cations of the same period (Fe^{2+} and Zn^{2+}) or group (Mg^{2+}) of the calcium in the periodic table were observed to form dihydrates when combined with L-lactate anions [228]. Furthermore, the lactate groups play an important role within the CL structure, enhancing the properties of this hydrated salt and paving the way for its wide use as a TCM. Specifically, the lactate groups ensure a suitable hydrophobicity of the molecule, protecting it from deliquescence. Moreover, the water solubility of CL is affected by the presence of organic lactate moieties. The solubility in water has been experimentally determined to be 50 g dm^{-3} at 20 °C, aligning with the data reported in the scientific literature [229,230]. Nevertheless, this value is significantly lower than the water solubility of common inorganic salt hydrates used as TCM. For instance, the solubility of LiCl, LiBr, and $CaCl_2$ are 569 [231], 1600 [232], and 745 g dm^{-3} [233], respectively, at the same temperature. This markedly lower solubility of CL compared to other inorganic hydrated salts ensures greater resistance to the phenomenon of deliquescence, as discussed in § **1.4.3** section.

In addition, this organic salt is inexpensive, non-toxic, non-corrosive, environmentally safe, and widely available due to its broad range of applications. These attributes make calcium L-lactate pentahydrate (CL) a promising material for TCES at low-temperatures. Recently, a European patent (#102022000007847) has been filed on the use of calcium lactate as a component in thermal systems for thermochemical heat storage, demonstrating the novelty of employing this salt hydrate, and organic hydrated salts in general, as materials for thermochemical storage. The patent's inventors are collaborators within the research group where the author of this thesis conducted his PhD research.

This chapter discusses the reversibility of the dehydration and hydration processes, as well as the structural, chemical, and morphological modifications that occurred in the salt hydrate during this cycle. These findings are assessed in the context of

employing the material for thermochemical heat storage applications. The data here presented has been recently published in [189].

2.2. Dehydration and hydration kinetics models for CL

The dehydration and hydration behaviors of a material are crucial factors in evaluating its reliability for TCES applications. Keeping this in mind, Sakata and colleagues developed kinetic models describing the dehydration and hydration processes of calcium L-lactate, with the aim of assessing its potential as a pharmaceutical excipient [222,223]. They examined the dehydration/hydration behavior of calcium L-lactate pentahydrate and anhydrous forms under various storage temperature and humidity conditions.

The dehydration process of calcium L-lactate pentahydrate was studied using thermogravimetric-differential thermal analysis (TG-DTA) with isothermal experiments conducted at different temperatures: 55, 60, 70, and 80 °C. At all these temperatures, the dehydration profile of CL appeared as a straight line, and the dehydration rate increased with temperature [222]. By applying the Hancock and Sharp kinetic method [234], which is based on solid-state kinetic model equations, Sakata *et al.* were able to determine the reaction mechanism. The kinetic model fitting suggests that the dehydration of CL was best described by a zero-order mechanism (Polany-Winger equation). Furthermore, the CL dehydration process follows the same kinetic model at both low and high temperatures, enabling the estimation of the time required to almost fully dehydrate the salt hydrate powder. For instance, approximately 15 days were estimated to be needed at 40 °C [222]. Additionally, Sakata *et al.* observed a significant particle aggregation in the salt powder after dehydration, a behavior that was also observed in CL tablets. In tablet formulation, the material contracts in thickness and diameter during dehydration, resulting in a loss of hardness. Moreover, the micropore radius of CL tablets increases during the process, leading to a different kinetics model compared to the powder dehydration reaction. The dehydration of CL tablets might involve water vapor diffusion and other reaction processes. Since the dehydration of the bulk powder occurs much faster than that of the tablets, the rate-determining step of the dehydration of CL tablets might be the process of diffusion from the micropores [223]. Considering these aspects, it is

plausible that organizing CL in a pellet configuration would likely limit the system reliability.

On the other hand, the anhydrous salt was subjected to hydration experiments at 25 °C under different relative humidity conditions (31, 43, 60 and 75%). The hydrated fraction was determined by differential scanning calorimetry (DSC) and the data were analyzed to determine the reaction mechanism using the Hancock and Sharp method [234]. In this case, the hydration kinetic of the anhydrous salt was best described by a three-dimensional diffusion model (Ginstiling-Brounshtein equation). Generally, the hydration of solid-phase materials can be described by four fundamental processes: the diffusion of water in the vapor phase, the hydration of the solid surface by water from the vapor phase, the diffusion of water in the solid phase, and the reaction to form hydrates. In the case of calcium lactate, the kinetic model established that the rate-determining step of the hydration process is the diffusion of water in the solid phase. When this process is the rate-determining step, the other processes can be considered negligible [222].

In conclusion, Sakata and coworkers' studies indicate that the dehydration of CL proceeds more rapidly than the reverse hydration process [222]. Due to this discrepancy, adjustments are required to enhance the salt hydration kinetics. Accordingly, § **Chapter 3** presents attempts to improve the salt hydration kinetics by the realization of composite materials using a porous matrix for dispersing the salt particles.

2.3. Materials and methods

This chapter discusses the thermochemical properties of calcium L-lactate pentahydrate (CL) as promising TCM for low-temperatures applications. The salt hydrate has been purchased from Sigma Aldrich and has the molecular formula $[CH_3CH(OH)COO]_2Ca \cdot 5H_2O$ with a molecular weight of 308.29 g mol^{-1}. The material was provided as a fine powder with an average grain size of 100 to 150 μm, as specified by the supplier, and was used without further treatment.

2.3.1. Physical, structural, chemical, and morphological characterizations

The real density of CL powder was measured using a helium pycnometer (Ultrapyc 5000 Foam, Anton Paar) at 20 °C, based on the average of five measurements. The salt density will be used to estimate the volumetric heat storage capacity of CL.

In addition, *ex situ* X-ray diffraction (XRD) analysis was performed on the CL powder during the dehydration process, using a D8 Advance Bruker diffractometer configured in a Bragg-Brentano theta-2theta setup, with Cu Kα radiation at 40 V and 40 mA. The powder was heated in an oven under static air conditions at selected temperatures of 40, 50, 60, 70, and 80 °C, and allowed to equilibrate for specific time periods (15 minutes or 2 hours). Following each heat treatment, XRD analysis was performed. Each scan was executed in the 2θ range of 5-40°, with a step increment of 0.010° and a duration of 0.1 seconds per step. This kind of experiment allows to evaluate the structural change occurred by the salt hydrate during its dehydration reaction.

The chemical characterization of CL and its dehydrated and rehydrate forms was carried out by Fourier-transform infrared spectroscopy (FTIR, Spectrum Two Perkin Elmer) in transmission mode, covering a wavenumber range from 400 cm-^{1} to 4000 cm^{-1}, with a spectral resolution of 4 cm^{-1} and a scan count of 46. This analysis was performed on the as-received powder (CL), the heat-treated dehydrated powder (CL DEH), and the re-hydrated samples at various rehydration periods (CL/H*n*h, where *n*h denotes the number of hours).

The morphological characteristics of CL powder were analysed in its purchased form as well as in its dehydrated and rehydrated states, employing an environmental scanning electron microscope (ESEM, FEI Quanta 450) with an accelerating voltage of 5 kV. This analysis included observations made during the hydration and dehydration processes. The material was first dehydrated in an oven at 80 °C for 12 hours, after which it was introduced into the ESEM chamber to capture micrographs in a controlled environment with water vapor. The relative humidity (p/p_0) was varied from 0% to 93% by adjusting the temperature and water vapor pressure within the ranges of 5-40 °C and 10-800 Pa, respectively. Micrographs were specifically obtained after a 30-minute equilibration period under isothermal conditions at 40 °C, during which the water vapor pressure was varied from 10 Pa to 810 Pa (representing 0.1-10.9% relative humidity). Subsequently, under isobaric conditions at 810 Pa, the chamber temperature was reduced from 40 °C to 5 °C, resulting in relative humidity values ranging from 10.9% to 93%. Micrographs were obtained while the sample was maintained under the maximum p/p_0 conditions for intervals of 30, 60, and 120 minutes. The analysis was completed by dehydrating the sample at a temperature of

60 °C, with a water vapor pressure set at 10 Pa. For illustrative purposes, a schematic of the ESEM analysis conditions is included in **Figure 2.2**.

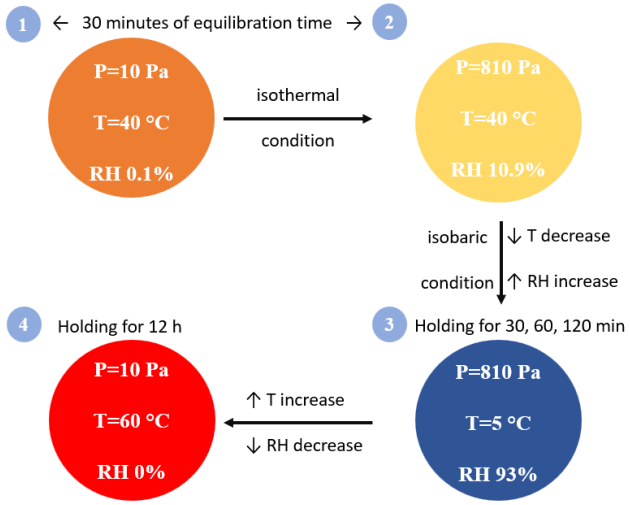

Figure 2.2 Schematic representation of environmental scanning electron microscopy (ESEM) conditions.

2.3.2. Thermal stability

The thermal stability of purchased CL was evaluated by coupled thermogravimetric-differential scanning calorimetric (TG-DSC) analysis. The instrument used was a simultaneous thermal analyzer (STA Jupiter F3 Netzsch). The analysis was conducted in an inert atmosphere (120 mL min^{-1} of Ar) using a Pt crucible with a holed lid and with a sample mass of ~10 mg. The sample was gradually heated from room temperature to 900 °C at a rate of 10 °C min^{-1} to evaluate the thermal degradation of the material. The gaseous species released from the apparatus were analysed via a mass spectrometer (MS, Discovery, TA Instruments).

2.3.3. Thermochemical characterization under isothermal conditions

The dehydration behavior of hydrate salt was investigated by isothermal thermogravimetric (TG) analyses. Experiments were conducted at various temperatures (40, 60, 70, and 80 °C) under inert atmosphere (120 mL min^{-1} of Ar) for 2 hours by using the previously described STA apparatus.

2.3.4. Evaluation of the heat storage capacity

The evaluation of heat storage capacity was conducted using the previously described apparatus in a coupled TG-DSC mode, which allowed for the measurement of mass and heat flow during an isothermal experiment at 80 °C for 2 hours, under an

inert atmosphere (120 mL min^{-1} of Ar). A platinum crucible with a holed lid was selected for this purpose, containing a sample mass of approximately 10 mg. The holed crucible was specifically chosen to mitigate convection losses when compared to open crucibles. An empty crucible was utilized as a reference. The heat storage capacity per mass unit (Q_S^m(kJ kg^{-1})) have been determined by integrating the specific heat flow (hf (mW mg^{-1})) during the reaction period [235]:

$$Q_S^m(kJ\ kg^{-1}) \int_{t_i}^{t_f} hf\ dt \quad (2.1)$$

2.3.5. Thermogravimetric dynamic vapor sorption analyses

Hydration and dehydration cycles were executed on commercial CL powder, to monitor salt mass variations during the processes. The analyses have been conducted within a controlled environment, characterized by regulated temperature and vapor pressure, as well as measurable mass changes. This process utilized a thermogravimetric dynamic vapor sorption (DVS) system (DVS Vacuum Surface Measurement Systems). The system is equipped with a micro-balance (precision of ±0.1 μg) and a water vapor pressure flow controller located within the measuring chamber. Before the testing phase, the sample was subjected to dehydration at 150 °C in vacuum for 2 hours. The hydration and dehydration processes were performed in two modes: (i) isothermal and (ii) isobar, utilizing various partial pressures (1200, 2550, 3500 Pa). The cyclability of the material was analyzed through three isothermal cycles at 30 °C, with the p/p_0 ratio ranging from 0 to 90%.

2.4. Results and discussion

2.4.1. Thermochemical and structural stability

This paragraph characterizes the thermochemical behavior of CL during dehydration reactions examined under different conditions, within its thermal stability range. It also discusses the salt structural changes occurring during the dehydration process.

Figure 2.3 illustrates the TG profile for the commercially available CL, which is subjected to heating from room temperature to 900 °C at a rate of 10 °C min^{-1} in an inert atmosphere (Ar at a flow rate of 120 mL min^{-1}). The analysis of evolved gas species through MS reveals three distinct slope changes, each associated with different

peaks in the gas species detected. The primary gases released during this process are identified as H_2O and CO_2. The observed mass change of approximately 24.5% within the temperature range of 40-150 °C corresponds to a peak in the H_2O evolution profile, thereby suggesting a likely connection to the dehydration reaction.

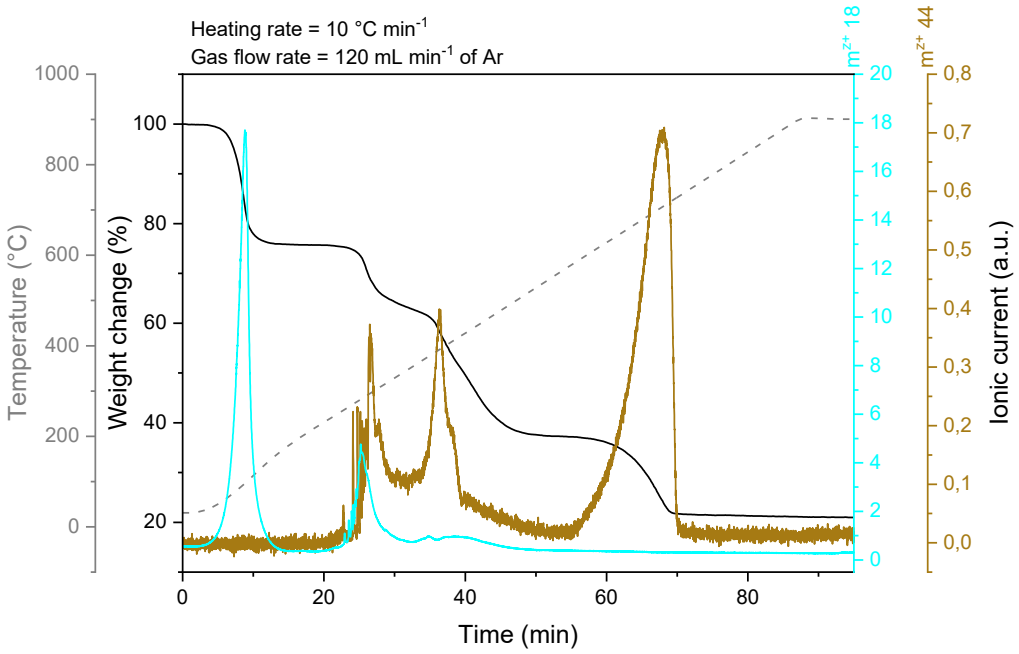

Figure 2.3 TG profile of CL as purchased heating up the sample from r.T. up to 900 °C by 10 °C min^{-1} under an inert atmosphere (Ar 120 mL min^{-1}). Detected gaseous evolved species by MS: ionic masses (m x^{z+}) 44 (CO_2) and 18 (H_2O).

The theoretical mass change associated with the dehydration (Δm_{th}^{D}) of one mole of CL can be expressed as:

$$\Delta m_{th}^{D}(\%) = \frac{M_{CL}-M_{CL\ DEH}}{M_{CL}} \cdot 100 = 29.2\% \qquad (2.2)$$

Where M_{CL} and $M_{CL\ DEH}$ are respectively, the molecular weight of pentahydrate (308.29 g mol^{-1}) and anhydrous (218.29 g mol^{-1}) calcium L-lactate. Correspondingly, the definition of the theoretical mass change due to the hydration (Δm_{th}^{H}) of one mole of CL DEH is as follows:

$$\Delta m_{th}^{H}(\%) = \frac{M_{CL}-M_{CL\ DEH}}{M_{CL\ DEH}} \cdot 100 = 41.2\% \qquad (2.3)$$

Taking into account Equation (2.2), it is clear that within low-temperatures range, only part of the water content (4.2 molecules) is released by the material. The subsequent mass change of roughly 12.6% that occurs between 260-300 °C is

associated with the release of both H_2O and CO_2, which exceeds the theoretical mass change linked to the complete dehydration of CL. This observation supports the idea that the lactate groups begin to thermally decompose. The thermal degradation of CL continues up to 720 °C. In fact, the weight change reaches a plateau over this temperature, resulting in a total mass loss of approximately 79.1%, with no further evolved gas species observed. The total weight loss observed at 900 °C is comparable to the theoretical weight loss predicted for CaO, which is considered the final product of the degradation process, estimated to be approximately 81.8%. A more in-deep investigation of CL thermal degradation will be provided in § **Chapter 3**, utilizing different characterization techniques.

The dehydration process shows that the release of water is not complete within the typical temperature range for low-temperatures applications. The remaining water molecules are expected to be released at temperatures above 200 °C, coinciding with the degradation of the lactate moieties. As a result, quantification is not feasible using the investigated techniques.

Isothermal TG analyses carried out in the temperature range of 40-80 °C (as shown in **Figure 2.4**) demonstrate that the material can complete the previously discussed dehydration process within 2 hours, starting at a temperature of 60 °C. The isothermal tests at 70 and 80 °C confirm that the material is able to lose ~4.2 H_2O molecules, in investigated conditions. Due to the increased reaction rate at 80 °C, this has been chosen as the optimal operational temperature for dehydration. In contrast, the dehydration process at 40 °C is only partial within 2 hours and is not the optimum temperature for the system, as outlined in § **2.2** section. However, it cannot be ruled out that the material could partially function at this temperature, and characterization under these conditions may be useful for considering low-temperature applications, such as in residential settings. To facilitate its use in thermochemical heat storage and prevent thermal decomposition, the operating temperature range of CL under an inert atmosphere for its dehydration reaction is 40–150 °C.

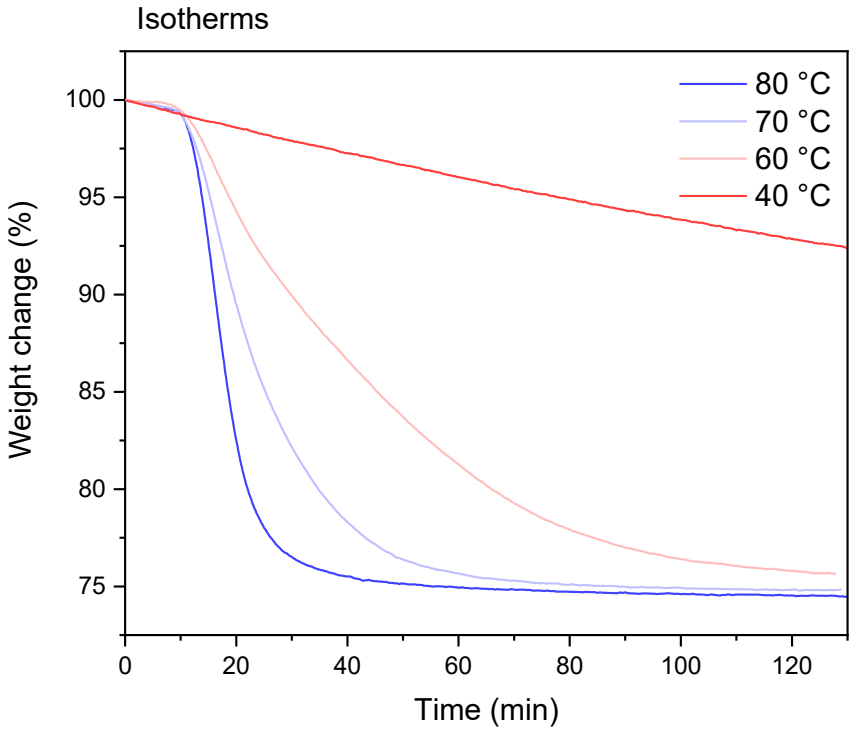

Figure 2.4 Isothermal TG analyses in the temperature range 40-80 °C.

The *ex situ* XRD patterns for the CL powder during dehydration are depicted in **Figure 2.5**. The crystalline form of CL in its pentahydrate state is recognizable through the comparison of the PDF 00-070-1076 with the XRD pattern at ambient temperature [227]. At 60 °C, a reduction in the intensity of the characteristic peaks associated with crystalline CL is noted. As the temperature is increased to 70 °C, the transition from crystalline to amorphous dehydrated CL DEH is observed, which is finalized at 80 °C. After maintaining an isothermal condition at 80 °C for 2 hours, no further alterations are noted. In brief, CL is crystalline in its pentahydrate form, and anhydrous in dehydrated phase.

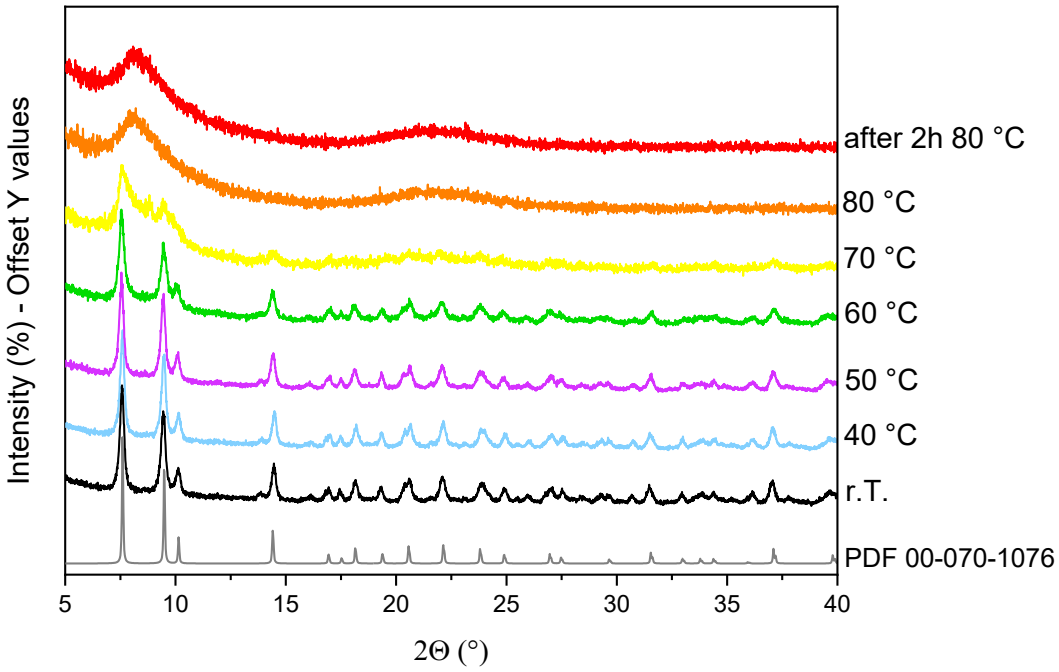

Figure 2.5 XRD analysis on *ex situ* thermally treated CL at varying temperature (from r.T to 80 °C).

2.4.2. Dehydration/Hydration cyclic reversibility

The assessment of cyclic reversibility regarding dehydration and hydration has been performed using isothermal (**Figure 2.6**) and isobaric measurements (**Figure 2.7**). Particularly, **Figure 2.6** shows sorption and desorption isotherms under three cycles at 30 °C. The mass changes, indicative of water uptake, are calculated according to Equation (2.3), which refers to the dehydrated mass of the sample. The second Y-axes reports the number of water molecules adsorbed by material. The findings from the isothermal experiments (**Figure 2.6**) indicate that a type III adsorption curve, classified by IUPAC, is obtained for each cycle, implying a weak interaction between the adsorbent (salt) and the adsorbate (water vapor). In addition, samples are slightly overhydrated at high relative humidity (p/p_0 = 90%). In fact, the mass increase corresponds to a number of water molecules greater than the expected five, which suggests that the water coordination sphere interacts with extra water molecules through hydrogen bonding.

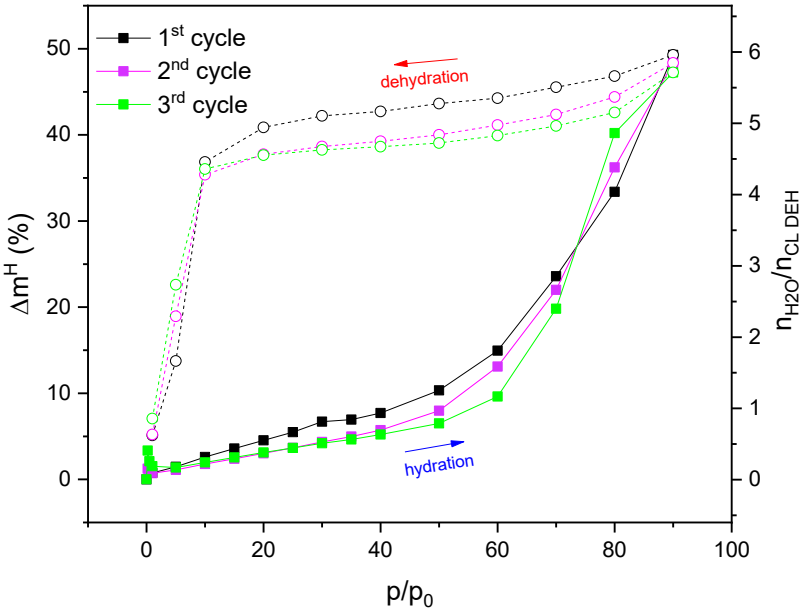

Figure 2.6 Three dehydration/hydration isothermal cycles at 30 °C.

A significant hysteresis is clearly observed between the hydration and dehydration processes (**Figure 2.6**) across the entire p/p_0 range, with the amplitude diminishing as cycling rises. This observation indicates that the dehydration reaction tends to take place primarily under conditions of significantly reduced p/p_0, which is generally associated with a kinetic barrier. This means that the rate of water diffusion into and out of the material's bulk is a limiting factor. Particularly, if the vapor diffusion pathways are tortuous or become constricted during hydration, the material takes longer to reach equilibrium, especially at higher relative pressures. Similarly, during dehydration, slow water removal occurs, and especially if the water is trapped within the structure, resulting in hysteresis. In addition, CL undergoes structural changes during water uptake and release, as seen in previous section. During hydration, the material absorbs water, forming a hydrate phase by restructuring the crystal lattice to accommodate the water molecules. This process involves breaking and reforming bonds, which requires activation energy. Upon dehydration, the reverse process occurs; however, the material might not revert to its starting anhydrous amorphous structure immediately. The dehydration pathway could involve different intermediate states or a slower kinetic process due to the need to overcome energy barriers for water removal and structural reorganization. This kinetic hindrance can lead to water retention at lower relative pressures than expected, widening the hysteresis loop. This is precisely what has been observed for CL, where a rapid reduction in water content

is noted only at 10% p/p_0 for all analyzed cycle. Moreover, the analysis suggests that the relative pressures associated with the heat storage process (desorption) and those related to the heat release process (sorption) are markedly distinct. This situation may restrict the material's ability to distribute the stored heat under necessary intermediate operating conditions. The large observed hysteresis in CL may also have significant negative implications for its performance as TCM. For instance, reduced energy storage capacity in practical cycles, the same cycles stability, reduced energy efficiency and implications for system design and operation are all aspects that should be taken into careful consideration and further investigated. Overall, the hysteresis considerations discussed in this section refer to pure hydrated salt but are generally valid for all CL-based composites that will be presented in the following chapters.

As regards cyclability, it is noteworthy that the material displays very similar cyclic behavior, marked by only a minimal decrease in the final water uptake.

The data presented in **Figure 2.7** regarding isobar measurements at 1200, 2550, and 3500 Pa indicate that the complete hydration and dehydration reaction takes place exclusively at 3500 Pa and at temperature of 30 °C, corresponding to about 80% p/p_0, and it is in agreement with isothermal analysis. Furthermore, at 50 °C and 3500 Pa, a significant increase in water absorption is observed, which is approximately equivalent to 4 H_2O molecules.

In conclusion, while calcium L-Lactate pentahydrate (CL) shows potential for TES, the pronounced hysteresis poses challenges. It necessitates careful consideration of the operating conditions to ensure effective energy storage and release. Optimizing the charging and discharging parameters to maximize the usable capacity within the hysteresis loop, and understanding the kinetics of the phase transitions, will be crucial for developing an efficient TES system based on this material. Further research could explore strategies to mitigate hysteresis. Further studies could investigate methods to reduce hysteresis. An initial investigation into this was conducted by depositing the organic salt hydrate onto a porous clay material, as detailed in § **Chapter 3**.

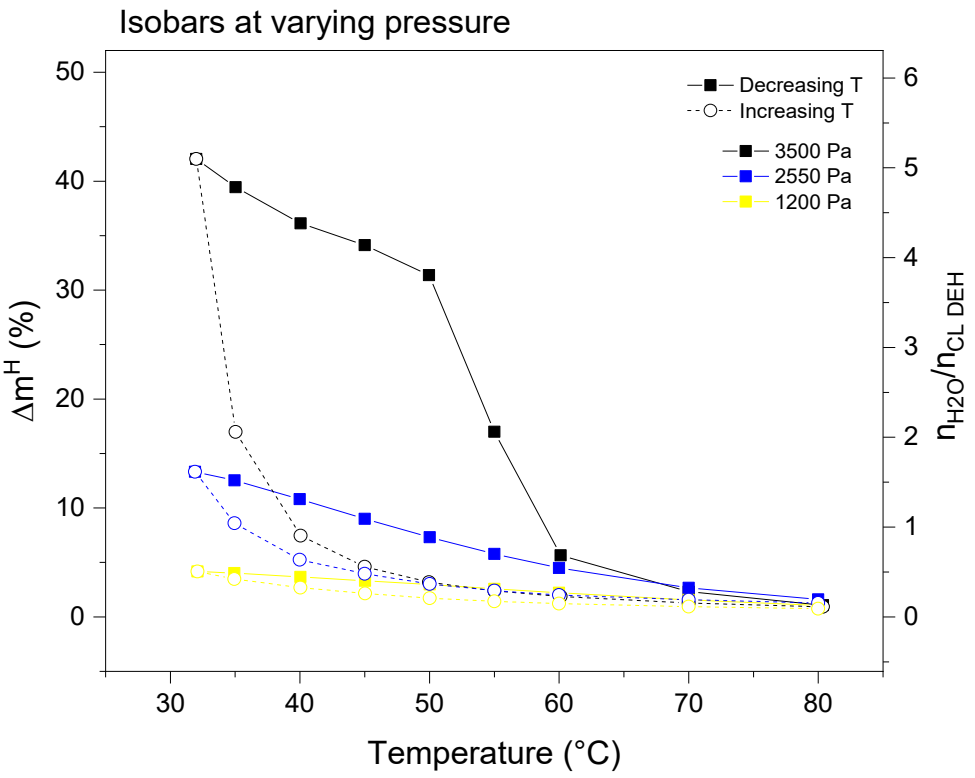

Figure 2.7 DVS analysis of CL DEH under isobaric conditions.

The integrity of the material and the structural reversibility of the dehydration/hydration cycle have been substantiated by FTIR spectroscopy (**Figure 2.8**). The material was dehydrated in a static oven at 80 °C for 2 hours and then rehydrated in a controlled humidity chamber at 30 °C and 80% of RH for 2 hours (CL/H2h) and 6 hours (CL/H6h). The spectral profile of commercial CL displays signals associated with O–H stretching at 3129 cm^{-1} and C–H stretching at 2975 cm^{-1}. Two notable peaks at 1567 cm^{-1} and 1394 cm^{-1} are attributed to the asymmetric and symmetric stretching of the carboxylate $-CO^{2-}$ group, respectively. Additionally, signals for C–O stretching at 1113 cm^{-1} and C–H bending at 897 cm^{-1} are evident at lower wavenumbers. However, the peaks related to metal–oxygen stretching and bending in the carboxylate region are found below 400 cm^{-1}, which is outside the detection range of mid-infrared FTIR spectrometers and cannot be detected.

The characteristic features of the lactate structure remain unchanged during the processes of dehydration and rehydration, indicating that the molecular structure of the salt does not undergo any additional modifications as a result of the dehydration/hydration cycle. The only exception to this is the intensity of the O–H stretching at 3129 cm^{-1}, which, as expected, exhibits some variation. In the case of

dehydrated salt (CL DEH), the O–H stretching is predicted to have a lower intensity than that of the fresh material, due to the absence of adsorbed water. After rehydration (CL/H2h), the intensity of the signal increases and remains almost unchanged even when the hydration time is prolonged to 6 hours (CL/H6h).

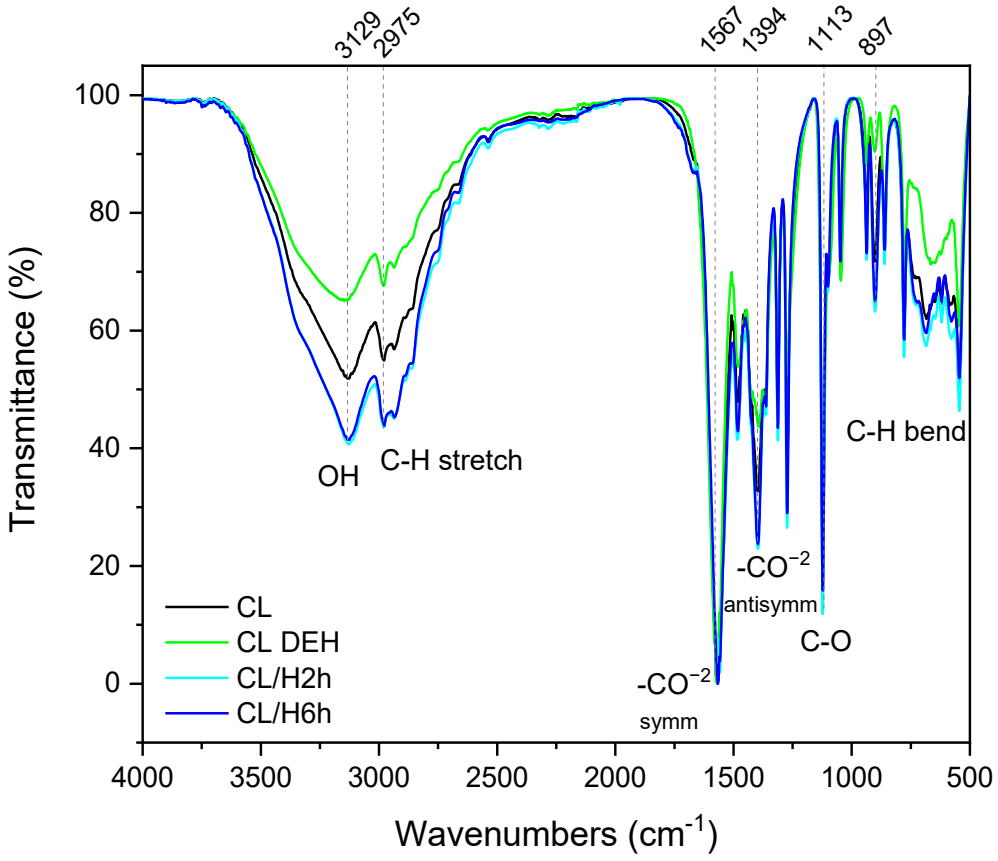

Figure 2.8 FTIR spectra of fresh CL, after dehydration at 80 °C for 2h (CL DEH), hydrated for 2h (CL/H2h) and 6h (CL/H6h) at 30 °C under a p/p_0 of 80%.

The same samples have been analyzed by scanning electron microscopy (SEM) analyses (**Figure 2.9**). The fresh material displays a very compact structure (illustrated in **Figure 2.9a**) and it is formed of small particles with irregular shapes, mainly consisting of very thin filaments that are densely bundled together, as seen in the higher magnification image (**Figure 2.9b**). There are no significant changes observed post-dehydration (**Figure 2.9c**). On the other hand, rehydrated samples undergo significant changes in morphology. After just two hours, a short fiber-like form is noticeable, with particles closely packed together (**Figure 2.9d**). The average length and thickness are about 2 µm and 100 nm, respectively. When hydration is extended to six hours, an

increase in the length (from 5 to 8 μm) and thickness (around 300 nm) of the fiber-like particles can be observed (**Figure 2.9e**).

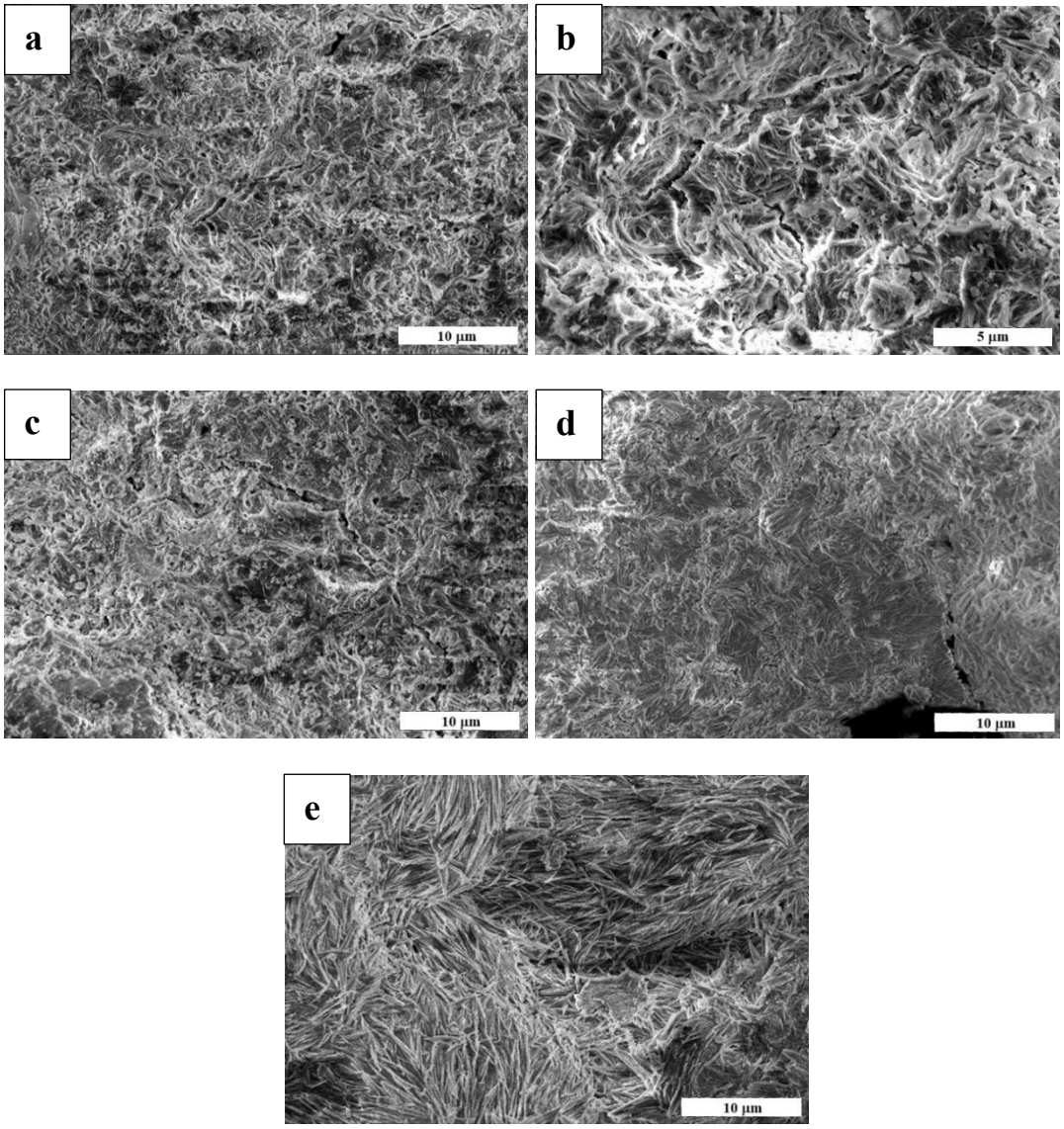

Figure 2.9 SEM micrographs of (a) low and (b) high magnification of fresh CL, (c) CL DEH, (d) CL/H2h and (e) CL/H6h.

The reported morphology corresponds with the observations of Seesanong *et al.* [217] and Kiran-Yildirim *et al.* [219]. It is noteworthy, however, that in [222], the filamentous structure is associated with anhydrous calcium L-lactate. This confirmation indicates that the morphological characterization of calcium L-lactate is still a matter of controversy, highlighting the need for further investigation. The morphological changes noted are correlated with structural modifications of the material, as evidenced by XRD diffraction patterns of CL DEH samples that underwent hydration for two and six hours (**Figure 2.10**). The mass uptake, as calculated in

relation to the dehydrated mass of CL DEH according to Equation (2.3), is around 30% for 2 hours and 45% for 6 hours of hydration, corresponding to 3.6 and 5.5 moles of water, respectively. This suggests that the material was nearly fully rehydrated after two hours, while it became overhydrated after six hours. XRD analyses performed at both hydration intervals indicate a more amorphous structure than that of fresh material. Furthermore, a peak at $2\theta = 21.4°$ is significantly more prominent in the sample that underwent 6 hours of hydration. The growth of CL DEH fibers should be linked to a specific crystallographic orientation, leading to a heightened intensity in the XRD analysis along this direction, thereby providing an explanation for the peak noted earlier.

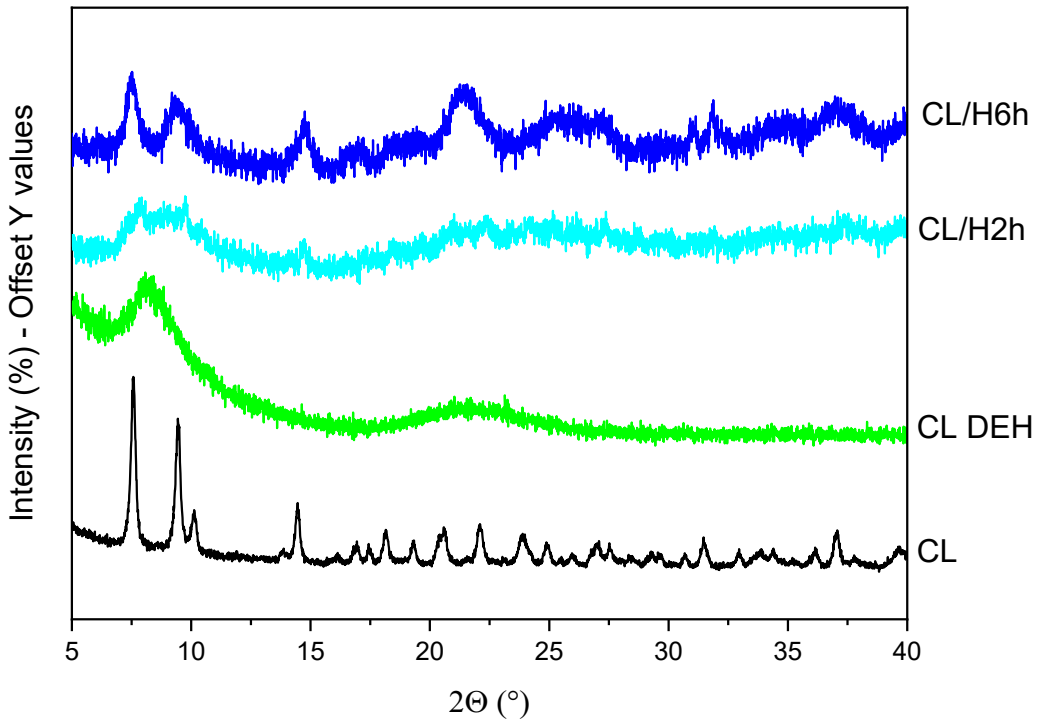

Figure 2.10 XRD patterns comparison of fresh CL, after dehydration at 80 °C for 2h (CL DEH), hydrated for 2h (CL/H2h) and 6h (CL/H6h) at 30 °C under a p/p_0 of 80%.

A detailed *in situ* morphological study of the salt was executed through the use of environmental scanning electron microscopy (ESEM), which simulated the cycles of hydration and dehydration. This technique provided the opportunity to monitor morphological modifications under dynamic conditions while varying the relative humidity. To accomplish this, temperature and water vapor pressure were adjusted within the ranges of 5-60 °C and 10-810 Pa, respectively, in order to vary the chamber p/p_0. The material was subjected to dehydration *ex situ* at 80 °C. Upon entering the

SEM chamber, the relative pressure (p/p_0) was incrementally raised from 0% to 93% during the analysis to promote the hydration reaction. After this phase, the p/p_0 was gradually lowered to 0%, and the temperature was increased to 60 °C, which is the maximum temperature that the instrument can reach, to observe the dehydration process of the salt. The sample was held under these conditions for 12 hours to ensure effective dehydration. More comprehensive details about the experimental setup are illustrated in **Figure 2.2**.

The micrographs depicted in **Figure 2.11** were obtained under significant pressure and temperature conditions within the climatic chamber of the microscope. The area selected for analysis is representative of overall morphology. At consistent magnification, the growth of the salt volume is noticeable as the p/p_0 value increases (compare **Figure 2.11a**, **b**, **c**), which is also associated with the appearance of cracks (as shown by the arrows in the figures). Likely, the formation of these cracks would accommodate the mass transfer through the more internal areas of the sample. Additionally, extending the time from 30 to 60 or 120 minutes at the highest p/p_0 does not reveal any significant volume expansion (see **Figure 2.11c**, **d**, **e**).

In addition, a large area of the salt surface reveals the formation of an alveolar shroud at a p/p_0 of 93%. Studies in the literature suggest that the hydration of crystalline salts often involves a two-step solid-solid transition. Initially, a wetting layer forms, which then promotes the nucleation and growth of the hydrated salt phase. Consequently, it is plausible to conclude that the shroud observed in the SEM image of the salt surface (**Figure 2.11**) corresponds to the wetting layer. Longer hydration times do not produce morphological modifications that are discernible at this magnification level. The deliquescence effect is excluded, as it would have caused a gradual liquefaction of the salt, resulting in a more significant alteration of the sample's contour, similar to the changes observed in deliquescent inorganic salts.

After maintaining the sample at a temperature of 60 °C for 12 hours under 0% p/p_0, a distinct contraction in the particle volume is observed, along with a reduction in the crack size (**Figure 2.11a**, **e**, **f**). As a result, the initial morphology has been restored.

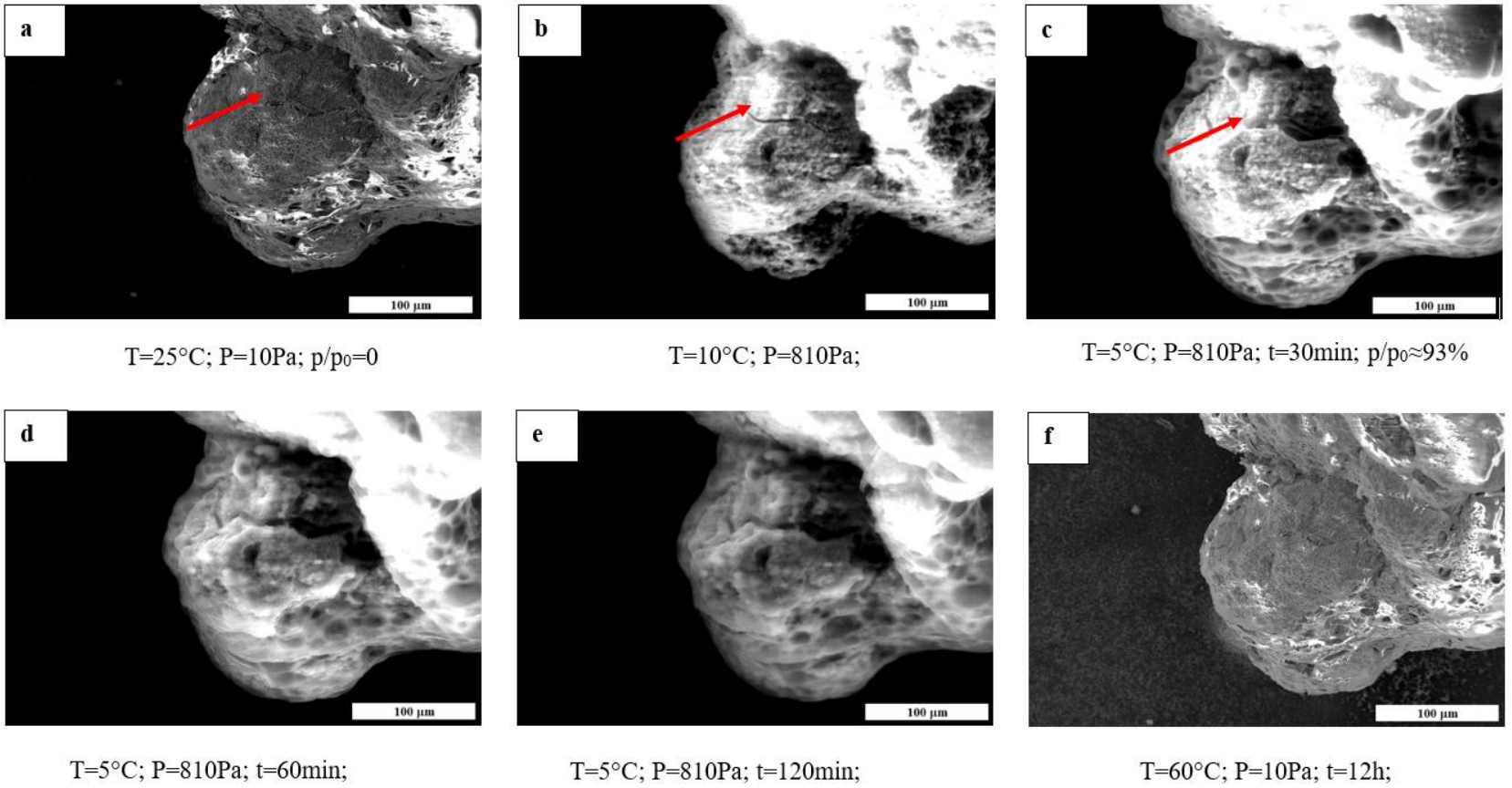

Figure 2.11 Selected ESEM micrographs of CL DEH under varying temperature and water vapor pressure in the ranges of 5-60 °C and 10-810 Pa, respectively. The selected conditions mimic a hydration/dehydration cycle. Micrograph (a) is taken at the beginning of *in situ* analysis on *ex situ* dehydrated sample. Micrograph (b) is taken at increasing p/p_0. Micrographs (c), (d), (e) are taken at the highest p/p_0 at different holding times of 30, 60 and 120 minutes, respectively. Micrograph (f) is taken after holding the sample at 60 °C for 12h under 0% p/p_0.

The *in situ* morphological analysis provides a means to directly observe the reversible nature of salt hydration and dehydration processes. When CL DEH undergoes hydration, it is enveloped by a wetting layer that is responsible for the hydrated phase. The stability of this transitional phase during a 120-minute analysis period indicates the deliquescence resistance of CL DEH. Following dehydration due to an increase in temperature, the material retains its stability and reverts to its original morphology.

2.4.3. Heat storage capacity

The heat storage capacity of fresh CL was analyzed using a coupled TG-DSC apparatus and isothermal experiments at 80 °C per 2 h under inert atmosphere. **Figure 2.12** shows analysis results. In the conditions described, only one thermal event was observed during the dehydration process. The calculated heat storage capacity, derived from the integration of the endothermic peak (Equation (2.1)), amounts to 1127 kJ kg^{-1} (based on the mass of the hydrated salt), corresponding to a weight loss of 24.8%, which corroborates previous results.

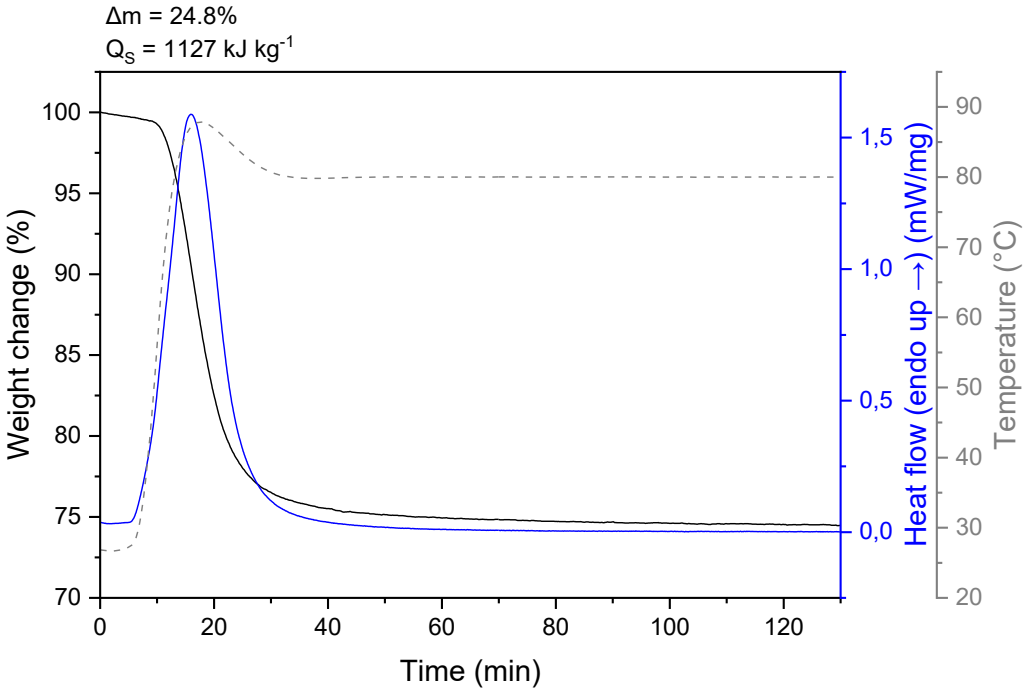

Figure 2.12 Dehydration TG-DSC profiles for the evaluation of the heat storage capacity of CL.

This significant reduction in mass is associated with the release of 4.2 water molecules, as calculated in accordance with Equation (2.2), which aligns with findings

documented in [218]. The determined heat storage capacity is greater than the values reported in references [222] (762 kJ kg^{-1}) and [218] (811 kJ kg^{-1}), which utilized materials of lesser purity, a broad [222] or unspecified [218] grain size, and a DSC apparatus under a constant nitrogen flow with an open lid [222], in addition to a markedly different heating rate [218,222]. Thus, the variations in the measured storage capacities can be ascribed to the distinctly different experimental conditions employed [236].

In **Table 2.1** are listed the density values of CL (ρ_P) and of salt after dehydration treatment at 80 °C for 2 hours (ρ_A). These two configurations represent the limit conditions in which the organic salt could be found. The densities are measured by an He pycnometer on powder materials at 20 °C.

Table 2.1 Density values of calcium L-lactate pentahydrate and calcium L-lactate anhydrous expressed in kg m^{-3} and measured through an He pycnometer at 20 °C.

Materials	**Density values (kg m^{-3})**
Calcium L-lactate pentahydrate	1505
Calcium L-lactate anhydrous	1609

The measured values take into account the volume shrinkage/expansion that salt undergoes respectively during dehydration and hydration processes. An estimation of volume change ΔV(%) is established with the following equation:

$$\Delta V(\%) = \frac{\rho_A - \rho_P}{\rho_A} \cdot 100 = 6.5\% \quad (2.4)$$

The effect of volume change is negligible as indicated by Equation (2.4) allowing to determine volumetric heat storage/release capacity without a meaningful error. Taking into account the salt density (ρ_P), reported in **Table 2.1**, the volumetric heat storage capacity Q_S^v(MJ m^{-3}) is determined through the following equation [163,237]:

$$Q_S^v(\text{MJ m}^{-3}) = Q_S^m(\text{kJ kg}^{-1}) \cdot \rho_P(\text{kg m}^{-3}) \quad (2.5)$$

The obtained value is 1696 MJ m^{-3} (or 471 kWh m^{-3}). The heat storage capacities per mass and volume unit enable the ranking of this organic salt among the most competitive inorganic counterparts, such as LiCl (845 kJ kg^{-1}) and $CaCl_2$ (837 kJ kg^{-1}) [62,238,239]. Nevertheless, these last two salts require their confinement into a host

matrix to prevent leakages associated with their deliquescence at very low relative humidity [240,241], thus reducing significantly their storage/release capacity up to 70%. The **Table 2.2** provides a comparison with several employed inorganic salt hydrates for low-temperatures applications. It lists some thermophysical characteristics that make CL particularly interesting. Additionally, CL stands out by avoiding the risk of generating by-products, which is a common issue with other salt hydrates like chloride- and sulfur-based counterparts that can experience instability issues. For instance, chlorides, particularly when dehydrated beyond 140 °C, decompose, releasing volatile HCl, leading to potential corrosion problems within the system [62,133]. Moreover, the operational conditions of CL are less restrictive compared to other inorganic salts. Deliquescence phenomena are absent even at high relative humidity values, and no decomposition occurs below 200 °C. Unlike some inorganic systems with critical dehydration temperatures that can limit their efficiency, e.g. $MgSO_4$ [62], CL proves more robust.

Table 2.2 Comparison of the thermophysical characteristics (molecules of H_2O involved in the dehydration process (n_{mol}); heat storage capacity per mass (Q^m) and volume (Q^v) of material and working conditions (dehydration (T_{deh}) and hydration (T_{hyd}) temperatures)) of CL and other selected common inorganic salt hydrates.

Material	n_{mol}	Q^m (kJ kg^{-1})	Q^v (kWh m^{-3})	T_{deh} (°C)	T_{hyd} (°C)	Ref.
$CL \cdot 5H_2O$	4.2	1127	471	40-100	60-30	[189]
$SrBr_2 \cdot 6H_2O$	5	948	433	52	45	[62]
$SrCl_2 \cdot 2H_2O$	1	302	164	52	46	[62]
$MgSO_4 \cdot 6H_2O$	4	986	558	91-123	10	[62]
$MgCl_2 \cdot 6H_2O$	1.3	352	153	104	61	[238]
$CaCl_2 \cdot 2H_2O$	2	837	542	111	63	[238]
$LiCl \cdot H_2O$	1	845	486	80	73	[242]
$K_2CO_3 \cdot 1.5H_2O$	1.5	580	356	65	59	[242]

Further and notable advantages of CL and for its applicability in real operating systems are the inexpensiveness, non-toxicity, and large availability.

2.5. General remarks and future outlooks

The findings reported here and published in [189] present the first experimental evaluation of the thermochemical properties of calcium L-lactate pentahydrate (CL) for applications in thermochemical energy storage. The material demonstrates the capability to release nearly all of its water molecules within the temperature range of 40-100°C, rendering it a promising candidate for low-temperatures thermochemical heat storage. In addition, it has been demonstrated that the material possesses strong

thermal stability up to 150 °C, thereby removing the need for any strategies to prevent its decomposition, (e. g. such as restricting the maximum charging temperature, maintaining a low heating rate during the charging phase, or employing porous matrices, etc.) which are often required for certain inorganic salts. Multiple characterization techniques have been utilized to determine the most effective dehydration and hydration conditions. In particular, the dehydration of CL is optimally achieved by heating the material to 80 °C for 2 hours. Furthermore, the hydration process has been confirmed to be fully reversible at a vapor pressure of 3500 Pa and a temperature below 35 °C. It was noted that the process of dehydration and hydration exhibited full reversibility across three cycles, while preserving the chemical integrity of the salt. Morphological and structural changes were observed in the material throughout these cycles, with hydration conditions and time serving as the primary determinants of the final morphology and structure. Notably, although the calcium lactate particles swelled significantly during hydration, the salt was capable of returning to its original size during the dehydration process. To fully assess CL potential, the heat storage capacity was estimated to be 1127 kJ kg^{-1} (or 1696 MJ m^{-3}).

These favorable results elevate this organic salt as a strong competitor to inorganic options. In addition, calcium L-lactate is economical, non-toxic, abundantly available, and does not exhibit deliquescence issues. This further supports the concept that new candidate materials for thermochemical heat storage may be found within the family of organic salt hydrates. Ongoing studies are focused on assessing the material's durability through multiple cycles of dehydration and hydration under realistic conditions.

Chapter 3 Deposition of CL on sepiolite matrix

3.1. Influence of porous matrices in enhancing TES properties

As discussed in § **Chapter 1**, limitations remain in the widespread implementation of TES technologies within realistic systems. Numerous challenges have been faced, and several solutions still need to be found, particularly for TCMs systems. In fact, it is known that the number of scientific literature focused on TCMs is significantly smaller than that of the other two TES systems [213]. While challenges related to material stability, cost, and system integration persist, the potential of TCMs to provide consistent energy storage in conjunction with renewable sources remains a driving force behind ongoing research and development initiatives [243]. A method for improving performance is the implementation of composite materials. By combining diverse elements, composites enable the development of advanced TES with superior thermal attributes, enhanced stability, and greater energy storage efficiency, ultimately supporting the consistent integration of renewable energy [244,245].

An intriguing possibility is the use of porous materials as host matrix for salt hydrates. Salt in matrix represents a special type of composites in which host compounds can be classified into three categories based on the dimensions of their pore widths: microporous (pore widths of less than 2 nm), mesoporous (pore widths from 2 nm to 50 nm), and macroporous (pore widths greater than 50 nm) [246]. Although the major purpose of a host matrix is to contain the salt and prevent leakages, its porosity adds extra advantages to the composite. Their increased surface area contributes to enhancing energy and mass transfer. A suitable host matrix should also prevent deliquescence and control hydration; otherwise, the composite will pass into the solution phase [247]. Commonly used porous materials in this kind of composites are zeolites, MOFs, silicon compounds and carbonaceous materials.

A novel investigated approach involves the exploration of natural porous clays as matrix supports for TCMs, representing a significant and innovative step towards more economically viable and scalable energy storage solutions. This emerging research focuses on the abundance and low cost of clays, while simultaneously aiming to improve TCM performance through enhanced mass and heat transfer facilitated by the clay's unique structural characteristics. For instance, Ait Ousaleh *et al.* realized a suitable matrix by blending natural bentonite with graphite as support to stabilize three

hydrated salts ($SrCl_2 \cdot 6H_2O$, $CaCl_2 \cdot 6H_2O$, and $LiCl \cdot H_2O$). The composites exhibited high energy storage density and good thermal conductivity. The cyclability assessment showed that over 90% of the stored heat was retained after 10 cycles, confirming the bentonite as an excellent support to enhance the thermophysical properties of chloride-based TCMs and stabilize the hydrated salt structure under operating temperature and humidity conditions. Additionally, the compatibility test of copper in contact with the bentonite-based TCMs revealed a significant improvement in the corrosion resistance of copper, up to 43% [248].

3.2. Sepiolite: an abundant and low-cost mineral matrix

In the context of composite materials, sepiolite, a naturally occurring clay mineral, has gained recognition as a potential matrix material for thermochemical systems. Its exceptional characteristics, including a high surface area, a porous structure, and notable thermal stability, make sepiolite a compelling choice for hosting PCMs or other types of adsorbent materials [249–252]. To enhance the functionality of sepiolite-based thermochemical systems, the addition of calcium L-lactate pentahydrate (CL) will be examined. Even though CL demonstrates excellent properties that position it favorably against standard inorganic hydrated salts researched for low-temperatures applications, this salt hydrate has some limits that hinder its prompt adoption as a TCES solution [218,222]. The main drawbacks are linked to the slow hydration kinetics and issues of agglomeration. From this perspective, Sakata *et al.* has shown that the diffusion of water in the solid phase is likely the critical rate-limiting step in the hydration process of CL. It is noteworthy that salt dispersion to a porous matrix, such as sepiolite, can help in the separation of CL particles by stimulating the hydration process through a more effective distribution of vapor within the solid phase [222]. The enhanced distribution of CL on the clay surface further enables a more efficient separation of salt particles, facilitating the volume shrinkage and expansion processes that occur during the dehydration and hydration phases, thus helping to prevent agglomeration issues.

Sepiolite versatile characteristics render it an adequate matrix for the dispersion of CL particles. The mineral garners attention due to its sorptive, rheological, optical, and catalytic properties [253]. These features provoke significant interest and support a wide array of industrial applications. In addition, sepiolite is characterized as a non-

swelling fibrous clay that preserves its structural integrity in systems with high salt concentrations. The application scope of sepiolite may differ according to its agglomeration state. Many industrial sectors utilize the unique property of sepiolite to form needle-like bundles that attach to each other, which form rigid particles. This agglomeration process produces a material that is not only highly porous but also exhibits a remarkable capacity for absorption [254]. On the contrary, rheological properties are related to separation of fibers into single needles, as seen in the case of sepiolite in mortars, where the mineral enhances mechanical resistance by inducing a network structure within the concrete matrix [255–257]. Following the scope of the current thesis, Salustro *et al.* recently published a work on thermal characterization of cement-based composite materials for TCES [258]. In cited paper, authors varied the proportions of sepiolite for enhancing porosity and reducing composite costs.

As can be deduced, the selection of sepiolite as the porous matrix for dispersing CL was driven by its unique structural and surface properties, offering distinct advantages over other natural clays like bentonite, kaolin, and attapulgite, for developing a novel thermochemical composite. Beyond its fibrous morphology, sepiolite possesses a significant internal surface area due to its channel-like structure. This fibrous nature allows for a more open and interconnected pore network, ideal for housing and finely dispersing the salt particles, ensuring a large contact area between the salt and the surrounding environment, crucial for efficient hydration and dehydration kinetics.

Similar to sepiolite, attapulgite also has a fibrous, chain-like structure; however, sepiolite typically exhibits a larger pore volume and a more open pore system, allowing for better infiltration and stabilization of the salt [253]. Conversely, bentonite, while having a high surface area, is characterized by a layered structure that swells significantly in the presence of water. This swelling can lead to structural instability, potential particle agglomeration, and reduced permeability for water vapor, hindering rapid mass transfer during sorption cycles. While it can intercalate materials, its lamellar nature might limit uniform and stable dispersion of a salt hydrate over many cycles. Also, kaolin presents a layered structure with a relatively low surface area and limited interlayer swelling. Its compact, plate-like morphology and often larger particle size offer fewer active sites and less accessible pore volume for salt dispersion, potentially leading to lower overall energy storage capacity and slower kinetics compared to sepiolite [259].

Furthermore, the unique open channel and tunnel structure of sepiolite provides a highly accessible and relatively uniform pore network. This might facilitate rapid and efficient diffusion of water vapor into and out of the composite. This is critical for achieving good cycling stability and kinetics in a thermochemical material. The pore structures of bentonite and kaolin, instead, are either prone to collapse (bentonite's interlayers) or are inherently less developed and less accessible (kaolin's compact structure), which could impede water vapor diffusion and limit the kinetics of the thermochemical reactions.

The theoretical general formula of sepiolite is $Mg_8Si_{12}O_{30}(OH)_4 \cdot (H_2O)_4 \cdot 8H_2O$, which reflects the presence of structural water molecules. In terms of its structural arrangement, sepiolite comprises tetrahedral-octahedral-tetrahedral ribbons that extend along the c-axis, thereby forming individual fibers, as shown in **Figure 3.1**. Each tetrahedron is made up of a silicon atom surrounded by four oxygen atoms, while magnesium ions are octahedrally coordinated by oxygen atoms, hydroxyl groups, or water molecules. The ribbons are interconnected via an inverted Si-O-Si bond, resulting in a continuous tetrahedral sheet that is linked to non-continuous octahedral sheets. This designation classifies sepiolite as a phyllosilicate. The discontinuities in the octahedral sheets permit the formation of rectangular cavities. The cross-sectional area of these tunnel-like micropores is approximately 3.7x10.6 $Å^2$, contributing to the high specific surface area and exceptional sorptive properties of sepiolite, particularly after the thermal removal of zeolitic water. In addition, the terminal Mg^{2+} ions located at the edges of the octahedral sheets complete their coordination with two molecules of structural water, which are hydrogen-bonded to the zeolitic water molecules contained within the cavities [254,260,261].

As stated before, single fibers tend to aggregate, resulting in the formation of bundles. In this context, the surface properties of sepiolite are influenced not only by its structural microporosity but also significantly by the agglomeration of the material, which is a critical factor in determining the final values of specific surface area and porosity. These properties are indeed the outcome of the combined effects of intracrystalline (or structural) microporosity and textural porosity, which includes inter-fiber microporosity and mesoporosity [262].

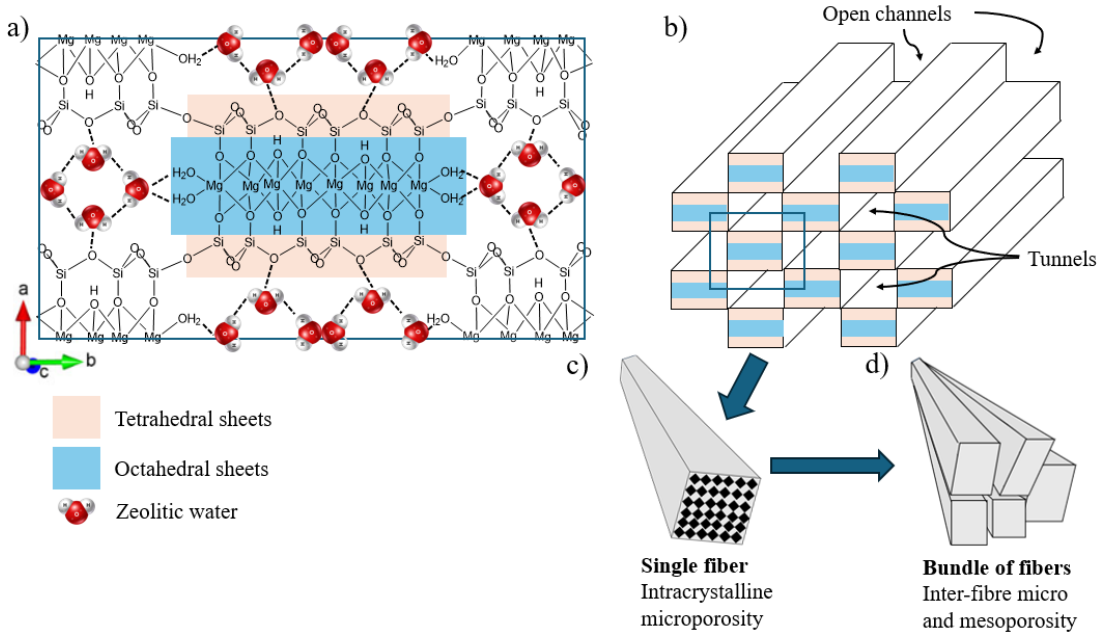

Figure 3.1 a) Unit cell of sepiolite projected on the ab plane. The c-axis points towards the reader. b) Three-dimensional representation of sepiolite structure showing open channels and internal cavities (tunnels). c) Representation of a single sepiolite fiber showing structural intracrystalline microporosity. d) Schematic representation of sepiolite fibers reunited in a bundle highlighting the textural porosity.

Small polar molecules can penetrate the tunnels of the clay matrix by either displacing zeolitic water or by utilizing the cavities that are freed during thermal dehydration. The formation of hydrogen bonds by these guest molecules allows them to be firmly anchored within the mineral structure [263]. In spite of its hydrophilic properties, sepiolite is able to contain small organic polar molecules within its cavities, which allows for the formation of hydrogen bonds at different positions [264,265].

The application of sepiolite in TES has been widely studied. Fujiwara and Sato [266] examined the mineral's ability to reversibly adsorb and desorb water, considering its potential as a CHP. Their research revealed that, while sepiolite has a relatively low adsorption capacity, it offers multiple advantages for this type of technology: 1) it can be directly utilized without binders to create various shapes, such as pellets, which helps to avoid a reduction in energy density; 2) there are no cracking problems during the cycles of adsorption and desorption; 3) the clay remains stable at high temperatures. Recent studies have emphasized the application of sepiolite as a matrix for PCMs. The literature has extensively investigated the use of sepiolite for the loading of organic PCMs [267–270]. Moreover, there have been attempts to incorporate inorganic hydrated salts [251] or eutectic mixtures of hydrated salts [250] into the cavities of sepiolite for LHS applications. In all cited research, the composite

materials were synthesized via vacuum impregnation, and characterization analyses revealed no changes in the crystalline structure of either sepiolite or the PCMs, indicating that the active phase is securely encapsulated within the rigid structure of the clay during operational conditions. The formation of the composite is predominantly determined by physical interactions and hydrogen bonding. The addition of PCMs to sepiolite has led to improvements in both TES capacity and cycling stability. Considering the low cost and the extensive natural reserves of sepiolite, this mineral is an excellent candidate for use as a support material in thermal energy storage applications.

In this chapter, it has been assessed, for the first time, the potential of a novel composite TCM, developed through the combination of sepiolite and CL. The clay provides an effective matrix for the salt dispersion. In this regard, pertinent studies have highlighted the chemical affinity of sepiolite for organic polar molecules and the favorable interactions between sepiolite and CL-similar chemical compounds. It is noteworthy that the literature does not contain any reported examples of materials that incorporate both CL and sepiolite. However, Fukushima *et al.* have produced nanocomposites by melt-blending polylactic acid with various amounts of clay. Significant improvements in thermal and thermomechanical properties were observed in these materials [271]. Given the analogous chemical structures of polylactic acid and CL, it is logical to suggest that a positive chemical affinity may exist between sepiolite clay and the CL salt. The incorporation of the CL molecule into mineral cavities may be limited by steric constraints [272]. Nevertheless, complementary characterization techniques have been applied to investigate the interactions among the pristine materials. Reported findings further illustrate that the hydration and dehydration processes retain their reversibility, even with the deposition of CL on the clay surface. Additionally, it has been established that modifying the composition of composite materials can significantly impact the catalytic activity of clay in relation to the thermal stability of salt. The thermochemical behavior of the prepared composites is also influenced by their deposition on the sepiolite matrix. The research specifically examined the role of salt dispersion in enhancing hydration and dehydration processes. The volumetric heat release capacities of the materials analysed were estimated and found to be promising when compared to the primary sepiolite-based composites for LHS applications. To the best of the author's knowledge, the synthesis and

characterization of composite materials derived from sepiolite, which incorporate an organic salt hydrate as TCM, signify a novel contribution to the existing scientific literature. There has been a singular report of another binary composite material that combines the thermochemical properties of an inorganic hydrated salt ($CaCl_2 \cdot 6H_2O$) with the advantageous adsorption features of sepiolite [273].

The data presented in this chapter are the result of the author's research activity conducted during his stay at Institute of Catalysis and Petrochemistry (ICP-CSIC) of Madrid (Spain). Specifically, the synthesis and the structural, chemical, physical, and thermal characterizations of the composite materials were carried out under the supervision of Dr. Juan Manuel Coronado at ICP-CSIC.

3.3. Materials and methods

3.3.1. Reagents and preparation method

For the preparation of the composite materials, Pangel S9 (85% sepiolite), kindly supplied by Tolsa SA (Spain), was utilized together with calcium L-lactate pentahydrate (Thermo Scientific, purity ≥ 98%). The chemical composition of Pangel S9, analysed using inductively coupled plasma optical emission spectroscopy (ICP-OES), is provided in **Table 3.1**. Both materials were applied without any additional purification steps. The synthetic procedure involved the use of *N,N*-dimethylformamide (DMF), supplied by Honeywell (purity ≥ 99.8%), as dispersing medium.

Table 3.1 Chemical composition of Pangel S9 (sepiolite 85%) detected by ICP-OES.

Pangel S9	%wt.
SiO_2	69.4
MgO	23.8
Al_2O_3	4.0
CaO	0.7
Fe_2O_3	1.4
K_2O	0.5
Na_2O	0.2

The composite materials were synthesized using a method that employs an organic volatile solvent, specifically DMF, to disperse sepiolite, as has been previously reported. DMF was preferred over other solvents, such as water, due to its ability to achieve effective dispersion of sepiolite fibers in the solution and to ensure the

complete dissolution of CL. Initially, the raw sepiolite was dehydrated in an oven at 120 °C for 24 hours to extract the zeolitic water from its cavities. A measured quantity (175-350 mg) of the resulting clay was then sonicated in 3 mL of DMF for one hour, followed by stirring for two hours. In the subsequent step, the necessary weight percentage (%wt.) of CL in relation to dehydrated sepiolite, required to prepare approximately 500 mg of the final product, was dissolved in 1 mL of DMF at room temperature while being stirred continuously. The two solutions were then amalgamated and mixed vigorously overnight, promoting the evaporation of the solvent. The resulting slurry was dried at 80 °C for 24 hours to ensure complete solvent removal. Finally, the dried composite material was ground to a fine powder. The synthetic procedure is represented in **Figure 3.2**.

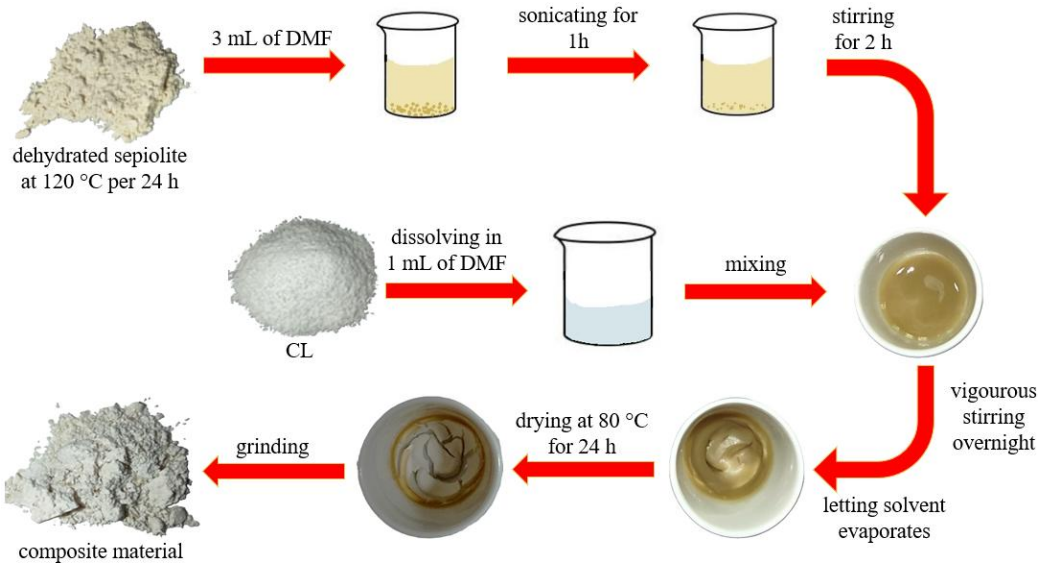

Figure 3.2 Synthetic procedure for preparing sepiolite and CL based composite materials, using DMF as dispersing medium.

In **Table 3.2**, the composite materials are listed with their respective nominal weight fractions of the constituents. These materials are labelled as "S-CL," indicating the precursor materials, with a subsequent number that denotes the salt content in %wt.

Table 3.2 Code of realized composite materials with the corresponding nominal weight fraction of constituents.

Code	Sepiolite (%wt.)	CL (%wt.)
S-CL30	70	30
S-CL50	50	50
S-CL65	35	65

Given that the dehydration of the deposited salt occurs during the final drying treatment [189], it is necessary to hydrate the composite materials prior to conducting structural and chemical characterization analyses to evaluate the reversibility of hydration and dehydration reactions. To achieve this, the composite materials were placed in a crucible within a sealed vessel containing a water reservoir and were left for 24 hours at 30 °C to ensure complete hydration of the samples (**Figure 3.3**). The equilibrium between the vapor phase and liquid phase inside the hermetic closed vessel facilitates the hydration process. The hydrated material is referred by the previously defined code, followed by "/H24h". For example, S-CL30/H24h indicates the composite material with 30%wt. of CL that has been hydrated for 24 hours in the vessel.

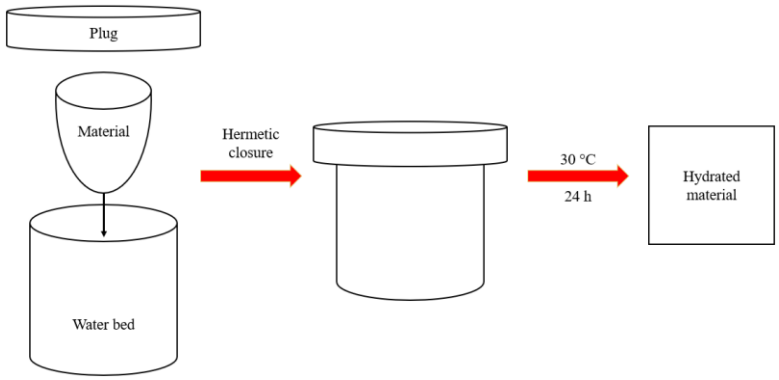

Figure 3.3 Description of the system used for hydrating sample.

3.3.2. Structural, chemical and physical characterization analyses

Structural investigations of sepiolite and synthesized materials were executed via powder X-ray diffraction (XRD) techniques, utilizing an X'Pert Pro PANalytical diffractometer. The analyses were conducted with Cu Kα radiation (λ = 1.5406 Å) at a scanning rate of 0.2° s^{-1} over a 2θ range of 4-30°, with an accumulation time set at 50 s. All diffractograms were normalized with respect to the intensity of the highest peak. The chemical characterization utilized Fourier-transform infrared spectroscopy (FTIR). Experiments were conducted on both the initial and prepared powder materials

with a JASCO FT/IR-4700 spectrometer. The spectra were collected in the range of 4000 to 400 cm^{-1}, with a resolution of 4 cm^{-1}. To minimize the effects of moisture and CO_2, all spectra were subjected to background compensation. The reported spectra were also normalized with respect to the absorbance of the highest peak. Specific surface areas and pore volumes of sepiolite and composite materials were evaluated through nitrogen adsorption/desorption analyses at -196 °C, using an Asap 2020 Micromeritics instrument. The samples were degassed at 120 °C for 16 hours under vacuum before the measurements.

3.3.3. Thermogravimetric characterization

The thermal stability of both pristine and synthesized materials was investigated through thermogravimetric (TG) analyses using a PerkinElmer STA 6000 instrument, which was coupled with a PerkinElmer Frontier FTIR spectrometer for the examination of the gases released. Approximately 20 mg of samples were heated in an open pan, with a ramp rate of 10 °C per minute from 30 °C to 600 °C in an air atmosphere at a flow rate of 20 mL per minute. The FTIR spectra of the resulting gases were recorded twice at a resolution of 2 cm^{-1} within the range of 4000-1000 cm^{-1}. To avoid gas condensation, the transfer line between the TGA and FTIR was maintained at 200 °C during the experiment.

3.3.4. Thermogravimetric dynamic vapor sorption analyses

Water vapor adsorption and desorption experiments were executed to evaluate the uptake and release behavior of sepiolite and composite materials under controlled environmental conditions. The mass fluctuations were monitored using a dynamic vapor sorption (DVS) analyzer (DVS Vacuum). The instrumentation includes a micro-balance (precision ± 0.1 μg) and a water vapor pressure flow control system within the sample holder chamber. The entire apparatus is maintained in a temperature-controlled environment at 30 °C. Before initiating water adsorption, the sample (~10 mg) was activated (degassed) at 80 °C under vacuum (~0.1 Pa) for 3 hours to determine its dry weight. Subsequently, a valve was opened to connect the evaporator, containing liquid water, with the sample chamber. Isothermal adsorption and desorption experiments were then executed at 30 °C, with partial pressures increasing from 0 to 0.9 (p/p_0). The pressure was kept constant during each step until the sample weight reached a state of equilibrium [197].

3.3.5. Thermochemical characterization under saturated vapor conditions

The thermochemical behavior of both pristine and the most promising materials was investigated through coupled thermogravimetric and differential scanning calorimetric (TG-DSC) analyses under saturated vapor conditions. The experimental setup utilized a closed system featuring a TG-DSC analyzer (Setaram Themys One), which was customized to include a pump for evacuation and an evaporator. The analysis was conducted with a temperature ramp of 10 °C per minute to 80 °C, followed by a 2 h isotherm at this temperature. During these stages, the dehydrated sample was held under vacuum (~1.6 Pa) to ensure the removal of any adsorbed moisture or gases. Once the isotherm was completed, the evacuation was stopped, and the evaporator ($P_{evaporator}$ = 3150 Pa) was opened. The sample was then cooled to 28 °C, followed by a final 2 h isotherm at this temperature. The recorded increases in mass and heat during the cooling phase are associated with the hydration process of the sample [274]. In order to evaluate the volumetric heat release capacity of the studied materials, the real density of the powders was determined using a helium pycnometer (Ultrapyc 5000, Anton Paar) at 20 °C.

3.3.6. Morphological characterization

The investigation of sepiolite and composite morphologies was conducted using a scanning electron microscope (SEM, FEI Quanta 450) set at an accelerating voltage of 5 kV within a high vacuum setting (10^{-4} Pa). The analysis included both the synthesized composite materials and those subjected to a 2 h hydration treatment with the method of hydration vessel (**Figure 3.3**).

3.4. Results and discussion

3.4.1. Structural and chemical characterizations

Structural characterization was achieved through XRD analyses, which were employed to evaluate the purity of the initial sepiolite and to observe the reversibility of dehydration and hydration processes in the composite materials. The XRD pattern of the precursor sepiolite, shown in **Figure 3.4**, exhibits the characteristic diffraction peaks of the clay, aligning with previously published data [275,276]. A comparison with the identified phase (PDF 01-080-5015) is also provided [277]. The characteristic peaks of sepiolite are evident in the diffractograms of the composite materials, and as

the salt content increases, the resulting patterns exhibit a noisier signal, highlighting their amorphous characteristics and suggesting the presence of dehydrated CL. In fact, it is important to note that CL, after a heating treatment at 80 °C for 24 hours, becomes dehydrated (amorphous phase) [189].

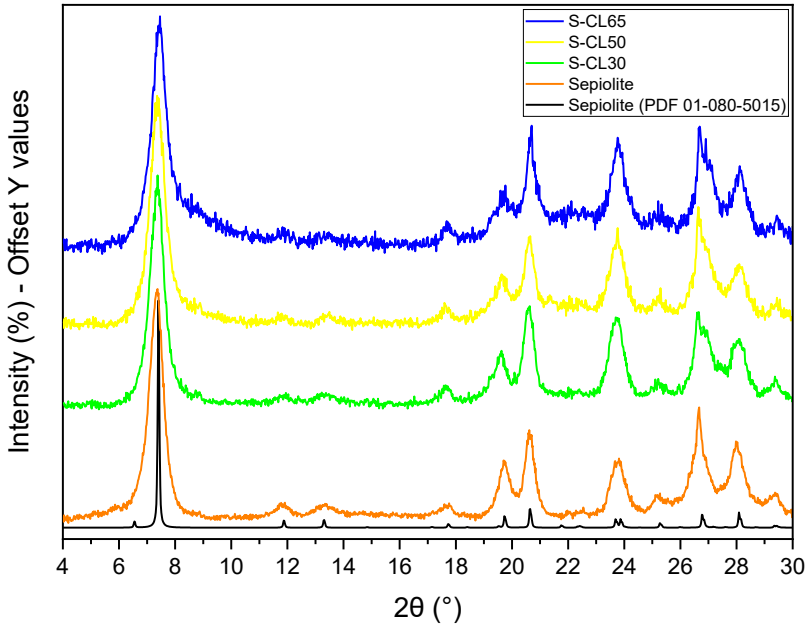

Figure 3.4 XRD patterns of sepiolite and dehydrated composite materials. It is furnished a comparison among pristine sepiolite and the reference PDF.

The crystallinity of the salt is fully restored after a hydration period of 24 hours, as shown in **Figure 3.5**. The crystalline peaks of hydrated CL were identified in line with the referenced PDF 00-070-1076 phase [227] for S-CL65/H24h, the identification is valid for all hydrated composites, as shown in **Figure 3.5**. The analysis revealed that the intensity of the sepiolite peaks decreases with higher salt content, resulting in certain mineral peaks being either partially or completely covered by the signals from CL. In conclusion, structural evaluations have validated the presence of sepiolite in the composites, and it is important to note that the clay does not obstruct the reversibility of the salt hydration reaction in these composite materials.

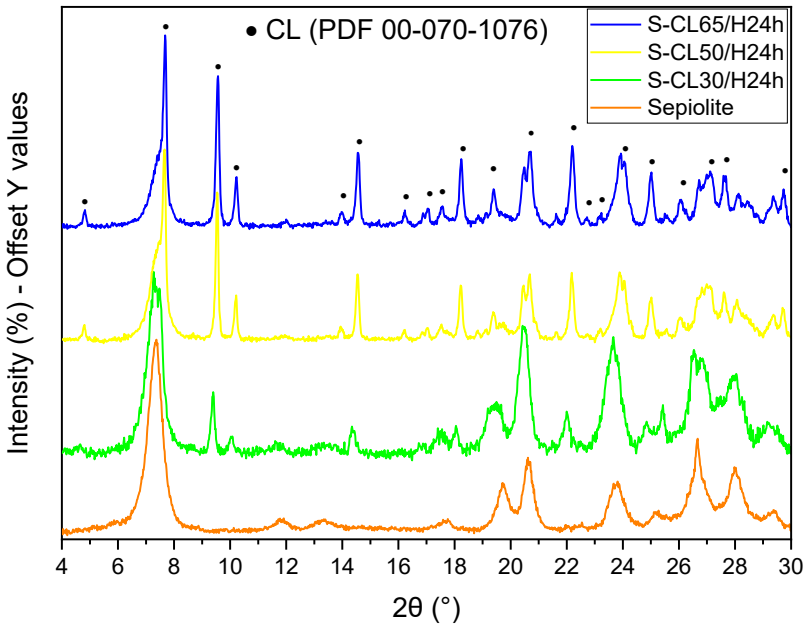

Figure 3.5 XRD patterns of hydrated composite materials. Phase identification of calcium L-lactate pentahydrate is provided according to the referred phase (PDF 00-070-1076). Diffractogram of sepiolite is reported for comparison.

The reversibility of the chemical structure during the dehydration and hydration processes, along with the integrity of all materials analysed, has been confirmed through FTIR analyses. **Figure 3.6** provides a comparative analysis of the FTIR spectra for sepiolite, CL, and composite materials. The spectra for the pristine materials correspond to samples that were thermally treated at 80 °C for 24 hours, allowing for an appropriate comparison with the synthesized materials under the same conditions. The thermally treated sepiolite and CL are marked with the label "DEH" in **Figure 3.6**. This section presents a detailed investigation into the primary FTIR signals of sepiolite and CL. The DEH spectra for sepiolite reveal a notable weak band between 3700 and 2900 cm^{-1}, which corresponds to the intermolecular O–H stretching of water molecules. As predicted, this band flattens after the dehydration process and intensifies with hydration. Additionally, other peaks in this region are attributed to various forms of water molecules integrated into the mineral's structure, including zeolitic water, octahedrally coordinated hydroxyl groups linked to magnesium, and edge Mg–OH bonds [275,276]. The band located at 1655 cm^{-1} corresponds to the bending of adsorbed water molecules [275]. The spectral range from 1400 to 400 cm^{-1} is characteristic of silicate minerals, associated with Si–O bonds in the tetrahedral sheet and Mg–O stretching vibrations in the octahedral sheet. The weak band at 1210

cm^{-1} is particularly notable for minerals that exhibit tetrahedral sheet inversion, attributed to the Si–O–Si bond [275,278]. The intense band near 1000 cm^{-1} is typical of the tetrahedral layer in sepiolite, linked to Si–O vibrations [275]. Lastly, the bands at 785 and 645 cm^{-1} are attributed to the bending vibrations of Mg–OH [275,278]. In the case of CL DEH, the spectral analysis shows a significant band between 3625 and 3010 cm^{-1}, which is associated with O–H stretching. The peak at 2979 cm^{-1}, along with those at 778 and 687 cm^{-1}, is attributed to C–H stretching and bending vibrations, respectively [217,220]. The robust band at ~1569 cm^{-1} corresponds generally to C=O stretching, while the notable peaks at 1260 and 1122 cm^{-1} are indicative of C–O stretching in esters and secondary alcohols, respectively [279,280]. The results here reported are in good agreement with the FTIR signals peaks described in § 2.4.2 section and obtained with a different equipment.

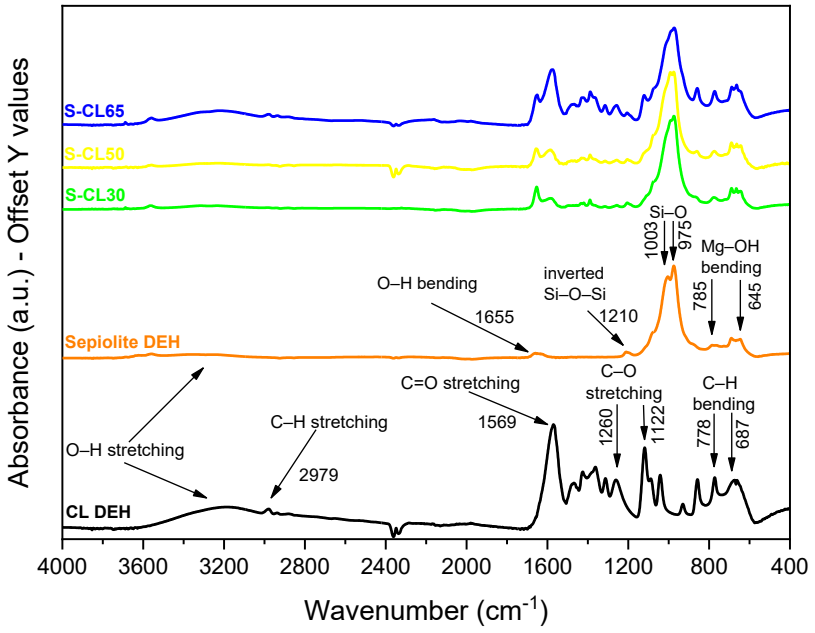

Figure 3.6 FTIR spectra of CL DEH, sepiolite DEH and composite materials.

The spectra of the synthesized composite materials are also illustrated in **Figure 3.6**. These spectra reveal a broad band attributed to the O−H stretching, as well as a peak at ~1569 cm^{-1} attribute to carbonyl stretching. Furthermore, the composite spectra display additional characteristic peaks related to CL and sepiolite. The analysis of composite spectra indicated that certain distinctive CL peaks shifted towards higher wavenumbers. Notably, shifts of 6 and 4 cm^{-1} were identified for the carbonyl (~1569 cm^{-1}) and secondary alcohol C–O stretching (~1122 cm^{-1}) bands, respectively. These

shifts are attributed to the heightened energy requirements for the vibration of CL chemical bonds when confined within the sepiolite matrix. Additionally, as the concentration of CL in the composites increases, the shifts of the selected peaks become less pronounced and more similar to the spectrum of the pure salt, suggesting a lower ability to penetrate the matrix or a less uniform distribution among the sepiolite fibers. It was determined that no new peaks emerged in the composites, other than those from the starting materials, indicating the absence of covalent bonds between the salt and clay. Moreover, salt peaks become more pronounced in comparison to the peaks of sepiolite, at increasing CL content.

The spectra of pristine materials, which include the pure sepiolite and CL, are illustrated in **Figure 3.7** along with the spectra of the hydrated composites. As expected, the intensity of the broad O−H stretching band increases with hydration in both spectra. The increased water content also affects the intensity and width of the O−H bending in the hydrated sepiolite. A significant hump has been observed, attributed to the larger number of different water molecules involved in the vibration. In a similar manner, the peak at 1260 cm^{-1} in the CL DEH spectra shifts to 1273 cm^{-1}, exhibiting greater intensity and a narrower profile with hydration, which indicates that the functional group is involved in coordinating water. What is clear is that the FTIR spectrum of CL undergoes significant changes during the dehydration phase, yet it returns to its original profile once hydration occurs, indicating the reversibility of the dehydration and hydration processes. Furthermore, the characteristic peaks of the starting materials are identifiable in the composite spectra, mirroring the shifts observed during dehydration. Significantly, the peaks associated with CL become increasingly prominent in comparison to those of sepiolite as the salt content increases.

In conclusion, the hydrated composites display the specific peaks of the precursor materials, confirming that the hydration reaction is not hindered by the deposition on the sepiolite matrix. This observation is supported by XRD characterization, and FTIR analyses have additionally confirmed the reversibility of the salt dehydration and hydration reactions in the composite materials. Moreover, the chemical stability of the composites under the conditions investigated has been successfully demonstrated.

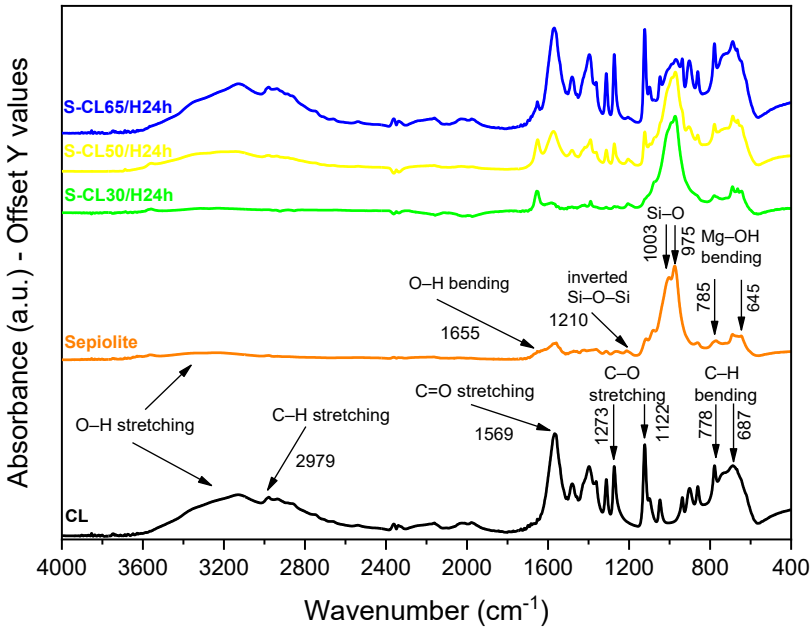

Figure 3.7 FTIR spectra of CL, sepiolite and hydrated composite materials.

3.4.2. Physical characterization

The physical properties of the sepiolite matrix and its composites were analysed using conventional techniques. Surface areas and pore volumes were calculated through nitrogen adsorption and desorption isotherms, with samples previously degassed at 120 °C for 16 hours. The specific surface area was then derived using the Brunauer–Emmett–Teller (BET) method and identified as S_{BET}. For pore volume assessment, the Barrett–Joyner–Halenda (BJH) approach was employed. The isotherms for the precursor sepiolite and S-CL30 are reported in **Figure 3.8**, indicating that both materials are categorized as microporous-mesoporous, corresponding to type IV isotherms according to IUPAC classification [281]. The S_{BET} value for sepiolite is indicated in **Table 3.3** and corresponds with the data found in the literature [253,262]. It is essential to note that the internal cavities of the clay were freed of zeolitic water under the specified degassing conditions. However, the tunnels within the sepiolite matrix are not accessible to CL molecules due to steric factors [272]. In the composite materials, an increase in salt concentration caused a sharp decline in surface area values, as presented in **Table 3.3**. These results suggest that CL is deposited on the outer surface of the clay, leveraging the mineral's high hydrophilicity. This configuration results in salt obstructing the internal cavities, leading to a significant

reduction in surface area values, as the internal cavities, which contribute to the large specific surface area of the clay, become inaccessible.

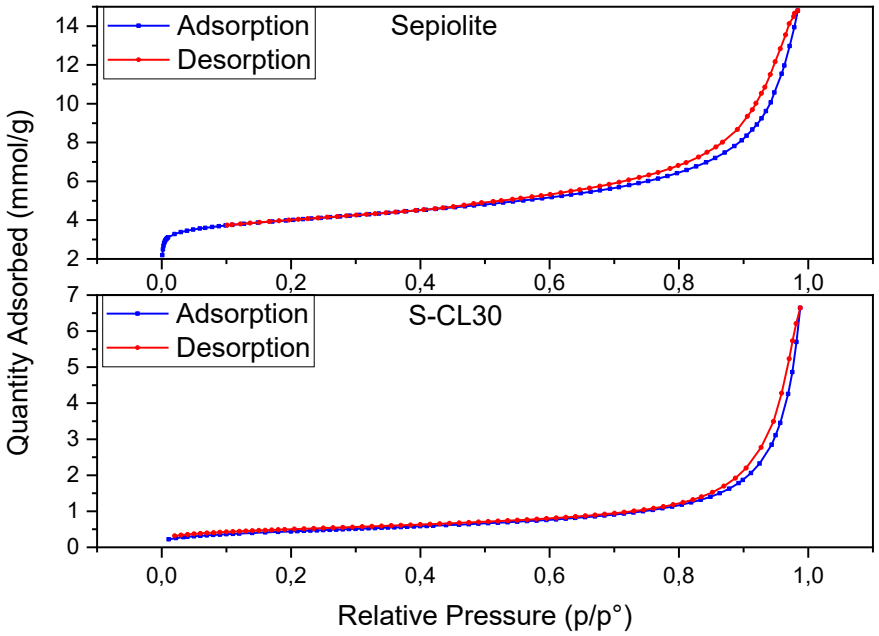

Figure 3.8 Nitrogen adsorption/desorption isotherms at -196 °C of sepiolite and S-CL30.

Analysing the nitrogen adsorption and desorption isotherms enables the assessment of total pore volume, which is consistent with previously reported data. A trend similar to that of BET surface areas was noted in the pore volume behavior. As the salt concentration increased, a notable decrease in cumulative pore volume was observed, as detailed in **Table 3.3**.

Table 3.3 BET surface area and total pore volume of host matrix and composite materials.

Material	BET surface area (m^2 g^{-1})	Total pore volume (cm^3 g^{-1})
Sepiolite	291	0.130
S-CL30	36	0.011
S-CL50	3	0.006
S-CL65	1	0.004

These observations further support the notion that CL can obstruct the internal cavities of sepiolite and disperse within the clay fibers, thereby influencing the textural porosity, as reported in **Figure 3.1d**. In this regard, the specific surface area and total pore volume provide critical insights into the distribution of salt on the matrix surface. The significant surface area of sepiolite not only supports the salt hydrate particles, ensuring their uniform distribution, but is also likely to enhance the mass transfer

channels for water vapor, thereby contributing positively to the thermochemical properties of the salt [282]. In light of the observations made, it is clear that of the composite materials analysed, only S-CL30 presents a considerable surface area that might facilitate vapor exchange with the underlying layers during the processes of dehydration and hydration. The other composites, on the other hand, are completely covered by salt, which could hinder the exchange of vapor.

3.4.3. Thermal stability

The high surface area of sepiolite not only provides essential support for the salt hydrates but also enhances the catalytic activity of the clay. This attribute may influence the degradation of CL by promoting its oxidation [283,284]. Therefore, an analysis was carried out to investigate and compare the thermal stability of the precursor and composite materials. The TG profile of pristine sepiolite is presented in **Figure 3.9a**. This figure also includes the differential thermogravimetric (DTG) curve, which help to better distinguish the associated thermal events. The DTG signals are calculated as the first derivative of the percentage mass variation with respect to time. The mineral undergoes a three-step dehydration process between 30-600 °C, which is in agreement with the literature [275,285]. The initial weight loss of 8.8% observed in the temperature range of 30-160 °C is linked to the removal of water that is physically adsorbed on the clay's external surface, as well as zeolitic water present in the internal cavities. The next phase, occurring between 160-330 °C, corresponds to the loss of approximately half of the coordinated water that is more weakly associated with the edge Mg^{2+}. This dehydration process resulted in a mass decrease of 2.4%, which is in agreement with the calculated value of 2.8%. Given these conditions, the sepiolite structure begins to fold, yet this process remains reversible, allowing for recovery through hydration. Moreover, there is a significant agreement between the experimental water loss of 2.3% and the calculated loss of 2.8% for the third dehydration step, which occurs at temperatures exceeding 330 °C [284,286]. By the end of this step, approximately at 600 °C, all remaining coordinated water has been lost [284,286], causing the structure to fold irreversibly [254,276]. A schematic representation of the dehydration steps is here provided [275,284]:

Step 1) $Mg_8Si_{12}O_{30}(OH)_4{\cdot}(H_2O)_4{\cdot}8H_2O \rightarrow Mg_8Si_{12}O_{30}(OH)_4{\cdot}(H_2O)_4 + 8H_2O$

Step 2) $Mg_8Si_{12}O_{30}(OH)_4{\cdot}(H_2O)_4 \rightarrow Mg_8Si_{12}O_{30}(OH)_4{\cdot}(H_2O)_2 + 2H_2O$

Step 3) $Mg_8Si_{12}O_{30}(OH)_4 \cdot (H_2O)_2 \rightarrow Mg_8Si_{12}O_{30}(OH)_4 + 2H_2O$

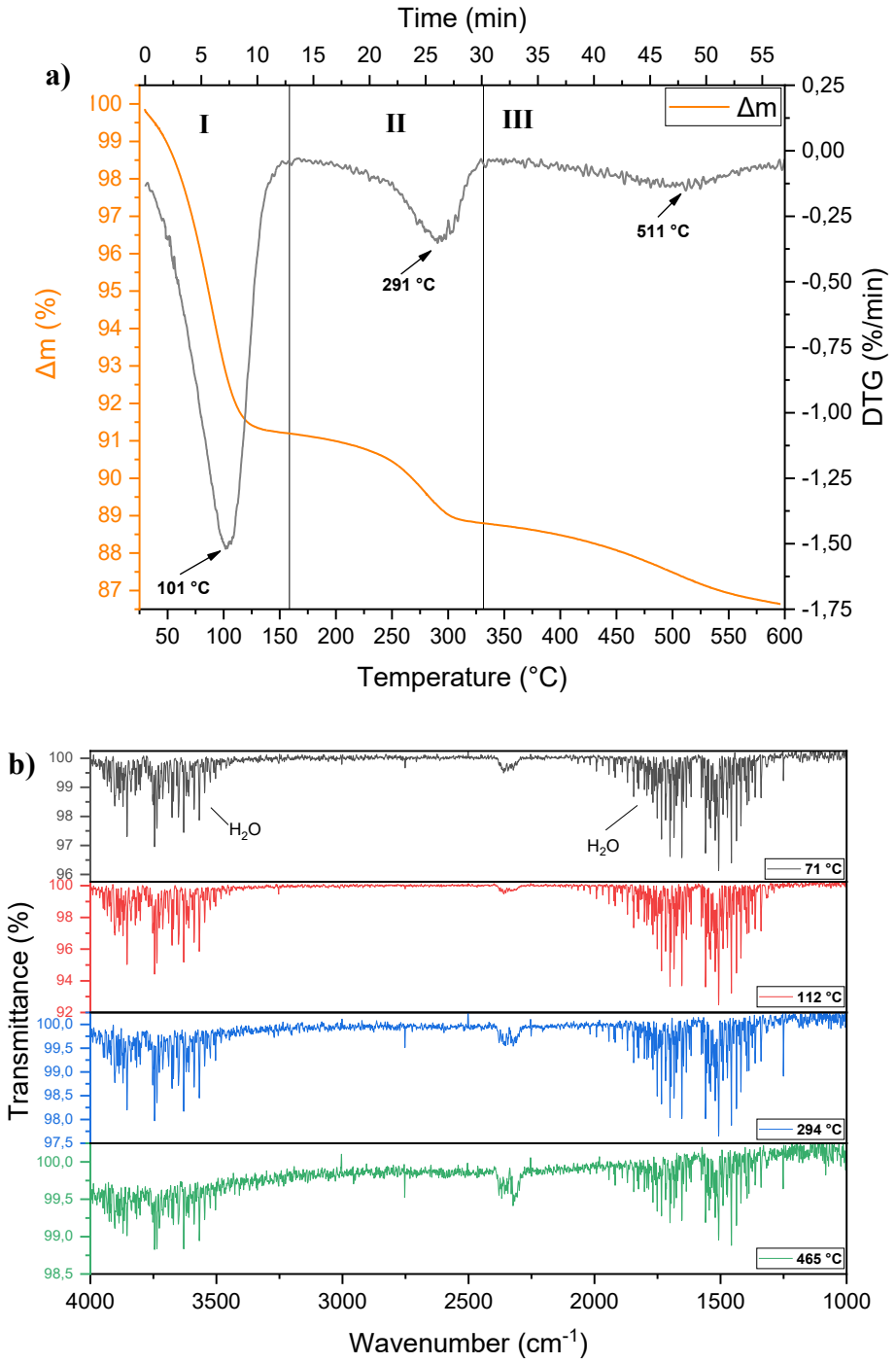

Figure 3.9 a) TG and DTG profiles of pristine sepiolite from 30 to 600 °C in air atmosphere. The three dehydration steps are marked. b) FTIR spectra of exhausted gases developed during the TGA of pristine sepiolite collected at different temperatures.

At higher temperature ranges (here not investigated), specifically around 700 °C, a transient amorphous phase is generated, while at 800 °C, the dehydroxylation of the octahedrally coordinated hydroxyl groups is observed. This final step leads to the

conversion of sepiolite into enstatite [275,286]. Consequently, the thermal stability of the materials analyzed was assessed up to 600 °C, which occurs before the mineral transitions to the amorphous phase. The FTIR spectra of exhaust gases collected during the TGA of sepiolite at various temperatures are shown in **Figure 3.9b**. These profiles illustrate that sepiolite undergoes a dehydration process from low temperatures up to 600 °C. The release of physically adsorbed water is detected at 71 °C, while zeolitic water molecules trapped within the clay cavities are released at 112 °C. At higher temperatures, coordinated crystal water is expelled during the second (294 °C) and third (465 °C) dehydration steps. The alterations in transmittance intensity suggest that the most pronounced release of water occurs during the initial dehydration step, a conclusion that aligns with TG data.

The TG analysis of commercial calcium L-lactate pentahydrate (CL) in the temperature range of 30-600 °C demonstrates three distinct thermal events (illustrated in **Figure 3.10a**). The initial event involves the nearly complete dehydration of the salt, occurring up to 200 °C, which results in a mass decrease of 26.2%. This finding is in agreement with literature data [219,225], and corresponds to the loss of 4.5 water molecules. The release of water during this dehydration phase was monitored using coupled FTIR spectroscopy, as depicted by the grey spectrum in **Figure 3.10b**. In **Figure 3.10a**, the thermal events identified in the second (260-360 °C) and third (360-480 °C) ranges are referred to as "Lactate degradation" and "CO_2 release," respectively, based on the main processes associated with these temperatures [225]. The onset of thermal degradation of organic groups occurs at temperatures above 260 °C, as demonstrated by the red spectrum in **Figure 3.10b**. This stage is also characterized by the release of remaining water molecules. The research conducted by Mastronardo *et al.* reveals that the second dehydration step is associated with the thermal degradation of lactate moieties [189]. In a related study, Komesu *et al.* demonstrated that lactate groups can undergo decomposition through several pathways, resulting in the formation of distinct intermediates that are characteristic of carboxylic acids [287]. The research conducted by Komesu *et al.* indicates that lactate groups decompose through various pathways, leading to the formation of distinct carboxylic acid-type intermediates [287]. This finding suggests that the FTIR spectra of the exhausted gases produced will display signals associated with the stretching of C=O and C-H bonds. The third stage of the process involves the complete

decomposition of residual organic matter through a combustion reaction, resulting in the production of carbon dioxide, as depicted in the blue and green spectra in **Figure 3.10b**. The presence of carbon monoxide signals in these spectra is accounted for the combustion reaction occurring in an environment with low oxygen content [225].

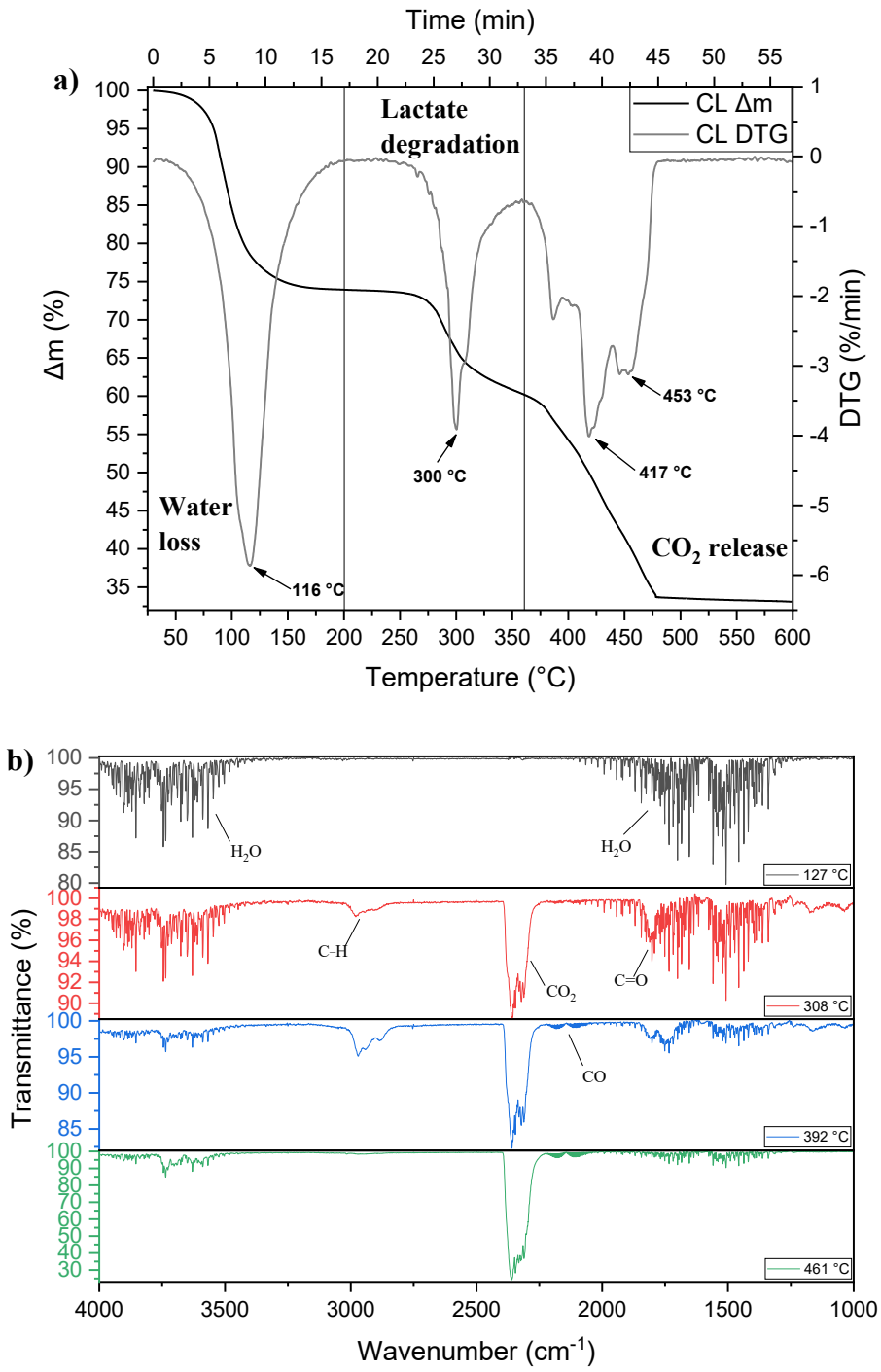

Figure 3.10 a) TG and DTG profiles of pristine calcium L-lactate pentahydrate (CL) from 30 to 600 °C in air atmosphere. The three thermal events are marked. b) FTIR spectra of exhausted gases developed during the TGA of pristine CL collected at different temperatures.

At the conclusion of the combustion process, calcium carbonate is reported as the only product of the reaction [189,225]. At higher temperatures, which are not explored in this study, a conversion to calcium oxide is expected to occur [288].

The TG profiles for the prepared composites are depicted in **Figure 3.11**. Each curve can be generally segmented into three main thermal events, resembling the profile observed for pure CL. The exhaust gases spectra resulting from the thermogravimetric analysis of S-CL30 and S-CL65 are shown in **Figure 3.12a** and **Figure 3.12b**, respectively. The spectra for the composite S-CL50 are not shown, as they follow profiles that are quite similar to those of S-CL65.

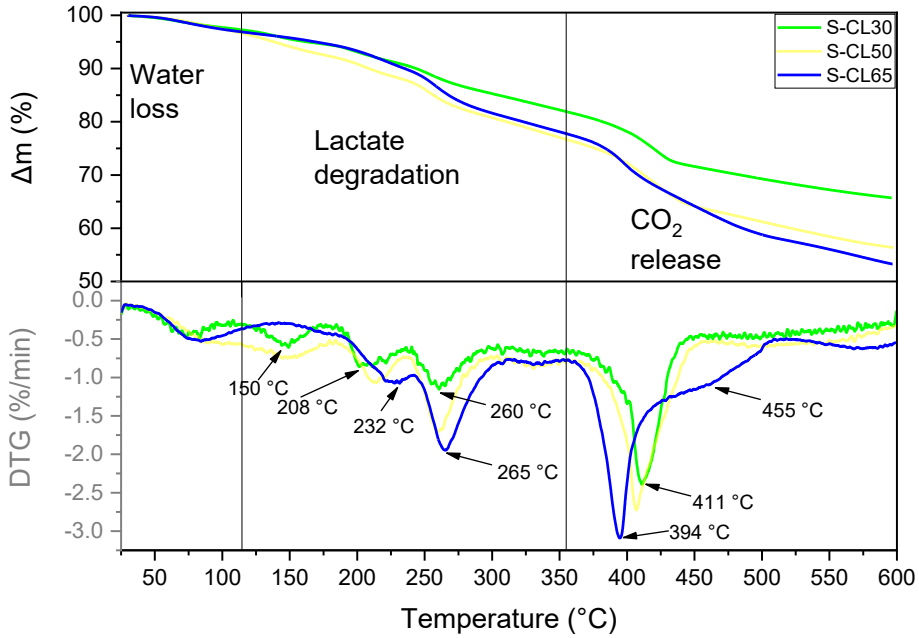

Figure 3.11 TG and DTG profiles of prepared composite materials from 30 to 600 °C in air atmosphere. Like the case of CL, three main thermal events were detected.

Below 115 °C, all synthesized materials showed a release of physically and chemically adsorbed water, as confirmed by the corresponding FTIR spectra. This release is attributed to minimal moisture adsorption that took place during sample manipulation, since the measurements were conducted on dehydrated composites. It is noteworthy that the degradation of lactate in the composites occurs at lower temperatures compared to pure CL. The degradation process begins at around 130 °C. A peak related to carbonyl stretching is present in the red spectra at 133 °C and 150 °C for S-CL30 and S-CL65, respectively (**Figure 3.12**), while for pure CL, the corresponding FTIR peak is found at 308 °C (**Figure 3.10b**). Additionally, the DTG signals show that S-CL30 presents a distinct local minimum at approximately 150 °C,

which is linked to the degradation of lactate moieties. At the same temperature, the lactate groups in S-CL65 begin to degrade, as shown by the low intensity of the FTIR signals. However, the complete degradation process occurs at temperatures above 200 °C, as reflected in the FTIR spectra (blue spectra in **Figure 3.12**) corresponding to the two local minima of the DTG signals at 208 °C and 232 °C. These results indicate that the carbonyl peak becomes more pronounced, and signals associated with C−H stretching have also been detected. In addition, two new peaks at 1082 and 1380 cm^{-1} were found, which are attributed to a different degradation mechanism of the lactate moieties. In addition, the DTG peaks observed at 260 °C and 265 °C for the composites with the lowest and highest salt contents, respectively, are indicative of the materials composition. In particular, sepiolite and CL present clear DTG peaks at 291 °C and 300 °C, respectively. As the salt content in the composites increases, a shift towards higher temperatures for the related thermal events is evident. These results suggest that the incorporation of CL into the sepiolite matrix modifies the thermal degradation pathway of the salt. The green spectra recorded at 277 °C and 274 °C for S-CL30 and S-CL65, respectively, align closely with the CL spectrum at 392 °C (illustrated in **Figure 3.10b**). This alignment is marked by a reduction in the carbonyl band and the identification of a CO_2 peak as principal signal. The release of water during this period is likely due to the second dehydration phase that sepiolite experiences at similar temperatures.

Generally, a shift towards lower temperatures was observed with the reduction of salt content in the composites, which can be ascribed to the catalytic properties of sepiolite [283]. This situation makes it challenging to fully understand the degradation process undergone by CL. Specifically, an effect related to composite formulations was noted: at low salt content in the composite (i.e. for S-CL30), the catalytic effect of the mineral is more pronounced due to the higher amount of sepiolite and to the salt even distribution onto the matrix. Conversely, as the CL content increases (such in the case of S-CL65), the greater coverage and reduced clay content diminish the catalytic activity of sepiolite, resulting in a slight delay in the degradation temperatures. For the S-CL50 composite, an intermediate scenario was observed, owing to the equal composition of the material. Lastly, the range of temperatures involved in the lactate degradation step for the composites (~130-350 °C) is broader than that of the pure salt (260-360 °C).

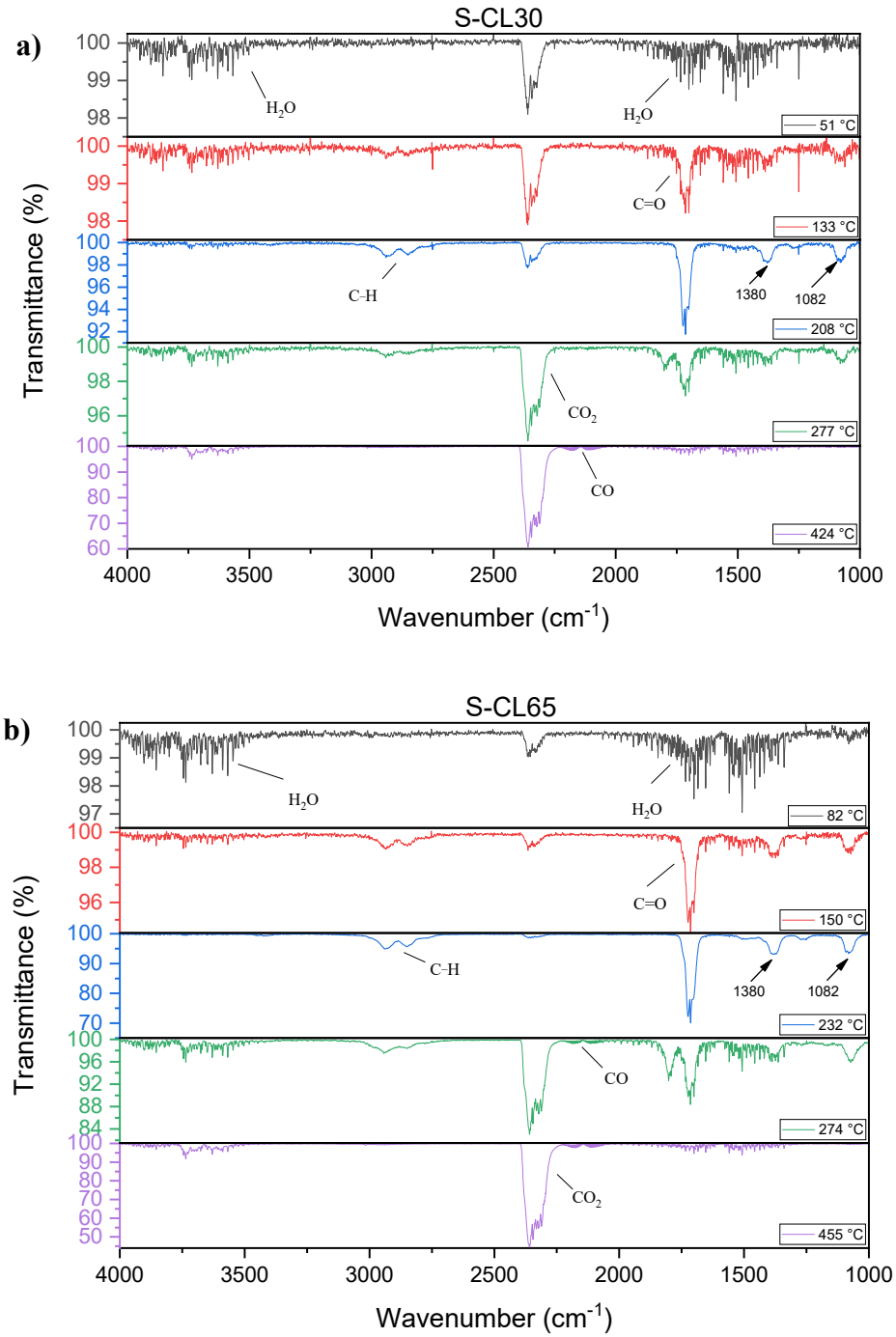

Figure 3.12 a) FTIR spectra of exhausted gases developed during the TGA of S-CL30 collected at different temperatures. b) FTIR spectra of exhausted gases developed during the TGA of S-CL65 collected at different temperatures.

The release of CO_2 occurs within temperature ranges that are analogous to those of pure CL. At temperatures exceeding 380 °C, the primary event is the emission of CO_2 due to the combustion of remaining organic matter, as evidenced by the purple spectra (**Figure 3.12**). The peaks corresponding to water in the final spectra are likely a result of the third dehydration step of sepiolite or water molecules generated during the

combustion reaction. As anticipated, the release of CO_2 is higher with increased salt content in the composites. Furthermore, S-CL65 shows a distinct shoulder in the DTG signals at temperatures above 455 °C, indicating that the process is not fully complete and continues at higher temperatures, as also reflected in the TG curves.

In summary, this study investigated the thermal stability of pristine and composite materials at temperatures up to 600 °C. All examined materials displayed three distinct thermal events, which were characterized through FTIR analysis of the gases produced. Sepiolite demonstrated three dehydration steps, with the initial step involving the release of physically and chemically adsorbed water up to about 120 °C. CL also released water within a similar temperature range while undergoing thermal degradation at higher temperatures. The composite materials maintained thermal stability up to approximately 130 °C, and the study discussed the catalytic effect of sepiolite on the degradation of the organic salt, although the specific species generated were not investigated, as this was outside the scope of the research. From an application perspective, composite materials are ideal for thermochemical systems at low-temperature applications. Furthermore, sepiolite and CL undergo dehydration processes at temperatures lower than 120 °C, which is a crucial consideration for the aim of conducted research. This phase involves the release of both physically and chemically bound water. Although the thermal stability of the hydrated composites has not been explored, the established reversibility of hydration and dehydration processes implies that the hydrated materials may also release water at temperatures below 120 °C, which could be utilized for TCES purposes.

3.4.4. Thermogravimetric dynamic vapor sorption characterization

The thermochemical behavior of both pristine and composite materials during hydration and dehydration cycles was assessed using a thermogravimetric dynamic vapor system (DVS) under isothermal conditions at 30 °C, with the relative humidity (RH) in the chamber varied from 0% to 90%. The results are shown in **Figure 3.13**. The isotherms for pure salt have been previously documented in § **2.4.2** section and are included for comparison. For the composite materials, the mass variations, which indicate water uptake, were normalized with respect to the salt hydrate content. It is significant to note that the normalization was based on the CL content rather than the sepiolite, although both components are involved in the hydration and dehydration

processes. This occurs because the salt acts as the active phase, while the sepiolite matrix is utilized as a support to enhance the thermochemical properties of the CL.

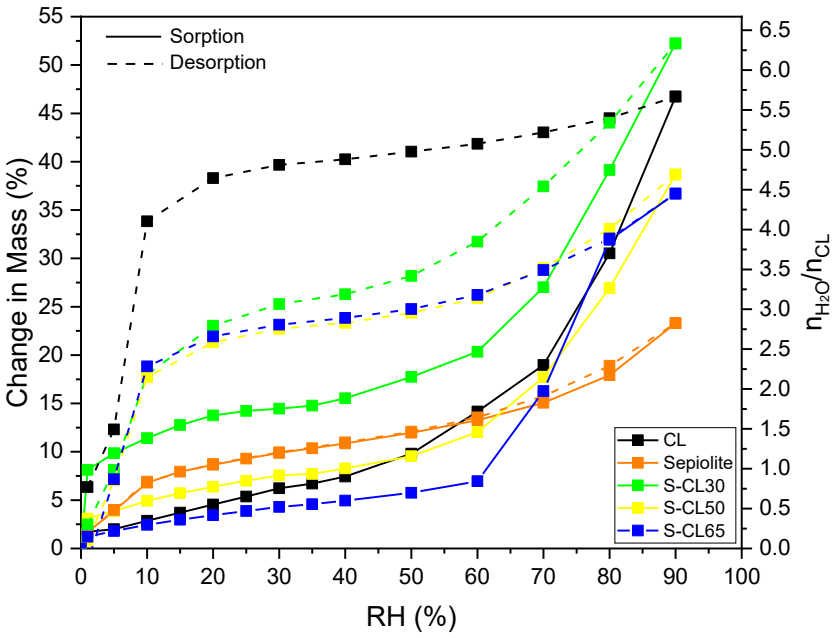

Figure 3.13 Water vapour sorption/desorption isotherms at 30 °C of pristine and synthesized materials. The isotherms of composites were normalized with respect to the CL content in each material.

Sepiolite has an overall water uptake of ~23% at the highest vapor partial pressure. The hydration and dehydration processes of this clay are completely reversible, achievable by varying the relative humidity. In contrast, CL displays a considerable hysteresis between the sorption and desorption phases [218]. This hysteresis is related to a kinetic barrier, as the dehydration reaction is only promoted at low partial pressure values. A notable mass decrease is observed when relative humidity falls below 10%. This indicates a significant difference between desorption and sorption conditions at the same temperature, which is dependent on vapor pressure [189].

According to Equation (2.3), the theoretical mass change due to the complete hydration of anhydrous CL is 41.2%. This threshold value corresponds to the pentahydrate state. When this value is surpassed, the material becomes over-hydrated, leading to interactions between the excess water and the water coordination sphere through hydrogen bonds. The amount of water molecules (n_{H2O}) involved in the sorption process during DVS experiments can be calculated from the right Y-axis of **Figure 3.13**. However, as n_{H2O} is determined in relation to the moles of CL (n_{CL}) it is not particularly relevant for the sepiolite isotherms.

Among the prepared composites, S-CL30 is the only one that surpasses the CL absorption at the highest vapor partial pressure. When the composite exceeds five water molecules, it reaches a state of over-hydration, with the sepiolite matrix likely playing a pivotal role in this phenomenon. The physical adsorption of water vapor within the cavities of the matrix may enhance the chemical absorption of the hydrated salt [273].

Moreover, the uniform dispersion of CL on the sepiolite surface, particularly evident in S-CL30, significantly reduces the hysteresis. Generally, hysteresis between the sorption and desorption isotherms indicates that water diffusion through the material structure is slower as the lattice re-arranges during hydration [289]. In this context, an adequate distribution over the matrix surface ensures higher and more uniform vapor diffusion in the solid phase, enhancing the material hydration kinetics.

The two additional composite materials reveal analogous water uptake characteristics, although they differ in the degree of hysteresis. In particular, an increase in the salt content of the composites results in a decrease in the absorbed water and a widening of the hysteresis. The hysteresis of the materials examined was quantified through DVS analysis, with the percentage variations summarized in **Table 3.4**. This quantification was achieved by calculating the ratios of the areas (A) under the curves, as specified in following equation:

$$\Delta A(\%) = \frac{A_{composite}}{A_{CL}} \cdot 100 \qquad (3.1)$$

Table 3.4 Percentage variations of investigated materials DVS hysteresis, calculated as the ratios of the areas between the desorption and sorption curves, according to Equation (3.1).

Material	Area (a.u.)	ΔA (%)	Hysteresis Decrease (%)
S-CL30	212.2	9.4	90.6
S-CL50	508.4	22.5	77.5
S-CL65	786.5	34.8	65.2
CL	2263.2	100	0

At lower CL contents, the hydrated salt is more dispersed on the sepiolite surface and the various CL layers deposited on the clay are more susceptible to the decrease in vapor pressure during dehydration, tending to release water more easily. This results in a narrowing of the gap between the absorption and desorption isotherms, leading to a reduction in hysteresis. Conversely, with greater quantities of salt, an accumulation

is observed between the different CL layers, and the inner layers are less affected by the decrease in vapor pressure. Lower RH values will be necessary to desorb the material.

As mentioned, the S-CL30 composite exhibits the greatest reduction in hysteresis (the S-CL30 hysteresis is 9.4% of the CL one), indicating a higher vapor transfer capacity due to the improved distribution of salt on the sepiolite. To support this, the efficiency in reducing hysteresis is shown in **Figure 3.14**, calculated by normalizing each sorption isotherm with respect to the corresponding hysteresis area. The data reveals that the composites capability to decrease hysteresis increases as the CL content diminishes. These reductions in hysteresis confirms that the issue of salt agglomeration is limited for all the investigated composites. This further demonstrates that S-CL30 is the best-performing among the composite materials investigated, as also evidenced by BET experiments.

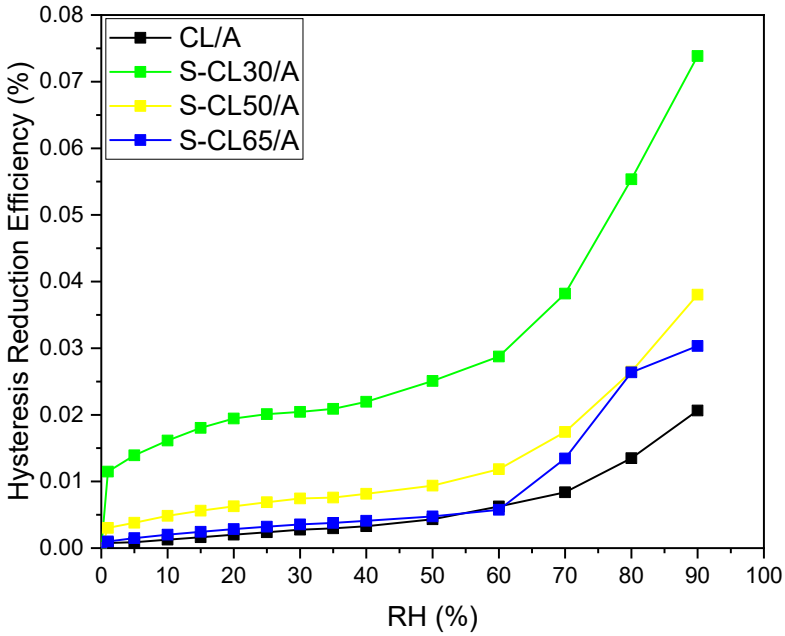

Figure 3.14 Hysteresis reduction efficiency of investigated materials.

In contrast, the other composite materials, particularly S-CL50 and S-CL65, exhibit a less pronounced hysteresis decrease, showing a 77.5% and 65.2% reduction compared to pure CL, respectively. This confirms that the deposition of salt over the sepiolite porous matrix remains beneficial at higher CL loads. In fact, the hysteresis decrease efficiency of the latter composites is higher compared to CL, particularly at higher vapor partial pressures (**Figure 3.14**). Nevertheless, S-CL30 has the better

efficiency, suggesting that once a certain salt content is exceeded in the formulation, the salt covers the surface of the matrix, slightly limiting the vapor exchange processes. This behavior is frequently observed in the scientific literature, as the TCM content over clay porous matrices generally does not exceed 30% by weight [248,273].

3.4.5. Evaluation of materials heat release capacities

The heat release capacities of CL, sepiolite, and S-CL30 were analysed using a custom-designed TG-DSC apparatus that operates under saturated vapor pressure conditions (static conditions). This modified apparatus was utilized to simulate the hydration reaction of the materials under investigation, while monitoring their mass changes and the heat released. The hydration reaction was performed by cooling the samples from 80 °C to 28 °C at a saturated vapor pressure of 3150 Pa, followed by a 2 hours stabilization period at this condition. Before the analysis, the samples were thermal treated in vacuum at 80 °C for 2 hours to ensure maximum dehydration without compromising the materials stability, removing any physically adsorbed gases. The subsequent analysis was conducted on the most promising material identified among the examined composites. **Figure 3.15** presents the mass increases attributed to vapor sorption, which were recorded during the final cooling and isothermal phases.

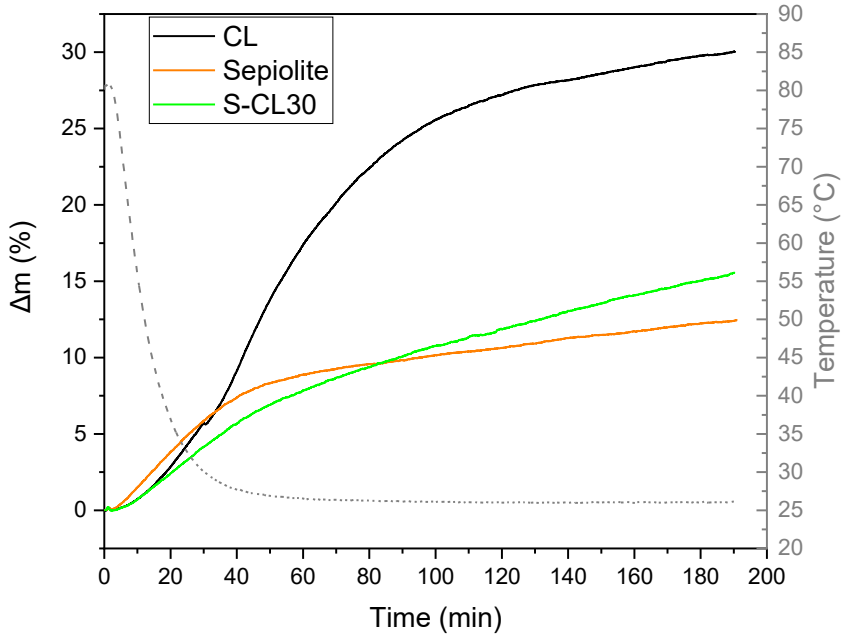

Figure 3.15 TG profiles of investigated materials recorded during the temperature decrease from 80 °C to 28 °C under a water vapor pressure of 3150 Pa.

The mass variations were calculated with respect to the initial mass of the dehydrated sample. The pristine materials maintained an almost uniform TG profile at the end of the cooling isotherm. The total water uptake recorded was 30.1% for CL and 12.4% for sepiolite, while the S-CL30 composite exhibited a sorption capacity of 15.5%, indicating an intermediate level of uptake at described conditions.

The heat release capacities of the materials were determined by integrating the exothermic peaks from the DSC profiles over time for each material, although these profiles are not shown here. **Table 3.5** presents the enthalpies associated with the hydration reaction ($\Delta H_{hydration}$), calculated in relation to the mass of the initial dehydrated material. It also includes the actual densities of the materials examined, measured at 20 °C using a helium pycnometer on powder samples. The volumetric heat release capacities (Q_R^v) were calculated using the material densities (ρ) in accordance with Equation (2.4) [176] and are provided in **Table 3.5**.

Table 3.5 List of calculated hydration enthalpies, measured real densities and estimated volumetric release capacities (Q_R^v) of investigated materials.

Material	**$\Delta H_{hydration}$ (kJ kg^{-1})**	**Density (kg m^{-3})**	**Q_R^v (MJ m^{-3})**
CL	892	1505	1342
Sepiolite	254	2394	608
S-CL30	467	2299	1073

The energy released by CL is consistent with the gravimetric energy storage capacity outlined by Mastronardo *et al.* [189]. The result for sepiolite of 254 kJ kg^{-1} aligns with literature findings under similar operational conditions [266]. Moreover, the real density of the clay is consistent with previously reported values [290]. The density of the composite (S-CL30) falls within the range of precursor materials, as does its hydration heat. Considering the reversible nature of the dehydration and hydration processes, along with the principle of energy conservation, it is plausible to assert that the volumetric storage capacity is comparable to the calculated value Q_R^v. In other words, the dehydration reaction of the materials, treated under the described saturated vapor conditions, involves an amount of heat analogous to the one released during the hydration process. Given the favorable characteristics of S-CL30, a comprehensive comparison with other sepiolite-based composite materials that contain PCMs/TCMs is now presented (**Table 3.6**).

Table 3.6 List of most investigated PCMs/TCMs combined with sepiolite to prepare composite materials for TES applications. For each material, the corresponding class (PCMs or TCMs) and its nominal weight fraction in the composite are reported. Additionally, for PCMs, the enthalpy associated with the melting process and the corresponding temperature are specified. For TCMs, the gravimetric energy storage/release capacities, the temperature range for the dehydration reaction, and the investigated temperature of hydration are included.

Class	**Material**	**Content (%wt.)**	**ΔH (kJ kg^{-1})**	**$T_{melting}$ (°C)**	**$T_{dehydration}$ (°C)**	**$T_{hydration}$ (°C)**	**Reference**
TCM	CL	30	467	/	40-100	30	this study
PCM	EHS*	90	185	38.1	/	/	[250]
PCM	$CaCl_2 \cdot 6H_2O$	70	87.9	34.9-43.7-52.4	/	/	[251]
PCM	Stearic acid	35	76.10	71.0	/	/	[267]
PCM	Lauric acid	60	82.6	42.5	/	/	[269]
PCM	Paraffin	50	62.08	40.02	/	/	[291]
PCM	Decanoic acid	50	35.69	28.65	/	/	[291]
PCM	FAEM**	42	76.16	22.86	/	/	[292]
TCM	$CaCl_2$	30	1026	/	30-120	20	[273]

*EHS (eutectic hydrated salt): inorganic eutectic mixture of $Na_2HPO_4 \cdot 12H_2O$ and $Na_2SO_4 \cdot 10H_2O$ in a 1:1 weight ratio.

**FAEM (fatty acid eutectic mixture): organic eutectic mixture of capric acid and stearic acid (83:17%w/w, respectively).

The dehydration temperature range for S-CL30, as detailed in **Table 3.6**, is consistent with the operational conditions analysed by Mastronardo *et al.* for pure CL [189]. The literature provides an extensively examination of sepiolite-based composite materials that incorporate PCMs, while only a single example is provided for binary composites with a TCM as the active phase [273]. Various methods of preparation, including direct techniques [291] and vacuum impregnation [251], have been utilized to develop these composites, all of which leverage the liquid state of PCMs at nearly ambient temperatures to facilitate their integration among the solid sepiolite fibers and within the clay's structural voids. This technique removes the need for a solvent. In the evaluation of inorganic and organic PCMs, composites that contain inorganic materials allow for a higher loading of salt hydrates and show larger melting enthalpies [250]. However, they are susceptible to material leakage after repeated melting and freezing cycles. Utilizing organic PCMs improves the stability against leakage. The leakage issue is facilitated by the deliquescence phenomenon [293]. Organic compounds, with their low or absent solubility in water, effectively prevent or stabilize the creation of a wetting surface layer when exposed to moisture, thereby avoiding any leakage [190]. On this perspective, the development of a composite material derived from $CaCl_2$, designed for TES applications, faces significant limitations due to the deliquescence of the hydrated salt under working conditions, even though it possesses a high energy storage capacity. The study referenced in [273] reveals a gravimetric storage capacity of 1026 kJ kg^{-1}, as expected, much higher than that of composites with PCMs and more than twice that of S-CL30, which has a capacity of 467 kJ kg^{-1}. This variation can be explained by the elevated dehydration enthalpy linked to the hydrated forms of $CaCl_2$ when compared with pure CL [142]. However, the authors also note the instability of the composite particles, which turn moist and pasty after extended sorption durations of 100 hours at 10 °C and 73% of relative humidity [273].

Considering the insights presented, employing an organic hydrated salt appears to be a promising strategy for preparing sepiolite-based composite materials, as it can prevent deliquescence and related leakage issues. Ongoing activities are focusing on evaluating the stability of composite materials over hydration/dehydration processes, a critical aspect requiring particular attention. In fact, this kind of study could yield important findings regarding the long-term stability of sepiolite-based composite

materials, thereby reinforcing their application as thermochemical systems for low-temperatures uses.

3.4.6. Morphological observations on sepiolite-based composite materials

The SEM morphologies of sepiolite are presented at two distinct magnifications in **Figure 3.16**. The pristine sepiolite is characterized by particles of different dimensions and a notable fibrous structure, which can be observed even at lower magnifications (**Figure 3.16a**). At higher magnification (**Figure 3.16b**), the sepiolite fibers tend to bind together, while still retaining porous and cavities within the fiber folds [262]. This fibrous arrangement creates an appropriate matrix for the deposition of hydrated salts.

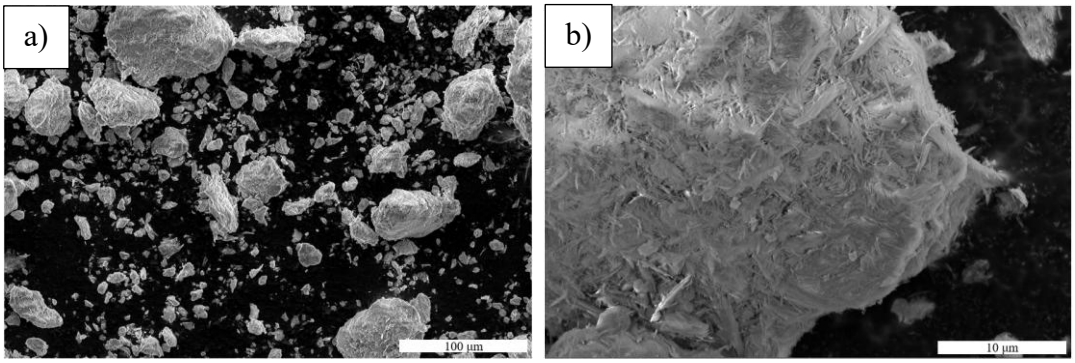

Figure 3.16 SEM micrographs of pristine sepiolite at different magnifications.

The fibrous nature of sepiolite is still discernible in the morphology of the S-CL30 composite, as shown in **Figure 3.17a**. Additionally, small, irregularly shaped particles consisting of tightly bundled, very thin filaments have been observed in all composites. This morphology is attributed to the CL component, and its identification becomes increasingly difficult at lower salt concentrations [189]. With an increase in CL loading, as illustrated in **Figure 3.17c** and **Figure 3.17e**, the spaces between the sepiolite fibers seem to be filled with salt, indicating that the CL has permeated the porous matrix [273]. Moreover, at higher salt concentrations, the composite particles tend to agglomerate, resulting in a more bundled morphology.

After the hydration treatment for 2h, as shown in **Figure 3.3**, a significant morphological alteration was observed, attributed to the rehydration of the CL component [189]. The salt particles specifically adopted a fibrous form and demonstrated a tendency to cluster [219]. These salt fibers extended over the surfaces of the sepiolite, thereby occluding the pores within the matrix. Notably, the composite material with lower CL content, illustrated in **Figure 3.17b**, still preserved a

considerable level of macroporosity, which allowed for enhanced vapor exchange between the underlying layers and the environment. Conversely, as the salt content increased **(Figure 3.17d** and **Figure 3.17f**), the composite surface appeared increasingly compact, which hindered vapor exchange and restricted the hydration process. The morphologies presented in the composites further clarify the relationship between structure and properties of these materials, clearly indicating that an even distribution of salt within the matrix facilitates the exchange of water vapor.

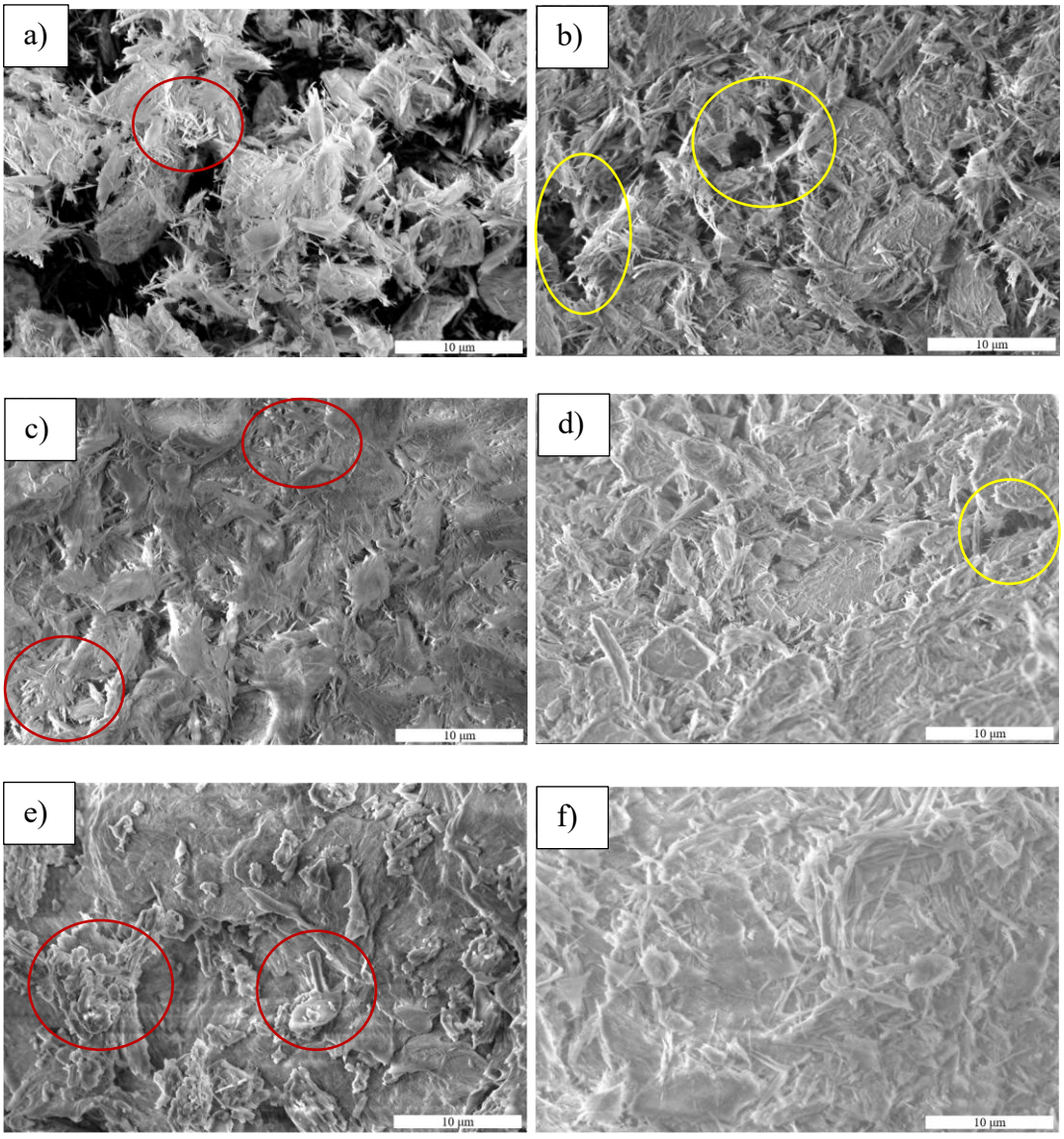

Figure 3.17 SEM micrographs of: a-b) S-CL30 before and after hydration treatment, respectively; c-d) S-CL50 before and after hydration treatment, respectively; e-f) S-CL65 before and after hydration treatment, respectively. Red circles indicate the presence of CL particle. Yellow circles indicate the presence of pores.

3.5. General remarks and future outlooks

This chapter investigated the feasibility of novel composite materials and their potential as thermochemical systems for low-temperatures applications. The composites leverage the favorable properties of sepiolite to disperse a recently assessed organic hydrate salt as TCM. The strategy involves dispersing the CL over a porous matrix to enhance the salt hydration and dehydration reactions.

The composites were synthesized using DMF for clay dispersion and salt solubilization. Materials with different CL contents (30-50-65%wt.) were realized, demonstrating the applicability of the synthetic process. The prepared samples were characterized by XRD and FTIR to investigate materials under structural and chemical points of view. The BET analyses indicated the optimum composition among investigated composites for promoting vapor exchange processes and enhancing the beneficial effects of salt dispersion. The thermal stability of the composites was also investigated and compared to that of the pristine materials, revealing that the degradation of the salt organic groups in the prepared samples occurs at lower temperatures than in the pure salt. Nevertheless, the studied materials are deemed stable for thermochemical heat storage applications at low-temperatures (<120 °C). The hydration processes were investigated under two different vapor conditions (dynamic and static) further demonstrating that S-CL30 exhibits the best capacity to absorb water vapor, by showing an adequate dispersion of the salt on the matrix, as verified by SEM micrographs. On this purpose, a reviewer correctly argued that composites with lower salt content (i.e., 20%wt.) could further favor vapor exchange, potentially accelerating salt hydration and dehydration kinetics. This is a high-impact aspect for operability in continuous cycles in thermochemical reactors. However, reducing the CL content in the composite will reduce the storage capacity, considering that CL contributes more to the storage capacity than clay. Further research should determine an optimum between formulations to ensure improved performance in terms of both kinetics and storage capacity. To fully evaluate the potential of the S-CL30 composite, its gravimetric release capacity was compared with that of the main sepiolite-based composites (with PCMs and TCMs) for energy storage applications, and the results are promising.

The use of these composite materials is encouraging due to the presence of an organic hydrated salt that does not exhibit deliquescence-related issues under operating

conditions. The insights on the beneficial effect of sepiolite in facilitating the hydration/dehydration reactions of CL prompt the utilization of this matrix for the dispersion of TCMs, given the excellent adsorption properties and low cost of the clay, as well as the limited number of examples reported in the literature. Ongoing studies are aimed at assessing the durability of the composite materials to multiple dehydration/hydration cycles under realistic operating conditions. Further investigations can incorporate composite materials in mortars to exploit the beneficial effect of CL deposition onto the sepiolite matrix. In addition to improved thermochemical aspects, the deposition on sepiolite contributes to increasing the composite's mechanical resistance and integrity, thanks to the clay's fibrous structure. This property is also exploited in the preparation of mortars, where sepiolite reinforces. The development of the CL composites investigated in this chapter fits perfectly into the context of this thesis, since sepiolite's structural characteristics can ensure more effective salt dispersion within a complex matrix like mortars and improve the entire system's mechanical behavior.

Chapter 4 Composite plaster mortars with CL

4.1. Composite mortars integrated with PCMs and TCMs

The use of PCMs and TCMs in buildings is recognized as a promising strategy for enhancing energy efficiency through thermal energy storage and release [126]. Directly integrating these materials into mortar composites to increase the thermal mass of building envelopes is gaining greater success in the scientific literature, although the mortar formulation often requires adjustment [124].

For instance, Frazzica *et al.* developed a cement mortar composites with commercial microencapsulated PCMs to reduce building energy consumption in Mediterranean climates. The PCMs used were Micronal DS 5038X and Micronal DS 5040X with melting points of 26 °C and 23 °C, respectively. The microcapsules were added at 5-15% by weight of the dry mortar. Additional water was needed to optimize the mortar workability at increasing PCM content, as it retains water during preparation. Authors evinced, through thermal and morphological analyses, that the mixing process created a homogeneous dispersion of the PCM capsules in the cement mortar matrix. Furthermore, experimental testing, in reproduced environmental conditions, demonstrated the PCM-mortar composites can dampen temperature fluctuations and shift peak temperatures by improving thermal comfort of around 15% annually in the Messina region, compared to plain cement mortar [124].

Cementitious composite materials with a TCM were instead investigated by Lavagna *et al.* [294]. This study introduces a novel approach for synthesizing cement-based composite sorbent materials. In fact, the methodology involves incorporating $MgSO_4$ salt into the matrix. Particularly, the composites were prepared by mixing cement paste with a salt-containing aqueous solution, allowing control over porosity through the water to cement ratio (w/c ratio). This parameter is also critical in influencing the mechanical properties of the cement matrix. Characterization revealed an energy density range of 0.088-0.2 GJ m^{-3} for space heating in temperate climates. The composites also exhibited hydro-thermal stability over 100 cycles [294]. Further studies assessed thermal properties and cost [258,295], exploring the use of sepiolite to enhance porosity and reduce overall costs. The top-performing composite achieved an energy density of 0.0085 GJ m^{-3} and a storage cost of 9.30 € kWh^{-1}, comparable or superior to other materials, like Zeolite 13X/$MgSO_4$ and silica gel/$CaCl_2$. However,

the authors suggest additional efforts are needed to integrate these composites into the global market, such as reducing cement content or finding more affordable alternatives [258].

A cementitious composite material with a TCM was also investigated by Clark and Farid. In three distinct works, they assessed the potential of a cascade TCES system to improve thermal and exergy energy efficiencies in residential applications [296–298]. First, they proposed creating a porous concrete composite embedded with $SrCl_2 \cdot 6H_2O$ (50% wt.). For this, a known quantity of hydrated salt was added to a dry mixture of Portland cement powder, reducing, in this way, the amount of water typically required for the impregnation approach. A subsequent stepwise heating program removed unbound water and developed the porous structure. The concrete composite's performance was found comparable to that of zeolite 13X in terms of energy density (136 vs 164 kWh m^{-3}, respectively), and the cement-composite exhibited good cyclability, too [298]. Next, they studied the hydration reaction kinetics of pure salt and salt combined in the cement composite, developing models to determine the salt's hydration behavior while held in the porous matrix. The models revealed the slower reaction rate due to mass diffusion limitations. Authors also empirically developed a shrinking-core model for salt in the cement porous matrix, combining chemical reaction and moisture diffusion to define the overall reaction rate. These kinetic models can predict the performance of a packed bed TCES system [297]. Finally, they realized the cascade system, investigating it in a lab-scale reactor and comparing it to traditional single-material systems. The cascade system used a bed of zeolite 13X beneath the $SrCl_2$-cement composite material. The volumetric energy density ranged from 108-138 kWh m^{-3}, with dehydration temperatures of 50-130 °C and hydration conditions of 12 °C at 75% RH. The thermal and exergy efficiencies were analysed, and the cascade system was found to improve power output, temperature lift, and exergy efficiency by 6-38% compared to traditional salt-based systems. From a cost perspective, the cascade design allows leveraging the low cost of the salt and the efficiency of the zeolite 13X in a single system. Authors concluded that further research is required to improve the energy storage density or salt loading into cheapest concrete porous materials for this technology to become commercially viable [296].

In conclusion, embedding salt hydrates in concrete mortars presents promising avenues for enhancing energy efficiency in buildings, yet faces challenges, especially

in material preparation and cost. Adjustments to mortar formulation are often necessary, as seen with the addition of extra water to maintain workability when incorporating PCMs. Furthermore, despite the potential of the technology, the necessity to reduce cement content or find more affordable alternatives is evident to achieve commercial viability. For what has been said, in this thesis, the author approaches a novel strategy for selecting salt hydrates, evaluating the use of an innovative organic salt hydrate with intriguing characteristics for building applications. What is more, this chapter discusses the potentiality of CL incorporation in lime-based mortars as a novel and competitive solution for enhancing thermal comfort in residential applications.

4.2. Mortars with CL for self-healing

As discussed in the previous section, one of the aims of this thesis is to realize a composite mortar with calcium L-lactate pentahydrate (CL) for TCES applications. The use of CL in mortar, particularly in concrete, is not a novel concept in the scientific literature. In fact, several studies have assessed the potential of incorporating the salt with bacteria for self-healing applications.

As it is known, concrete is the most widely utilized construction material globally due to its strength, durability, and cost-effectiveness [299]. However, although the presence of micro cracks does not significantly alter the structural characteristics of buildings, the resulting increase in permeability from the network of these cracks can significantly compromise the durability of concrete structures, particularly in moist environments. Under specific conditions, as reported in literature, small fractures in concrete can undergo a healing process, that is identified as “autogenous healing” or “self-healing” of concrete. The main factors contributing to autogenous healing are generally attributed to various chemical, physical, and mechanical processes [300,301]. Nevertheless, it has been observed that the formation of calcium carbonate (calcite) plays a crucial role in the autogenous healing of concrete. In fact, it has been demonstrated that calcite may fill the voids and cracks on cement-based materials to prevent and heal the micro cracks formation [302–304]. Besides autogenous healing, cracks can be autonomously repaired by integrating a specific healing agent into the matrix.

In this context, Wiktor and Jonkers developed a two-component self-healing system with bacterial spores. Once germinated, these spores initiate the metabolic conversion of calcium lactate into calcium carbonate ($CaCO_3$), in accordance with the reaction reported below:

$$[CH_3CH(OH)COO]_2Ca + 6O_2 \rightarrow CaCO_3 + 5CO_2 + 5H_2O$$

Specifically, they evaluated the crack-healing ability of this two-component system immobilized in expanded clay particles, on aged concrete specimens. In this way, the expanded clay particles serve as an internal reservoir while also acting as a structural component of concrete and a protective matrix for the self-healing agent. Researchers prepared also control specimens without bacterial spores. Cracks were induced in distinct samples by a steel bar in the mortar specimens, which were then submerged in water for 100 days in an open-air bucket to enable the free diffusion of oxygen and carbon dioxide. Experiments showed that bacterial concrete could heal cracks up to 0.46 mm wide, while control specimens only healed cracks up to 0.18 mm wide [305].

In another study, Irwan *et al.* used *Enterococcus faecalis* with calcium lactate (as additional food source for the bacteria) in bioconcrete. The research reported an improvement of compressive strength and water permeability. Specifically, the calcium lactate, incorporated into the mixture, is present in concentrations of 0.001 mol dm^{-3}, 0.005 mol dm^{-3}, and 0.01 mol dm^{-3}. Tests for compressive strength and water penetration are conducted after 28 days. It has been determined that the addition of calcium lactate to bioconcrete significantly enhances its compressive strength, with an increase of up to 18.8%, resulting in a maximum strength of 42.8 MPa at a concentration of 0.005 mol dm^{-3}. This is notably higher than the control sample, which had a strength of 36 MPa, and the concrete that included only *Enterococcus faecalis*, which measured 38.2 MPa. Additionally, the trend in water penetration reflects similar improvements, as the combination of *Enterococcus faecalis* and calcium lactate leads to a decrease in water penetration. The highest reduction in water penetration, quantified at 26.2%, is observed with a calcium lactate concentration of 0.01 mol dm^{-3}, resulting in a penetration depth of 8.7 cm. This is notably lower than the control measurement of 11.8 cm and the 9.2 cm recorded for concrete with only *Enterococcus faecalis*. In conclusion, this study confirmed that the addition of calcium lactate as an

alternative nutrient for bacteria in concrete produces advantageous results regarding compressive strength and the ability to resist water penetration [306].

Subsequently, a similar study was reported by Vijay and Murmu that evaluated the effect on compressive strength and self-healing capability of the addition of calcium lactate and *Bacillus subtilis* bacteria in concrete. Particularly, *Bacillus subtilis* was added to the concrete both in spore form and culture form, while calcium lactate was added with concentrations in the range 0.5-2.5%wt., and then the materials were tested after a curing period of 7, 14 and 28 days. According to the obtained results, the incorporation of just 0.5%wt. of calcium lactate into the concrete led to an increase of 12% in compressive strength. Moreover, it was observed the healing process, and its efficiency are enhanced with a higher concentration of calcium lactate [307].

Chaerun *et al.*, instead, used *Lysinibacillus sphaericus* as bacterial component with calcium lactate. According to their experiments, the addition of calcium lactate pentahydrate (0.5%wt. of cement), combined with a 10% v/v bacterial inoculum, led to increases of 45% in compressive strength and 36% in indirect tensile strength. Moreover, the self-healing process was accelerated in the bacterial mortar enhanced with calcium lactate pentahydrate compared to the control specimen [308].

In conclusion, all these different researches confirm that the use of two-component system with bacteria and calcium lactate can improve the durability and mechanical properties of concrete enhancing the cracks self-healing.

4.3. Plaster mortars with CL

The intriguing capabilities of calcium L-lactate pentahydrate (CL) as a TCM material have been recently evaluated by Mastronardo *et al.* [189] and discussed in § **Chapter 2**. As CL presents a low solubility in water, it is resistant to deliquescence [190]. CL also demonstrates stability under operational conditions and has a significant storage capacity of 1127 kJ kg^{-1}, attributed to its five coordinated water molecules [189]. The dehydration process of CL occurs in a single step within the temperature range of 40-150 °C, indicating its potential for low-temperatures applications. Additionally, Mastronardo *et al.* have confirmed the reversibility of the hydration process [189].

This chapter explores the integration of CL into construction materials. For the first time, the thermal insulation features of the salt are employed to create a mortar that

not only allows for precise indoor climate control but also efficiently stores thermal energy. By embedding CL into the mortar, heat absorption is improved, which helps to prolong heat retention within the building and maintain thermal comfort. In this regard, an Italian patent (#102022000007862) on the use of mortars including calcium lactate has been recently filed [309]. Author of present thesis is one of the inventors, together with his supervisors and external collaborators who worked on the research. Natural hydraulic lime (NHL) was selected as the preferred mortar binder due to its high breathability and crystalline lattice structure. Moreover, the addition of inert filler with proved particle sizes ensures a significant level of porosity in the mortar. These attributes enable effective water vapor exchange with the environment, thereby enhancing the thermochemical processes related to salt dehydration and hydration. This emphasizes CL as a promising option for construction applications. The prepared mortars were designed to function as lime-based plasters. Plaster plays several key roles in the building envelope, contributing to its overall performance, protection, and aesthetics [310]. By using NHL, the resulting mortars are environmentally friendly and suitable for both internal and external facades. Plaster is the thicker component of the facade system, and its width varies based on the application (internal or external). Since it is the most present component, it is advantageous to use a plaster as matrix for the dispersion of the CL, allowing to increase the quantity of salt available for the entire building envelope and thus improving thermal efficiency.

In the designed plaster mortars, solar heat is expected to contribute to the dehydration of the hydrated salt through an endothermic reaction during the day, helping to lower indoor temperatures compared to the external environment. It is like the thermochemical effect of salt hydrate shields the indoor environment from higher outside temperature. At night, on the contrary, the increase in atmospheric humidity facilitates the exothermic hydration of the salt, causing indoor temperatures to rise. This process is depicted in the **Figure 4.1**.

In order to assess this, a comparative study was conducted, involving a reference sample and mortars with CL in the range of 1-5%wt. Workability tests and mechanical characterizations were performed on the prepared mortars after 14 and 28 days. Subsequently, the samples were examined through XRD, SEM, and DVS analyses, followed by thermal monitoring cycles to assess internal surface temperatures and weight variations.

The data presented in this chapter are the result of the author's activity conducted during a research period at Tradimalt Spa in Villafranca Tirrena (Italy), which is the industrial partner of the PhD project. Specifically, the preparation, the characterization of fresh mortar, and mechanical characterization at different aging periods were carried out under the supervision of Eng. Francesco Grungo in the laboratory of Tradimalt Spa. The thermal monitoring cycles to assess surface temperatures and weight variations of the plaster mortars were executed in collaboration with the research group of Prof. Anna Laura Pisello at the University of Perugia.

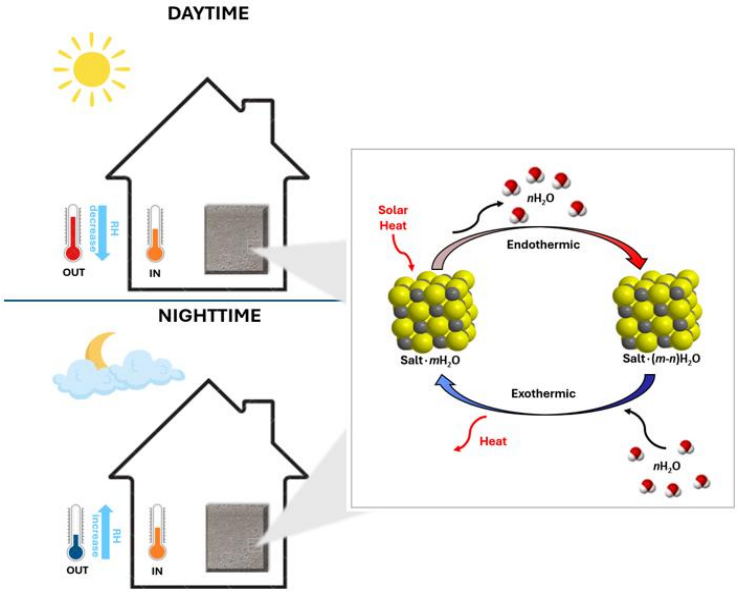

Figure 4.1 Description of dehydration and hydration processes undergone by the salt hydrate respectively during the day and the night. IN and OUT indicate the indoor and external temperatures, respectively. The light blue arrow (RH) exemplifies the relative humidity variation during the day and the night.

4.4. Materials and methods

4.4.1. Plaster mortar preparation

For the preparation of plaster mortars all the necessary materials were provided by Tradimalt Spa, while high grade calcium L-lactate pentahydrate (CL) was purchased by Thermo Scientific (purity ≥ 98%).

The dry constituents of mortar and their weight percentages (%wt.) are detailed in **Table 4.1** and divided into three categories. Natural hydraulic lime (NHL) was chosen as the mortar binder due to its high breathability. Lime is recognized for its superior capability to allow vapor exchange with the environment, which is critical for regulating indoor humidity and maintaining dry walls. The high breathability of lime

is attributed to its drying process, where it reacts with carbon dioxide in the air, preventing the formation of an insulating surface film, unlike cement. Furthermore, these gas exchanges with the environment facilitate the creation of a porous structure, which is advantageous for the purposes of this study [311]. Specifically, NHL5 from the Magistra line by Tradimalt Spa was used to prepare plaster mortars. This building lime is a commercially produced item that meets the requirements of the current UNI EN 459-1/2010 regulation [312]. Magistra plasters are suitable for renovation, and NHL5, in particular, is suitable for cultural heritage, as it combines high breathability with improved mechanical performance [313]. The number "5" in the NHL5 label indicates the compressive resistance class of the binder when mixed in specific weight proportions with certified aggregates, after 28 days of aging. The use of this type of plaster for the realization of mortars with CL, which is also suitable for renovation works, potentially expands the product's market and offers the possibility of exploiting the thermal properties of salt. This aligns well with the new strategies of renovation and energy efficiency of buildings, as desired by the European Union and described in § **1.1** section [4].

Table 4.1 Constituents of plaster mortar divided by type. Furthermore, the weight percentages (%wt.) of the various constituents are indicated.

Type of constituent	**Constituent**	**%wt.**
Binder	NHL 5	25
Aggregates (grey sands)	Ø 0-150 μm	75
	Ø 150-300 μm	
	Ø 300-600 μm	
	Ø 600-1200 μm	
Additives	Cellulose	< 0.1
	Starch	
	Air entraining agent	

As aggregates, grey sands of four different grain sizes were employed (**Table 4.1**). The sand ensures a significant level of porosity in the mortar and is able to work as “skeleton” of the structure during the hardening phase, reducing the shrinkage of the binder paste and preventing the onset of cracking phenomena. Furthermore, by partially replacing the binder, which is relatively more susceptible to environmental

factors, the aggregate improves the durability of the final product. The addition of aggregates improves also the workability of the fresh mix and many properties of the hardened material, such as mechanical strength and elastic modulus, depend on the quality and quantity of the aggregate introduced.

The addition of small amounts, less than 0.1%wt., of various additives can influence the workability and intrinsic characteristics of fresh mortars. Notably, cellulose is recognized for improving the mortar's ability to retain water. This helps prevent premature drying, ensuring proper hydration of the binder, and thereby enhances the workability of the fresh mortar. Moreover, cellulose leads to better strength development and reduced cracking. Furthermore, cellulose acts as a thickening agent, increasing the viscosity of the mortar and improving the adhesion of the plaster mortar to the substrate [314]. Starch in mortars also acts as a thickening agent and can offer some improvement in water retention and adhesion, contributing to better workability. By modifying the rheology and water retention, starch can contribute to a smoother and more workable plaster, potentially leading to a better surface finish [315]. The addition of air entraining agents to plaster mortars creates microscopic, stable air bubbles that offer several key benefits, improving the workability and freeze-thaw resistance of the mortars. The spherical air bubbles act like tiny ball bearings, reducing friction between particles and making the fresh mortar easier to mix, apply, and spread smoothly. This leads to better consistency and plasticity. Furthermore, the incorporation of air bubbles decreases the overall density of the mortar, making it lighter, which can be advantageous for reducing the load on the structure and improving handling [316].

The preparation of plaster mortars with and without CL was performed in line with the UNI EN 1015-2/2007 standard [317]. The dry constituents were combined with water and mixed for one minute in a planetary mixer. The mass of water added is proportional with the mass of dry constituents. Subsequently, commercial CL powder, in the range 1-5%wt. with respect to solid components, was introduced into the mixture and blended for another minute, until a consistent product was obtained. To enhance the workability of the mortars containing CL, it was crucial to increase the water content for each batch, leading to total percentages between 20% and 23% [124]. Three samples with different salt concentrations were prepared: A1 (1%wt.), A3 (3%wt.),

and A5 (5%wt.). **Figure 4.2** schematized procedure for preparing plaster mortars with CL.

Figure 4.2 Schematic procedure for preparing fresh plaster mortars with CL.

A control batch, referred to as A0, was prepared without CL for comparative analyses. **Table 4.2** reports the codes for all prepared samples along with their formulation characteristics.

Table 4.2 Codes of all prepared plaster mortar specimens. For each formulation is reported CL and water contents.

Codes	CL content (%wt.)	Water content (%wt.)
A0	0 - Reference	20
A1	1	21
A3	3	22
A5	5	23

For all the formulations, 100x100x20 mm^3 square base block specimens (as shown in **Figure 4.3**) were fabricated to evaluate the thermal capacities of the mortars. Any physical, structural, morphological and thermochemical characterizations were performed on the specimens described, after 28 days of aging, allowing the mortar to fully dry from the preparation water.

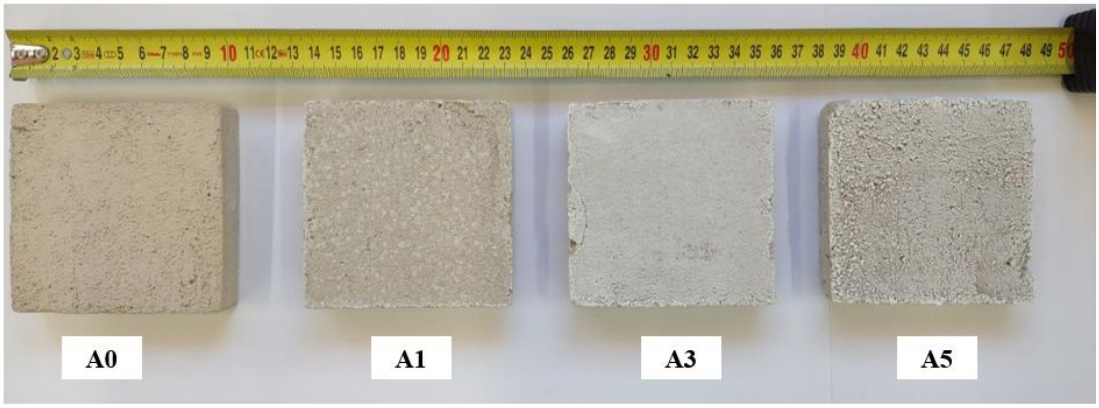

Figure 4.3 100×100×20 mm^3 square base block specimens after 28 days of aging.

4.4.2. Characterization of fresh plaster mortars

The workability of fresh mixed mortars was investigated by slump test using the flow table method, in agreement with the UNI EN 1015-3/2007 standard [318]. The test consists in measuring the spread of mortar after being subjected to a series of jolts on a flow table, considering that a higher spread diameter indicates a more fluid and workable mortar. The measure system includes a flow table, which is a circular brass table, typically 300 mm in diameter, mounted on a hinged support that allows it to be raised and dropped through a specific height. On its plate surface, the fresh mortar is poured, inside a truncated conical mold. The latter has top and bottom diameters of respectively 70 and 100 mm and a height of 60 mm. For compacting the mortar inside the mold, a tamper was used. After levelling the surface and lifting the mold, the mortar was subjected to 15 jolts of flow table provoking its spread on the table (**Figure 4.4**). The mortar spread has been measured along two distinct diameters, with respect to the initial position using a caliper. The results are reported as average of the two measures, for each plaster mortar batch [318].

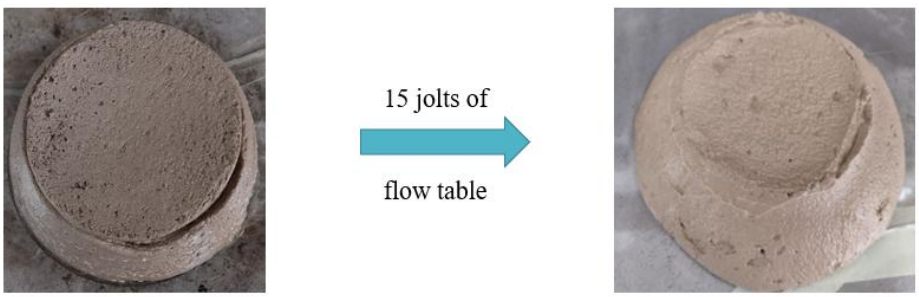

Figure 4.4 Spread of a fresh plaster mortar after 15 jolts of flow table.

4.4.3. Mechanical characterization

The hardened plaster mortars were mechanically characterized to evaluate their flexural and compressive strength. The flexural strength was determined by three-point loading of hardened mortar prisms to failure. The compressive strength was measured on the two parts resulting from the flexural test. The tests were conducted in accordance with the UNI EN 1015-11/2007 standard [319]. To prepare the160x40x40 mm^3 prisms, the fresh mortar was poured into a stainless-steel mold. The mold-filling was performed in two layers, each followed by 15 jolts of flow table to ensure uniform compaction and eliminate large air voids. After levelling the surface, the mold was stored in a polyethylene bag for 2 days in a climatic chamber. The specimens were then demoulded and stored in a controlled environment until testing. A schematization of described procedure is reported in **Figure 4.5**.

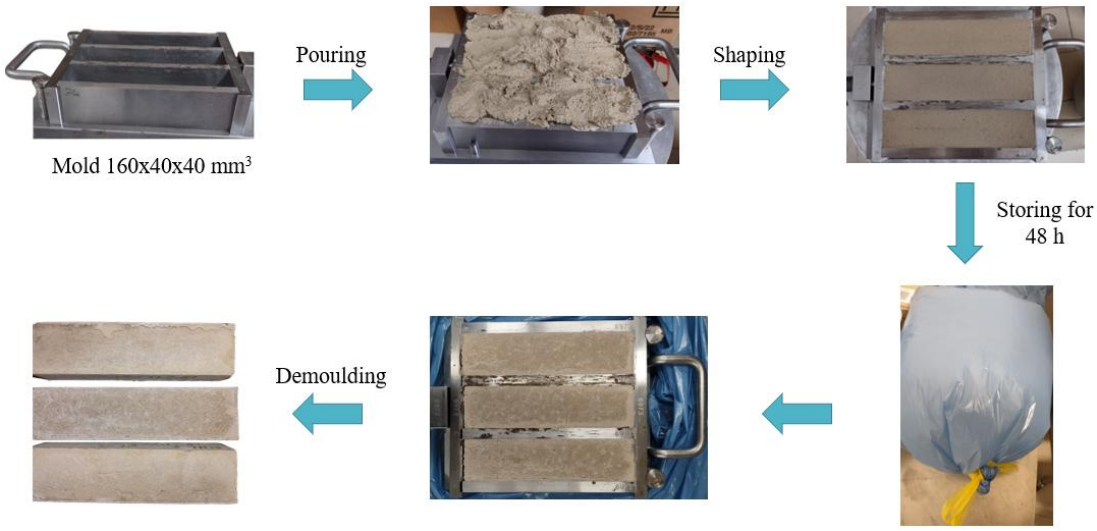

Figure 4.5 Schematic procedure for preparing 160x40x40 mm^3 prism mortars destined to mechanical characterization.

Considering the nature of the binder employed, it has been chosen to mechanically test plaster mortar after 14 and 28 days of hardening. NHL5, unlike concrete, exhibits a slow and gradual setting with a continuous increase in mechanical resistance over the months following setting [313]. The mechanical characterization was carried out on the prepared prisms using an AUTOMAX 65-L1352/LC (Controls). This instrument allows for flexural testing along one channel and compression testing, on the two previously broken ends, along the second channel. The flexural tests were performed with a force gradient of 50 N s^{-1}, while the compression tests were conducted with a gradient of 100 N s^{-1}. The flexural tests were executed using a three-

point bending system, with a distance of 100 mm between the supporting rollers. On the second channel, the compressive strength was directed along two steel plates with a surface area of 40x40 mm². The equipment was only capable of recording the applied force and the stress at the maximum peak value. Regarding the flexural tests, at least three specimens were tested for each batch and hardening period. This number was doubled for the compressive analysis, considering the nature of the test. The values reported for the mechanical tests represent the arithmetic mean of the results, with the error calculated using the maximum semi-dispersion method.

4.4.4. Physical, structural and morphological characterizations

The real densities of investigated plaster mortars were measured using a helium pycnometer (Ultrapyc 5000 Foam, Anton Paar) at 20 °C, based on the average of fifteen measurements. For the measures, mortar blocks of approximately volume of 30x25x25 mm^3 were used, after hardening of 28 days. The composite densities will be used to estimate the void percentage (%void) in mortars, which is an important parameter considering the scope of the thesis. This feature is calculated by making comparison among pycnometric (V_p) and geometric (V_g) volumes of described blocks. In fact, the pycnometer returns a real value of the volume occupied by the mortar, which does not include its internal voids. The geometric volume, on the other hand, also includes these voids in its calculation [320]. Therefore, the percentage of voids can be determined with the following equation:

$$\%void = \frac{V_g - V_p}{V_g} \cdot 100 \qquad (4.1)$$

The salt characterization in the composite mortars material was performed using X-Ray diffraction (XRD) and scanning electron microscope (SEM) analyses. Before conducting these characterizations, the mortars were ground into a coarse powder. XRD measurements were executed with a D8 Advance Bruker instrument, which employed a monochromatic Cu Kα radiation source at 40 kV and 40 mA. The samples were analyzed in the 2θ range of 5-50° using the Bragg-Brentano theta-2theta configuration with a scanning speed of 0.1° s^{-1}. The identification of different phases was facilitated by the PDF-4+ software. SEM images were captured using a Quanta 450 FEI with Large Field Detector (LFD) and an accelerating voltage of 5 kV in high vacuum (10^{-4} Pa).

4.4.5. Isotherms of water vapor sorption/desorption

Isotherms for vapor adsorption and desorption were carried out to investigate the water absorption and release capabilities of the prepared mortar materials under controlled environmental conditions. A dynamic vapor sorption (DVS) analyzer (DVS Vacuum) was employed to observe mass variations. The setup comprises a micro-balance with a precision of ±0.1 μg and a system for controlling water vapor pressure flow within the sample holder chamber. The entire system is enclosed in a temperature-controlled environment, maintained at 30 °C. To determine the dry weight before water adsorption, each sample, (~30 mg), was activated (degassed) at 80 °C under vacuum (~0.1 Pa) for 3 hours. Once this was completed, a valve connecting the evaporator, which contained liquid water, to the sample chamber was opened. Following this, isothermal adsorption and desorption experiments were performed at 30 °C, with partial pressures increasing from 0 to 0.9 (p/p_0).

4.4.6. Thermo-physical characterization under controlled boundary conditions

In collaboration with the University of Perugia, a thermo-physical characterization of mortars with hydrated salt was conducted under controlled boundary conditions. Thermal monitoring was performed on all samples to evaluate the impact of the salt on the mortars. A custom sample-holder in extruded polystyrene was designed to contain each sample at its center. A Tinytag sensor was then inserted into the sample-holder to monitor the internal air temperature and relative humidity. Furthermore, the internal and external surface temperatures were monitored using three type T thermocouples for each surface, connected to a National Instruments cDAQ-9184 data acquisition system. Another temperature/humidity Tinytag was positioned near the external surface of the sample. This system was placed on a KERN572 balance with a precision of 0.1 grams to allow for continuous weight monitoring [321,322]. The entire system setup is shown in **Figure 4.6a**.

The experimental setup involved the following steps:

- Initial mass stabilization of the square-based mortar specimens in an oven at 80 °C (approximately 2-3 days).

- Transfer of the samples into a climatic chamber at 80 °C at minimum relative humidity (RH).
- Placement of the sample inside the sample-holder.
- Thermal monitoring of the samples subjected to the following 24-hours total cycle (**Figure 4.6b**):
    - 2 hours of system stabilization under dehydration conditions (T = 50 °C and RH = 10%).
    - 3 hours of hydration (the temperature varies from 50 to 20 °C and the humidity increases from 10 to 95%).
    - 8 hours under the conditions thus obtained.
    - 3 hours of dehydration (the temperature varies from 20 to 50 °C and the humidity decreases from 95 to 10%).
    - 8 hours under the conditions thus obtained.

The first hour of the initial 2 hours of stabilization was subject to evident fluctuations and was not considered in the discussion of the results.

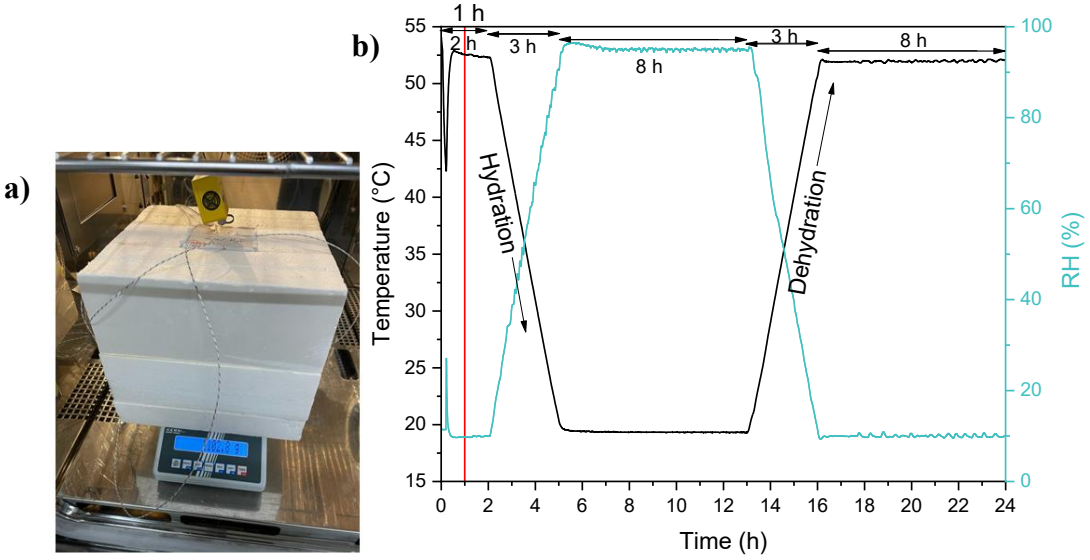

Figure 4.6 a) Picture of the system used for thermal monitoring of the prepared mortar samples; b) 24 h cycle in which the controlled boundary conditions are varied.

4.5. Results and discussion

4.5.1. Characterization of fresh plaster mortar

The consistency of the fresh mortar for all investigated batches was determined by the slump test using the flow table method, in accordance with the UNI EN 1015-3/2007 standard [318]. The resulting spread values provide an indication of the mortar's workability. Higher spread diameters are indicative of a more fluid and workable mortar, while lower values correspond to a less fluid or stiffer mortar. **Table 4.3** reports the average measured spread after 15 jolts on the flow table. For each specimen, the water content (in %wt.) used for mixing the mortar and the theoretical water to lime ratio (w/l ratio), based on the proportion of water and binder contents, were also reported.

Table 4.3 Measured spread for investigated fresh plaster mortars. It has been reported also the corresponding water content used for preparing mortar and the theoretical w/l ratio.

Material code	Water content (%wt.)	Th w/l ratio	Spread (cm)
A0	20	0.80	4.05
A1	21	0.84	3.54
A3	22	0.88	2.09
A5	23	0.92	1.96

It is clear that as the salt content increases, the spread decreases, making the fresh mortar more difficult to work, as it tends to set more quickly. To address this, more water was added to the mixture to facilitate the mortar's workability at increasing CL content. This phenomenon can be explained by the potential capability of CL to retain water, hindering the effect of the cellulose additive. CL seems to absorb the mortar's water more quickly than cellulose. This effectively reduces the water available for the reaction of NHL5, leading to a significant decrease in the actual w/l ratio, which is lower than the theoretical one indicated in **Table 4.3**. This lower w/l ratio significantly affects the workability and mechanical resistance. A low w/l ratio leads to higher density and strength of the mortar. Furthermore, a low w/l ratio makes the mixture more compact and difficult to work, increasing the nominal resistance to both bending and compression. However, considering the application purpose of plaster mortars, high mechanical resistance is not strictly necessary and can negatively impact the mortar's elasticity and its retire. It is more useful to obtain a mortar with greater workability and easier application by the operator. Further research should be directed

towards improving the formulation of mortars with CL, for example, by reducing or eliminating the cellulose content or increasing the water quantity. The use of other additives that can enhance the mixture's workability should also be considered, while taking into account the product's formula cost.

4.5.2. Mechanical characterization of plaster mortars

The mechanical resistance to flexure and compression of the mortar samples prepared according to the UNI EN 1015-11/2007 standard [319], were carried out as described in § **4.4.3** section. The values of flexural (σ_{fs}) and compressive (σ_{cs}) strength after 14 and 28 days of aging, with varying salt content in the mixture, are represented by the histograms in the **Figure 4.7**. Specifically, **Figure 4.7a** refers to the flexural strength, while **Figure 4.7b** refers to the compressive strength. The error bars for each histogram, calculated with the maximum semi-dispersion method, are also reported.

As a general trend, it was observed that the flexural and compressive strengths of all mortar samples increased from 14 to 28 days. This is a typical behavior of lime-based mortar materials as the carbonation reaction progresses [314]. The mortar without CL (blank sample) exhibited the lowest flexural and compressive strengths at both aging periods. In contrast, it is evident that as the salt content increases, both flexural and compressive resistances increase. This suggests that salt enhances strength development over time. To quantify the improvement in flexural and compressive strength, the percentage increase with respect to the blank sample was calculated. The obtained results are reported in **Table 4.4**. These calculations show a substantial increase in mechanical resistance after the addition of CL, particularly for compressive strength at higher concentrations. This behavior can be explained by the lower w/l ratio values, which lead to higher material compaction and an increase in mortar rigidity. Notably, with increasing salt content, an embrittlement of the plaster mortar was observed. A similar behavior is reported in the scientific literature when researchers explored the self-healing potential of CL with bacteria in concrete matrices [306,307].

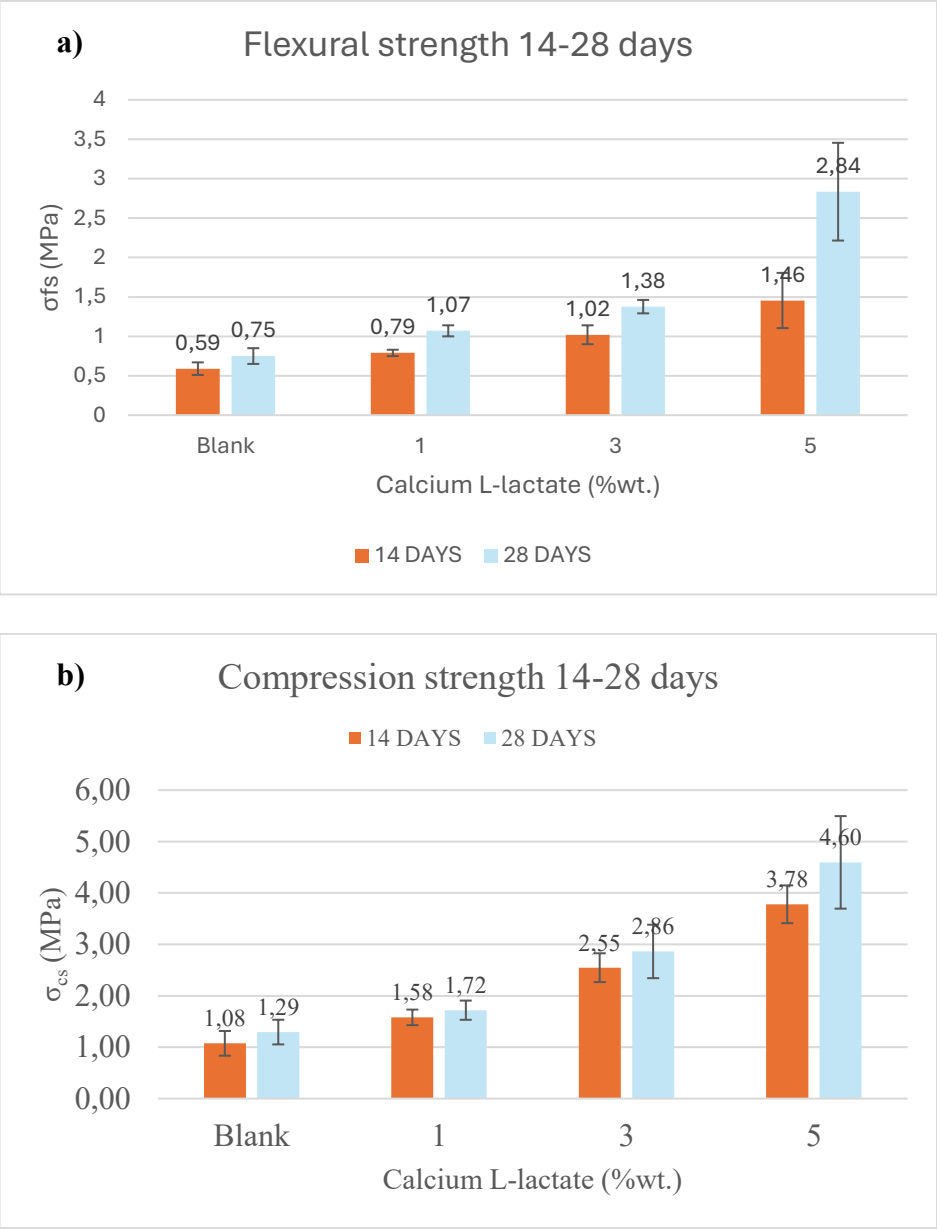

Figure 4.7 Values of flexural (a) and compressive (b) strength after 14 and 28 days of aging, at varying salt content in the mixture.

Table 4.4 Percentage increase in flexural ($\Delta\sigma_{fs}$) and compressive ($\Delta\sigma_{cs}$) strengths of the CL specimens at 14 and 28 days of hardening, calculated with respect to the corresponding values for A0 samples.

Material	$\Delta\sigma_{fs}$(%)		$\Delta\sigma_{cs}$(%)	
	14 days	28 days	14 days	28 days
A1	33.9	36.0	46.3	33.3
A3	81.4	84.0	136.1	106.2
A5	147.5	278.7	250.0	256.6

4.5.3. Physical, structural and morphological characterizations of plaster mortars

The real densities of plaster mortars with varying CL content were determined using a helium pycnometer at 20 °C. Analyses were conducted on mortar blocks approximately 30x25x25 mm^3 in size, after a 28-day curing period. The real densities of the investigated materials are reported in **Table 4.5**. It also lists the bulk density of the mortars, calculated as the ratio between the mass of the mortar blocks and their measured geometric volume. Additionally, %void calculated using Equation (4.1) is reported for each hardened mortar.

Table 4.5 Bulk and real densities of investigate plaster mortars. The percentage of voids (%void) calculated according to Equation (4.1) is also reported.

Material	Bulk Density (kg m^{-3})	Real Density (kg m^{-3})	%void
A0	1423	2688	47.1
A1	1448	2628	44.3
A3	1493	2602	41.1
A5	1549	2596	40.4

The results shown in **Table 4.5** indicate that as the salt content in the mortars increases, the percentage of voids (%void) decreases. This trend can be explained by considering the greater compaction of the mortar as the actual w/l ratio decreases, which is responsible for a lower presence of internal voids in the material. As shown in the case of composite materials with sepiolite (§ **3.4.6** section), the lower presence of voids hinders the water vapor exchange processes with the environment, potentially limiting and/or slowing down the thermochemical ability of the mortar-based composite. The influence of this aspect will be evaluated in the § **4.5.5** section where the prepared mortars are subjected to controlled hydration and dehydration cycles.

Considering the trend of the real densities of the mortars, a slight decrease in the measured densities is observed as the salt content increases. This behavior can be explained by examining the real density of the CL powder added to prepare the mortars with salt. Since the latter is 1505 kg m^{-3} (**Table 2.1**), which is lower than the density of the mortar without salt (2688 kg m^{-3}), a slight decrease in the densities of the specimens occurs as the salt content increases. The values are nonetheless very similar to each other, both due to the low TCM content and the compaction effect of the mortar as the CL content increases. It is important to remember that the real densities

measured by the pycnometer are determined by measuring the volume of the solid specimen examined, thus excluding the internal void volumes of the sample.

For the calculation of the bulk density, on the other hand, the void volumes are taken into account in the measurement of the geometric volume. Bulk density is defined as the mass of a material divided by its total volume. The total volume includes both the volume of the solid materials that make up the mortar (lime, aggregates, ecc.) and the volume of the internal voids. Therefore, if a mortar has a higher percentage of internal voids, it means that a larger portion of its total volume is occupied by "empty space" rather than solid material. Thus, at the same geometric or total volume (the same mold was used for all the specimens), mortars with a higher %void have lower masses and, consequently, also lower bulk densities. This explains the opposite behavior in bulk densities compared to the real densities.

The presence of CL in mortar composites has been demonstrated by XRD and SEM analyses. The diffractograms for CL and the ground mortar materials are presented in **Figure 4.8**. The black pattern indicates that calcium L-lactate pentahydrate (CL) exhibits a crystalline structure, with the phase identified as PDF 00-070-1076 [227]. The retention of these diffraction peaks in the composite materials demonstrates the presence of CL in mortars that include salt (A1, A3 and A5). Moreover, as the salt concentration increases, the peaks corresponding to CL become increasingly distinct. Despite the complexity of plaster mortars and the various chemical reactions that occur during the mixing with water, the integrity of the CL structure is maintained throughout the process. Besides the CL phase, two additional phases have been identified in composite materials containing calcite ($CaCO_3$) and calcium oxide (CaO), which are typical elements of building lime mortars [323]. The phase corresponding to $CaCO_3$ is identified as PDF 00-002-0629 [324], while the phase for CaO is noted as PDF 00-017-0912 [325]. As the salt content rises, the peaks related to the CL phase become increasingly prominent. The peak assignments for the A5 pattern are relevant to all mortars' diffractograms that exhibit the CL phase; however, for the purpose of brevity, they are only mentioned for the sample with the highest salt content. As expected, the XRD profile of A0 shows the same phases present in the other composite materials with the exclusion of CL phase.

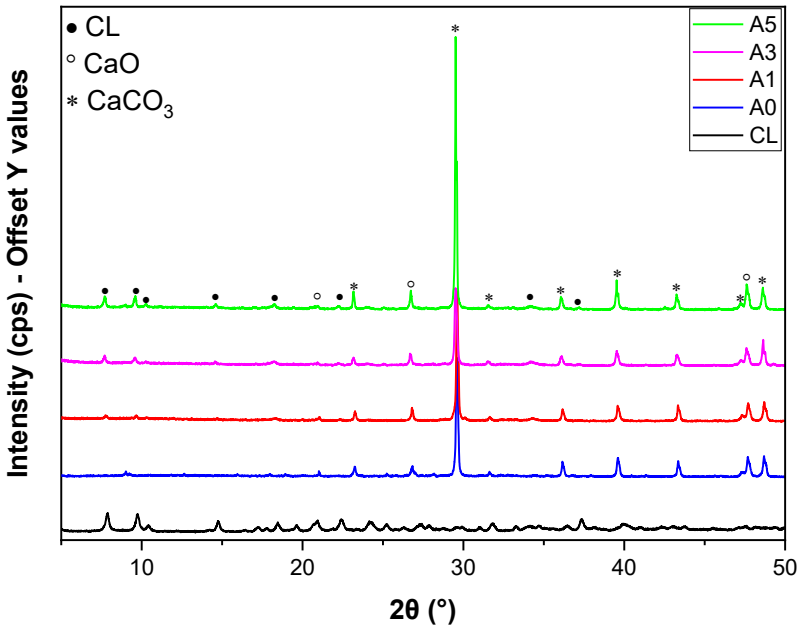

Figure 4.8 Diffractograms of calcium L-lactate pentahydrate (CL) and grinded plaster mortars.

As observed in **Figure 4.3**, the square-based mortar blocks containing CL exhibit the onset of white spots or patches attributed to the efflorescence of the salt used as TCM. In fact, CL has been reported to effloresce when giving off its crystal water at ordinary temperatures [222]. Efflorescence is a phenomenon that can occur in mortars, characterized by the formation of saline deposits on the surface. This process is closely linked to the presence of water and soluble salts within the material. Although, as stated in § **2.1** section, CL has a low solubility in water (50 g dm^{-3} at 20 °C), it remains a hydrated salt with a certain degree of solubility.

The soluble salts present in the mortar dissolve in the water present within. Subsequently, the water containing the dissolved salts migrates to the surface through the capillary network of material. This movement is driven by the evaporation of the surface water. When the water reaches the surface, it evaporates, leaving behind the dissolved salts. These salts, once their concentration exceeds their solubility limit, crystallize, forming the whitish or colored deposits that are visible as efflorescence. In the case of CL, the formation of surface efflorescence has been observed, which constitutes primarily an aesthetic problem [326]. In the case of the application of the studied mortars, i.e., for plasters, the efflorescence could also cause the detachment of the upper coatings applied, such as finishes and paints.

The efflorescence crystals collected from a 5%wt. mortar sample after 2 days of curing (**Figure 4.9a**) were analyzed by XRD analysis (**Figure 4.9b**), allowing the attribution of the formation of these surface salts to CL through comparison with the corresponding PDF [227].

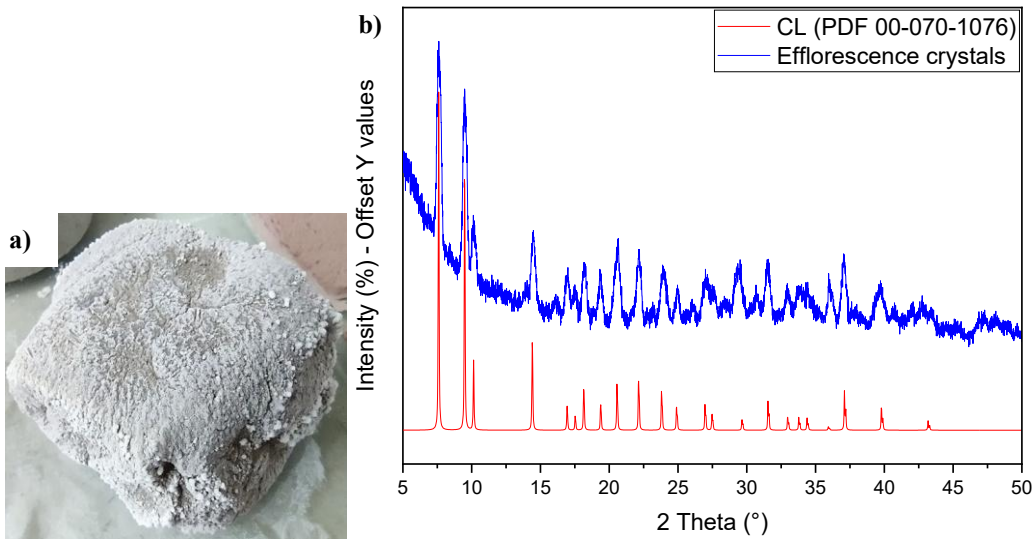

Figure 4.9 a) Formation of superficial efflorescence over an exceed mortar at 5%wt. after 2 days of curing. b) Diffractograms of efflorescence crystals and identified PDF.

The SEM micrographs shown in **Figure 4.10** display the morphologies of grinded mortars with (A1, A3 and A5) and without CL (A0). All micrographs show that mortars exhibit a dense microstructure. At lower magnification, the surface appears irregular due to contemporaneous presence of rough and smooth particles. The harsh morphology is attributed to the calcite phase (CC) [303], while regular surfaces are due to the presence of aluminum silicate (AS) in sand aggregates [327]. At higher magnification this kind of morphology is overall maintained for all investigated samples. CC and AS morphologies are evidenced in **Figure 4.10** with yellow and light blue arrows, respectively. In addition, mortars with salt exhibit the simultaneous presence of fiber-like particles, highlighted in red circles, which are attributed to the CL in re-hydration phase [189]. The presence of these peculiar structures increases as the salt content increases and, in particular, for A5 composite material (**Figure 4.10h**) the fiber-like structures are homogeneously distributed throughout the surface.

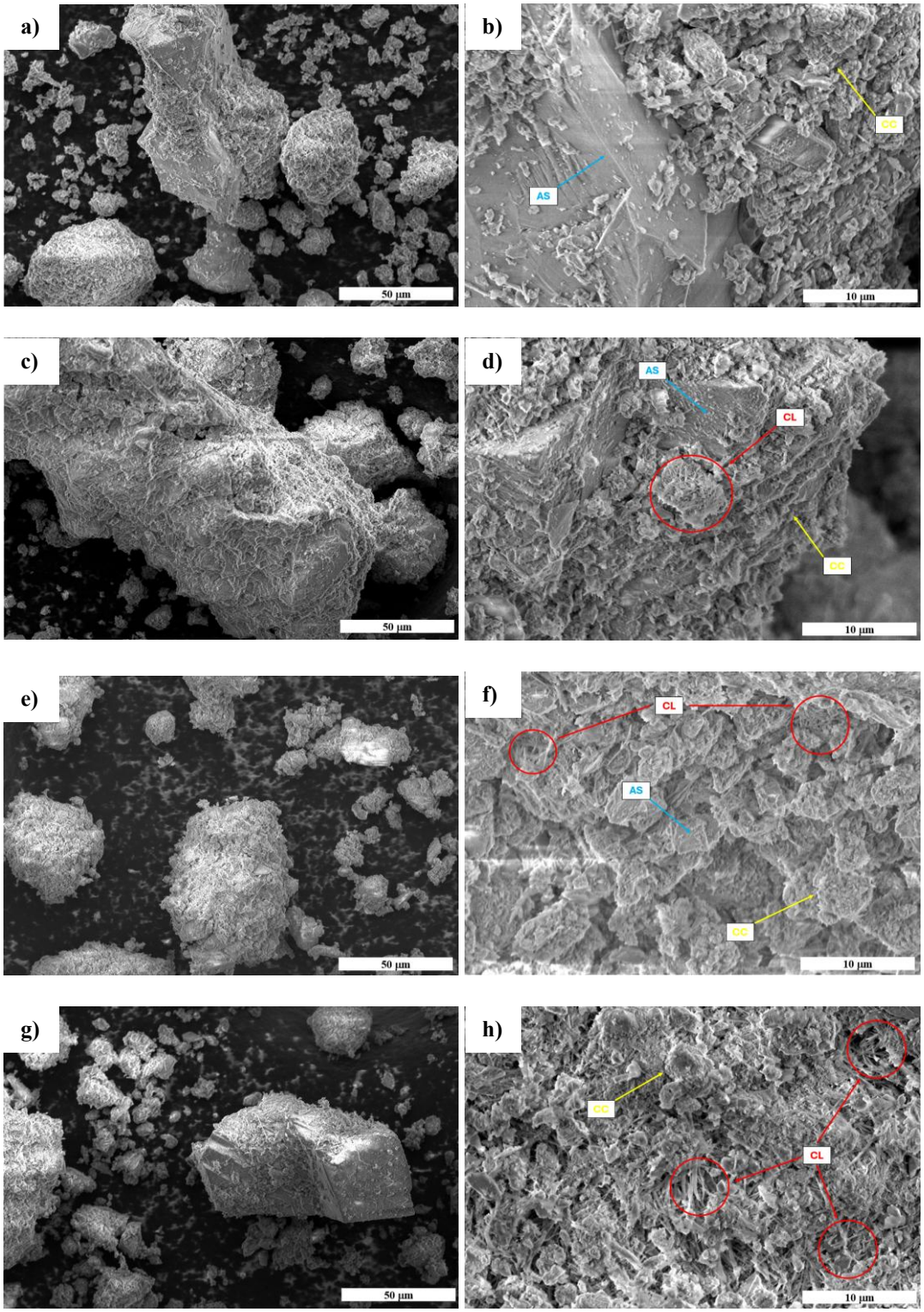

Figure 4.10 SEM micrographs of mortars with (A1, A3 and A5) and without CL (A0). a-b) A0 mortar; c-d) A1 mortar; e-f) A3 mortar; g-h) A5 mortar. Red circles indicate the presence of CL phase. Yellow and light blue arrow indicate the presence of calcite (CC) and aluminum silicate (AS) phases, respectively.

4.5.4. Thermogravimetric dynamic vapor sorption (DVS) analysis

The thermochemical behavior of the synthesized materials throughout hydration and dehydration cycles was assessed via a thermogravimetric dynamic vapor system maintained at isothermal conditions of 30 °C. The chamber's relative humidity varied from 0% to 90%, and the results are shown in **Figure 4.11**. The mass changes illustrated in the graph are linked to the samples' uptake and release of water, which is influenced by the vapor partial pressure in the chamber. The calculation of percentage variation for each sample is based on the corresponding dry weight recorded at the end of the degassing phase. The study highlights a remarkable water absorption potential in mortar composites containing CL, in contrast to materials that do not include salt. This sorption ability can be directly attributed to the presence of CL, since A0 plaster mortar shows minimal sorption, with a mass change of less than 1%. Mortars exhibit an increased sorption capacity as the salt content escalates. In particular, mass variations of 4.7%, 7.5%, and 8.8% were observed for the A1, A3, and A5 composites, respectively, at higher vapor partial pressure. The A5 specimen exhibited only a marginal increase in mass compared to A3, indicating that the hydration process is somewhat impeded by the higher salt concentration. This phenomenon can be attributed to the homogeneous distribution of CL particles within the sample, as depicted in **Figure 4.10h**. In this configuration, salt may obstruct the mortar's porosity, thereby restricting vapor exchange with the environment.

Another significant aspect linked to the presence of CL is the enhancement of hysteresis between the sorption and desorption phases with rising salt concentrations. As discussed in § **2.4.2** section, CL, under identical analytical conditions, displays substantial hysteresis, likely due to a kinetic barrier, as the dehydration reaction is predominantly facilitated at lower partial pressure values [189]. This phenomenon is advantageous for plaster mortar composites, as it extends the duration of the salt energy storage phase under intermediate partial pressure conditions (above approximately 20% of p/p_0), thereby decreasing heat dissipation to the environment.

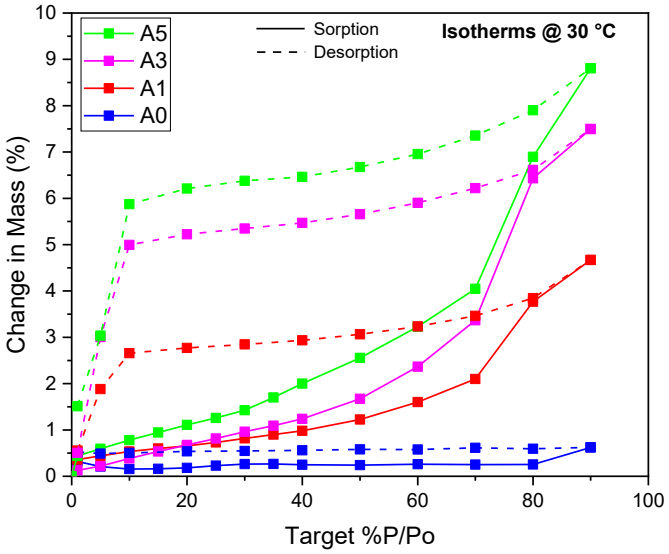

Figure 4.11 Water vapour sorption/desorption isotherms at 30 °C of prepared composite materials.

4.5.5. Thermal monitoring analysis

The thermal behavior of the mortar samples was assessed by subjecting them to thermal cycles, varying temperature and relative humidity (RH) in a climatic chamber over a 24-hour period. The treatment employed is presented in § **4.4.6** section. The mass variation (in percentage), calculated with respect to the dry mass of the investigated mortars at the end of stabilization phase in an oven at 80 °C, is reported in **Figure 4.12**.

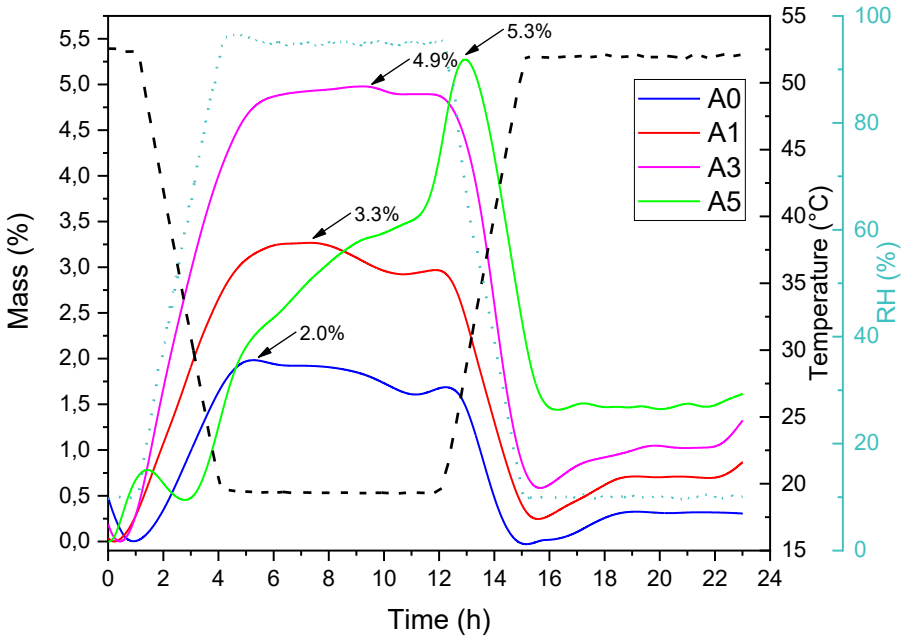

Figure 4.12 Monitoring of specimen mass during a diurnal hydration/dehydration cycle under controlled boundary conditions.

In the initial phase, all samples tend to stabilize their weights in accordance with the environmental conditions, achieving comparable weights at the start of the cooling phase. In the following phase, a significant increase in weight is observed in samples containing salt, due to the increase in humidity. Specifically, samples with salt demonstrate a higher rate of weight variation, and when humidity reaches 95%, they tend to absorb water more swiftly. In other words, as relative humidity increases and temperature decreases, all mortar specimens increase in mass at a higher rate as the salt content increases. The exception is specimen A5 (highest CL content), which reaches its maximum hydration (indicated by arrow with percentage in **Figure 4.12**) at the end of the hydration phase. Conversely, the specimen without salt (A0) reaches its maximum already at the end of the cooling phase. Meanwhile, mortar samples with intermediate amounts of CL reach their maximum hydration at progressively longer times during the 8-hour stabilization phase at the maximum RH condition. This behavior can be explained by considering the %void of the mortars shown in **Table 4.5**. Mortars with higher salt content require longer hydration times because they exhibit lower porosity, which slows the reaction itself, but are able to reach greater mass variation percentages in proportion to the salt content. A similar trend was observed for DVS results (**Figure 4.11**). In fact, here too, the mortars with salt are able to hydrate more than the mortar without salt, and their water release is slower and not entirely complete during the dehydration phase. For example, mortar A0 completely releases its water content at the end of the heating phase, stabilizing its mass variation at a value close to zero. Specimen A5, on the other hand, retains a water content greater than 1.5% of its dry weight at the end of the 8-hour isotherm at the maximum temperature. In general, the hydration percentages observed in DVS were higher than those observed during this monitoring for all mortar samples with CL. However, it should be remembered that the mass that could be analyzed in DVS was ~30 mg, while the mass of the 100x100x20 mm^3 square-based mortar specimens is in the order of 300 g, and therefore more representative of the actual hydration and dehydration processes of the salt in plaster mortar.

Based on the aforementioned observations, specimen A3 demonstrates the most favorable composition among those examined, exhibiting the most rapid hydration and dehydration kinetics under simulated conditions. Moreover, its mass remains relatively

stable during the isotherm, suggesting effective vapor exchange with the environment, which likely corresponds to an efficient energy storage capacity.

The ability of salt-containing mortars to absorb/release vapor is also demonstrated by the thermal monitoring performed on the mortar specimens during the thermo-physical characterization under controlled boundary conditions. To examine the charging and discharging phases, the external and internal surface temperatures of the samples were monitored. Since plaster mortars were designed to improve indoor thermal comfort, only the internal temperature trends are reported here (**Figure 4.13**).

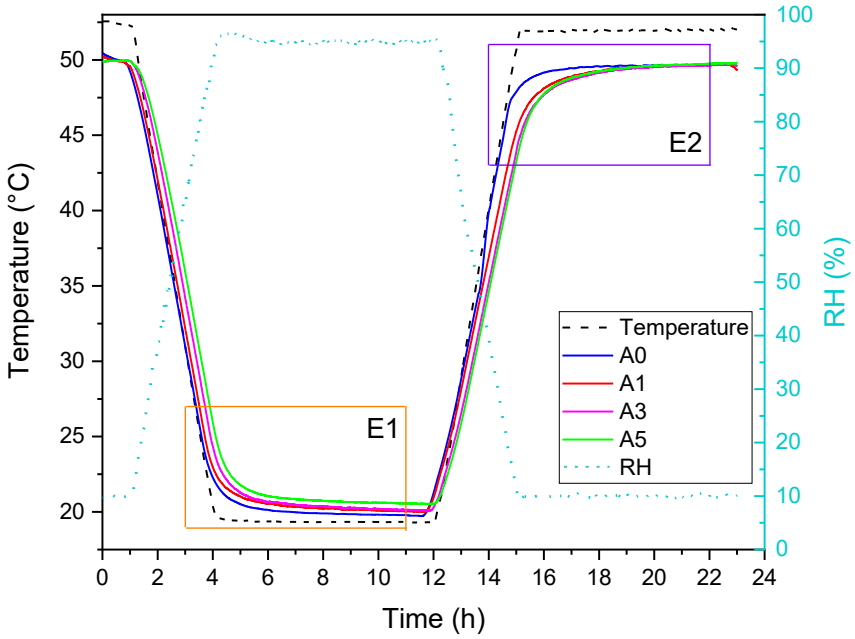

Figure 4.13 Monitoring internal surface temperatures of mortar composites during controlled hydration/dehydration conditions.

Monitoring the internal surface temperatures of the samples during the hydration/dehydration phase transitions revealed that the salt-containing mortars (A1, A3 and A5) experienced a delay in temperature changes compared to the sample without salt (A0). This delay is attributed to the hydration and dehydration processes associated with the presence of CL. Specifically, during the cooling phase shown in **Figure 4.14a**, the exothermic recombination of humidity with the salt contrasts the cooling, allowing the mortars with CL to maintain a higher surface temperature over a longer period. Conversely, during the heating phase depicted in **Figure 4.14b**, the salt undergoes an endothermic dehydration reaction, causing a delay in the increase of surface temperature. Tabulated data showed the temperature difference between the CL-containing mortars and the reference sample (A0) investigated under the same

conditions. The ΔT values were measured at 4 and 15 hours of analysis, corresponding to the end of the cooling and heating transition phases, respectively.

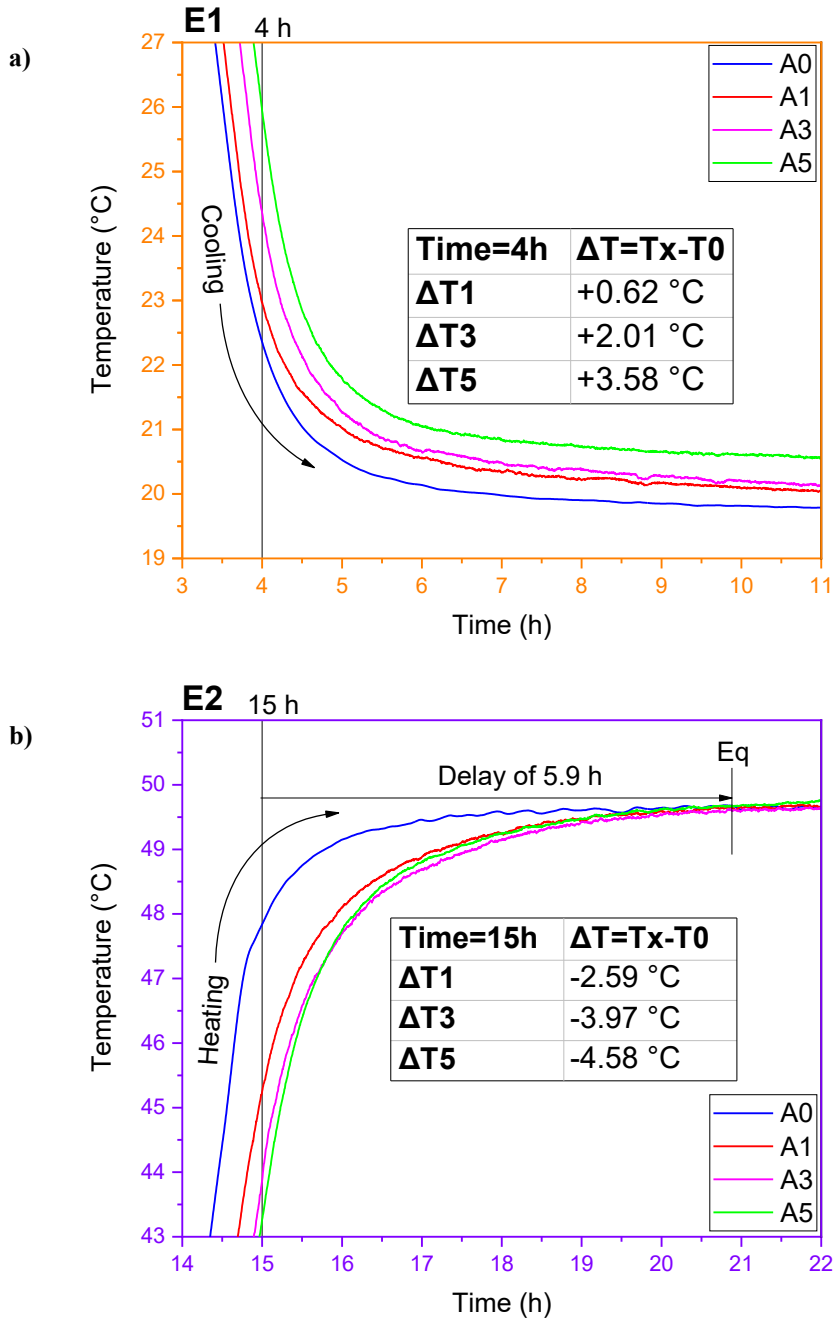

Figure 4.14 a) Enlargement of temperature transitions observed during the heating phase. b) Enlargement of temperature transitions observed during the heating phase.

Essentially, the addition of salt provides mortars with greater thermal inertia, as evidenced by the delay in reaching the same equilibration temperature as the mortar without salt. Although further studies are necessary to assess the reliability of plaster mortar with CL, these results are promising and encourage the use of TCM for enhancing thermal comfort in buildings. Furthermore, the addition of CL to the

investigated materials has demonstrated the potential for energy savings. In fact, a significant delay of approximately 6 hours was observed in the time required for the specimens with salt to reach the equilibrium temperature compared to those without salt (**Figure 4.14b**). This implies that users can delay the activation or usage at higher power of active cooling systems, resulting in substantial energy savings.

4.6. General remarks and future outlooks

This chapter focuses on assessing the effects of a newly studied organic salt hydrate, calcium L-lactate pentahydrate (CL), on the physical characteristics and thermal performance of composite plaster mortars. The aim is to encourage the progress of sustainable solutions in building materials and thermochemical applications. CL has recently been recognized as a thermochemical material, and for the first time, its thermal insulation properties are being utilized to create a mortar that enhances thermal comfort within buildings. The hydration and dehydration processes are crucial as they enable the material to capture heat when water molecules are released and to emit heat during hydration. The production of the mortar composites has been conducted in line with the conventional methods for preparing standard mortars. The workability of fresh mortars and the related issues have been discussed. Mechanical characterization has shown an outstanding improvement of both flexural and compressive strength of mortar composites at increasing salt content, attributed to salt capacity of retain water, thus provoking higher mortar compaction. Considerations on real and bulk densities have been discussed for determining the percentage of voids of hardened mortars, affecting water vapor exchange of studied materials. XRD and SEM analyses confirmed the presence of CL in mortars. The salt presence modifies the diffraction peaks in the samples, which affects their sorption properties. The material's ability to store heat during the release of water molecules and to release heat upon hydration is due to the hydration and dehydration processes. DVS analysis verified the reversibility of these processes, attributing the water uptake solely to the presence of CL. Observations from thermal monitoring demonstrate that mortars that include salt show a delay in their temperature changes. The presence of salt contributes to higher thermal inertia in these mortars, as evidenced by the extended time required to achieve the same equilibrium temperature as mortars lacking salt.

This facile combination of CL and construction materials supports the storage and discharge of solar heat, which enhances thermal comfort in buildings and illustrates the potential of this emerging class of thermochemical composite materials.

However, new strategies must be developed to improve the workability of the mortar, possibly by increasing the TCM content and thus improving mortar efficiency. The efflorescence of the salt must also be limited in order to obtain a homogeneous hardened product and improve its operational efficiency. Strategies may involve the use of inexpensive materials, like sepiolite, to improve the affinity of the hydrated salt with the mortar. An effective evaluation of the costs of the composite mortar, as well as a life cycle analysis of the materials used for its preparation, are useful to validate mortar use as a thermal and environmentally friendly material. Finally, studies have been conducted to evaluate the thermochemical capabilities of salt-containing mortars for diurnal operating cycles. However, more in-depth studies, which therefore require more time, will have to be carried out to evaluate the properties of these mortars for seasonal heat storage applications, where TCMs show improved capacities with respect to traditional TES systems.

Chapter 5 Composite plaster mortars with CL reinforced with basalt fibers

5.1. Basalt fibers for reinforcing mortar composites

As discussed previously, mortar materials are largely used for realizing building envelops. Construction materials, above all concrete, guarantee high affordability, availability, longevity, and exceptional compressive strength and stiffness. However, some characteristics of these materials, such as brittleness, low tensile strength, or susceptibility to humidity, are limiting factors since they can reduce the material's durability and functionality over the time. So, among the different possibilities, in the last years the use of polymer composites with reinforcing fillers has become prevalent in order to enhance the materials performance. Specifically, introducing fibers into mortars has a substantial impact on their mechanical properties, notably enhancing toughness and both compressive and tensile strength [328].

Fiber reinforced mortars (FRMs) incorporate short, discrete fibers into a mortar matrix to enhance its mechanical properties. These fibers, typically made of materials like rock, steel, glass, or polymers, serve to bridge micro-cracks that develop within the mortar under stress. This bridging action is the primary reason for the improved mechanical resistance, particularly in terms of flexural strength. By inhibiting crack propagation, fibers increase the mortar's ability to deform and absorb energy before failure, leading to a more ductile and resilient material. A schematic illustration in **Figure 5.1** shows how the fibers influence the crack propagation. It depicts the bridging action performed by the fibers in the mortar, in comparison to the case of mortars without fibers, both subjected to a bending force. The addition of fibers to mortars modifies their behavior under bending stress, leading to higher deformability of the material before failure. This enhanced performance makes FRMs attractive for various construction applications where improved tensile and flexural behavior is crucial [329,330]. The flexural characteristics of FRMs are determined by multiple factors, including the size of the fibers, the quantity of reinforcement, the distribution of the fibers, and the configuration of the manufacturing setup [331,332]. For instance, concerning short fibers the shape and aspect ratio of the reinforcement are important geometric parameters that affect the ability to resist the initiation and propagation of

cracks in the brittle cementitious matrix. These parameters significantly influence the mechanical strength and the deflection under applied loads. Moreover, this type of fiber offers the additional benefit of being easily formed into a variety of geometric shapes.

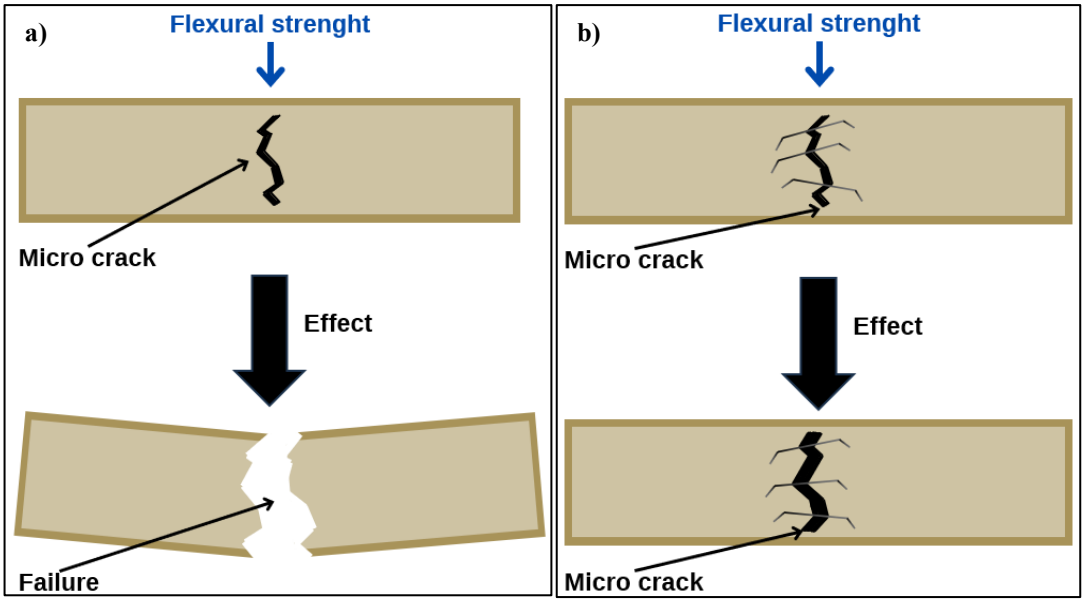

Figure 5.1 a) Effect of bending force on micro cracks present in a mortar. The applied force provokes specimen failure. b) Effect of bending force on micro cracks present in a fiber hooked-end reinforced mortar (FRM). The fibers contain the crack propagation, under the action of the applied force.

In their study, Wu *et al.* [333] explored the effects of three types of short steel fibers straight, corrugated, and hooked-end at different fiber volume contents (0.1%, 2%, and 3%) on the mechanical properties of fiber reinforced concrete. The results demonstrate that the compressive strength of concrete with 3% hooked-end and corrugated fibers increases by 48% and 59%, respectively, compared to that with straight fibers. Furthermore, the incorporation of fibers significantly affected the peak load and deflection. The use of corrugated polymeric short fibers, in contrast to the standard steel fibers, is a crucial factor in ensuring the proper workability of the mortar during the mixing process.

In a recent study, Gullì *et al.* [334] analyzed the effects of hooked-end steel fibers at different content levels on the flexural toughness of fiber-reinforced cement mortars through three-point bending tests. To maintain the workability of the mortar, three low weight fractions (0.3%, 0.5%, and 0.7%) and two cement matrices, M10 and M15 (characterized by a nominal compressive strength of 10 MPa and 15 MPa,

respectively), were considered. The results indicated a substantial increase in the mechanical bending behavior of the mortars with higher fiber content at varying cement matrices. A critical aspect addressed was the variation in flexural toughness with different fiber contents and matrix types. All composite mortars exhibited a toughness index ranging from 10 to 45, highlighting the effective strengthening and toughening influence of the hooked-end fiber addition. In contrast to unreinforced concrete, which typically experiences brittle and unforeseen failures due to the swift and catastrophic development of tensile cracks, the fiber reinforced samples showed a ductile response, retaining significant post-crack resistance even in composite mortars with low amounts of metal fibers.

A further approach, reported by Sanfilippo *et al.* involves using particular treatments with mildly alkaline solutions on the fibers to enhance their performance [335,336]. For instance, treatment with $NaHCO_3$ efficiently eliminates impurities, thereby promoting better crystallinity. More significantly, it greatly enhances the roughness and consistency of the fiber surface. This specialized surface modification leads to improved interfacial bonding with the geopolymer matrix, producing composites with a notable increase in flexural toughness of 82%, which is a crucial attribute for construction materials, in comparison to those reinforced with untreated fibers. Additionally, flexural strength is improved by 53%. So, this not only demonstrates the successful application of $NaHCO_3$ treatment but also its potential to contribute to the advancement of high-performance and more sustainable construction materials.

In fact, over the past few years, the incorporation of natural fibers as reinforcements in composite materials has generated increasing interest as a viable alternative to synthetic fibers. This trend is attributed to their unique properties, cost-effectiveness, health benefits, and recyclability. Flax fiber, specifically, is an economical and easily sourced bast fiber that is widely used as reinforcement in polymer matrix composites for various engineering applications, including those in construction. The most commonly used natural fibres are sisal and flax. However, in recent years, basalt fibers are increasingly being utilized as an innovative reinforcing material for concrete and polymer composites, thanks to their beneficial properties. These include chemical stability, non-toxicity, non-combustibility, high-temperature resistance, and effective thermal and acoustic insulation, along with mechanical characteristics that are superior

to those of glass fibers, that are commonly used [337,338]. For instance, Fiore *et al.* investigated the impact of basalt external layers on the durability characteristics of epoxy composites reinforced with flax. Specifically, the effect of external basalt layers on the mechanical degradation of flax composites in challenging environmental conditions was investigated through long-term aging tests. The study involved measuring water uptake, conducting three-point bending tests, and performing Charpy impact tests on both flax and hybrid flax-basalt laminates. The obtained results showed that as aging progresses, flax laminates show a much higher percentage of water uptake than flax-basalt laminates. In comparison, flax-basalt specimens maintained lower moisture absorption rates than those observed in flax laminates. Moreover, the quasi-static flexural properties of flax-basalt composites are consistently greater than those of flax composites under every aging condition. In addition, flax composites suffer a considerable reduction in performance as aging time extends. Specifically, a comparison between unaged samples and those aged for 60 days reveals a flexural modulus decrease of approximately 16% for flax-basalt composites and 56% for flax composites. Concerning flexural strength, flax composites undergo a 48% variation, while flax-basalt composites only experience a 10% change. Finally, the impact strength of hybrid flax-basalt composites remains relatively stable, whereas flax composites show an increase in energy absorption potential with extended aging periods. Besides, they confirm that incorporating basalt fibers into composites could be a viable strategy for enhancing their mechanical properties and overall durability [339].

This chapter examines the incorporation of basalt fibers into plaster mortars formulations presented in the previous chapter. Composite mortars were designed with basalt fiber content ranging from 0.05 to 0.2%wt. to address the fragility of plaster mortars containing CL. The addition of such rock fibers is expected to improve toughness and thermal insulation at increasing basalt content. The investigation involves mortars with a medium salt concentration (3%wt.), prepared with the addition of basalt fibers. For assessing fibers effect on raw mortar matrix, mortars with fibers (0.2%wt) but without CL were also prepared. Preliminary tests were conducted to investigate the influence of these fibers on mortar workability and their ability to store energy, through residual post-crack resistance processes, during bending experiments. The possibility of storing mechanical energy constitutes a further way by which

investigated composite fiber mortars can store energy, other than thermochemical solution given by salt presence.

The preparation of mortars with basalt fibers, together with their characterization, were carried out during author's research period at Tradimalt Spa laboratory, under the supervision of Eng. Francesco Grungo.

5.2. Materials and methods

5.2.1. Preparation of composite plaster mortars with basalt fibers

For the preparation of fiber reinforced plaster mortars, straight basalt fibers of 13 mm length were employed (**Figure 5.2a**). These fibers are commercial products and were kindly furnished by Tradimalt Spa (Italy). The preparation of plaster mortars with fibers was performed in line with the UNI EN 1015-2/2007 standard [317], following the procedure described in § **4.4.1** section. The dry constituents, including fibers, were combined with water and mixed for one minute in a planetary mixer. Subsequently, if it occurred, 3%wt. of commercial CL powder with respect to solid components, was introduced into the mixture and blended for another minute, until a consistent product was obtained. As previously discussed, it was chosen to evaluate the effect of basalt fibers with respect to NHL5 standard plaster mortars by adding 0.2%wt. of fibers. In addition, the influence of fibers in salt-enhanced mortars was studied by varying fibers content in the range 0.05-0.2%wt. The obtained FRMs have proved a high level of basalt fibers dispersion during mixing procedure, as demonstrated in **Figure 5.2b**, where the tiny "hair" showed are the basalt fibers.

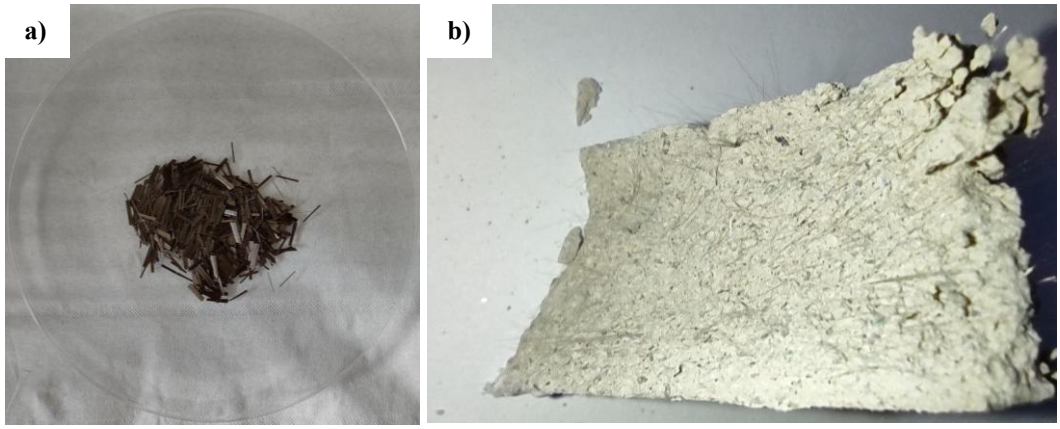

Figure 5.2 a) Commercial straight basalt fibers (13 mm length) used for preparation of reinforced plaster mortars. b) Magnification of broken piece of reinforced mortars at highest basalt fibers content (0.2%wt.).

The materials investigated in this chapter are listed in **Table 5.1** together with relative code and water content used for preparing them. The codes used for fiber reinforced plaster mortars reports the labels used in § **Chapter 4** for indicating CL content (A0 or A3) followed by "_Bxx", where B refers to the presence of basalt fibers while xx indicate their content by weight.

Table 5.1 Codes of all prepared plaster mortar specimens. For each formulation is reported CL, basalt fibers and water contents.

Material	CL content (%wt.)	Basalt fibers content (%wt.)	Water content (%wt.)
A0	0	0	20
A3	3	0	22
A0_B02	0	0.2	23
A3_B005	3	0.05	23
A3_B01	3	0.1	23
A3_B02	3	0.2	23

5.2.2. Characterization of fresh plaster mortar reinforced with basalt fibers

The characterization of investigated RFMs was conducted by slump test using the flow table method, in agreement with the UNI EN 1015-3/2007 standard [318], following the procedure described in § **4.4.2** section.

5.2.3. Mechanical characterizations

For the mechanical characterizations with flexural testing analyses, prismatic 160x40x40 mm^3 samples were prepared and stored for 28 days in agreement with UNI EN 1015-11/2007 standard [319], following the procedure described in § **4.4.3** section. In this case, a universal testing machine (Uniframe250, Controls) equipped with a 250 kN load cell was employed for three-point bending tests. The span length (L) for the analyses was set equal to 100 mm. A load-controlled gradient of 50 N s^{-1} was applied, in agreement to UNI EN 1015-11/2007 standard [319]. Three replicas for each batch were performed.

In addition, the flexural straights (σ_{fs}) of investigated specimens were calculated at different displacements, using the following equation:

$$\sigma_{fs}\ (\text{MPa}) = \frac{3F \cdot L}{2b \cdot h^2} \qquad (5.1)$$

Where F indicate the applied bending force (expressed in N), L is the span length, corresponding to 100 mm, while b and h indicate the width and the height of the beam, respectively, and both are 40 mm.

5.3. Results and discussion

5.3.1. Characterization of fresh plaster mortar reinforced with basalt fibers

For the preparation of plaster mortars reinforced with basalt fibers, it was necessary to increase the water content, compared to the A3 batch, in order to achieve an acceptable workability. Workability was determined by slump test using the flow table method [318]. **Table 5.2** lists the investigated materials along with their water content and spread values. As reported, the workability of mortars with fibers is similar to that of mortars without, at the same CL content. This is due to the strategy of using low fiber amounts to ensure comparable workability [334], validating further characterization analyses.

Table 5.2 Measured spread for investigated fresh plaster mortars reinforced with basalt fibers. It has been reported also the corresponding water content used for preparing mortar.

Material code	Water content (%wt.)	Spread (cm)
A3	22	2.09
A3_B005	23	2.99
A3_B01	23	2.77
A3_B02	23	2.63

5.3.2. Flexural behavior

Figure 5.3 presents typical load-displacement curves for mortars with and without CL, both fiber-reinforced and non-reinforced. For brevity, only one curve per investigated batch is shown, but the behavior is consistent across the three replicates.

The effect of the fibers is evident, as they result in a loss of stiffness and an increase in toughness of the investigated mortars. In fact, the unreinforced mortars exhibit the expected brittle behavior. The specimens display an almost linear elastic response until reaching the maximum load, which is approximately 0.30 kN and 0.61 kN for the A0 and A3 samples, respectively. Beyond this point, a catastrophic fracture of the sample occurs, resulting in a sudden and significant decline in its mechanical performance.

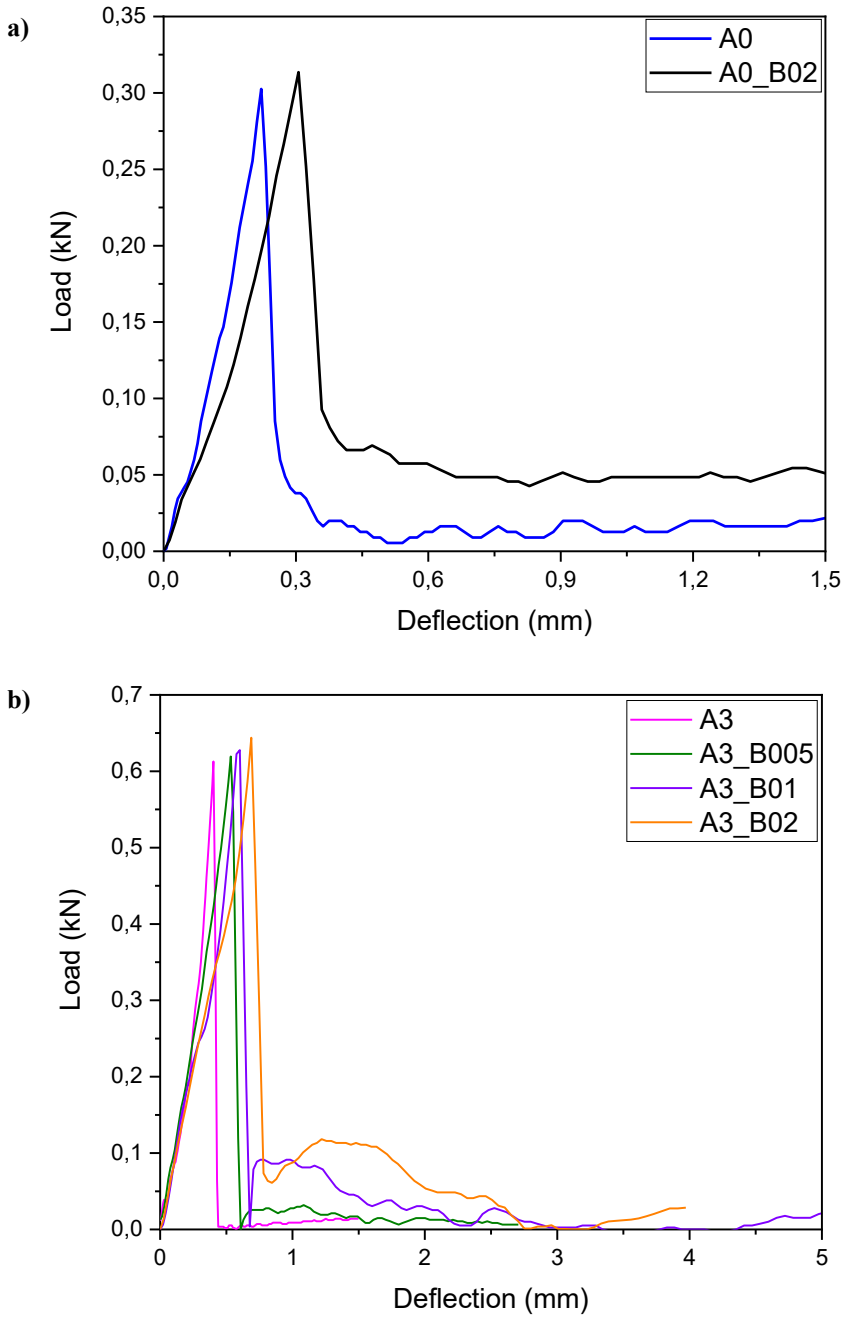

Figure 5.3 Load *vs* displacement curves for (a) mortars without CL and (b) mortars with 3%wt. of CL, under three-point flexural test.

The addition of straight fibers did not significantly modify the pre-cracking stage of the stress-strain curve. A linear behavior was maintained until matrix cracking occurred. However, the incorporation of basalt fibers had a notable impact on the post-cracking stage of the stress-strain response. Specifically, while the unreinforced mortars exhibited a sudden load collapse upon matrix cracking, the fiber-reinforced mortars experienced a progressive recovery of mechanical performance, exhibiting a deflection-hardening behavior. This was characterized by a monotonic increase in load

with increasing deformation, until a local maximum was reached. At this point, micro-cracks formed and evolved, coupled with local sliding at the fiber-matrix interface and fiber pull-out. As more fibers underwent pull-out, the mortar resistance decreased due to this local fiber sliding and pull-out of the remaining strengthening fiber bridges, resulting in a deflection-softening stage. The presence of these extensive energy dissipation mechanisms contributed to a significant increase in the deformation at failure of the reinforced composite mortars. These materials did not exhibit brittle behavior but rather displayed significant residual resistance after crack activation. This behavior can be attributed to the fibers, which provided a bridging effect that increased the energy dissipated during crack propagation. Increasing the fiber content and length has been shown to significantly enhance the bridging action, making it increasingly effective [340]. Furthermore, the fiber content plays a crucial role in improving the residual strength of the specimen. This effect becomes more relevant as the fiber content increases.

From a mechanical perspective, the flexural load-deflection curves observed for FRMs in **Figure 5.3** can be divided into three primary stages, as depicted in **Figure 5.4**: the elastic stage (1), the deflection-hardening stage (2), and the deflection-softening stage (3) [336,340].

1) Elastic stage: in the first stage, at low deflections, the micro-cracks are stable, and no damage propagation phenomena are observed. The load increases almost linearly with increasing deflection until the formation of the first crack in the brittle matrix. This is followed by a local maximum in the load (P_{FP}, point A), which is then followed by a sudden load drop.
2) Deflection-hardening stage: subsequently, as the deflection increases, the load progressively increases, exhibiting a deflection-hardening behavior. The material exhibits the maximum residual load (P_{MP}, point B). During this stage, the micro-cracks, triggered during the previous stage, grow and aggregate, forming a main macro-crack.
3) Deflection-softening stage: once a large macro-crack is formed, a gradual strength reduction with increasing deflection is observed. The deflection-softening stage begins. During this stage, the macro-cracks propagate from the bottom side toward the top side of the beam, leading to a reduction in the strength capacity of the sample.

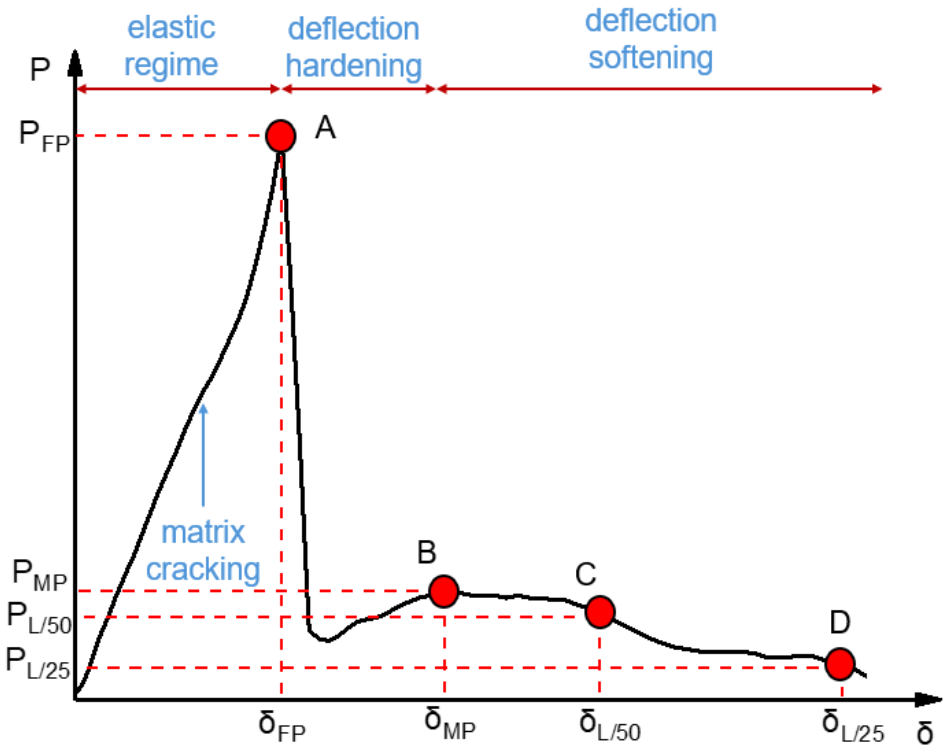

Figure 5.4 Flexural performance parameters on the three-point flexural curve.

As discussed previously, the fiber content has a notable influence on the hardening and softening portions of the load-deflection curve. Instead, to evaluate the toughening effects provided by fiber reinforcement, according to ASTM C1609/C1609M [341], specific reference points along the load decay trend of the load-deflection curve can be identified. Specifically, in this study, the load values at L/50 and L/25 deflection (corresponding to a deflection of 2 mm and 4 mm, respectively) were considered as a reference index of the effective toughening of the mortar (point C and point D in **Figure 5.4**, respectively).

Taking into account the discussion of **Figure 5.4**, **Table 5.3** lists the performance parameters of FRMs with 3%wt. of CL. It was decided to examine the flexural curves of only the salt-enhanced formulations to evaluate the energy storage capacities of the investigated mortars, which are obtained through the combination of thermochemical storage and residual resistance after crack activation (toughness). For this purpose, the toughness was calculated as the area under the load-deflection curve up to the L/50 and L/25 deflections. L indicates the span length of three-point bending system and corresponds to 100 mm. **Table 5.3** summarizes the main flexural performance parameters of the mortars from the three-point flexural test. P_{FP} and δ_{FP} are the first peak load and deflection, respectively, corresponding to point A of the reference curve

in **Figure 5.4**. Similarly, P_{MP} and δ_{MP} are the load and deflection at the maximum peak of the curve, corresponding to point B of the reference curve in **Figure 5.4**. $P_{L/50}$ and $P_{L/25}$ indicate the residual load at the net deflections of L/50 and L/25, respectively. Additionally, the flexural strains (σ_{fs}) calculated using Equation (5.1) for P_{FP} have been reported. The reported data represent the average of the results obtained from the three replicates. The errors, on the other hand, were calculated using the method of maximum semi-dispersion.

Analyzing the reported data, it is evident that the flexural strength of the mortar without fibers, for point A, is aligned with the value shown in **Figure 4.7a**. Additionally, considering the elastic regime of the load-deflection curves, no significant differences are observed with the fiber-free mortar as the fiber content increases. However, an increasing trend is observed in the deflection-hardening stage, where fibers allow for a progressive increase in P_{MP} values. This results in a remarkable increase in toughness, calculated up to $\delta_{L/50}$ and $\delta_{L/25}$, in FRMs as the fiber content increases, as visually illustrated in **Figure 5.5**. The graph depicts the relationship between basalt fiber content and the toughness of mortar composites. The general trend suggests that the addition of basalt fibers enhances the material's ability to absorb energy before failure. Notably, at lower fiber concentrations (0.05%wt.), the toughness values for both $T_{L/50}$ and $T_{L/25}$ are relatively close, indicating that the initial addition of small amounts of basalt fibers has a similar effect on toughness. Nonetheless, as fiber concentration increases (towards 0.1%wt. and 0.2%wt.), a significant divergence in toughness values is observed between the two curves. The $T_{L/25}$ curve shows a much steeper increase in toughness compared to the $T_{L/50}$ curve, implying that the benefits of increasing fiber content are more pronounced under the conditions represented by the $T_{L/25}$ curve.

Table 5.3 Flexural loads, deflections and toughness for all investigated composite mortars.

Composite mortars	P_{FP} (kN)	δ_{FP} (mm)	σ_{FP} (MPa)	P_{MP} (kN)	δ_{MP} (mm)	$P_{L/50}$ (kN)	$P_{L/25}$ (kN)	$T_{L/50}$ (mJ)	$T_{L/25}$ (mJ)
A3	0.62±0.02	0.45±0.06	1.45±0.04	-	-	-	-	-	-
A3_B005	0.63±0.01	0.57±0.04	1.48±0.02	0.041±0.010	1.01±0.07	0.032±0.017	0.011±0.004	208.0±8.6	233.4±27.2
A3_B01	0.66±0.03	0.74±0.11	1.55±0.07	0.107±0.027	1.13±0.23	0.043±0.020	0.022±0.020	323.4±9.7	380.2±58.7
A3_B02	0.66±0.06	0.72±0.06	1.54±0.14	0.183±0.030	1.22±0.05	0.117±0.005	0.025±0.022	434.8±42.7	547.8±69.8

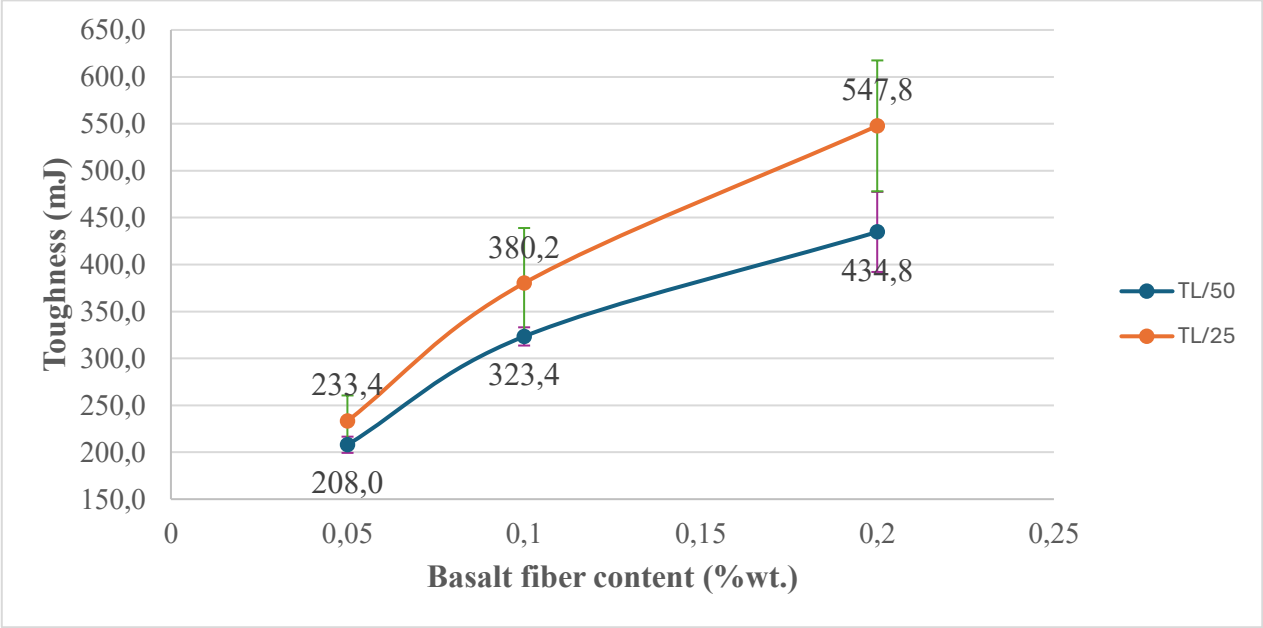

Figure 5.5 Relationship between basalt fiber content and the toughness of mortar composites at specified L/50 and L/25 deflections.

Considering that the ability of a material to store mechanical energy is closely related to its toughness, which represents the amount of energy a material can absorb before fracturing, the effect of fibers in improving the toughness of composite mortars has been demonstrated. Fibers enable the mortar to deform more significantly under load, allowing it to absorb energy that would otherwise be released as a sudden fracture in plain mortar. Additionally, the investigated materials have been designed to store thermochemical energy through the inclusion of a novel organic salt hydrate. Further studies will be conducted to evaluate the storage capacity of composite mortars containing CL, both with and without basalt fibers. Moreover, ongoing investigations are focused on assessing the behavior of fibers during compression tests and their influence on improving the passive thermal insulation of the studied mortars.

In conclusion, the results show that the bending loads and deflections increase with increasing fiber content, due to the enhanced load-carrying capacity of the fibers. This can be attributed to the combined effects of the crack-bridging action provided by the basalt fibers at the crack location, and the improved load-carrying capabilities facilitated by the strong bond strength between the fibers and the mortar matrix.

5.4. General remarks and future outlooks

In this chapter, the influence of the addition of rock fibers to improve the ductility and flexibility of NHL5 mortar matrices with CL was evaluated. In particular, the effect of straight basalt fibers of 13 mm length in mortars without CL and with an intermediate salt content (3%wt.) was analyzed. The aspects investigated were the workability of the mortar through spreading tests, and the mechanical behavior in bending.

The addition of fibers led to mortars requiring a higher amount of water to ensure a homogeneous distribution of the fibers within the mix. This resulted in spreading values that are slightly higher with respect to the corresponding mortar without fibers.

Considering, instead, the load-deflection curves obtained through three-point bending tests, a general trend was observed for the composite mortars with fibers. A first linear range was found for all the specimens investigated, indicating a negligible influence of the fibers in preventing the matrix from breaking. The presence of fibers reduces the stiffness of the prepared mortars, decreasing the slope of the linear range in the elastic regime of the curve. The behavior of mortars with fibers, however, differs

little in terms of flexural strength and mainly with respect to toughness. The fibers first ensure a deflection-hardening stage, resulting in residual resistance after crack activation. Subsequently, a deflection-softening stage occurs, provoking a gradual strength reduction with increasing deflection. During these processes, FRMs can absorb energy that would otherwise be released with fracture. The energy that could be stored depends on the specimens' toughness, and it has been demonstrated that increasing the fiber content progressively increases the toughness.

The investigated composite mortars have been designed to store energy not only through mechanical processes but also through thermochemical reactions by the addition of CL. Further studies will be conducted to investigate the total energy storage capacity, as well as to evaluate the influence of fibers on thermal insulation. Finally, ongoing studies are focused on determining the effect of fibers during compression tests, although it is expected to be more relevant in flexural behavior.

CONCLUSIONS

This thesis has explored the potential of calcium L-Lactate pentahydrate (CL) as a novel thermochemical material (TCM) for low-temperatures applications, with a particular focus on its integration into thermally active mortars with the aim of enhancing building comfort. The research has spanned from the fundamental characterization of CL to the development and testing of composite materials for their application in building systems.

Chapter 1 discusses the state of the art, furnishing the context and the motivation behind research in the field of thermal energy storage (TES). The chapter starts to discuss the growing demand for energy in the building sector and the need for effective solutions to reduce energy consumption, related to well-known environmental issues. The need to improve the energy efficiency of buildings, switch to renewable energy sources and implement innovative design and technology solutions is highlighted. TES technologies are also discussed as a promising solution to improve the energy efficiency of buildings. The chapter provides an overview of different TES technologies, including sensible heat storage (SHS), latent heat storage (LHS) and thermochemical energy storage (TCES). For each technology, the working principles, the materials used, the advantages and disadvantages are described. Besides, the classifications of TCMs and their applications in low-temperatures energy storage are discussed. Finally, the chapter introduces the concept of thermochemical materials and their potential for building applications. In particular, the use of organic salt hydrates, such as calcium L-lactate pentahydrate, is mentioned as promising TCMs for indoor climate control. This innovative class of salt hydrates presents the interesting advantage of being low soluble in water, resulting in a high resistence of deliquescence phenomenon, which is one of the main practical limitations of water sorption materials, in contrast to traditional inorganic salt hydrate.

Chapter 2 demonstrated the promising thermochemical properties of CL, highlighting its thermal and structural stability, and its favorable dehydration/hydration cyclic reversibility. The characterization of CL involved a comprehensive approach using techniques such as X-ray diffraction (XRD) to confirm the reversibility of reactions, from a pentahydrate crystalline structure to an amorphous dehydrated form. Fourier-transform infrared spectroscopy (FTIR) confirmed that the

molecular structure of CL remains unchanged during the dehydration and rehydration processes. Thermogravimetric dynamic vapor sorption (DVS) analysis was used to study the water vapor sorption and desorption behavior of the dehydrated CL. The results from this analysis contributed to the understanding of the material's interaction with water vapor during the hydration process. Furthermore, stability over three cycles has been demonstrated for CL. Thermogravimetric-differential scanning calorimetric (TG-DSC) analyses were used to study salt thermal stability and dehydration process, while scanning electron microscopy (SEM) examined its morphology. These analyses collectively established that CL presents several advantages over traditional inorganic salt hydrates, including a reduced risk of generating harmful by-products and robust performance under a wider range of operating conditions. Notably, CL avoids the deliquescence phenomenon, even at high relative humidity levels, and exhibits no decomposition below 200 °C. The material's heat storage capacity (471 kWh m^{-3}) and operational characteristics make it a compelling alternative for low-temperatures TES applications. This investigation paves the way for a more sustainable approach to indoor climate control.

Chapter 3 focused on enhancing the thermochemical properties of CL by dispersing salt particles onto a porous matrix. Sepiolite, a low-cost and abundant mineral, was shown to be an effective support material, addressed to enhance the hydration and dehydration reactions of CL. Composites with varying CL content were synthesized using DMF for clay dispersion and salt solubilization, demonstrating the viability of the synthetic approach. Characterization through XRD, FTIR, and BET analyses revealed the structural, chemical, and vapor exchange properties of the materials, identifying an optimal composition for promoting salt dispersion and vapor exchange. Thermal stability assessments indicated that while the organic groups of CL in the composites degrade at lower temperatures compared to pure salt, the materials remain stable for low-temperatures thermochemical heat storage. Hydration process investigations under different vapor conditions confirmed that composite at 30%wt. of CL (S-CL30) exhibits the best water vapor absorption capacity, attributed to adequate salt dispersion. Promising results were obtained when comparing the gravimetric release capacity of S-CL30 (298 kWh m^{-3}) with other sepiolite-based composites, and the use of these materials is encouraged due to the organic hydrated salt not exhibiting deliquescence. The low cost and excellent adsorption properties of sepiolite, coupled

with limited existing research, justify its use as a matrix for dispersing TCMs. Furthermore, the presence of sepiolite was found to play a crucial role in improving the hydration kinetics of CL. Sepiolite's high surface area and unique fibrous morphology facilitate water adsorption and distribution, promoting more efficient and complete hydration of the CL salt. This leads to enhanced reversibility of the dehydration/hydration process, which is critical for the long-term performance of the TCMs in TES applications. In conclusion, these findings demonstrate the potential of sepiolite-based composites for TES, providing a pathway to enhance the performance of thermochemical materials. Furthermore, these novel composite materials could be integrated into the building sector, where sepiolite already has various applications.

Chapter 4 and **Chapter 5** detailed the development and characterization of composite plaster mortars incorporating CL, with **Chapter 5** further exploring the reinforcement of these mortars with basalt fibers. **Chapter 4** investigated the impact of incorporating CL into plaster mortars, focusing on the evaluation of their workability, microstructure, and thermal behavior. The addition of CL, in the range 1-5%wt., was found to influence the mortars' workability, with adjustments to the mix design necessary to maintain suitable consistency for application. In terms of mechanical resistance, the addition of CL to the plaster mortars was found to increase both flexural and compressive strength. Specifically, the addition of CL resulted in substantial increases in mechanical resistance, particularly for compressive strength at higher CL concentrations. At 28 days of hardening, mortars with CL demonstrated increases in compressive strength ranging from 33.3% to 256.6% compared to the control samples without CL. XRD analysis revealed that the addition of CL did not significantly alter the crystalline structure of the mortar matrix, as well as that of the salt, while SEM showed that CL particles were well dispersed within the mortar. DVS results provided insights into the water vapor sorption behavior of the mortars, demonstrating the influence of CL on the material's interaction with vapor. Importantly, the controlled thermal monitoring of the mortars under realistic boundary conditions demonstrated that CL incorporation improved the mortars' ability to absorb heat and delayed the time required for specimens to reach thermal equilibrium with their surroundings. Specifically, mortars with CL exhibited temperature differences of approximately 2-4 °C compared to the control mortars during the peak heating and cooling phases in the investigated 24-hour cycle. Furthermore, the time taken for CL-

modified mortars to reach equilibrium temperature in the heating phase was delayed by approximately 6 hours compared to the control sample. This further demonstrates the potential of CL-modified mortars to contribute to energy savings by reducing the rate of heat transfer and improving thermal comfort within buildings. The use of natural hydraulic lime (NHL) as a binder in the mortar was also significant, contributing to the system's high breathability and unique crystalline lattice structure, enhancing its overall performance and compatibility with building applications.

Chapter 5 expanded on this research by examining the effect of basalt fiber reinforcement on the mechanical properties of the CL-modified mortars. The inclusion of basalt fibers (in the range 0.05-0.2%wt.) led to significative improvements in toughness of the composite mortars. Moreover, fibers enhance the material's ability to absorb energy before fracture, leading to a more ductile behavior. The composite mortars aim to store energy through both mechanical and thermochemical reactions. Workability, assessed through spreading tests, showed that fiber addition required more water for homogenous mixing, slightly increasing spreading values. Flexural performance, evaluated via three-point bending tests, revealed that fibers reduced mortar stiffness, with minimal impact on flexural strength. This improvement in mechanical performance, combined with the improved thermal behavior observed in **Chapter 4**, suggests that CL-modified, fiber-reinforced mortars can offer a balance of thermal and structural properties. Such a balance is crucial for their successful application in building systems, where materials must meet both thermal performance and structural integrity requirements.

Overall, this thesis has demonstrated the potential of CL as a viable TCM for low-temperatures applications. The innovative use of CL, both in its pristine form and when integrated with sepiolite and mortars, offers a range of possibilities for enhancing the energy efficiency and thermal comfort of buildings. This thesis has in fact explored the intriguing challenge of advancing the technology readiness level (TRL) from the first (assessment of CL as TCM) to the third stage (preparation of mortars with CL and validation of their core functionality and principles in laboratory tests). The obtained findings contribute to the development of more sustainable building materials and provide a foundation for future research and development in this field.

In fact, this research opens several practical avenues and signifies a considerable step forward for low-temperatures TCES, particularly in the building sector:

- Decarbonization of buildings: by enabling the storage of surplus thermal energy (e.g., from solar thermal collectors or waste heat) at low temperatures, these CL-based composite plaster mortars offer a pathway to reduce reliance on conventional heating/cooling systems, contributing directly to the decarbonization goals of the built environment and reducing operational energy consumption.
- Enhanced building comfort and energy efficiency: the ability of these materials to actively store and release heat allows for improved indoor thermal comfort by smoothing out temperature fluctuations. This dynamic thermal management can significantly decrease peak energy demands and optimize energy usage within residential and commercial buildings.
- Market potential for novel building materials: this work establishes a proof-of-concept for 'smart' building materials that go beyond passive thermal mass. It identifies CL as a viable and non-toxic salt hydrate for this purpose, paving the way for the development of commercially attractive plaster-based products that integrate energy storage functionality directly into building envelopes. The scalable nature of plaster production makes this technology particularly appealing for widespread adoption.
- Utilization of sustainable resources: the use of CL, derived from bio-renewable sources, aligns with principles of circular economy and sustainability in material science, offering an eco-friendly alternative to conventional energy storage materials.

While this thesis provides a robust foundation, several critical next steps are identified to translate these promising results into widespread practical application, opening avenues for future research and development:

- Further investigation into optimizing the performance of CL-based materials is warranted. This includes exploring different composite strategies, optimizing material integration, and enhancing material durability, hygrothermal stability, thermal conductivity, and reaction kinetics.

- Long-term performance evaluations of CL-based materials under repeated dehydration/hydration cycles in realistic operating conditions are crucial. This

will involve assessing their durability, stability, and effectiveness under various environmental conditions.

- Cost-effective implementation methods for CL-based materials need to be developed to facilitate their widespread adoption in the building industry.
- Additional research should focus on improving workability in mortar formulations with CL, while maintaining cost-effectiveness.
- Exploring the combination of CL with other materials and technologies, such as phase change materials (PCMs) and other types of fibers, could lead to the development of multifunctional building materials with enhanced properties.
- Further research is needed to scale up the production of CL-based materials and develop efficient manufacturing processes.
- Life cycle assessments should be conducted to evaluate the environmental impact and sustainability of CL-based materials.
- The integration of CL-based materials with smart building technologies and control systems should be explored to optimize their performance and energy savings.

By addressing these challenges and pursuing these research directions, it will be possible to further advance the development and application of CL-based materials, contributing to the creation of more sustainable, energy-efficient, and comfortable buildings.

DISSEMINATION

Article

Emanuela Mastronardo, Emanuele Previti, Luigi Calabrese, Candida Milone, *Experimental assessment of calcium L-lactate as thermochemical heat storage material*, J Energy Storage 108 (2025) 115065. https://doi.org/10.1016/j.est.2024.115065

Carolina Santini, Emanuele Previti, Emanuela Mastronardo, Luigi Calabrese, Claudia Fabiani, Anna Laura Pisello, *Salt-infused Sorption Mortars for Enhancing Thermal Energy Storage in Building Walls*, Energy Available online 9 June 2025, 137034.
https://doi.org/10.1016/j.energy.2025.137034

Proceedings

Proceedings of the 16th IEA ES TCP International Conference on Energy Storage (ENERSTOCK 2024)

Chair: Kévyn Johannes, INSA Lyon, France

Website: www.enerstock2024.org

Editor: Frédéric Kuznik, INSA Lyon, France

DOI: 10.5281/zenodo.13784976

Published: 18 September 2024

Influence of host matrices on the thermochemical energy storage capacity of novel organic salt hydrate, Emanuele Previti, Juan Manuel Coronado, Emanuela Mastronardo, Candida Milone, Luigi Calabrese, 245-248.

Patent

Emanuela Mastronardo, Emanuele Previti, Luigi Calabrese, Francesco Grungo, Giuseppe Gullì, Riccardo Bertino, *Malta comprendente calcio lattato*, #102022000007862 (2022).

Italian national conferences

IX Workshop nazionale AICIng Chemistry for sustainable materials, Ancona, 16-17/06/2022

Oral contribution: “New Calcium Lactate-SPEEK composite Coatings for Thermal Energy Storage Applications” - Emanuele Previti, Emanuela Mastronardo, Amani Khaskhoussi, Davide Palamara, Luigi Calabrese, Candida Milone

1st Congresso nazionale della Divisione di Chimica per le Tecnologie della Società Chimica Italiana, Napoli, 4-7/09/2022

Oral contribution: “Coatings of Calcium Lactate for Thermal Energy Storage Applications” - Emanuele Previti, Emanuela Mastronardo, Amani Khaskhoussi, Davide Palamara, Luigi Calabrese, Candida Milone

X Workshop nazionale AICIng Materiali e processi sostenibili nell’ambito di un’economia circolare e di una migliore qualità della vita, Perugia, 13-14/06/2024

Oral contribution: “Assessment of matrices influence on thermochemical behavior of novel organic hydrated salt” - Emanuele Previti, Luigi Calabrese, Juan Manuel Coronado, Emanuela Mastronardo, Candida Milone

XXVIII Congresso Nazionale SCI Chimica Elementi di Futuro, Milano, 26-30/08/2024

Oral contribution: “Innovative clay based hybrid materials for thermochemical energy storage applications” - Emanuele Previti, Luigi Calabrese, Juan Manuel Coronado, Emanuela Mastronardo, Candida Milone

International conferences

16th IEA ES TCP International Conference on Energy Storage ENERSTOCK 2024, Lyon (France), 5-7/06/2024

Oral contribution: “Influence of host matrices on the thermochemical energy storage capacity of novel organic salt hydrate” - Emanuele Previti, Juan Manuel Coronado, Emanuela Mastronardo, Candida Milone, Luigi Calabrese

30th SolarPACES Conference Concentrating Solar Power, Thermal, and Chemical Energy Systems, Rome (Italy) 8-11/10/2024

Poster contribution: “Novel Organic Hydrated Salt Based Mortars for Solar Heat Storage” - Emanuele Previti, Claudia Fabiani, Emanuela Mastronardo, Anna Laura Pisello, Carolina Santini, Luigi Calabrese

Summer school

21st Scuola AIMAT I Materiali nella Transizione Energetica, Ischia (Naples, Italy), 13-16/07/2022

Stay

Institute of Catalysis and Petrochemistry (ICP-CSIC) of Madrid (Spain), Supervisor: Dr. Juan Manuel Coronado, 01/03/2023 - 31/08/2023.

REFRENCES

[1] International Energy Agency, World Energy Outlook 2024, Paris, 2024. www.iea.org/terms.

[2] International Energy Agency, World Energy Outlook 2023, Paris, 2023. www.iea.org/terms.

[3] International Energy Agency, World Energy Outlook 2021, Paris, 2021. www.iea.org/weo.

[4] European Parliament, Directive (EU) 2024/1275 of the European Parliament and of the Council of 24 April 2024 on the energy performance of buildings, European Union, 2024. http://data.europa.eu/eli/dir/2024/1275/oj.

[5] Agency for Natural Resources and Energy, The 6th Strategic Energy Plan, Ministry of Economy, Trade and Industry (METI), Japan, 2021. https://www.enecho.meti.go.jp/category/others/basic_plan/pdf/strategic_energy_plan.pdf.

[6] Office of ENERGY EFFICIENCY & RENEWABLE ENERGY, National Definition of a Zero Emissions Building, U.S. DEPARTMENT OF ENERGY (DOE), United States of America, 2024. https://www.energy.gov/eere/buildings/national-definition-zero-emissions-building.

[7] U.S. Energy Information Administration, International Energy Outlook, Washington D.C., 2013. www.eia.gov.

[8] H. Harvey, R. Orvis, J. Rissman, Building Codes and Appliance Standards, in: Designing Climate Solutions, Island Press/Center for Resource Economics, 2018: pp. 201–214. https://doi.org/10.5822/978-1-61091-957-9_11.

[9] A. Ahmed, T. Ge, J. Peng, W.C. Yan, B.T. Tee, S. You, Assessment of the renewable energy generation towards net-zero energy buildings: A review, Energy Build 256 (2022). https://doi.org/10.1016/j.enbuild.2021.111755.

[10] P. Chastas, T. Theodosiou, D. Bikas, Embodied energy in residential buildings-towards the nearly zero energy building: A literature review, Build Environ 105 (2016) 267–282. https://doi.org/10.1016/j.buildenv.2016.05.040.

[11] S. De La Rue Du Can, V. Letschert, M. Mcneil, N. Zhou, J. Sathaye, Residential and Transport Energy Use in India: Past Trend and Future Outlook, 2009.

[12] R. Judkoff, Energy efficient buildings, in: Fundamentals of Materials for Energy and Environmental Sustainability, Cambridge University Press, 2011: pp. 491–508. https://doi.org/10.1017/CBO9780511718786.042.

[13] M. Medrano, J. Brouwer, V. McDonell, J. Mauzey, S. Samuelsen, Integration of distributed generation systems into generic types of commercial buildings in California, Energy Build 40 (2008) 537–548. https://doi.org/10.1016/j.enbuild.2007.04.005.

[14] J. Wang, Z.J. Zhai, Y. Jing, C. Zhang, Influence analysis of building types and climate zones on energetic, economic and environmental performances of BCHP systems, Appl Energy 88 (2011) 3097–3112. https://doi.org/10.1016/j.apenergy.2011.03.016.

[15] H.F. Chinchero, J. Marcos Alonso, A Review on Energy Management Methodologies for LED Lighting Systems in Smart Buildings, in: IEEE, 2020.

[16] F. AlFaris, A. Juaidi, F. Manzano-Agugliaro, Intelligent homes' technologies to optimize the energy performance for the net zero energy home, Energy Build 153 (2017) 262–274. https://doi.org/10.1016/j.enbuild.2017.07.089.

[17] E. Hoxha, T. Jusselme, On the necessity of improving the environmental impacts of furniture and appliances in net-zero energy buildings, Science of the Total Environment 596–597 (2017) 405–416. https://doi.org/10.1016/j.scitotenv.2017.03.107.

[18] I. Oropeza-Perez, P.A. Østergaard, Active and passive cooling methods for dwellings: A review, Renewable and Sustainable Energy Reviews 82 (2018) 531–544. https://doi.org/10.1016/j.rser.2017.09.059.

[19] A. de Gracia, L. Navarro, J. Coma, S. Serrano, J. Romaní, G. Pérez, L.F. Cabeza, Experimental set-up for testing active and passive systems for energy savings in buildings – Lessons learnt, Renewable and Sustainable Energy Reviews 82 (2018) 1014–1026. https://doi.org/10.1016/j.rser.2017.09.109.

[20] G. Cadelano, A. Bortolin, A. della Valle, G. Ferrarini, P. Cattaneo, F. Peron, G. Emmi, Thermal Behavior of a Historic Building Housing Books Across Past and Future Climate Scenarios, Heritage 7 (2024) 6916–6937. https://doi.org/10.3390/heritage7120320.

[21] C. de C. Lucarelli, M.M. Oliveira, J.C. Carlo, Climate-active building enclosures, PARC Pesquisa Em Arquitetura e Construção 14 (2023) e023023. https://doi.org/10.20396/parc.v14i00.8671581.

[22] S. Yuan, M. Grabon, Optimizing energy consumption of a water-loop variable-speed heat pump system, in: Appl Therm Eng, 2011: pp. 894–901. https://doi.org/10.1016/j.applthermaleng.2010.11.012.

[23] J. Krigger, Air-Source Heat Pumps, 2001.

[24] X. Lu, V. Adetola, Z. O'Neill, What are the impacts on the HVAC system when it provides frequency regulation? – A comprehensive case study with a Multi-Zone variable air volume (VAV) system, Energy Build 243 (2021). https://doi.org/10.1016/j.enbuild.2021.110995.

[25] X. Pang, M.A. Piette, N. Zhou, Characterizing variations in variable air volume system controls, Energy Build 135 (2017) 166–175. https://doi.org/10.1016/j.enbuild.2016.11.031.

[26] G.S. Okochi, Y. Yao, A review of recent developments and technological advancements of variable-air-volume (VAV) air-conditioning systems, Renewable and Sustainable Energy Reviews 59 (2016) 784–817. https://doi.org/10.1016/j.rser.2015.12.328.

[27] J. Romaní, G. Pérez, A. de Gracia, Experimental evaluation of a heating radiant wall coupled to a ground source heat pump, Renew Energy 105 (2017) 520–529. https://doi.org/10.1016/j.renene.2016.12.087.

[28] Z. Liu, L. Zhang, G. Gong, T. Han, Experimental evaluation of an active solar thermoelectric radiant wall system, Energy Convers Manag 94 (2015) 253–260. https://doi.org/10.1016/j.enconman.2015.01.077.

[29] C. Karmann, S. Schiavon, F. Bauman, Thermal comfort in buildings using radiant vs. all-air systems: A critical literature review, Build Environ 111 (2017) 123–131. https://doi.org/10.1016/j.buildenv.2016.10.020.

[30] M. González-Torres, L. Pérez-Lombard, J.F. Coronel, I.R. Maestre, D. Yan, A review on buildings energy information: Trends, end-uses, fuels and drivers, Energy Reports 8 (2022) 626–637. https://doi.org/10.1016/j.egyr.2021.11.280.

[31] X. Li, C. Shen, C.W.F. Yu, Building energy efficiency: Passive technology or active technology?, Indoor and Built Environment 26 (2017) 729–732. https://doi.org/10.1177/1420326X17719157.

[32] J. Romaní, G. Pérez, A. de Gracia, Experimental evaluation of a cooling radiant wall coupled to a ground heat exchanger, Energy Build 129 (2016) 484–490. https://doi.org/10.1016/j.enbuild.2016.08.028.

[33] B. Sun, P.B. Luh, Q.S. Jia, Z. Jiang, F. Wang, C. Song, Building energy management: Integrated control of active and passive heating, cooling, lighting, shading, and ventilation systems, IEEE Transactions on Automation Science and Engineering 10 (2013) 588–602. https://doi.org/10.1109/TASE.2012.2205567.

[34] D.K. Bhamare, M.K. Rathod, J. Banerjee, Passive cooling techniques for building and their applicability in different climatic zones—The state of art, Energy Build 198 (2019) 467–490. https://doi.org/10.1016/j.enbuild.2019.06.023.

[35] K. Kujundzic, S. Stamatovic Vuckovic, Principles of passive solar architecture as means of improving health and thermal comfort aspects of indoor environment, in: IOP Conf Ser Earth Environ Sci, Institute of Physics Publishing, 2020. https://doi.org/10.1088/1755-1315/410/1/012101.

[36] G. Gorgolis, D. Karamanis, Solar energy materials for glazing technologies, Solar Energy Materials and Solar Cells 144 (2016) 559–578. https://doi.org/10.1016/j.solmat.2015.09.040.

[37] N. Kumar Garg, PASSIVE OPTIONS FOR THERMAL COMFORT IN BUILDING ENVELOPES-AN ASSESSMENT, Solar Energy 47 (1991) 437–441.

[38] Z. Jiang, T. Kobayashi, T. Yamanaka, M. Sandberg, A literature review of cross ventilation in buildings, Energy Build 291 (2023). https://doi.org/10.1016/j.enbuild.2023.113143.

[39] S. Verbeke, A. Audenaert, Thermal inertia in buildings: A review of impacts across climate and building use, Renewable and Sustainable Energy Reviews 82 (2018) 2300–2318. https://doi.org/10.1016/j.rser.2017.08.083.

[40] L. Navarro, A. de Gracia, D. Niall, A. Castell, M. Browne, S.J. McCormack, P. Griffiths, L.F. Cabeza, Thermal energy storage in building integrated thermal systems: A review. Part 2. Integration as passive system, Renew Energy 85 (2016) 1334–1356. https://doi.org/10.1016/j.renene.2015.06.064.

[41] P.A.J. Donkers, L.C. Sögütoglu, H.P. Huinink, H.R. Fischer, O.C.G. Adan, A review of salt hydrates for seasonal heat storage in domestic applications, Appl Energy 199 (2017) 45–68. https://doi.org/10.1016/j.apenergy.2017.04.080.

[42] A. De Gracia, L.F. Cabeza, Phase change materials and thermal energy storage for buildings, Energy Build 103 (2015) 414–419. https://doi.org/10.1016/j.enbuild.2015.06.007.

[43] S.A. Memon, Phase change materials integrated in building walls: A state of the art review, Renewable and Sustainable Energy Reviews 31 (2014) 870–906. https://doi.org/10.1016/j.rser.2013.12.042.

[44] D.W. Hawes, D. Feldman, D. Banu, Latent heat storage in building materials Objectives of research in thermal storage building materials, 1993.

[45] A.S. Hariri, I.C. Ward, A Review of Thermal Storage Systems Used in Building Applications, 1988.

[46] IEA-ETSAP and IRENA ©, Technology Brief E17-Thermal Energy Storage ENERGY TECHNOLOGY SYSTEMS ANALYSIS PROGRAMME, 2013. www.etsap.org-www.irena.org.

[47] I. Sarbu, C. Sebarchievici, A comprehensive review of thermal energy storage, Sustainability (Switzerland) 10 (2018). https://doi.org/10.3390/su10010191.

[48] P. Arévalo, D. Ochoa-Correa, E. Villa-Ávila, Advances in Thermal Energy Storage Systems for Renewable Energy: A Review of Recent Developments, Processes 12 (2024) 1844. https://doi.org/10.3390/pr12091844.

[49] I. Dinçer, Marc. Rosen, Thermal energy storage : systems and applications, Wiley, 2011.

[50] C.B. Beggs, Ice thermal storage: Impact on United Kingdom carbon dioxide emissions, Building Services Engineering Research & Technology 15 (1994) 11–17.

[51] M. Yamaha, S. Misaki, The evaluation of peak shaving by a thermal storage system using phase-change materials in air distribution systems, HVAC and R Research 12 (2006) 861–869. https://doi.org/10.1080/10789669.2006.10391213.

[52] G. Sadeghi, Energy storage on demand: Thermal energy storage development, materials, design, and integration challenges, Energy Storage Mater 46 (2022) 192–222. https://doi.org/10.1016/j.ensm.2022.01.017.

[53] L. Miró, M.E. Navarro, P. Suresh, A. Gil, A.I. Fernández, L.F. Cabeza, Experimental characterization of a solid industrial by-product as material for high temperature sensible thermal energy storage (TES), Appl Energy 113 (2014) 1261–1268. https://doi.org/10.1016/j.apenergy.2013.08.082.

[54] Y. Tian, C.Y. Zhao, A review of solar collectors and thermal energy storage in solar thermal applications, Appl Energy 104 (2013) 538–553. https://doi.org/10.1016/j.apenergy.2012.11.051.

[55] I. Dincer, S. Dost, X. Li, PERFORMANCE ANALYSES OF SENSIBLE HEAT STORAGE SYSTEMS FOR THERMAL APPLICATIONS, Int J Energy Res 21 (1997) 1157–1171.

[56] G. Alva, Y. Lin, G. Fang, An overview of thermal energy storage systems, Energy 144 (2018) 341–378. https://doi.org/10.1016/j.energy.2017.12.037.

[57] L.F. Cabeza, A. Castell, C. Barreneche, A. De Gracia, A.I. Fernández, Materials used as PCM in thermal energy storage in buildings: A review, Renewable and Sustainable Energy Reviews 15 (2011) 1675–1695. https://doi.org/10.1016/j.rser.2010.11.018.

[58] A. Sharma, V. V. Tyagi, C.R. Chen, D. Buddhi, Review on thermal energy storage with phase change materials and applications, Renewable and Sustainable Energy Reviews 13 (2009) 318–345. https://doi.org/10.1016/j.rser.2007.10.005.

[59] Y. Portilla Nieto, Design and development of mixed metal oxides for high temperature thermochemical energy storage in active thermal barrier coating applications, Ph. D. Thesis, University of the Basque Country, 2022.

[60] C. Milone, Y. Kato, E. Mastronardo, Thermal energy storage with chemical reactions, in: Green Energy and Technology, Springer Verlag, 2018: pp. 15–32. https://doi.org/10.1007/978-3-319-96640-3_3.

[61] A. Solé, I. Martorell, L.F. Cabeza, State of the art on gas-solid thermochemical energy storage systems and reactors for building applications, Renewable and Sustainable Energy Reviews 47 (2015) 386–398. https://doi.org/10.1016/j.rser.2015.03.077.

[62] K.E. N'Tsoukpoe, H. Liu, N. Le Pierrès, L. Luo, A review on long-term sorption solar energy storage, Renewable and Sustainable Energy Reviews 13 (2009) 2385–2396. https://doi.org/10.1016/j.rser.2009.05.008.

[63] L. Pompei, F. Nardecchia, A. Miliozzi, Current, Projected Performance and Costs of Thermal Energy Storage, Processes 11 (2023). https://doi.org/10.3390/pr11030729.

[64] M.K.A. Sharif, A.A. Al-Abidi, S. Mat, K. Sopian, M.H. Ruslan, M.Y. Sulaiman, M.A.M. Rosli, Review of the application of phase change material for heating and domestic hot water systems, Renewable and Sustainable Energy Reviews 42 (2015) 557–568. https://doi.org/10.1016/j.rser.2014.09.034.

[65] Z. Wang, J. Wu, D. Lei, H. Liu, J. Li, Z. Wu, Experimental study on latent thermal energy storage system with gradient porosity copper foam for mid-temperature solar energy application, Appl Energy 261 (2020). https://doi.org/10.1016/j.apenergy.2019.114472.

[66] A.M. Pantaleo, S. Trevisan, F. Matteucci, L.F. Cabeza, Innovation trends on high-temperature thermal energy storage to defossilize energy systems, J Energy Storage 103 (2024) 114261. https://doi.org/10.1016/j.est.2024.114261.

[67] A.S. Garrigós, Phase change materials characterization (PCM) and thermochemical materials (TCM) development and characterization towards reactor design for thermal energy storage, University of Lleida, 2015. http://hdl.handle.net/10803/326741.

[68] R.N. Fisher, MULTISCALE ANALYSIS OF LOW-TEMPERATURE THERMOCHEMICAL ENERGY STORAGE WITH COMPOSITE MATERIALS, University of Birmingham, 2022.

[69] T. Chekifi, M. Boukraa, CFD applications for sensible heat storage: A comprehensive review of numerical studies, J Energy Storage 68 (2023). https://doi.org/10.1016/j.est.2023.107893.

[70] G. Li, Sensible heat thermal storage energy and exergy performance evaluations, Renewable and Sustainable Energy Reviews 53 (2016) 897–923. https://doi.org/10.1016/j.rser.2015.09.006.

[71] IEA, Thermal energy storage for solar and low energy buildings, 2005.

[72] G. Caputo, A. Giaconia, I. Balog, G. Canneto, C. Felici, Stoccaggio termico a calore sensibile a sali fusi a singolo serbatoio (termoclino), 2019.

[73] I. Dincer, S. Dost, A perspective on thermal energy storage systems for solar energy applications, Int J Energy Res 20 (1996) 547–557. https://doi.org/10.1002/(SICI)1099-114X(199606)20:6<547::AID-ER173>3.0.CO;2-S.

[74] S. Riahi, M. Liu, R. Jacob, M. Belusko, F. Bruno, Melt path formation in a high temperature molten salt horizontal shell and tube storage system for CSP plants, in: AIP Conf Proc, American Institute of Physics Inc., 2020. https://doi.org/10.1063/5.0028627.

[75] J.M. Kurley, P.W. Halstenberg, A. McAlister, S. Raiman, S. Dai, R.T. Mayes, Enabling chloride salts for thermal energy storage: Implications of salt purity, RSC Adv 9 (2019) 25602–25608. https://doi.org/10.1039/c9ra03133b.

[76] R.W. Mar, The Application of Molten Salts to Solar Large Power Systems*, ECS Proceedings Volumes 1981–9 (1981) 473–484. https://doi.org/10.1149/198109.0473pv.

[77] V. Basecq, G. Michaux, C. Inard, P. Blondeau, Short-term storage systems of thermal energy for buildings: a review, Advances in Building Energy Research 7 (2013) 66–119. https://doi.org/10.1080/17512549.2013.809271.

[78] L. Navarro, A. de Gracia, S. Colclough, M. Browne, S.J. McCormack, P. Griffiths, L.F. Cabeza, Thermal energy storage in building integrated thermal systems: A review. Part 1. active storage systems, Renew Energy 88 (2016) 526–547. https://doi.org/10.1016/j.renene.2015.11.040.

[79] P.D. van Schalkwyk, J.A.A. Engelbrecht, M.J. Booysen, Thermal Stratification and Temperature Variation in Horizontal Electric Water Heaters: A Characterisation Platform†, Energies (Basel) 15 (2022). https://doi.org/10.3390/en15082840.

[80] T. Benakopoulos, W. Vergo, M. Tunzi, R. Salenbien, S. Svendsen, Overview of solutions for the low-temperature operation of domestic hot-water systems with a circulation loop, Energies (Basel) 14 (2021). https://doi.org/10.3390/en14113350.

[81] R. Mabrouk, H. Naji, A.C. Benim, H. Dhahri, A State of the Art Review on Sensible and Latent Heat Thermal Energy Storage Processes in Porous Media: Mesoscopic Simulation, Applied Sciences (Switzerland) 12 (2022). https://doi.org/10.3390/app12146995.

[82] Mohammad Arif Kamal, The Study of Thermal Mass as a Passive Design Technique for Building Comfort and Energy Efficiency, Journal of Civil Engineering and Architecture 5 (2011). https://doi.org/10.17265/1934-7359/2011.01.009.

[83] S. Burgess, X. Wang, A. Rahbari, M. Hangi, Optimisation of a portable phase-change material (PCM) storage system for emerging cold-chain delivery applications, J Energy Storage 52 (2022). https://doi.org/10.1016/j.est.2022.104855.

[84] B. Nie, J. Chen, Z. Du, Y. Li, T. Zhang, L. Cong, B. Zou, Y. Ding, Thermal performance enhancement of a phase change material (PCM) based portable box for cold chain applications, J Energy Storage 40 (2021). https://doi.org/10.1016/j.est.2021.102707.

[85] J. Jaguemont, N. Omar, P. Van den Bossche, J. Mierlo, Phase-change materials (PCM) for automotive applications: A review, Appl Therm Eng 132 (2018) 308–320. https://doi.org/10.1016/j.applthermaleng.2017.12.097.

[86] Y. Kou, K. Sun, J. Luo, F. Zhou, H. Huang, Z.S. Wu, Q. Shi, An intrinsically flexible phase change film for wearable thermal managements, Energy Storage Mater 34 (2021) 508–514. https://doi.org/10.1016/j.ensm.2020.10.014.

[87] J. Shi, W. Aftab, Z. Liang, K. Yuan, M. Maqbool, H. Jiang, F. Xiong, M. Qin, S. Gao, R. Zou, Tuning the flexibility and thermal storage capacity of solid-solid phase change materials

towards wearable applications, J Mater Chem A Mater 8 (2020) 20133–20140. https://doi.org/10.1039/c9ta13925g.

[88] F. Souayfane, F. Fardoun, P.H. Biwole, Phase change materials (PCM) for cooling applications in buildings: A review, Energy Build 129 (2016) 396–431. https://doi.org/10.1016/j.enbuild.2016.04.006.

[89] A.M. Khudhair, M.M. Farid, A review on energy conservation in building applications with thermal storage by latent heat using phase change materials, Energy Convers Manag 45 (2004) 263–275. https://doi.org/10.1016/S0196-8904(03)00131-6.

[90] Y. Li, N. Nord, Q. Xiao, T. Tereshchenko, Building heating applications with phase change material: A comprehensive review, J Energy Storage 31 (2020). https://doi.org/10.1016/j.est.2020.101634.

[91] K. Merlin, J. Soto, D. Delaunay, L. Traonvouez, Industrial waste heat recovery using an enhanced conductivity latent heat thermal energy storage, Appl Energy 183 (2016) 491–503. https://doi.org/10.1016/j.apenergy.2016.09.007.

[92] D.S. Jayathunga, H.P. Karunathilake, M. Narayana, S. Witharana, Phase change material (PCM) candidates for latent heat thermal energy storage (LHTES) in concentrated solar power (CSP) based thermal applications - A review, Renewable and Sustainable Energy Reviews 189 (2024). https://doi.org/10.1016/j.rser.2023.113904.

[93] P. Royo, L. Acevedo, V.J. Ferreira, T. García-Armingol, A.M. López-Sabirón, G. Ferreira, High-temperature PCM-based thermal energy storage for industrial furnaces installed in energy-intensive industries, Energy 173 (2019) 1030–1040. https://doi.org/10.1016/j.energy.2019.02.118.

[94] J.C. Gomez, High-Temperature Phase Change Materials (PCM) Candidates for Thermal Energy Storage (TES) Applications, 2011. http://www.osti.gov/bridge.

[95] M.Y. Abdelsalam, H.M. Teamah, M.F. Lightstone, J.S. Cotton, Hybrid thermal energy storage with phase change materials for solar domestic hot water applications: Direct versus indirect heat exchange systems, Renew Energy 147 (2020) 77–88. https://doi.org/10.1016/j.renene.2019.08.121.

[96] Y. Yuan, N. Zhang, W. Tao, X. Cao, Y. He, Fatty acids as phase change materials: A review, Renewable and Sustainable Energy Reviews 29 (2014) 482–498. https://doi.org/10.1016/j.rser.2013.08.107.

[97] A. Solé, H. Neumann, S. Niedermaier, I. Martorell, P. Schossig, L.F. Cabeza, Stability of sugar alcohols as PCM for thermal energy storage, Solar Energy Materials and Solar Cells 126 (2014) 125–134. https://doi.org/10.1016/j.solmat.2014.03.020.

[98] R. Raud, R. Jacob, F. Bruno, G. Will, T.A. Steinberg, A critical review of eutectic salt property prediction for latent heat energy storage systems, Renewable and Sustainable Energy Reviews 70 (2017) 936–944. https://doi.org/10.1016/j.rser.2016.11.274.

[99] R.A. Mitran, S. Ioniţă, D. Lincu, D. Berger, C. Matei, A Review of Composite Phase Change Materials Based on Porous Silica Nanomaterials for Latent Heat Storage Applications, Molecules 26 (2021). https://doi.org/10.3390/MOLECULES26010241.

[100] Y. Özonur, M. Mazman, H.Ö. Paksoy, H. Evliya, Microencapsulation of coco fatty acid mixture for thermal energy storage with phase change material, Int J Energy Res 30 (2006) 741–749. https://doi.org/10.1002/er.1177.

[101] C.Y. Zhao, G.H. Zhang, Review on microencapsulated phase change materials (MEPCMs): Fabrication, characterization and applications, Renewable and Sustainable Energy Reviews 15 (2011) 3813–3832. https://doi.org/10.1016/j.rser.2011.07.019.

[102] Y. Konuklu, M. Ostry, H.O. Paksoy, P. Charvat, Review on using microencapsulated phase change materials (PCM) in building applications, Energy Build 106 (2015) 134–155. https://doi.org/10.1016/j.enbuild.2015.07.019.

[103] B.K. Choure, T. Alam, R. Kumar, A review on heat transfer enhancement techniques for PCM based thermal energy storage system, J Energy Storage 72 (2023). https://doi.org/10.1016/j.est.2023.108161.

[104] X. Chen, P. Cheng, Z. Tang, X. Xu, H. Gao, G. Wang, Carbon-Based Composite Phase Change Materials for Thermal Energy Storage, Transfer, and Conversion, Advanced Science 8 (2021). https://doi.org/10.1002/advs.202001274.

[105] J. Wang, H. Xie, Z. Xin, Y. Li, L. Chen, Enhancing thermal conductivity of palmitic acid based phase change materials with carbon nanotubes as fillers, Solar Energy 84 (2010) 339–344. https://doi.org/10.1016/j.solener.2009.12.004.

[106] J. Wu, Y. Feng, C. Liu, H. Li, Heat transfer characteristics of an expanded graphite/paraffin PCM-heat exchanger used in an instantaneous heat pump water heater, Appl Therm Eng 142 (2018) 644–655. https://doi.org/10.1016/j.applthermaleng.2018.06.087.

[107] C.Y. Zhao, W. Lu, Y. Tian, Heat transfer enhancement for thermal energy storage using metal foams embedded within phase change materials (PCMs), Solar Energy 84 (2010) 1402–1412. https://doi.org/10.1016/j.solener.2010.04.022.

[108] J.M. Mahdi, E.C. Nsofor, Melting enhancement in triplex-tube latent heat energy storage system using nanoparticles-metal foam combination, Appl Energy 191 (2017) 22–34. https://doi.org/10.1016/j.apenergy.2016.11.036.

[109] N. Beaupere, U. Soupremanien, L. Zalewski, Nucleation triggering methods in supercooled phase change materials (PCM), a review, Thermochim Acta 670 (2018) 184–201. https://doi.org/10.1016/j.tca.2018.10.009.

[110] P. Sittisart, M.M. Farid, Fire retardants for phase change materials, Appl Energy 88 (2011) 3140–3145. https://doi.org/10.1016/j.apenergy.2011.02.005.

[111] X. Chen, Z. Tang, Y. Chang, H. Gao, P. Cheng, Z. Tao, J. Lv, Toward Tailoring Chemistry of Silica-Based Phase Change Materials for Thermal Energy Storage, IScience 23 (2020) 101606–101637. https://doi.org/10.1016/j.isci.

[112] W. Wang, C. Wang, W. Li, X. Fan, Z. Wu, J. Zheng, X. Li, Novel phase change behavior of n-eicosane in nanoporous silica: Emulsion template preparation and structure characterization using small angle X-ray scattering, Physical Chemistry Chemical Physics 15 (2013) 14390–14395. https://doi.org/10.1039/c3cp51875b.

[113] C. Matei, L. Buhălţeanu, D. Berger, R.A. Mitran, Functionalized mesoporous silica as matrix for shape-stabilized phase change materials, Int J Heat Mass Transf 144 (2019). https://doi.org/10.1016/j.ijheatmasstransfer.2019.118699.

[114] H. Liu, J. Niu, X. Wang, D. Wu, Design and construction of mesoporous silica/n-eicosane phase-change nanocomposites for supercooling depression and heat transfer enhancement, Energy 188 (2019). https://doi.org/10.1016/j.energy.2019.116075.

[115] Y. Li, Q. Liu, Y. Liu, D. Wang, W. Song, Y. Chen, J. Liu, Calcium chloride hexahydrate/nano-SiO2 composites as form-stable phase change materials for building energy conversation: The influence of pore size of nano-SiO2, Energy Build 208 (2020). https://doi.org/10.1016/j.enbuild.2019.109672.

[116] M. Telkes, Thermal energy storage, in: Workshop on Solar Energy Storage Subsystems for the Heating and Cooling of Buildings, Charlottesville, 1975.

[117] G.A. Lane, Solar heat storage : latent heat materials, Volume II Technology, CRC Press, 1986.

[118] D. Zhou, C.Y. Zhao, Y. Tian, Review on thermal energy storage with phase change materials (PCMs) in building applications, Appl Energy 92 (2012) 593–605. https://doi.org/10.1016/j.apenergy.2011.08.025.

[119] A. Kurdi, N. Almoatham, M. Mirza, T. Ballweg, B. Alkahlan, Potential phase change materials in building wall construction—a review, Materials 14 (2021). https://doi.org/10.3390/ma14185328.

[120] A. Karaipekli, A. Sari, Capric acid and palmitic acid eutectic mixture applied in building wallboard for latent heat thermal energy storage, J SCI IND RES 66 (2007).

[121] D. Feldman, D. Banu, D. Hawes, E. Ghanbari, Obtaining an energy storing building material by direct incorporation of an organic phase change material in gypsum wallboard, Solar Energy Materials 22 (1991) 231–242.

[122] J. Kissock, J. Hanning, T. Whitney, M. Drake, Testing and simulation of phase change wallboard for thermal storage in buildings, in: International Solar Energy Conference, New York, 1998: pp. 45–52. https://research.ebsco.com/linkprocessor/plink?id=8246be00-6912-3be9-.

[123] T. Lee, D.W. Hawes, D. Banu, D. Feldman, Control aspects of latent heat storage and recovery in concrete, Solar Energy Materials & Solar Cells 62 (2000) 217–237.

[124] A. Frazzica, V. Brancato, V. Palomba, D. La Rosa, F. Grungo, L. Calabrese, E. Proverbio, Thermal performance of hybrid cement mortar-PCMs for warm climates application, Solar Energy Materials and Solar Cells 193 (2019) 270–280. https://doi.org/10.1016/j.solmat.2019.01.022.

[125] M. Hadjieva, R. Stoykov, T. Filipova, Composite salt-hydrate concrete system for building energy storage, Renew Energy 19 (2000) 111–115. www.elsevier.com/locate/renene.

[126] E. Mohseni, W. Tang, S. Wang, Development of thermal energy storage lightweight structural cementitious composites by means of macro-encapsulated PCM, Constr Build Mater 225 (2019) 182–195. https://doi.org/10.1016/j.conbuildmat.2019.07.136.

[127] M.T. Plytaria, E. Bellos, C. Tzivanidis, K.A. Antonopoulos, Financial and energetic evaluation of solar-assisted heat pump underfloor heating systems with phase change materials, Appl Therm Eng 149 (2019) 548–564. https://doi.org/10.1016/j.applthermaleng.2018.12.075.

[128] M.M. Farid, X.D. Chen, Domestic electrical space heating with heat storage, Proc Instn Mech Engrs 213 (1999).

[129] E. Osterman, V. Butala, U. Stritih, PCM thermal storage system for “free” heating and cooling of buildings, Energy Build 106 (2015) 125–133. https://doi.org/10.1016/j.enbuild.2015.04.012.

[130] L.F. Cabeza, L. Navarro, A.L. Pisello, L. Olivieri, C. Bartolomé, J. Sánchez, S. Álvarez, J.A. Tenorio, Behaviour of a concrete wall containing micro-encapsulated PCM after a decade of its construction, Solar Energy 200 (2020) 108–113. https://doi.org/10.1016/j.solener.2019.12.003.

[131] S. Kuravi, J. Trahan, D.Y. Goswami, M.M. Rahman, E.K. Stefanakos, Thermal energy storage technologies and systems for concentrating solar power plants, Prog Energy Combust Sci 39 (2013) 285–319. https://doi.org/10.1016/j.pecs.2013.02.001.

[132] A. Gil, M. Medrano, I. Martorell, A. Lázaro, P. Dolado, B. Zalba, L.F. Cabeza, State of the art on high temperature thermal energy storage for power generation. Part 1-Concepts, materials and modellization, Renewable and Sustainable Energy Reviews 14 (2010) 31–55. https://doi.org/10.1016/j.rser.2009.07.035.

[133] P. Tatsidjodoung, N. Le Pierrès, L. Luo, A review of potential materials for thermal energy storage in building applications, Renewable and Sustainable Energy Reviews 18 (2013) 327–349. https://doi.org/10.1016/j.rser.2012.10.025.

[134] Y. Zhang, R. Wang, Sorption thermal energy storage: Concept, process, applications and perspectives, Energy Storage Mater 27 (2020) 352–369. https://doi.org/10.1016/j.ensm.2020.02.024.

[135] M.S. Fernandes, G.J.V.N. Brites, J.J. Costa, A.R. Gaspar, V.A.F. Costa, A thermal energy storage system provided with an adsorption module – Dynamic modeling and viability study, Energy Convers Manag 126 (2016) 548–560. https://doi.org/10.1016/j.enconman.2016.08.032.

[136] L.F. Cabeza, A. Solé, C. Barreneche, Review on sorption materials and technologies for heat pumps and thermal energy storage, Renew Energy 110 (2017) 3–39. https://doi.org/10.1016/j.renene.2016.09.059.

[137] A. Mehari, Z.Y. Xu, R.Z. Wang, Thermal energy storage using absorption cycle and system: A comprehensive review, Energy Convers Manag 206 (2020). https://doi.org/10.1016/j.enconman.2020.112482.

[138] A.J. Carrillo, J. González-Aguilar, M. Romero, J.M. Coronado, Solar Energy on Demand: A Review on High Temperature Thermochemical Heat Storage Systems and Materials, Chem Rev 119 (2019) 4777–4816. https://doi.org/10.1021/acs.chemrev.8b00315.

[139] B. Stutz, N. Le Pierres, F. Kuznik, K. Johannes, E. Palomo Del Barrio, J.P. Bédécarrats, S. Gibout, P. Marty, L. Zalewski, J. Soto, N. Mazet, R. Olives, J.J. Bezian, D.P. Minh, Storage of thermal solar energy, C R Phys 18 (2017) 401–414. https://doi.org/10.1016/j.crhy.2017.09.008.

[140] G. Ervin, Solar Heat Storage Using Chemical Reactions*, J Solid State Chem 22 (1977) 1–61.

[141] L. André, S. Abanades, G. Flamant, Screening of thermochemical systems based on solid-gas reversible reactions for high temperature solar thermal energy storage, Renewable and Sustainable Energy Reviews 64 (2016) 703–715. https://doi.org/10.1016/j.rser.2016.06.043.

[142] K.E. N'Tsoukpoe, T. Schmidt, H.U. Rammelberg, B.A. Watts, W.K.L. Ruck, A systematic multi-step screening of numerous salt hydrates for low temperature thermochemical energy storage, Appl Energy 124 (2014) 1–16. https://doi.org/10.1016/j.apenergy.2014.02.053.

[143] S. Roger-Lund, J. Darkwa, M. Worall, J. Calautit, R. Boukhanouf, A Review of Thermochemical Energy Storage Systems for District Heating in the UK, Energies (Basel) 17 (2024). https://doi.org/10.3390/en17143389.

[144] R.P. Merchán, M.J. Santos, A. Medina, A. Calvo Hernández, High temperature central tower plants for concentrated solar power: 2021 overview, Renewable and Sustainable Energy Reviews 155 (2022). https://doi.org/10.1016/j.rser.2021.111828.

[145] D. Liu, L. Xin-Feng, L. Bo, Z. Si-quan, X. Yan, Progress in thermochemical energy storage for concentrated solar power: A review, Int J Energy Res 42 (2018) 4546–4561. https://doi.org/10.1002/er.4183.

[146] L. Kumar, M. Hasanuzzaman, N.A. Rahim, Global advancement of solar thermal energy technologies for industrial process heat and its future prospects: A review, Energy Convers Manag 195 (2019) 885–908. https://doi.org/10.1016/j.enconman.2019.05.081.

[147] P. Pardo, A. Deydier, Z. Anxionnaz-Minvielle, S. Rougé, M. Cabassud, P. Cognet, A review on high temperature thermochemical heat energy storage, Renewable and Sustainable Energy Reviews 32 (2014) 591–610. https://doi.org/10.1016/j.rser.2013.12.014.

[148] A. Ahmad, Y. Ding, A thermochemical energy storage based cooling and heating system: Modelling, experimental validation and lab-scale demonstration, Energy Convers Manag 247 (2021). https://doi.org/10.1016/j.enconman.2021.114748.

[149] Y. Ding, S.B. Riffat, Thermochemical energy storage technologies for building applications: a state-of-the-art review, International Journal of Low-Carbon Technologies 8 (2013) 106–116. https://doi.org/10.1093/ijlct/cts004.

[150] D. Vanhoudt, B. Claessens, R. Salenbien, J. Desmedt, The use of distributed thermal storage in district heating grids for demand side management, Energy Build (2017). http://arxiv.org/abs/1702.06005.

[151] H. Bao, Z. Ma, Thermochemical energy storage, Storing Energy: With Special Reference to Renewable Energy Sources (2022) 651–683. https://doi.org/10.1016/B978-0-12-824510-1.00028-3.

[152] M. Schmidt, M. Linder, A Novel Thermochemical Long Term Storage Concept: Balance of Renewable Electricity and Heat Demand in Buildings, Front Energy Res 8 (2020). https://doi.org/10.3389/fenrg.2020.00137.

[153] T. Yan, R.Z. Wang, T.X. Li, L.W. Wang, I.T. Fred, A review of promising candidate reactions for chemical heat storage, Renewable and Sustainable Energy Reviews 43 (2015) 13–31. https://doi.org/10.1016/j.rser.2014.11.015.

[154] G. Whiting, D. Grondin, S. Bennici, A. Auroux, Heats of water sorption studies on zeolite-MgSO4 composites as potential thermochemical heat storage materials, Solar Energy Materials and Solar Cells 112 (2013) 112–119. https://doi.org/10.1016/j.solmat.2013.01.020.

[155] S. Wu, C. Zhou, E. Doroodchi, R. Nellore, B. Moghtaderi, A review on high-temperature thermochemical energy storage based on metal oxides redox cycle, Energy Convers Manag 168 (2018) 421–453. https://doi.org/10.1016/j.enconman.2018.05.017.

[156] S.A. Kalogirou, Solar thermal collectors and applications, Prog Energy Combust Sci 30 (2004) 231–295. https://doi.org/10.1016/j.pecs.2004.02.001.

[157] N. Yu, R.Z. Wang, L.W. Wang, Sorption thermal storage for solar energy, Prog Energy Combust Sci 39 (2013) 489–514. https://doi.org/10.1016/j.pecs.2013.05.004.

[158] B. Michel, P. Neveu, N. Mazet, Comparison of closed and open thermochemical processes, for long-term thermal energy storage applications, Energy 72 (2014) 702–716. https://doi.org/10.1016/j.energy.2014.05.097.

[159] W. Wongsuwan, S. Kumar, P. Neveu, F. Meunier, A review of chemical heat pump technology and applications, Applied Thermal Engineering 21 (2001) 1489–1519. www.elsevier.com/locate/apthermeng.

[160] H. Zondag, B. Kikkert, S. Smeding, R. de Boer, M. Bakker, Prototype thermochemical heat storage with open reactor system, Appl Energy 109 (2013) 360–365. https://doi.org/10.1016/j.apenergy.2013.01.082.

[161] A. Hauer, ADSORPTION SYSTEMS FOR TES-DESIGN AND DEMONSTRATION PROJECTS, in: Thermal Energy Storage for Sustainable Energy Consumption, 2007. http://www.zeo-tech.de.

[162] V. Palomba, A. Frazzica, Recent advancements in sorption technology for solar thermal energy storage applications, Solar Energy 192 (2019) 69–105. https://doi.org/10.1016/j.solener.2018.06.102.

[163] E. Piperopoulos, E. Mastronardo, M. Fazio, M. Lanza, S. Galvagno, C. Milone, Enhancing the volumetric heat storage capacity of Mg(OH)2 by the addition of a cationic surfactant during its synthesis, Appl Energy 215 (2018) 512–522. https://doi.org/10.1016/j.apenergy.2018.02.047.

[164] E. Mastronardo, L. Bonaccorsi, Y. Kato, E. Piperopoulos, M. Lanza, C. Milone, Thermochemical performance of carbon nanotubes based hybrid materials for MgO/H2O/Mg(OH)2 chemical heat pumps, Appl Energy 181 (2016) 232–243. https://doi.org/10.1016/j.apenergy.2016.08.041.

[165] E. Mastronardo, L. Bonaccorsi, Y. Kato, E. Piperopoulos, C. Milone, Efficiency improvement of heat storage materials for MgO/H2O/Mg(OH)2 chemical heat pumps, Appl Energy 162 (2016) 31–39. https://doi.org/10.1016/j.apenergy.2015.10.066.

[166] A.J. De Jong, L. Van Vliet, C. Hoegaerts, M. Roelands, R. Cuypers, Thermochemical Heat Storage - From Reaction Storage Density to System Storage Density, in: Energy Procedia, Elsevier Ltd, 2016: pp. 128–137. https://doi.org/10.1016/j.egypro.2016.06.187.

[167] L. André, S. Abanades, Evaluation and performances comparison of calcium, strontium and barium carbonates during calcination/carbonation reactions for solar thermochemical energy storage, J Energy Storage 13 (2017) 193–205. https://doi.org/10.1016/j.est.2017.07.014.

[168] C. Ortiz, Thermochemical energy storage based on carbonates: A brief overview, Energies (Basel) 14 (2021). https://doi.org/10.3390/en14144336.

[169] N.R. Rhodes, A. Barde, K. Randhir, L. Li, D.W. Hahn, R. Mei, J.F. Klausner, N. Auyeung, Solar Thermochemical Energy Storage Through Carbonation Cycles of SrCO3/SrO Supported on SrZrO3, ChemSusChem 8 (2015) 3793–3798. https://doi.org/10.1002/cssc.201501023.

[170] C. Ortiz, J.M. Valverde, R. Chacartegui, L.A. Perez-Maqueda, P. Giménez, The Calcium-Looping (CaCO3/CaO) Process for Thermochemical Energy Storage in Concentrating Solar Power Plants: A critical review, Renewable and Sustainable Energy Reviews 113 (2019) 109252.

[171] S. Zare Ghorbaei, H. Ale Ebrahim, Carbonation reaction of strontium oxide for thermochemical energy storage and CO2 removal applications: Kinetic study and reactor performance prediction, Appl Energy 277 (2020). https://doi.org/10.1016/j.apenergy.2020.115604.

[172] D. Mahon, G. Claudio, P. Eames, An experimental study of the decomposition and carbonation of magnesium carbonate for medium temperature thermochemical energy storage, Energies (Basel) 14 (2021). https://doi.org/10.3390/en14051316.

[173] E. Alonso, C. Pérez-Rábago, J. Licurgo, E. Fuentealba, C.A. Estrada, First experimental studies of solar redox reactions of copper oxides for thermochemical energy storage, Solar Energy 115 (2015) 297–305. https://doi.org/10.1016/j.solener.2015.03.005.

[174] A.P. Muroyama, A.J. Schrader, P.G. Loutzenhiser, Solar electricity via an Air Brayton cycle with an integrated two-step thermochemical cycle for heat storage based on Co3O4/CoO redox reactions II: Kinetic analyses, Solar Energy 122 (2015) 409–418. https://doi.org/10.1016/j.solener.2015.08.038.

[175] Z. Zhang, L. Andre, S. Abanades, Experimental assessment of oxygen exchange capacity and thermochemical redox cycle behavior of Ba and Sr series perovskites for solar energy storage, Solar Energy 134 (2016) 494–502. https://doi.org/10.1016/j.solener.2016.05.031.

[176] E. Mastronardo, X. Qian, J.M. Coronado, S.M. Haile, A and B site Co-doping of CaMnO3: a route to enhanced heat storage properties, J Mater Chem A Mater 11 (2023) 8858–8872. https://doi.org/10.1039/d2ta07779e.

[177] E. Mastronardo, X. Qian, J.M. Coronado, S.M. Haile, The favourable thermodynamic properties of Fe-doped CaMnO3for thermochemical heat storage, J Mater Chem A Mater 8 (2020) 8503–8517. https://doi.org/10.1039/d0ta02031a.

[178] R.J. Clark, A. Mehrabadi, M. Farid, State of the art on salt hydrate thermochemical energy storage systems for use in building applications, J Energy Storage 27 (2020). https://doi.org/10.1016/j.est.2019.101145.

[179] A. Gutierrez, S. Ushak, V. Mamani, P. Vargas, C. Barreneche, L.F. Cabeza, M. Grágeda, Characterization of wastes based on inorganic double salt hydrates as potential thermal energy

storage materials, Solar Energy Materials and Solar Cells 170 (2017) 149–159. https://doi.org/10.1016/j.solmat.2017.05.036.

[180] M. Deutsch, D. Müller, C. Aumeyr, C. Jordan, C. Gierl-Mayer, P. Weinberger, F. Winter, A. Werner, Systematic search algorithm for potential thermochemical energy storage systems, Appl Energy 183 (2016) 113–120. https://doi.org/10.1016/j.apenergy.2016.08.142.

[181] K. Posern, K. Linnow, M. Niermann, C. Kaps, M. Steiger, Thermochemical investigation of the water uptake behavior of MgSO4 hydrates in host materials with different pore size, Thermochim Acta 611 (2015) 1–9. https://doi.org/10.1016/j.tca.2015.04.031.

[182] F. Trausel, A.J. De Jong, R. Cuypers, A review on the properties of salt hydrates for thermochemical storage, in: Energy Procedia, Elsevier Ltd, 2014: pp. 447–452. https://doi.org/10.1016/j.egypro.2014.02.053.

[183] Q. Huang, G. Lu, J. Wang, J. Yu, Thermal decomposition mechanisms of MgCl2·6H2O and MgCl2·H2O, J Anal Appl Pyrolysis 91 (2011) 159–164. https://doi.org/10.1016/j.jaap.2011.02.005.

[184] R. Wijnhorst, M. Demmenie, E. Jambon-Puillet, F. Ariese, D. Bonn, N. Shahidzadeh, Softness of hydrated salt crystals under deliquescence, Nat Commun 14 (2023). https://doi.org/10.1038/s41467-023-36834-0.

[185] S. Wang, A. Stahlbuhk, M. Steiger, Hydration and deliquescence behavior of calcium chloride hydrates, Fluid Phase Equilib 585 (2024). https://doi.org/10.1016/j.fluid.2024.114171.

[186] C. Peng, L. Chen, M. Tang, A database for deliquescence and efflorescence relative humidities of compounds with atmospheric relevance, Fundamental Research 2 (2022) 578–587. https://doi.org/10.1016/j.fmre.2021.11.021.

[187] H. Veith, C. Luebbert, G. Sadowski, Predicting deliquescence relative humidities of crystals and crystal mixtures, Molecules 26 (2021). https://doi.org/10.3390/molecules26113176.

[188] J.R. Schroeder, K.D. Beyer, Deliquescence relative humidities of organic and inorganic salts important in the atmosphere, Journal of Physical Chemistry A 120 (2016) 9948–9957. https://doi.org/10.1021/acs.jpca.6b08725.

[189] E. Mastronardo, E. Previti, L. Calabrese, C. Milone, Experimental assessment of calcium L-lactate as thermochemical heat storage material, J Energy Storage 108 (2025) 115065. https://doi.org/10.1016/j.est.2024.115065.

[190] E. Mastronardo, E. La Mazza, D. Palamara, E. Piperopoulos, D. Iannazzo, E. Proverbio, C. Milone, Organic Salt Hydrate as a Novel Paradigm for Thermal Energy Storage, Energies (Basel) 15 (2022). https://doi.org/10.3390/en15124339.

[191] H. Yang, C. Wang, L. Tong, S. Yin, L. Wang, Y. Ding, Salt Hydrate Adsorption Material-Based Thermochemical Energy Storage for Space Heating Application: A Review, Energies (Basel) 16 (2023). https://doi.org/10.3390/en16062875.

[192] A. Shkatulov, R. Joosten, H. Fischer, H. Huinink, Core-Shell Encapsulation of Salt Hydrates into Mesoporous Silica Shells for Thermochemical Energy Storage, ACS Appl Energy Mater 3 (2020) 6860–6869. https://doi.org/10.1021/acsaem.0c00971.

[193] S.P. Casey, D. Aydin, J. Elvins, S. Riffat, Salt impregnated desiccant matrices for 'open' thermochemical energy conversion and storage – Improving energy density utilisation through hygrodynamic & thermodynamic reactor design, Energy Convers Manag 142 (2017) 426–440. https://doi.org/10.1016/j.enconman.2017.03.066.

[194] E. Previti, J.M. Coronado, E. Mastronardo, C. Milone, L. Calabrese, Influence of host matrices on the thermochemical energy storage capacity of novel organic salt hydrate, in: K. Johannes (Ed.), Proceedings of the 16th IEA ES TCP International Conference on Energy Storage, Lyon, 2024: pp. 245–248. https://doi.org/10.5281/zenodo.13784976.

[195] D. Alby, F. Salles, J. Fullenwarth, J. Zajac, On the use of metal cation-exchanged zeolites in sorption thermochemical storage: Some practical aspects in reference to the mechanism of water vapor adsorption, Solar Energy Materials and Solar Cells 179 (2018) 223–230. https://doi.org/10.1016/j.solmat.2017.11.020.

[196] M.F. De Lange, K.J.F.M. Verouden, T.J.H. Vlugt, J. Gascon, F. Kapteijn, Adsorption-Driven Heat Pumps: The Potential of Metal-Organic Frameworks, Chem Rev 115 (2015) 12205–12250. https://doi.org/10.1021/acs.chemrev.5b00059.

[197] L. Calabrese, D. Palamara, E. Piperopoulos, E. Mastronardo, C. Milone, E. Proverbio, Deviceful LiCl salt hydrate confinement into a macroporous silicone foam for low-temperature heat storage application, Journal of Science: Advanced Materials and Devices 7 (2022). https://doi.org/10.1016/j.jsamd.2022.100463.

[198] E. Mastronardo, E. Piperopoulos, D. Palamara, A. Frazzica, L. Calabrese, Morphological Observation of LiCl Deliquescence in PDMS-Based Composite Foams, Applied Sciences (Switzerland) 12 (2022). https://doi.org/10.3390/app12031510.

[199] L. Calabrese, V. Brancato, V. Palomba, A. Frazzica, L.F. Cabeza, Magnesium sulphate-silicone foam composites for thermochemical energy storage: Assessment of dehydration behaviour and mechanical stability, Solar Energy Materials and Solar Cells 200 (2019). https://doi.org/10.1016/j.solmat.2019.109992.

[200] L. Calabrese, V. Brancato, V. Palomba, A. Frazzica, L.F. Cabeza, Assessment of the hydration/dehydration behaviour of MgSO4·7H2O filled cellular foams for sorption storage

applications through morphological and thermo-gravimetric analyses, Sustainable Materials and Technologies 17 (2018). https://doi.org/10.1016/j.susmat.2018.e00073.

[201] S. Hongois, F. Kuznik, P. Stevens, J.J. Roux, Development and characterisation of a new MgSO4-zeolite composite for long-term thermal energy storage, Solar Energy Materials and Solar Cells 95 (2011) 1831–1837. https://doi.org/10.1016/j.solmat.2011.01.050.

[202] E. Courbon, P. D'Ans, A. Permyakova, O. Skrylnyk, N. Steunou, M. Degrez, M. Frère, Further improvement of the synthesis of silica gel and CaCl2 composites: Enhancement of energy storage density and stability over cycles for solar heat storage coupled with space heating applications, Solar Energy 157 (2017) 532–541. https://doi.org/10.1016/j.solener.2017.08.034.

[203] A. Permyakova, S. Wang, E. Courbon, F. Nouar, N. Heymans, P. D'Ans, N. Barrier, P. Billemont, G. De Weireld, N. Steunou, M. Frère, C. Serre, Design of salt-metal organic framework composites for seasonal heat storage applications, J Mater Chem A Mater 5 (2017) 12889–12898. https://doi.org/10.1039/c7ta03069j.

[204] B.G.P. Van Ravensteijn, P.A.J. Donkers, R.C. Ruliaman, J. Eversdijk, H.R. Fischer, H.P. Huinink, O.C.G. Adan, Encapsulation of Salt Hydrates by Polymer Coatings for Low-Temperature Heat Storage Applications, ACS Appl Polym Mater 3 (2021) 1712–1726. https://doi.org/10.1021/acsapm.0c01186.

[205] D. Palamara, P. Bruzzaniti, L. Calabrese, E. Proverbio, Effect of degree of sulfonation on the performance of adsorbent SAPO-34/S-PEEK composite coatings for adsorption heat pumps, Prog Org Coat 154 (2021). https://doi.org/10.1016/j.porgcoat.2021.106193.

[206] M.A. Mahmud, N. Abir, F.R. Anannya, A. Nabi Khan, A.N.M.M. Rahman, N. Jamine, Coir fiber as thermal insulator and its performance as reinforcing material in biocomposite production, Heliyon 9 (2023). https://doi.org/10.1016/j.heliyon.2023.e15597.

[207] P.M. Weaver, ON BENEFICIAL ANISOTROPIC EFFECTS IN COMPOSITE STRUCTURES, in: 43rd AIAA/ASME/ASCE/AHS/ASC Structures, Structural Dynamics, and Materials Conference, 2002.

[208] C. Knoll, D. Müller, W. Artner, J.M. Welch, A. Werner, M. Harasek, P. Weinberger, Probing cycle stability and reversibility in thermochemical energy storage – CaC2O4·H2O as perfect match?, Appl Energy 187 (2017) 1–9. https://doi.org/10.1016/j.apenergy.2016.11.053.

[209] M. Schmidt, V. Sourmelis, V. Kühl, M. Linder, Zero Emission Heating with Calcium Oxide and Water: Development and Demonstration of First Pilot Scale Thermochemical Heating System for Buildings, Res Sq (2024). https://doi.org/10.21203/rs.3.rs-4963060/v1.

[210] J. Werner, J. Smith, B. Stöger, W. Artner, A. Werner, P. Weinberger, Characterization of Ca-Dicarboxylate Salt Hydrates as Thermochemical Energy Storage Materials, Crystals (Basel) 13 (2023). https://doi.org/10.3390/cryst13101518.

[211] E. Previti, C. Foti, O. Giuffrè, F. Saija, J. Sponer, G. Cassone, Ab initio molecular dynamics simulations and experimental speciation study of levofloxacin under different pH conditions, Physical Chemistry Chemical Physics 23 (2021). https://doi.org/10.1039/d1cp03942c.

[212] S. Kiyabu, P. Girard, D.J. Siegel, Discovery of Salt Hydrates for Thermal Energy Storage, J Am Chem Soc 144 (2022) 21617–21627. https://doi.org/10.1021/jacs.2c08993.

[213] L.F. Cabeza, A. de Gracia, G. Zsembinszki, E. Borri, Perspectives on thermal energy storage research, Energy 231 (2021). https://doi.org/10.1016/j.energy.2021.120943.

[214] M. Frigione, M. Lettieri, A. Sarcinella, Phase change materials for energy efficiency in buildings and their use in mortars, Materials 12 (2019). https://doi.org/10.3390/ma12081260.

[215] L.C. Sögütoglu, M. Steiger, J. Houben, D. Biemans, H.R. Fischer, P. Donkers, H. Huinink, O.C.G. Adan, Understanding the Hydration Process of Salts: The Impact of a Nucleation Barrier, Cryst Growth Des 19 (2019) 2279–2288. https://doi.org/10.1021/acs.cgd.8b01908.

[216] N. Xie, Z. Huang, Z. Luo, X. Gao, Y. Fang, Z. Zhang, Inorganic salt hydrate for thermal energy storage, Applied Sciences (Switzerland) 7 (2017). https://doi.org/10.3390/app7121317.

[217] S. Seesanong, Y. Wongchompoo, B. Boonchom, C. Sronsri, N. Laohavisuti, K. Chaiseeda, W. Boonmee, Economical and Environmentally Friendly Track of Biowaste Recycling of Scallop Shells to Calcium Lactate, ACS Omega 7 (2022) 14756–14764. https://doi.org/10.1021/acsomega.2c00112.

[218] J.B. De Maere D'aertrycke, J. Morlot, K. Robeyns, Y. Filinchuk, T. Leyssens, Exploring the solid-state phases and thermodynamics of calcium L-lactate, Food Chem 325 (2020). https://doi.org/10.1016/j.foodchem.2020.126884.

[219] B. Kiran-Yildirim, S. Titiz-Sargut, P. Sayan, Calcium Lactate Pentahydrate Crystallization in the Presence of Pentanoic Acid, Chem Eng Technol 41 (2018) 1244–1251. https://doi.org/10.1002/ceat.201700672.

[220] S. Hee Cheong, Physicochemical Properties of Calcium Lactate Prepared by Single-Phase Aragonite Precipitated Calcium Carbonate, Res. J. Pharm. Biol. Chem. Sci. 7 (2016) 1786–1794.

[221] R. Sarrate, J.R. Ticó, M. Miñarro, C. Carrillo, A. Fàbregas, E. García-Montoya, P. Pérez-Lozano, J.M. Suñé-Negre, Modification of the morphology and particle size of pharmaceutical excipients by spray drying technique, Powder Technol 270 (2015) 244–255. https://doi.org/10.1016/j.powtec.2014.08.021.

[222] Y. Sakata, S. Shiraishi, M. Otsuka, Characterization of dehydration and hydration behavior of calcium lactate pentahydrate and its anhydrate, Colloids Surf B Biointerfaces 46 (2005) 135–141. https://doi.org/10.1016/j.colsurfb.2005.10.004.

[223] Y. Sakata, S. Shiraishi, K. Takayama, M. Otsuka, Effect of pulverization and dehydration on the pharmaceutical properties of calcium lactate pentahydrate tablets, Colloids Surf B Biointerfaces 51 (2006) 149–156. https://doi.org/10.1016/j.colsurfb.2006.07.004.

[224] R. Alves de Oliveira, A. Komesu, C.E. Vaz Rossell, R. Maciel Filho, Challenges and opportunities in lactic acid bioprocess design—From economic to production aspects, Biochem Eng J 133 (2018) 219–239. https://doi.org/10.1016/j.bej.2018.03.003.

[225] S. Polat, Thermal degradation of calcium lactate pentahydrate using TGA/FTIR/MS: thermal kinetic and thermodynamics studies, Indian Chemical Engineer 64 (2022) 402–415. https://doi.org/10.1080/00194506.2021.2017359.

[226] J.B. de Maere d'Aertrycke, K. Robeyns, J. Willocq, T. Leyssens, Cocrystallization as a tool to solve deliquescence issues: The case of L-lactic acid, J Cryst Growth 472 (2017) 3–10. https://doi.org/10.1016/j.jcrysgro.2017.02.025.

[227] G.F. Tansman, P.S. Kindstedt, J.M. Hughes, Powder X-ray diffraction can differentiate between enantiomeric variants of calcium lactate pentahydrate crystal in cheese, J Dairy Sci 97 (2014) 7354–7362. https://doi.org/10.3168/jds.2014-8277.

[228] A. Apelblat, E. Manzurola, J. Van Krieken, G.L. Nanninga, Solubilities and vapour pressures of water over saturated solutions of magnesium-l-lactate, calcium-l-lactate, zinc-l-lactate, ferrous-l-lactate and aluminum-l-lactate, Fluid Phase Equilib 236 (2005) 162–168. https://doi.org/10.1016/j.fluid.2005.06.018.

[229] N. Kubantseva, R.W. Hartel, Solubility of calcium lactate in aqueous solution, Food Reviews International 18 (2002) 135–149. https://doi.org/10.1081/FRI-120014355.

[230] G. Eigenmann, I. Ubaldini, VOLUME SECONDO, in: NUOVO DIZIONARIO DI MERCEOLOGIA E CHIMICA APPLICATA, HOEPLI, Milano, 1973: p. 750.

[231] Sigma-Aldrich, Safety Data Sheet LiCl, (n.d.).

[232] Sigma-Aldrich, Safety data Sheet LiBr, (n.d.).

[233] Sigma-Aldrich, Safety data Sheet CaCl2, (n.d.).

[234] J.D. Hancock, J.H. Sharp, Method of Comparing Solid-state Kinetic Data and Its Application to the Decomposition of Kaolinite, brucite and BaCO3, Journal of The American Ceramic Society- 55 (1972) 74–77.

[235] H. Zhang, J. Baeyens, G. Cáceres, J. Degrève, Y. Lv, Thermal energy storage: Recent developments and practical aspects, Prog Energy Combust Sci 53 (2016) 1–40. https://doi.org/10.1016/j.pecs.2015.10.003.

[236] E. Barbosa, A.K. Menon, Thermodynamic and kinetic characterization of salt hydrates for thermochemical energy storage, MRS Commun 12 (2022) 678–685. https://doi.org/10.1557/s43579-022-00264-8.

[237] E. Mastronardo, X. Qian, J.M. Coronado, S.M. Haile, A and B site Co-doping of $CaMnO_3$: a route to enhanced heat storage properties, J Mater Chem A Mater 11 (2023) 8858–8872. https://doi.org/10.1039/D2TA07779E.

[238] S. Tescari, G. Lantin, M. Lange, S. Breuer, C. Agrafiotis, M. Roeb, C. Sattler, Numerical Model to Design a Thermochemical Storage System for Solar Power Plant, Energy Procedia 75 (2015) 2137–2143. https://doi.org/10.1016/j.egypro.2015.07.347.

[239] Storing Energy, with Special Reference to Renewable Energy Sources, Chemistry International 38 (2016). https://doi.org/10.1515/ci-2016-0627.

[240] V. Brancato, L.G. Gordeeva, A. Sapienza, V. Palomba, S. Vasta, A.D. Grekova, A. Frazzica, Y.I. Aristov, Experimental characterization of the LiCl/vermiculite composite for sorption heat storage applications, International Journal of Refrigeration 105 (2019) 92–100. https://doi.org/10.1016/j.ijrefrig.2018.08.006.

[241] E. Mastronardo, E. Piperopoulos, D. Palamara, A. Frazzica, L. Calabrese, Morphological Observation of LiCl Deliquescence in PDMS-Based Composite Foams, Applied Sciences (Switzerland) 12 (2022). https://doi.org/10.3390/app12031510.

[242] T.M. Letcher, Storing Energy: With Special Reference to Renewable Energy Sources, 2016. https://doi.org/10.1515/ci-2016-0627.

[243] T.D. Humphries, K.T. Møller, W.D.A. Rickard, M.V. Sofianos, S. Liu, C.E. Buckley, M. Paskevicius, Dolomite: A low cost thermochemical energy storage material, J Mater Chem A Mater 7 (2019) 1206–1215. https://doi.org/10.1039/c8ta07254j.

[244] G.G.D. Han, H. Li, J.C. Grossman, Optically-controlled long-term storage and release of thermal energy in phase-change materials, Nat Commun 8 (2017). https://doi.org/10.1038/s41467-017-01608-y.

[245] Z. Xiaoqin, H. Jin, C. Zhaosheng, L. Jiansheng, S. Jialin, N. Ben-Abdallah, Review on Development and Investigations of Phase Change Materials in Thermal Energy Storage, MRS Online Proceedings Library (2008).

[246] K. S. W. SING, D. H. EVERETT, R. A. W. HAUL, L. MOSCOU, R. A. PIEROTTI, J. ROUQUEROL, T. SIEMIENIEWSKA, REPORTING PHYSISORPTION DATA FOR GAS/SOLID SYSTEMS with Special Reference to the Determination of Surface Area and Porosity, 1985.

[247] D. Mohapatra, J. Nandanavanam, Salt in matrix for thermochemical energy storage - A review, in: Mater Today Proc, Elsevier Ltd, 2023: pp. 27–33. https://doi.org/10.1016/j.matpr.2022.05.453.

[248] H. Ait Ousaleh, S. Sair, S. Mansouri, Y. Abboud, M. Zahouily, A. Faik, A. El Bouari, Enhanced inorganic salts stability using bentonite clay for high-performance and low-cost thermochemical energy storage, J Energy Storage 49 (2022). https://doi.org/10.1016/j.est.2022.104140.

[249] N. Xie, X. Gao, Y. Zhong, R. Ye, S. Chen, L. Ding, T. Zhong, Enhanced thermal performance of Na2HPO4·12H2O composite phase change material supported by sepiolite fiber for floor radiant heating system, Journal of Building Engineering 56 (2022). https://doi.org/10.1016/j.jobe.2022.104747.

[250] X. Zhu, V. Vinokurov, D. Kopitsyn, D.G. Shchukin, Sepiolite Nanocarriers as a Matrix for Controlled Thermal Energy Storage, ACS Omega 6 (2021) 25828–25834. https://doi.org/10.1021/acsomega.1c04392.

[251] W. Cui, H. Zhang, Y. Xia, Y. Zou, C. Xiang, H. Chu, S. Qiu, F. Xu, L. Sun, Preparation and thermophysical properties of a novel form-stable CaCl2·6H2O/sepiolite composite phase change material for latent heat storage, J Therm Anal Calorim 131 (2018) 57–63. https://doi.org/10.1007/s10973-017-6170-2.

[252] F. Santiago, A.E. Mucientes, M. Osorio, F.J. Poblete, Synthesis and swelling behaviour of poly(sodium acrylate)/sepiolite superabsorbent composites and nanocomposites, Polym Int 55 (2006) 843–848. https://doi.org/10.1002/pi.2016.

[253] E. Galan, PROPERTIES AND APPLICATIONS OF PALYGORSKITE-SEPIOLITE CLAYS, 1996.

[254] A. Preisinger, X-RAY STUDY OF THE STRUCTURE OF SEPIOLITE, Clays Clay Miner (1959).

[255] C. Wu, S. Kou, Effects of high-calcium sepiolite on the rheological behaviour and mechanical strength of cement pastes and mortars, Constr Build Mater 196 (2019) 105–114. https://doi.org/10.1016/j.conbuildmat.2018.11.130.

[256] T. Kavas, E. Sabah, M.S. Çelik, Structural properties of sepiolite-reinforced cement composite, Cem Concr Res 34 (2004) 2135–2139. https://doi.org/10.1016/j.cemconres.2004.03.015.

[257] S. Martínez-Ramírez, F. Puertas, M.T. Blanco-Varela, G.E. Thompson, EFFECT OF DRY DEPOSITION OF POLLUTANTS ON THE DEGRADATION OF LIME MORTARS WITH SEPIOLITE, 1998.

[258] S. Salustro, L. Lavagna, V. Fernicola, D. Smorgon, A. Mondello, E. Chiavazzo, M. Pavese, Thermal characterization and cost analysis of cement-based composite materials for

thermochemical energy storage, J Energy Storage 93 (2024). https://doi.org/10.1016/j.est.2024.112308.

[259] D.P. Kgabi, A.A. Ambushe, Characterization of South African Bentonite and Kaolin Clays, Sustainability (Switzerland) 15 (2023). https://doi.org/10.3390/su151712679.

[260] A. Esteban-Cubillo, R. Pina-Zapardiel, J.S. Moya, M.F. Barba, C. Pecharromán, The role of magnesium on the stability of crystalline sepiolite structure, J Eur Ceram Soc 28 (2008) 1763–1768. https://doi.org/10.1016/j.jeurceramsoc.2007.11.022.

[261] W. Kuang, G.A. Facey, C. Detellier, B. Casal, J.M. Serratosa, E. Ruiz-Hitzky, Nanostructured Hybrid Materials Formed by Sequestration of Pyridine Molecules in the Tunnels of Sepiolite, Chemistry of Materials 15 (2003) 4956–4967. https://doi.org/10.1021/cm034867i.

[262] M. Suárez, E. García-Romero, Variability of the surface properties of sepiolite, Appl Clay Sci 67–68 (2012) 72–82. https://doi.org/10.1016/j.clay.2012.06.003.

[263] S. Inagaki, Y. Fukushima, H. Doi, O. Kamigaito, PORE SIZE DISTRIBUTION AND ADSORPTION SELECTIVITY OF SEPIOLITE, Clay Miner 25 (1990) 99–105.

[264] E. Ruiz-Hitzky, Molecular access to intracrystalline tunnels of sepiolite, J Mater Chem 11 (2001) 86–91. https://doi.org/10.1039/b003197f.

[265] M.R. Weir, G.A. Facey, C. Detellier, 1H, 2H and 29Si solid state NMR study of guest acetone molecules occupying the zeolitic channels of partially dehydrated sepiolite clay, Stud Surf Sci Catal 129 (2000) 551–558.

[266] I. Fujiwara, M. Sato, Adsorption of Water Vapor on Sepiolite for Chemical Heat Pumps, Journal of Chemical Engineering of Japan 25 (1992) 599–601.

[267] W.T. Yan, J. Du, W.B. Ye, Y. Hong, Experimental study of thermal performance on the adsorption of stearic acid into different morphology sepiolite, J Therm Anal Calorim 147 (2022) 4523–4532. https://doi.org/10.1007/s10973-021-10861-9.

[268] D. V. Voronin, E. Ivanov, P. Gushchin, R. Fakhrullin, V. Vinokurov, Clay composites for thermal energy storage: A review, Molecules 25 (2020). https://doi.org/10.3390/molecules25071504.

[269] Q. Shen, J. Ouyang, Y. Zhang, H. Yang, Lauric acid/modified sepiolite composite as a form-stable phase change material for thermal energy storage, Appl Clay Sci 146 (2017) 14–22. https://doi.org/10.1016/j.clay.2017.05.035.

[270] Q. Shen, S. Liu, J. Ouyang, H. Yang, Sepiolite supported stearic acid composites for thermal energy storage, RSC Adv 6 (2016) 112493–112501. https://doi.org/10.1039/c6ra22015k.

[271] K. Fukushima, D. Tabuani, G. Camino, Poly(lactic acid)/clay nanocomposites: Effect of nature and content of clay on morphology, thermal and thermo-mechanical properties, Materials Science and Engineering C 32 (2012) 1790–1795. https://doi.org/10.1016/j.msec.2012.04.047.

[272] M. Vavrusova, R. Liang, L.H. Skibsted, Thermodynamics of dissolution of calcium hydroxycarboxylates in water, J Agric Food Chem 62 (2014) 5675–5681. https://doi.org/10.1021/jf501453c.

[273] S. Wei, W. Zhou, R. Han, J. Gao, G. Zhao, Y. Qin, C. Wang, Influence of minerals with different porous structures on thermochemical heat storage performance of CaCl2-based composite sorbents, Solar Energy Materials and Solar Cells 243 (2022). https://doi.org/10.1016/j.solmat.2022.111769.

[274] V. Brancato, L.G. Gordeeva, A. Caprì, A.D. Grekova, A. Frazzica, Experimental comparison of innovative composite sorbents for space heating and domestic hot water storage, Crystals (Basel) 11 (2021). https://doi.org/10.3390/cryst11050476.

[275] Th. Peraki, A. Orfanoudaki, Study of raw and thermally treated sepiolite from the Mantoudi area, Euboea, Greece, J Therm Anal Calorim 91 (2008) 589–593.

[276] C. Serna, J.L. Ahlrichs, M. Serratosa, FOLDING IN SEPIOLITE CRYSTALS, Clays Clay Miner (1975) 452–457.

[277] M.S. Del Río, E. García-Romero, M. Suárez, I. Da Silva, L. Fuentes-Montero, G. Martínez-Criado, Variability in sepiolite: Diffraction studies, American Mineralogist 96 (2011) 1443–1454. https://doi.org/10.2138/am.2011.3761.

[278] M.A. Vicente-Rodriguez, M. Suarez, M. Angel Bafiares-Mufioz, J. De Dios Lopez-Gonzalez, Comparative FT-IR study of the removal and structural modifications during acid silicates of octahedral cations treatment of several, Spectrochimica Acta Part A (1996).

[279] M. Mititelu, E. Moroșan, A.C. Nicoară, A.A. Secăreanu, A.M. Musuc, I. Atkinson, J.P. Cusu, G.M. Nițulescu, E.A. Ozon, I. Sarbu, T.D. Balaci, Development of Immediate Release Tablets Containing Calcium Lactate Synthetized from Black Sea Mussel Shells, Mar Drugs 20 (2022). https://doi.org/10.3390/md20010045.

[280] Lee, Kim, Preparation and Characteristics of Calcium Lactate from Black Snail, Nutraceuticals and Food 8 (2003) 166–172.

[281] Y. Zhang, D. Shao, J. Yan, X. Jia, Y. Li, P. Yu, T. Zhang, The pore size distribution and its relationship with shale gas capacity in organic-rich mudstone of Wufeng-Longmaxi Formations, Sichuan Basin, China, Journal of Natural Gas Geoscience 1 (2016) 213–220. https://doi.org/10.1016/j.jnggs.2016.08.002.

[282] H. Yang, C. Wang, L. Tong, S. Yin, L. Wang, Y. Ding, Salt Hydrate Adsorption Material-Based Thermochemical Energy Storage for Space Heating Application: A Review, Energies (Basel) 16 (2023). https://doi.org/10.3390/en16062875.

[283] Z. Zhan, M. Xu, B. Li, Synergistic effects of sepiolite on the flame retardant properties and thermal degradation behaviors of polyamide 66/aluminum diethylphosphinate composites, Polym Degrad Stab 117 (2015) 66–74. https://doi.org/10.1016/j.polymdegradstab.2015.03.018.

[284] G. Tartaglione, D. Tabuani, G. Camino, Thermal and morphological characterisation of organically modified sepiolite, Microporous and Mesoporous Materials 107 (2008) 161–168. https://doi.org/10.1016/j.micromeso.2007.04.020.

[285] A. Álvarez, J. Santarén, A. Esteban-Cubillo, P. Aparicio, Current industrial applications of palygorskite and sepiolite, in: Dev Clay Sci, Elsevier B.V., 2011: pp. 281–298. https://doi.org/10.1016/B978-0-444-53607-5.00012-8.

[286] A. Alvarez, SEPIOLITE: PROPERTIES AND USES, Developments in Sedimentology 37 (1984) 253–287.

[287] A. Komesu, P.F. Martins Martinez, B.H. Lunelli, J. Oliveira, M.R. Wolf MacIel, R. MacIel Filho, Study of lactic acid thermal behavior using thermoanalytical techniques, J Chem 2017 (2017). https://doi.org/10.1155/2017/4149592.

[288] N. Yamaguchi, Y. Masuda, Y. Yamada, H. Narusawa, C. Han-Cheol, Y. Tamaki, T. Miyazaki, Synthesis of CaO-SiO2 Compounds Using Materials Extracted from Industrial Wastes, Open Journal of Inorganic Non-Metallic Materials 05 (2015) 1–10. https://doi.org/10.4236/ojinm.2015.51001.

[289] E. Tieger, V. Kiss, G. Pokol, Z. Finta, M. Dušek, J. Rohlíček, E. Skořepová, P. Brázda, Studies on the crystal structure and arrangement of water in sitagliptin l-tartrate hydrates, CrystEngComm 18 (2016) 3819–3831. https://doi.org/10.1039/c6ce00322b.

[290] L. Tian, L. Wang, K. Wang, Y. Zhang, J. Liang, The Preparation and Properties of Porous Sepiolite Ceramics, Sci Rep 9 (2019). https://doi.org/10.1038/s41598-019-43918-9.

[291] Y. Konuklu, O. Ersoy, Preparation and characterization of sepiolite-based phase change material nanocomposites for thermal energy storage, Appl Therm Eng 107 (2016) 575–582. https://doi.org/10.1016/j.applthermaleng.2016.07.012.

[292] A. Sarı, R.K. Sharma, G. Hekimoğlu, V. V. Tyagi, Preparation, characterization, thermal energy storage properties and temperature control performance of form-stabilized sepiolite based composite phase change materials, Energy Build 188–189 (2019) 111–119. https://doi.org/10.1016/j.enbuild.2019.02.008.

[293] Y. Wang, S. Gao, H. Zhong, B. Zhang, M. Cui, M. Jiang, S. Wang, Z. Wang, Heterogeneous wettability and radiative cooling for efficient deliquescent sorbents-based atmospheric water harvesting, Cell Rep Phys Sci 3 (2022). https://doi.org/10.1016/j.xcrp.2022.100879.

[294] L. Lavagna, D. Burlon, R. Nisticò, V. Brancato, A. Frazzica, M. Pavese, E. Chiavazzo, Cementitious composite materials for thermal energy storage applications: a preliminary

characterization and theoretical analysis, Sci Rep 10 (2020) 12833. https://doi.org/10.1038/s41598-020-69502-0.

[295] A. Mondello, M. Morciano, L. Lavagna, M. Pavese, E. Chiavazzo, Advancing thermochemical storage: Synthesis and characterization of cement-based composite materials, in: J Phys Conf Ser, Institute of Physics, 2024. https://doi.org/10.1088/1742-6596/2766/1/012218.

[296] R.J. Clark, M. Farid, Experimental investigation into cascade thermochemical energy storage system using SrCl2-cement and zeolite-13X materials, Appl Energy 316 (2022). https://doi.org/10.1016/j.apenergy.2022.119145.

[297] R.J. Clark, M. Farid, Hydration reaction kinetics of SrCl2 and SrCl2-cement composite material for thermochemical energy storage, Solar Energy Materials and Solar Cells 231 (2021). https://doi.org/10.1016/j.solmat.2021.111311.

[298] R.J. Clark, M. Farid, Experimental investigation into the performance of novel SrCl2-based composite material for thermochemical energy storage, J Energy Storage 36 (2021). https://doi.org/10.1016/j.est.2021.102390.

[299] H.M. Jonkers, Self Healing Concrete: A Biological Approach, in: Self Healing Materials: An Alternative Approach to 20 Centuries of Materials Science, 2007: pp. 195–204.

[300] S.K. Ghosh, Self-healing Materials, 2009.

[301] C.-M. Aldea, W.-J. Song, J.S. Popovics, S.P. Shah, EXTENT OF HEALING OF CRACKED NORMAL STRENGTH CONCRETE, JOURNAL OF MATERIALS IN CIVIL ENGINEERING (2000).

[302] M. Vaezi, S.A. Zareei, M. Jahadi, Recycled microbial mortar: Effects of bacterial concentration and calcium lactate content, Constr Build Mater 234 (2020). https://doi.org/10.1016/j.conbuildmat.2019.117349.

[303] C. Stuckrath, R. Serpell, L.M. Valenzuela, M. Lopez, Quantification of chemical and biological calcium carbonate precipitation: Performance of self-healing in reinforced mortar containing chemical admixtures, Cem Concr Compos 50 (2014) 10–15. https://doi.org/10.1016/j.cemconcomp.2014.02.005.

[304] N. Hearn, Self-sealing, autogenous healing and continued hydration: What is the difference?, Materials and Structures/Mat~riaux et Constructions 31 (1998) 563–567.

[305] V. Wiktor, H.M. Jonkers, Quantification of crack-healing in novel bacteria-based self-healing concrete, Cem Concr Compos 33 (2011) 763–770. https://doi.org/10.1016/j.cemconcomp.2011.03.012.

[306] J.M. Irwan, L.H. Anneza, N. Othman, A.F. Alshalif, Compressive strength and water penetration of Concrete with Enterococcus Faecalis and calcium lactate, in: Key Eng Mater, Trans Tech

Publications Ltd, 2016: pp. 345–349. https://doi.org/10.4028/www.scientific.net/KEM.705.345.

[307] K. Vijay, M. Murmu, Effect of calcium lactate on compressive strength and self-healing of cracks in microbial concrete, Frontiers of Structural and Civil Engineering 13 (2019) 515–525. https://doi.org/10.1007/s11709-018-0494-2.

[308] S.K. Chaerun, R. Syarif, R.K. Wattimena, Bacteria incorporated with calcium lactate pentahydrate to improve the mortar properties and self-healing occurrence, Sci Rep 10 (2020). https://doi.org/10.1038/s41598-020-74127-4.

[309] E. Mastronardo, L. Calabrese, E. Previti, F. Grungo, G. Gullì, R. Bertino, MALTA COMPRENDENTE CALCIO LATTATO, 102022000007862, 2022.

[310] E. Baccega, M. Bottarelli, Granular PCM-Enhanced Plaster for Historical Buildings: Experimental Tests and Numerical Studies, Energies (Basel) 15 (2022). https://doi.org/10.3390/en15030975.

[311] J. Grilo, P. Faria, R. Veiga, A. Santos Silva, V. Silva, A. Velosa, New natural hydraulic lime mortars - Physical and microstructural properties in different curing conditions, Constr Build Mater 54 (2014) 378–384. https://doi.org/10.1016/j.conbuildmat.2013.12.078.

[312] UNICEMENTO, UNI EN 459-1, UNI EN, Italy, 2002.

[313] Tradimalt Spa, NHL5 Technical Data Sheet, (n.d.). https://www.tradimalt.com/wp-content/uploads/2018/03/calce-idraulica-NHL-3.5-e-5.pdf (accessed April 17, 2025).

[314] E. Spychał, R. Dachowski, The influence of hydrated lime and cellulose ether admixture on water retention, rheology and application properties of cement plastering mortars, Materials 14 (2021). https://doi.org/10.3390/ma14195487.

[315] A. Izaguirre, J. Lanas, J.I. Álvarez, Behaviour of a starch as a viscosity modifier for aerial lime-based mortars, Carbohydr Polym 80 (2010) 222–228. https://doi.org/10.1016/j.carbpol.2009.11.010.

[316] G. Ke, J. Zhang, B. Tian, J. Wang, Characteristic analysis of concrete air entraining agents in different media, Cem Concr Res 135 (2020). https://doi.org/10.1016/j.cemconres.2020.106142.

[317] UNICEMENTO, UNI EN 1015-2, UNI EN, Italy, 2007.

[318] UNICEMENTO, UNI EN 1015-3, UNI EN, Italy, 2007. www.uni.com.

[319] UNICEMENTO, UNI EN 1015-11, UNI EN, Italy, 2007. www.uni.com.

[320] S. Jacobsen, B. Arntsen, Aggregate packing and -void saturation in mortar and concrete proportioning, Materials and Structures/Materiaux et Constructions 41 (2008) 703–716. https://doi.org/10.1617/s11527-007-9275-4.

[321] C. Fabiani, A.L. Pisello, Coupling the transient plane source method with a dynamically controlled environment to study PCM-doped building materials, Energy Build 180 (2018) 122–134. https://doi.org/10.1016/j.enbuild.2018.09.008.

[322] C. Fabiani, A.L. Pisello, Coupling controlled environmental forcing and transient plane source method: An innovative thermal characterization procedure for building insulation materials, Appl Therm Eng 130 (2018) 254–263. https://doi.org/10.1016/j.applthermaleng.2017.10.155.

[323] T. Zheng, C. Qian, Y. Su, Influences of different calcium sources on the early age cracks of self-healing cementitious mortar, Biochem Eng J 166 (2021). https://doi.org/10.1016/j.bej.2020.107849.

[324] G. Nagelschmidt, Röntgenographische Untersuchungen an Tonen. I. Die Röntgendiagramme einiger in Tonen vorkommender Mineralien. II. Der Mineralbestand des Mallisser Tones, Z Kristallogr Cryst Mater (1934) 120–145. https://doi.org/10.1524/zkri.1934.87.1.120.

[325] M. Ikram, A. Muhammad Khan, A. Haider, J. Haider, S. Naz, A. Ul-Hamid, A. Shahzadi, W. Nabgan, T. Shujah, I. Shahzadi, S. Ali, Facile Synthesis of La- and Chitosan-Doped CaO Nanoparticles and Their Evaluation for Catalytic and Antimicrobial Potential with Molecular Docking Studies, ACS Omega 7 (2022) 28459–28470. https://doi.org/10.1021/acsomega.2c02790.

[326] V. Vinichenko, V.A. Ryazanova, A.I. Gabitov, Y.A. Udalova, A.S. Salov, Efflorescence processes in exterior wall surface of buildings, in: Materials Science Forum, Trans Tech Publications Ltd, 2019: pp. 115–121. https://doi.org/10.4028/www.scientific.net/MSF.968.115.

[327] R. Malathy, S.R. Rajagopal Sentilkumar, A.R. Prakash, B.B. Das, I.M. Chung, S.H. Kim, M. Prabakaran, Use of Industrial Silica Sand as a Fine Aggregate in Concrete—An Explorative Study, Buildings 12 (2022). https://doi.org/10.3390/buildings12081273.

[328] M.M. Alam, N. Loreal, A. Habib, R. Begum, Mechanical Properties of Synthetic Fibers Reinforced Mortars, Article in International Journal of Scientific and Engineering Research 4 (2013). http://www.ijser.org.

[329] Y. Zeng, A. Tang, Comparison of effects of basalt and polyacrylonitrile fibers on toughness behaviors of lightweight aggregate concrete, Constr Build Mater 282 (2021). https://doi.org/10.1016/j.conbuildmat.2021.122572.

[330] J. Blazy, R. Blazy, Polypropylene fiber reinforced concrete and its application in creating architectural forms of public spaces, Case Studies in Construction Materials 14 (2021). https://doi.org/10.1016/j.cscm.2021.e00549.

[331] S.H. Park, D.J. Kim, G.S. Ryu, K.T. Koh, Tensile behavior of ultra high performance hybrid fiber reinforced concrete, Cem Concr Compos 34 (2012) 172–184. https://doi.org/10.1016/j.cemconcomp.2011.09.009.

[332] S.T. Kang, Y. Lee, Y.D. Park, J.K. Kim, Tensile fracture properties of an Ultra High Performance Fiber Reinforced Concrete (UHPFRC) with steel fiber, Compos Struct 92 (2010) 61–71. https://doi.org/10.1016/j.compstruct.2009.06.012.

[333] Z. Wu, C. Shi, W. He, L. Wu, Effects of steel fiber content and shape on mechanical properties of ultra high performance concrete, Constr Build Mater 103 (2016) 8–14. https://doi.org/10.1016/j.conbuildmat.2015.11.028.

[334] G. Gullì, R. Bertino, F. Grungo, D. Palamara, P. Bruzzaniti, L. Calabrese, Flexural Toughening of Hooked-End Steel Fibers Reinforced Mortars, Applied Science and Engineering Progress 17 (2024) 7030.

[335] C. Sanfilippo, V. Fiore, L. Calabrese, B. Megna, A. Valenza, Impact of Surface Treatment on the Strengthening of Geopolymer Composites Reinforced with Short Sisal Fibers, JOM 76 (2024) 4514–4525. https://doi.org/10.1007/s11837-024-06700-5.

[336] C. Sanfilippo, V. Fiore, L. Calabrese, B. Megna, A. Valenza, Effect of sodium bicarbonate treatment on the properties of sisal fibers and their geopolymer composites, Case Studies in Construction Materials 21 (2024). https://doi.org/10.1016/j.cscm.2024.e03536.

[337] V. Dhand, G. Mittal, K.Y. Rhee, S.J. Park, D. Hui, A short review on basalt fiber reinforced polymer composites, Compos B Eng 73 (2015) 166–180. https://doi.org/10.1016/j.compositesb.2014.12.011.

[338] V. Fiore, T. Scalici, G. Di Bella, A. Valenza, A review on basalt fibre and its composites, Compos B Eng 74 (2015) 74–94. https://doi.org/10.1016/j.compositesb.2014.12.034.

[339] V. Fiore, T. Scalici, L. Calabrese, A. Valenza, E. Proverbio, Effect of external basalt layers on durability behaviour of flax reinforced composites, Compos B Eng 84 (2016) 258–265. https://doi.org/10.1016/j.compositesb.2015.08.087.

[340] G. Gullì, D. Palamara, P. Bruzzaniti, R. Bertino, F. Grungo, L. Calabrese, Flexural Toughening of a Cementitious Mortar Reinforced with Wave-Shaped Short Plastic Fibers, JOM 75 (2023) 537–548. https://doi.org/10.1007/s11837-022-05623-3.

[341] Test Method for Flexural Performance of Fiber-Reinforced Concrete (Using Beam With Third-Point Loading), ASTM International, West Conshohocken, PA, United States, 2012. https://doi.org/10.1520/C1609_C1609M-12.

PhD scholarship co-financed with resources from the
National Operational Programme Research and Innovation 2014-2020 (CCI 2014IT16M2OP005),
European Social Fund resources REACT-EU, Action I.1 “Innovative Doctorates with industrial characterization”, Action IV.4 “Doctorates and research contracts on innovation topics” and Action IV.5 “Doctorates on Green topics”

UNIONE EUROPEA
Fondo Sociale Europeo